Charge-Carrier Transport and Recombination Dynamics in Metal Halide Perovskites



Timothy Crothers
St Edmund Hall
University of Oxford

A thesis submitted for the degree of
Doctor of Philosophy
Hilary 2019

Acknowledgements

Firstly, I would like to thank Laura Herz for her fantastic supervision, mentoring and support over the course of my DPhil. Secondly, I am indebted to Michael Johnston for his great help in the lab, and role as an honorary second supervisor. I would also like to thank the British taxpayer for the funding I have received from the UK's Engineering and Physical Sciences Research Council (EPSRC).

I would like to thank everyone in the Herz-Johnston group, for their support in matters both scientific as well as social. The course of my DPhil has been made much straighter by the help and friendship I have received and by the fortifying effects of regular tea-breaks. I am particularly grateful to Rebecca Milot for her amazing patience and kindness in looking after me and teaching me how to "make electrons dance" and to Jay Patel for his marathon sample making efforts. I would also like to thank Djamshid Damry for his expertise in THz beam alignment and Alex Knight for many helpful conversations and crosswords. A further thanks to all of the helpful strangers on Stack Overflow, who've solved many a programming dilemma.

Outside of work I would particularly like to thank several friends, including Hannah Behrens and Matt Deakin, as well as, Jonathan Mannouch, Oliver Bartlett, Jon Hunt and many others at St. Ebbes Church for their friendship and support. I have also been grateful to be a part of the Oxford University Mountaineering Club, and for the fantastic friends I have met there, Particularly Matt, Tom, Alex, Dave, Mark, Kerry, Lina, Dave and Jody, for their camaraderie and great support when I've been discouraged.

Finally, I would also like to thank my parents and sister for their constant support and for great times of rest when I've been at home. Furthermore, I am deeply thankful to Hannah Crothers for her immeasurable love and support, especially while writing this thesis, it would not have happened without her.

Abstract

Metal halide perovskites (MHPs) are among the most promising materials for use in next generation optoelectronic devices – promising inexpensive, yet efficient solar cells. Although much research has been focused on trap-mediated monomolecular charge-carrier recombination in these materials, there is still uncertainty surrounding the role of intrinsic bimolecular recombination. This thesis addresses the role of bimolecular recombination in MHPs using ultrafast THz spectroscopy and modelling of charge-carrier dynamics.

By developing a new dynamical model, which accounts for not only charge-carrier recombination, but charge-carrier diffusion and photon-reabsorption, it is demonstrated that these charge-carrier transport processes greatly slow the rate of charge-carrier recombination. A model is created, which quantifies the reduction in charge-carrier recombination rate for a MHP sample, due to charge-carrier redistribution. It is established that the effect of charge-carrier transport processes is equivalent to an order of magnitude decrease in the bimolecular recombination rate, for a typical 300-nm thick MHP film.

It is shown that typical measurements of the radiative bimolecular recombination constant in the widely used MHP, $CH_3NH_3PbI_3$, are strongly affected by photon re-absorption, which masks a much larger intrinsic bimolecular recombination rate constant. By investigating a set of films whose thickness varies between 50 nm and 533 nm, it is found that the bimolecular charge recombination rate appears to slow by an order of magnitude as the film thickness increases. However, by using a dynamical model that accounts for photon re-absorption and charge-carrier diffusion it is determined that a single intrinsic bimolecular recombination coefficient, of value $6.8 \times 10^{-10}\,\mathrm{cm^3\,s^{-1}}$, is common to all samples irrespective of film thickness.

The charge-carrier dynamics in a mixed two-dimensional/three-dimensional (2D/3D) MHP film are also studied, using optical-pump-THz-probe spectroscopy and dynamical modelling. It is shown that charge-carrier diffusion efficiently mediates the transport of charge carriers from quasi-2D perovskite domains into 3D domains, meaning that the the quantum confinement of the quasi-2D domains will not prohibit charge-carrier extraction from these films. Furthermore, it is also demonstrated how the blue-shift in the quasi-2D PL spectrum, with respect to the 3D phase absorption onset, allows increased re-absorption of the radiative emission from quasi-2D domains, helping to offset their increased radiative recombination rates.

Contents

List of Publications **xi**

1 Introduction **1**

2 Optoelectronic Properties of Metal Halide Perovskites **7**

2.1 Overview of Metal Halide Perovskites 7

2.2 Metal Halide Perovskite Solar Cells 9

2.2.1 The Evolution of the Perovskite Solar Cell 9

2.2.2 Future Challenges 12

2.2.3 2D Perovskites 13

2.3 Optoelectronic Properties of $MAPbI_3$ 15

2.3.1 Absorption of Light 16

2.3.2 Nature of the Charge Carriers 18

2.3.3 Charge-Carrier Diffusion Length 21

2.3.4 Charge-Carrier Recombination Processes in $MAPbI_3$ 23

2.3.5 Modelling Charge-Carrier Recombination in $MAPbI_3$ 28

3 Experimental Details **33**

3.1 THz Spectroscopy 34

3.1.1 Time-Domain Terahertz Spectroscopy 34

3.1.2 Optical-Pump-Terahertz-Probe Spectroscopy 35

3.2 Experimental Details of the OPTP System 40

3.2.1 Terahertz Generation 40

3.2.2 Terahertz Detection 41

3.2.3 Extraction of Charge-Carrier THz Mobility 44

3.2.4 Description of the OPTP System 45

3.3 Fourier Transform Infra-Red Spectroscopy 51

3.3.1 Operational Principle of a Michelson Interferometer 51

3.3.2 Referencing an FTIR 54

3.3.3 Description of the FTIR System 55

4 Optical and Dynamical Models **57**
4.1 Transfer Matrix Methods . . . 58
4.1.1 Basic Definitions . . . 58
4.1.2 Derivation of Transfer Matrices . . . 59
4.1.3 Calculation of Reflected and Transmitted Power . . . 64
4.1.4 Inclusion of Incoherent Layers . . . 64
4.1.5 Energy Flow From a Lossy Medium . . . 66
4.1.6 Possible Improvements to the Model . . . 68
4.2 Modelling Charge-Carrier Dynamics . . . 70
4.2.1 Representing Charge-Carrier Density . . . 70
4.2.2 Modelling Charge-Carrier Diffusion . . . 73
4.2.3 Modelling Reabsorption of Emitted PL . . . 79
4.2.4 Models Used for Charge-Carrier Recombination . . . 86

5 Modelling Charge-Carrier Dynamics in $MAPbI_3$ **93**
5.1 Simulation of charge-carrier dynamics in $MAPbI_3$ Thin Films . . . 95
5.2 Effect of Transport Processes on Charge-Carrier Dynamics . . . 95
5.3 Quantifying the Differences Between Dynamical Models . . . 102
5.3.1 Comparing Different Representations of the Initial Charge-Carrier Distribution . . . 104
5.3.2 Comparing the Standard and Self-Absorption Models For a Flat Charge-Carrier Distribution . . . 108
5.3.3 Comparing the Standard and Self-Absorption Models in Pump-Probe Experiments . . . 110
5.4 Questions Addressed in this Chapter . . . 116

6 Intrinsic Bimolecular Charge-Carrier Recombination in $MAPbI_3$ **117**
6.1 Experimental Details . . . 120
6.1.1 Evaporation of $MAPbI_3$ thin Films . . . 120
6.1.2 Structural Characterisation . . . 120
6.1.3 Optical Characterisation . . . 121
6.1.4 Optical-Pump-Terahertz-Probe Spectroscopy . . . 121
6.2 Discussion . . . 122
6.3 Questions Addressed in this Chapter . . . 136

7 Charge-Carrier Dynamics in Mixed 2D/3D Perovskite Films **139**
7.1 Sample Preparation . . . 141
7.2 Initial Sample Characterisation . . . 142
7.2.1 Steady State and Time-Resolved Photoluminescence . . . 142
7.2.2 Steady-State Absorption . . . 145
7.2.3 Optical-Pump-Terahertz-Probe Spectroscopy . . . 145

7.3 Modelling Charge-Carrier Dynamics in the Quasi-2D/3D Perovskite . . . 146
7.3.1 Model Used for the Perovskite Film . . . 146
7.3.2 Description of Dynamical Model . . . 150
7.3.3 Correction of the PL Spectrum for Self-Absorption . . . 151
7.4 Fits to THz Photoconductivity Data . . . 154
7.5 Analysis of the Shape of the THz Photoconductivity Transients . . . 158
7.5.1 Impact of Charge-Carrier Diffusion . . . 159
7.5.2 Impact of Photon-Reabsorption . . . 165
7.5.3 Impact of the Thickness of the Quasi-2D Region . . . 172
7.5.4 Summary . . . 176
7.6 Questions Addressed in this Chapter . . . 178

8 Conclusion **181**

List of Abbreviations **185**

Appendices

A Supplementary Derivations for Transfer Matrix Formalism **191**
A.1 Supporting Argument for Derivation of Interface Matrix . . . 191
A.2 The Inverse of the Interface Matrix . . . 192
A.3 Energy Flow Between Two Lossy Media at Normal Incidence . . . 193

B Supporting Information and Methods for Chapter 6 **195**
B.1 Material Preparation . . . 195
B.1.1 Cleaning of Substrates . . . 195
B.1.2 Thermal Co-Evaporation of $MAPbI_3$ . . . 195
B.2 Initial Material Characterisation . . . 197
B.2.1 Scanning Electron Microscopy . . . 197
B.2.2 Grazing Incidence Wide Angle X-Ray Scattering (GIWAXS) . . . 199
B.3 Photoluminescence Spectra . . . 202
B.4 FTIR . . . 204
B.4.1 FTIR Transfer Matrix Model . . . 204
B.4.2 Extraction of Quartz Complex Refractive Index . . . 204
B.4.3 Extraction of Perovskite Complex Refractive Index . . . 206
B.4.4 Comparison of Methods Used to Extract Absorption Coefficient . . . 210
B.4.5 Correction of Absorption Data for Scattering . . . 211
B.5 THz Spectroscopy . . . 213
B.5.1 THz Mobility . . . 213
B.5.2 Global Fits to Photoconductivity Transients . . . 213
B.5.3 PL Redistribution Matrices . . . 216
B.6 Charge carrier decay for Thick and Thin Films . . . 217

C Supporting Information and Methods for Chapter 7 **219**
C.1 Steady-State and Time-Resolved Photoluminescence 219
C.2 Description of the Fitting of THz Photoconductivity Transients 219
C.3 Can Photon Re-absorption Cause a Photoconductivity Rise? 220
C.4 Comparing the Simulations with Real Data 224

References **233**

List of Publications

Crothers, T. W.; Milot, R. L.; Patel, J. B.; Parrott, E. S.; Schlipf, J.; Müller-Buschbaum, P.; Johnston, M. B. and Herz, L. M. 'Photon reabsorption masks intrinsic bimolecular charge-carrier recombination in $CH_3NH_3PbI_3$ perovskite'. *Nano Lett.*, 2017, **17**, 5782–5789.

Davies, C. L.; Filip, M. R.; Patel, J. B.; **Crothers, T. W.**; Verdi, C.; Wright, A. D.; Milot, R. L.; Giustino, F.; Johnston, M. B. and Herz, L. M. 'Bimolecular recombination in methylammonium lead triiodide perovskite is an inverse absorption process'. *Nat. Commun.* 2018, **9**, 293.

Noel, N. K.; Wenger, B.; Habisreutinger, S. N.; Patel, J. B.; **Crothers, T. W.**; Wang, Z.; Nicholas, R. J.; Johnston, M. B.; Herz, L. M. and Snaith, H. J. 'Highly Crystalline Methylammonium Lead Tribromide Perovskite Films for Efficient Photovoltaic Devices'. *ACS Energy Lett.* 2018, **3**, 1233–1240.

Motti S. G.; **Crothers, T. W.**; Yang R; Wang J.; Johnston M. B.; Herz L. M. 'Heterogeneous Photon Recycling and Charge Diffusion Enhance Charge Transport in Quasi-2D Lead-Halide Perovskite Films'. *Nano Lett.*, submitted

1 Introduction

The current world population is estimated to be 7.2 billion and is predicted to grow to 10.9 billion by 2100 [1]. With this rising population comes an increase in energy consumption, with global demand for power set to sky-rocket [2]. At the same time, the energy production sector is under mounting pressure to reduce emissions of greenhouse gases, meaning that renewable sources of energy are increasingly being sought as an alternative to fossil fuels [3].

Solar power is one of the main renewable energy technologies rising to meet this challenge [4] and has consequently become the world's fastest-growing energy source [5]. Whereas expansion of the solar energy market has so far been supported by government incentives, to progress further a new generation of materials is required which can combine high power conversion efficiencies (PCEs) with low processing costs [6].

One of the most promising groups of new materials being developed are metal halide perovskites (MHPs), which have emerged as a new solar cell technology within the last seven years [7]. MHPs are particularly exciting as they have transcended the long established trade-off between cell cost and efficiency; being able to boast PCEs comparable to silicon or CdTe [8], while maintaining low material and processing costs [9].

The remarkable progress of MHP solar cells has been supported by much behind-the-scenes effort, focused on unravelling the fundamental physics which underpins the success of these materials. A wide variety of techniques have been applied to characterise the nature of charge carriers, recombination mechanisms and charge-carrier transport properties in MHPs [10, 11], providing useful insights to inform MHP solar cell design. However, the development of MHPs is still underway, as long-term stability and undesired charge-carrier trapping, caused by material defects still remain challenging[12].

Beyond the charge-carrier losses caused by material defects the ultimate efficiency of a solar cell will be limited by radiative recombination [13, 14], which arises as the reverse process of light-absorption by a solar cell [15, 16]. However, as material processing in MHP solar cells improves towards the radiative limit, the nature of radiative recombination in these materials, and its impact of the charge-carrier dynamics is still not clearly understood. Therefore, the improvement of high-quality perovskite solar cells can be aided by a greater understanding of the intrinsic radiative losses.

The Structure of this Thesis

The focus of this thesis is on understanding radiative recombination of charge carriers in MHPs, using ultra-fast Terahertz (THz) spectroscopy and dynamical modelling. The structure of the thesis is split into three introductory chapters, which describe the relevant literature and technical background of the work, followed by three results chapters.

Chapter 2 sets out the background of MHPs, briefly outlining their history and development as solar devices, before laying out some of the key challenges they must overcome to become commercially viable. The second part of the chapter focusses on the photophysics of these materials, concentrating mainly on the archetypal MHP, methylammonium lead triiodide ($CH_3NH_3PbI_3$ or $MAPbI_3$), and charge-carrier recombination processes in semiconductors.

In Chapter 3, the experimental techniques used to investigate MHPs are described, focussing in particular on optical-pump-Terahertz-probe (OPTP) spectroscopy. This ultrafast spectroscopic technique enables sub-picosecond (ps) measurement of the charge-carrier dynamics and mobility of semiconductors, in a non-contact manner. As OPTP spectroscopy is used throughout the later chapters to study the charge-carrier recombination dynamics in perovskite thin-films, the experimental details and operational principles are described in depth.

Chapter 4 presents a new model for describing the charge-carrier dynamics of MHPs in OPTP experiments. This self-absorption model extends previous models of charge-carrier recombination, by additionally considering the transport of charge carriers through the depth of a perovskite film due to diffusion and photon re-absorption. Details of the model implementation are presented, including the 2D matrices used to represent charge-carrier transport. The transfer matrix formalism used to optically model MHP samples is also outlined.

With the technical details and background literature laid out, the subsequent chapters focus on applying the new self-absorption model to understand the charge-carrier dynamics within different MHP thin-films. As each chapter is described, the key points which it addresses are listed. The main MHP material which is considered in these chapters is $CH_3NH_3PbI_3$ ($MAPbI_3$), as this MHP material has been widely used, both in solar cells, as well as in fundamental studies.

Chapter 5 analyses how charge-carrier diffusion and photon re-absorption affect the charge-carrier dynamics in a set of simulated $MAPbI_3$ films, contrasting dynamical simulations with and without these charge-carrier transport processes. Having demonstrated that charge-carrier transport and, more generally, the distribution of charge carriers within a perovskite film dramatically impact bimolecular recombination, the chapter then quantifies the differences between the self-absorption model and previous work, which

has not accounted for charge-carrier transport.

Important questions addressed include:

- **What are the effects of charge-carrier diffusion and photon re-absorption on the charge-carrier recombination rate in $MAPbI_3$ thin films?**
- **When trying to determine the bimolecular recombination rate of a perovskite film, is the spatial distribution of charge carriers important?**
- **Can a quantitative link be made between bimolecular recombination rates reported in previous studies and those predicted by the new self-absorption model?**

In Chapter 6 the charge-carrier dynamics in a set of $MAPbI_3$ films, whose thicknesses vary between 50 nm and 533 nm, is investigated using OPTP spectroscopy. Although the rate of charge-carrier recombination appears to slow down in the thicker $MAPbI_3$ films, using the self-absorption model it is shown that there is a single intrinsic bimolecular recombination rate of $6.8 \times 10^{-10}\,cm^3\,s^{-1}$, common to all films.

Important questions addressed include:

- **Why does the charge-carrier recombination rate in the $MAPbI_3$ films studied show a dependence on the film thickness?**
- **If bimolecular recombination in $MAPbI_3$ is intrinsic, how can this be reconciled with the wide range of values reported in literature?**
- **How do the transport layers in a MHP device affect radiative losses?**

Chapter 7 describes a study of the charge-carrier dynamics in a perovskite film containing a mix of 3D $MAPbI_3$ and quasi-2D perovskite domains. Such mixed 2D/3D perovskite films are of great interest, as compared to conventional 3D MHP materials, they show improved long-term stability. OPTP spectroscopy and modelling are used to

study the poorly-understood transfer of charge carriers between the quasi-2D and 3D domains and additionally, the role of photon re-absorption in these materials is addressed. Significantly, this represents the first device-level modelling of charge-carrier transfer in these complicated quasi-2D structures.

Important questions addressed include:

- **Is charge-carrier transfer between the quasi-2D and 3D domains in the mixed 2D/3D perovskite film mediated by charge-carrier diffusion or photon re-absorption?**
- **Does the current study provide evidence for charge-carrier transfer from the quasi-2D region into the 3D region and/or from the 3D region into the quasi-2D region?**
- **How do the charge-carrier dynamics in the mixed 2D/3D perovskite film compare with those of regular 3D $MAPbI_3$?**
- **How does the blue-shifting of the quasi-2D perovskite PL affect the charge-carrier dynamics in these samples?**

Finally, in Chapter 8 a brief summary of the results presented in this thesis is given, along with a future outlook.

2

Optoelectronic Properties of Metal Halide Perovskites

Contents

2.1 Overview of Metal Halide Perovskites 7
2.2 Metal Halide Perovskite Solar Cells 9
2.2.1 The Evolution of the Perovskite Solar Cell 9
2.2.2 Future Challenges 12
2.2.3 2D Perovskites 13
2.3 Optoelectronic Properties of $MAPbI_3$ 15
2.3.1 Absorption of Light 16
2.3.2 Nature of the Charge Carriers 18
2.3.3 Charge-Carrier Diffusion Length 21
2.3.4 Charge-Carrier Recombination Processes in $MAPbI_3$ 23
2.3.5 Modelling Charge-Carrier Recombination in $MAPbI_3$ 28

2.1 Overview of Metal Halide Perovskites

The term 'perovskite' refers to any material with the crystal structure of $CaTiO_3$ (named after the Russian Minerologist Count Lev Perovski [17]) and encompasses a large family of structures. Generically, the perovskite structure has the formula ABX_3, as shown in Figure 2.1. The A site is in the centre of the unit cell, the B site is at the origin and the X sites are at the {1/2, 1/2, 0} positions. As there is a large range of possible choices for each of

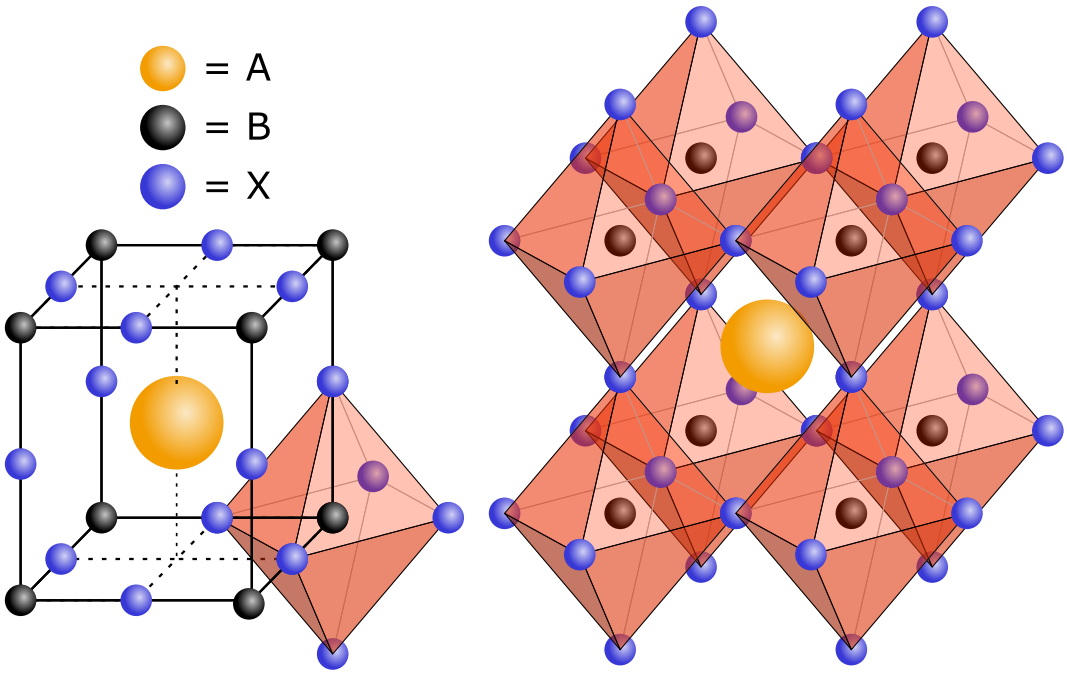


Figure 2.1: Diagram illustrating the unit cell of a generic perovskite crystal structure on the left, along with a view of the BX_3 octahedra, to the right. The idealised cubic structure is shown, but tetragonal and orthorhombic structures are also possible.

the A, B and X ions, there are many possible perovskite materials, although the structure will only be stable for certain combinations of ionic radii [18, 19]. Certain perovskites, notably those with oxygen or halides on the X sites have been heavily researched, as they can display a wide range of useful properties, such as superconductivity [20].

The focus of this thesis is on a class of perovskites known as metal halide perovskites (MHPs), in which the A cation is an organic species (or caesium), the B cation is lead, and the X sites are occupied by halides. This results in a crystal structure composed of corner-sharing metal halide octahedra held in position by the organic molecule, as indicated on the right side of Figure 2.1.

MHPs are of specific interest as they have excellent optoelectronic properties for use in solar cells and as light emitting diodes (LEDs). In keeping with their partly-organic nature MHPs can be easily processed using spin-coating [21], thermal evaporation [22] or large-scale roll-to-roll processes [23, 24]. Paired with this easy processing, lead-halide

perovskite solar cells also boast excellent power-conversion efficiencies (PCEs), with device efficiency having developed rapidly [25–27] such that it is now on parity with CdTe and multi-crystalline silicon [8]. It is this combination of high PCE with low processing and material costs which sets MHPs apart from other photovoltaic technologies [28].

In the following sections an overview of the development of perovskite solar cells is given, before describing their optoelectronic properties. A particular focus is given here to the archetypal MHP, methylammonium lead triiodide, ($CH_3NH_3PbI_3$ or simply $MAPbI_3$), which is the subject of the investigations carried out in later chapters.

2.2 Metal Halide Perovskite Solar Cells

2.2.1 The Evolution of the Perovskite Solar Cell

Despite the current success and high efficiencies of MHP solar cells, they have a surprisingly brief history, spanning less than ten years. Although many MHP structures had been synthesised and transistors developed using a tin MHP [29] in the 20$^{\text{th}}$ century, it was not until 2009 that perovskites were first incorporated into a solar cell.

The first application of MHPs to photovoltaics was the use of $MAPbBr_3$ as light absorbers in dye sensitised solar cells (DSSCs) [30], where they replaced the light absorbing dyes [31]. These perovskite-sensitised cells used a thin layer of perovskite to absorb light, but relied on a mesoporous TiO_2 scaffold and a solid or liquid hole transport layer to transport the charge carriers [32]. Using this architecture, the PCE of these perovskite-sensitised DSSCs improved rapidly, reaching a record value of 9.7%[33]

A step change in cell design came in 2012 when Snaith *et al.* replaced the n-type TiO_2 with an Al_2O_3 scaffold, which has a wide band-gap of 7–9 eV [25], therefore blocking transfer of electrons from the perovskite into the Al_2O_3. They found that the insulating Al_2O_3 scaffold increased the open-circuit voltage (V_{oc}) and PCE of the perovskite cell, meaning that the transport of electrons through the perovskite was actually more efficient

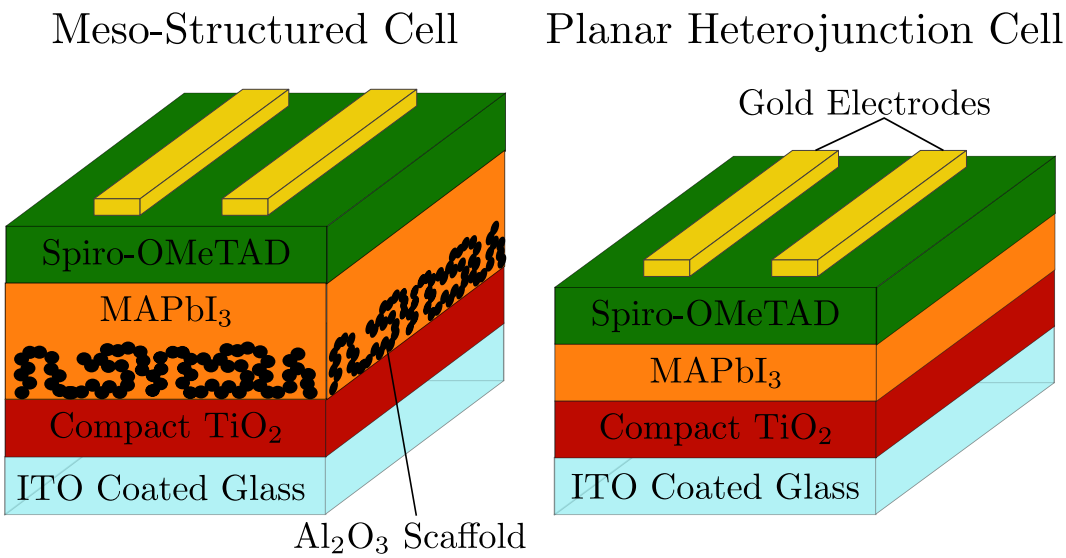


Figure 2.2: Cross-sectional diagram showing meso-structured and planar device architectures. While the meso-structured device employs an Al_2O_3 scaffold to reduce pinholes in the $MAPbI_3$ layer, the planar device relies upon the deposition procedure to produce a continuous $MAPbI_3$ film. In this representative example, holes are extracted by the Spiro-OMeTAD layer, while compact TiO_2 removes electrons from the perovskite.

than through the TiO_2 layer. Using the perovskite layer to both absorb light and transport the electrons removes the need for an inefficient TiO_2 scaffold and avoids the problem of having to optimise TiO_2 pore size [34]. With this confirmation of the charge transport properties, perovskite solar cells were established as an independent technology, rather than a subclass of DSSCs. This first type of MHP solar cell is known as a meso-structured device, and has the architecture shown on the left side of Figure 2.2.

Following the observed success of the Al_2O_3 scaffold, Ball *et al.* investigated the effect of the scaffold thickness [35], finding that the scaffold acted to increase uniformity of the perovskite layer, reducing pinholes and ensuring better coverage. However, it also reduced the short-circuit current (J_{sc}) by introducing smaller perovskite grain sizes inside the scaffold, lowering the quality of the film and leading to more charge trapping by defects at the grain boundaries. These findings led to the development of a new "planar heterojunction" cell architecture, where the scaffold was completely removed and replaced with a thin layer of compact TiO_2 on top of which the perovskite layer was deposited.

An outline of the architecture of a planar heterojunction cell is shown on the right side of Figure 2.2. The planar heterojunction cell was found by Liu *et al.* to give an efficiency of over 15% [26]. This improved performance was attributed to higher phase purity and lower amounts of PbI_2 in the vapour-deposited cells. Early solution processed planar heterojunction devices were also plagued by pinholes, which reduce the shunt resistance of a device, however, significant improvements in the deposition procedure have overcome this obstacle, giving uniform perovskite layers [36, 37].

The development of the planar heterojunction cell was the last major shift in device design. Further improvements to device efficiency have focussed on the materials and processing as opposed to the cell architecture. These improvements have come from refinements of the morphology and composition of the perovskite layer itself, as well as experimentation with the other layers in the device stack. Through a rapid period of development, this optimisation of the planar heterojunction led to a PCE of over 20% [38] in 2015, only six years after MHPs had first been used in DSSCs. The breaking of this 20% PCE barrier was a much sought after milestone, demonstrating that MHP solar cells are no longer simply an emerging technology, but are now comparable in performance to Si or CdTe, as shown in Figure 2.3.

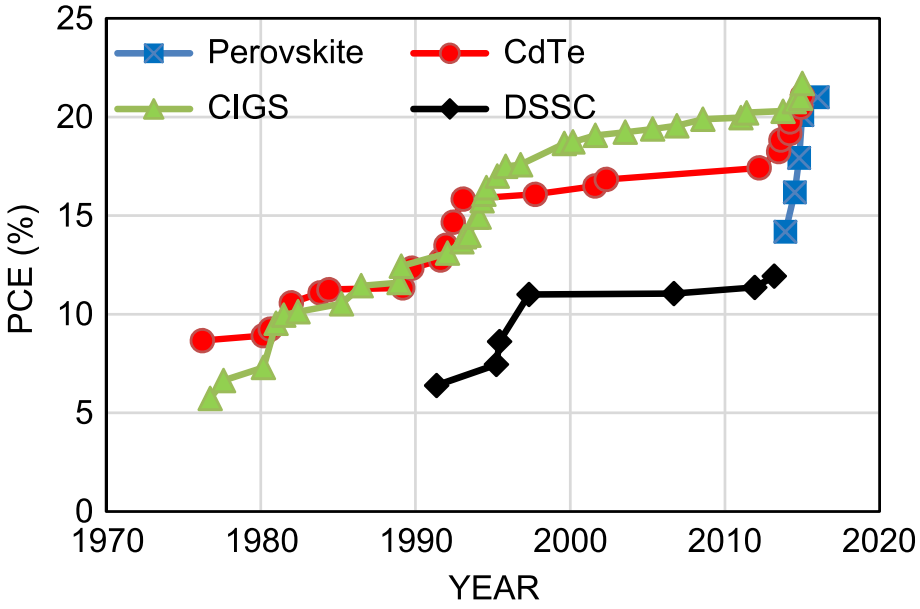


Figure 2.3: Graph showing the rise in power conversion efficiency (PCE) of Perovskite Solar cells, reproduced from [39], with permission from Elsevier.

2.2.2 Future Challenges

Despite the success of the perovskite solar cells, there remain many unanswered questions about their operation and a range of challenges which still need to be addressed.

One serious barrier which must be overcome before any real-world use of MHPs is the degradation of current devices when exposed to water or increased temperatures [40]. As cycles of heating, as well as atmospheric moisture will be experienced by any solar module, this instability must be overcome.

As well as extrinsic factors, MHP solar cells also display different current-voltage curves when scanning from open-circuit voltage (V_{oc}) to short-circuit, compared with the reverse scan. This is often referred to as hysteresis and represents an intrinsic instability [41], linked with the movement of ions under solar device operating conditions [42]. This hysteresis has also linked with the presence of traps at the interfaces between the perovskite and transport layers [43, 44], suggesting that, to achieve a stable power output from a perovskite cell, the bulk material quality as well as the interfaces must be carefully engineered. Such stabilisation of the power output is essential if MHP solar

cells are to be held at their maximum power points [45].

A third challenge is to refine the electron and hole transport layers used in MHP solar cells. The interfaces between these transport layers and the perovskite are critical to device performance as they impact the structure of the perovskite and the density of trap sites present at the interfaces [46]. Additionally, the module price of an MHP cell is currently dominated by the cost of the hole transport material, spiro-OMeTAD [12]. This means that for perovskites to be competitive with established PV technologies, further work on new lower-cost interface layers is required.

Finally, as material processing improves, radiative bimolecular recombination will become the dominant charge-carrier loss mechanism, with internal photoluminescence quantum efficiencies of over 90% already being reported at AM 1.5 [47]. Where the PCE is limited by radiative charge-carrier recombination, MHP solar cells can be further improved by employing light trapping designs to minimise radiative losses [48]. This is the challenge primarily addressed by the work in this thesis.

However, considering the rapid progress of MHP solar cells so far, there is every possibility that these challenges will be overcome. This will be made easier through a better understanding of the fundamental properties of the perovskite, both in isolation as well as in conjunction with charge-carrier transport layers.

2.2.3 2D Perovskites

In $MAPbI_3$ and other MHPs which have been successfully applied in solar cells, the organic cation is always quite small, producing the 3D network of BX_6^{4-} shown in Figure 2.1. However, if the $CH_3NH_3^+$ cation is replaced by a large organic cation, the BX_6^{4-} octahedra will become separated, producing quantum confinement in the layers. These pure 2D perovskite structures can have exciton binding energies of more than 300 meV [49], making them poor materials for solar cells. Yet if a mix of small and

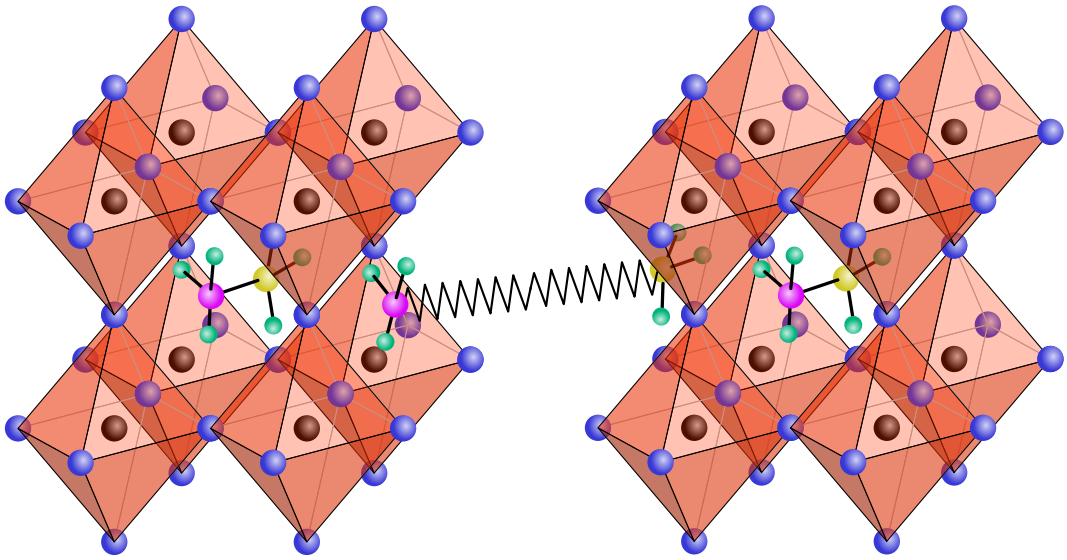


Figure 2.4: An illustration of a mixed 2D/3D perovskite structure, showing how large organic cations cause separation of the BX_3 octahedra, forming dielectric barriers and creating Quasi-2D regions of perovskite.

large organic cations is used, a quasi-2D perovskite can be formed, having regions of 3D perovskite, separated by planes of the large organic cations, as illustrated in Figure 2.4; these structures are known as Ruddlesden–Popper Perovskites. Such layered 2D/3D structures have been demonstrated to have an increased resistance to degredation by moisture, but typically also have lower a PCE, compared with $MAPbI_3$ [50]. Additionally, these structures show reduced current-voltage hysteresis in PV devices [51], and the variation in the size of the organic cations offers another degree of freedom for further optimisation [52]. Due to their increased stability, layered perovskite structures are being explored as a possible route towards increasing the stability of MHP solar cells, with the reported stabilised power output being as high as 19.9% [53–56].

The interest in Ruddleston-Popper perovskites also has expanded beyond creating more stable solar cells, with their incorporation into a range of other optoelectronic devices including transistors, lasers and LEDs [57–59] For light emitting devices, the large exciton binding energy of these materials is an asset, increasing the efficiency of radiative recombination over non-radiative losses. Concentration of charge carriers in

the low band-gap regions leads to higher radiative efficiencies [60], and lower thresholds for amplified stimulated emission [57].

However, as with 3D perovskites there are still many unanswered questions surrounding the charge-carrier dynamics in this group of materials, particularly over the mechanism for charge-carrier separation within the perovskite film [61]. Therefore, although Ruddleston-Popper perovskites have already shown huge promise in solar cells and as light emitters, further work is needed to unravel the charge-carrier dynamics within these structures.

2.3 Optoelectronic Properties of $MAPbI_3$

The meteoric rise in MHP solar cell performance has been supported by extensive studies, which have helped to expose the basic properties of $MAPbI_3$ and other MHPs, highlighting the similarity of their optoelectronic properties to those of traditional inorganic semiconductors. In this section, the optoelectronic properties of $MAPbI_3$ will be summarised, in terms of the operational steps of a solar cell, from absorption of light by the absorbing material, (or active layer) to the extraction of charge carriers into the charge transfer layers on each side of the active layer and at each point the relevant aspects of $MAPbI_3$ will be discussed.

However, it is first important to note that while MHP solar cells are composed of a stack of many layers, in spectroscopic studies it is more common to study perovskite films in isolation. As such, Figure 2.5 shows a cross-section of both a generic planar heterojunction device structure and a spectroscopic sample, consisting of only a $MAPbI_3$ film supported by a quartz substrate. This allows fundamental studies of the perovskite material to be conducted, independent of the other components of a real device.

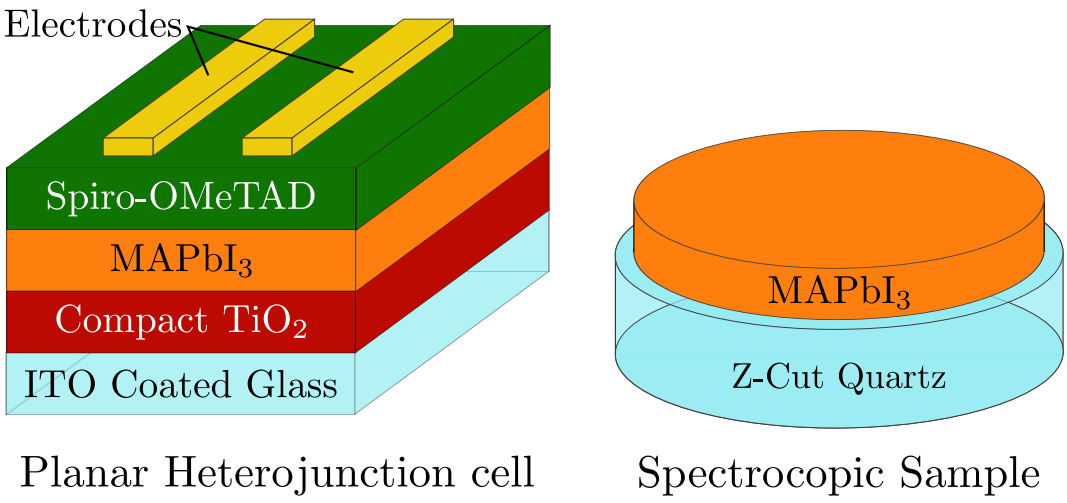


Figure 2.5: Cross-sectional diagram showing the difference between a sample used in a spectroscopic study and a planar heterojunction MHP solar cell. Particularly for THz studies, the highly conducting ITO and gold electrodes must be removed as they are highly reflective to THz radiation.

2.3.1 Absorption of Light

The first requirement for a good active layer in a solar cell is that it must be able to efficiently absorb sunlight. The ability of a material to absorb light is fundamentally determined by the band-gap and the strength of the above-gap absorption.

The Optimum Band-Gap. The constraint of absorbing as much of incident solar spectrum as possible favours a low band-gap. However, this must be balanced against the drop in output power caused by the reduction of the V_{oc} in lower band-gap cells [62]. The satisfaction of these two constraints famously led to the calculation, by Shockley and Queisser, of an optimal band-gap of 1.1 eV for a single-junction solar cell, illuminated by a black body with temperature 6000 K [14]. More recently, rather than modelling the sun as a black body, the PV (Photovoltaic) community has adopted a standardised solar spectrum known as the A.M. (air mass) 1.5 spectrum, which better simulates sunlight at moderate latitudes [63]. With this change in the illuminating spectrum, the maximum PCE is shifted to 33%, for a band-gap of 1.34 eV [64].

Traditional photovoltaic technologies have band-gaps around this value, with the band-gap in GaAs being 1.34 eV, while silicon is slightly lower at 1.12 eV [65]. For $MAPbI_3$, the band-gap value is reported to be around 1.6 eV at room temperature [15, 66, 67]. This sits close to the optimal value, meaning that the predicted maximum PCE is just over 30% [64].

In fact, the high band-gap of $MAPbI_3$ opens the possibility of creating a silicon-perovskite tandem cell, with the MHP more efficiently collecting the high energy photons. By employing a mixed-halide MHP with an optimum band-gap, such silicon perovskite tandem devices could reach a theoretical PCE of over 41% [68]. With such high efficiencies possible, significant effort has been invested into developing silicon-perovskite tandem cells and a PCE of 28% has been achieved [69–71]. Since perovskite solar cells will face immense competition from already-established silicon cells, tandem devices could prove a more disruptive technology than single junction MHP cells [72].

The Strength of Above-Gap Absorption. An efficient active layer in a solar cell, must not simply have the correct band-gap, but needs to strongly absorb any incident above-gap light. The strength of absorption determines the volume of material required to absorb incident light. This means that a thinner active layer can be used to absorb the same amount of light, if the absorption coefficient of a material is larger.

Direct semiconductors (CdTe, GaAs) are typically able to absorb most of the available light in under a µm. In contrast silicon cells are much thicker, often being 100s of µm thick [73, 74], as the band-gap is indirect and the absorption much weaker.

The nature of the band-gap in $MAPbI_3$ has been the subject of controversy over the last few years. Several calculations of the band structure from first principle have suggested that the electronic band-gap may be indirect [75, 76]. However, in terms of the optical band-gap, $MAPbI_3$ clearly displays the strong absorption onset characteristic of a direct gap semiconductor [31, 77]. Therefore, regardless of whether the band-gap

may be very slightly indirect at low temperatures, in discussing room temperature absorption it can be confidently considered as direct. This strong absorption means that typically only 300 nm of $MAPbI_3$ is required to almost completely absorb incident light. Such a thin active layer is a benefit, as it reduces the distance charge carriers must travel to be extracted from the device.

The near optimal band-gap and strong optical absorption of $MAPbI_3$ make it comparable to other successful direct-gap semiconductors such as GaAs [78].

The Shape of the Absorption Edge. Finally, by investigating the sharpness of the absorption edge, a measure of the material quality of a semiconductor can be determined. Typically the absorption onset will show an exponential rise in the absorption at the band edge which varies with temperature [79]. This is known as an Urbach tail, and is caused by sub-gap trap states related to defects in the material which provide a density of states for transitions below the band-gap [78]. Qualitatively speaking, the longer the Urbach tail, the greater the number of trap states present in the material, although the Urbach tail also includes a temperature-dependant contribution from phonon-broadening [80].

In $MAPbI_3$ there is only a very small Urbach energy of around 15 meV at room temperature [17, 81], which indicates a high material quality, although there is some sample-to-sample variation in the shape of the absorption spectrum, associated with different amounts of light scattering [82]. This value is much lower than is typically found in other solution processed materials which tend to have a large degree of disorder. Indeed the steepness of the absorption edge and the strength of the absorption in $MAPbI_3$ is comparable to CdTe and GaAs [83].

2.3.2 Nature of the Charge Carriers

The absorption of a photon results in the promotion of an electron into the conduction band leaving behind a hole in the valance band. The next requirement for a good

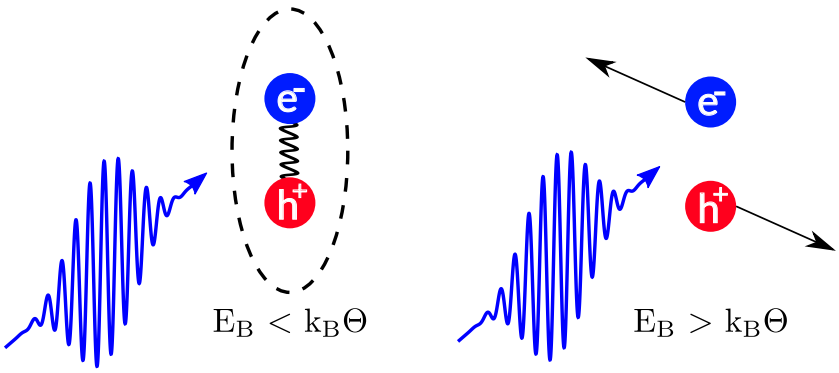


Figure 2.6: Illustration of the formation of an exciton or free electron and hole, depending on the strength of the exciton binding energy E_B, relative to the thermal energy $k_B\Theta$.

active layer is that the resultant charge carriers can be separated from each other and extracted as current.

Excitons or Free Charges? When an electron-hole pair is generated in a semiconductor, the two charge carriers can either separate as free charge carriers, or remain electrostatically bound together, forming an exciton, as illustrated in Figure 2.6. For a given material, exciton formation depends on the strength of the electrostatic attraction between the charge carriers (known as the exciton binding energy, E_B), compared to the thermal energy, $k_B\Theta$.

Inorganic semiconductors typically have small exciton binding energies, with E_B being only 4.4 meV in GaAs and 11 meV in CdTe [84, 85]. At room temperature (298 K), the thermal energy $k_B\Theta = 25.7$ meV, meaning that excitons in these materials will be thermally dissociated, even without an external electric field. Organic semiconductors typically have much larger exciton binding energies on the order of hundreds of meV [86], meaning that, even at room temperature, absorption results in the formation of stable excitons.

Whether free charge carriers or excitons are initially formed in the absorbing layer of a solar cell is important, as for any current to be extracted the exciton binding energy must be overcome and the charge carriers separated. For inorganic semiconductors where E_B is small, the charge carriers can be separated using the electric field created by the different

work functions of the layers adjacent to the absorber. However, the situation in organic PV cells is more complex, as the more tightly bound excitons cannot be broken apart by an electric field across the absorbing layer. Instead, the active layer in organic PV cells is composed of a blend of (an electron) donor and acceptor material. Light absorption in each material generates excitons, which are separated by the strong electric field formed at the junction between the two materials [87]. As excitons have very short lifetimes and diffusion lengths, the two materials are blended together on a 10 nm scale, meaning no point in the active layer is far from a junction [88]. This architecture is known as a bulk heterojunction, as the interface between donor and acceptor is ditributed throughout the bulk of the active layer. Free charge carriers are generated only when excitons diffuse to the donor/acceptor interface, meaning that organic PV is severely limited by exciton lifetimes and the difficulty in the initial separation of charge carriers [89, 90].

Charge Carriers in $MAPbI_3$ As discussed above, the formation of free charge carriers rather than excitons is highly desirable for solar cells, therefore, it is important to understand the nature of the initially generated charge carriers in $MAPbI_3$, and to determine E_B.

A range of experimental methods have been employed to calculate the exciton binding energy in $MAPbI_3$, including studying the temperature-dependent broadening of the absorption edge [91], fits of Elliot's theory to the absorption spectrum [15, 92] or through magnetoabsorption measurements [93]. Across these different techniques a range of values for E_B from 2 to 50 meV have been produced [10]. The small values found for E_B point towards free charge carriers at room temperature, while investigations using both OPTP spectroscopy [94] and transient absorption (TA) [95, 96] have independently detected the existence of free charge carriers and a lack of excitons in room temperature studies of $MAPbI_3$.

Given the weak binding energy and the evidence from pump-probe experiments, a consensus has now been reached that free charge carriers, rather than excitons are the dominant species in $MAPbI_3$ at room temperature.

2.3.3 Charge-Carrier Diffusion Length

Once charge carriers have been formed in a material, they must be able to travel out of the active layer before they recombine. The material properties which determine whether charge carriers are able to be extracted from the active layer are: the charge-carrier mobility, μ, which determines the rate at which charge carriers travel and the lifetime τ, which is the time window for charge carriers to reach the interfaces with their respective transport layers and be extracted. These two properties can be combined to calculate the average distance travelled by a charge carrier, known as the diffusion length. At a given temperature, Θ, this is given by

$$L_d = \sqrt{\frac{\mu\tau \mathrm{k_B}\Theta}{e}}, \tag{2.1}$$

and acts as a key metric for characterising charge-carrier transport in a semiconductor.

The diffusion length sets an upper limit on the thickness of the active layer, since only charge carriers within L_d of a transport layer can be extracted. This means that while having a thicker active layer will lead to more light being absorbed, the resulting increase in current is limited by L_d. Therefore, an effective active layer must have a short absorption length and a long charge-carrier diffusion length, which requires charge carriers to have a long lifetime and a high mobility.

In $MAPbI_3$, measurements of the charge-carrier mobility using THz spectroscopy have reported a value in the region of 10 to 30 $\mathrm{cm^2\,V^{-1}\,s^{-1}}$ [94, 97], a value supported by DFT calculations [98]. This sits two orders of magnitude above the values typical for organic semiconductors [99], but at least two orders of magnitude lower than GaAs or Silicon [100]. Therefore, the context behind claims of high charge-carrier mobility

in MHPs are with respect to other solution processed semiconductors, rather than traditional inorganic semiconductors.

Due to these respectable charge-carrier mobility values, as well as long lifetimes (discussed in the next section), MHPs have demonstrated excellent charge-carrier diffusion lengths, exceeding the ∼300 nm thickness used in planar heterojunction devices. Indeed, the success of the planar hetreojunction cells in itself demonstrates the ambipolar transport properties of the perovskite, as it relies upon both electrons and holes being transported across the film. Crucially, the electron and hole were found to have similar diffusion lengths, preventing the unwanted build up of space charge inside the perovskite layer [77].

Initial estimates of the electron-hole diffusion lengths were reported as ∼100nm for $MAPbI_3$ and above 1 μm for a mixed halide perovskite $MAPbI_{3-x}Cl_x$ [101]. Since these first results, a number of studies using transient impedance, and hall probe measurements have reported charge-carrier diffusion lengths of tens or hundreds of µm, particularly in single crystals [102, 103]. This would mean that the diffusion length in $MAPbI_3$ is beyond that seen in other direct gap semiconductors (the minority carrier diffusion lengths are around 20 µm in GaAs and only a few microns in GaN [104]). However, care must be taken, as in other semiconductors diffusion lengths are measured when both charge carriers are present, while in transient impedance measurements of single crystals, only one carrier may be present throughout the bulk of the crystal [105]. Because of this, TRPL measurements may provide charge-carrier lifetimes which can be more directly equated to other materials, since PL is only generated in regions where electrons and holes are both present. Regardless of any disputes over the charge-carrier diffusion lengths reported in single crystals, the crucial point is that typical charge-carrier diffusion lengths in $MAPbI_3$ clearly exceed the width of the active layers found in planar heterojunction solar cells. This means that charge carriers will be able to travel a sufficient distance to be efficiently extracted from the perovskite layer, and so diffusion length will not limit cell performance.

As a final point, in order for current to be drawn from a solar cell, good ohmic contact must be made between the absorption layer and the charge-carrier transfer layers which extract the electrons and holes. However, as this thesis is primarily concerned with the fundamental properties of the perovskite layer itself, a discussion of these transport layers is not included.

2.3.4 Charge-Carrier Recombination Processes in $MAPbI_3$

The final property necessary for an effective absorbing layer is a long charge-carrier lifetime. This is essential, as an aggressive recombination rate will mean that many of the absorbed charge carriers will be lost before being extracted from the active layer. The recombination of free charge carriers in a semiconductor, such as $MAPbI_3$, can be described by a rate equation

$$\frac{dn}{dt} = -R(n)n \tag{2.2}$$

where n is the charge-carrier density and R is the recombination rate. There are a number of different processes by which charge carriers can recombine and so R is composed of several terms:

$$R(n) = k_1 + k_2 n + k_3 n^2 \tag{2.3}$$

Here, k_3 represents the Auger recombination rate constant, k_2 the bimolecular recombination rate constant and k_1 the monomolecular recombination rate. Since the three processes have a different dependence on n, they will each be dominant in a certain n range, as shown in Figure 2.7. The different charge-carrier recombination processes will now be discussed, highlighting in each case the time-scales and fluences at which they are important.

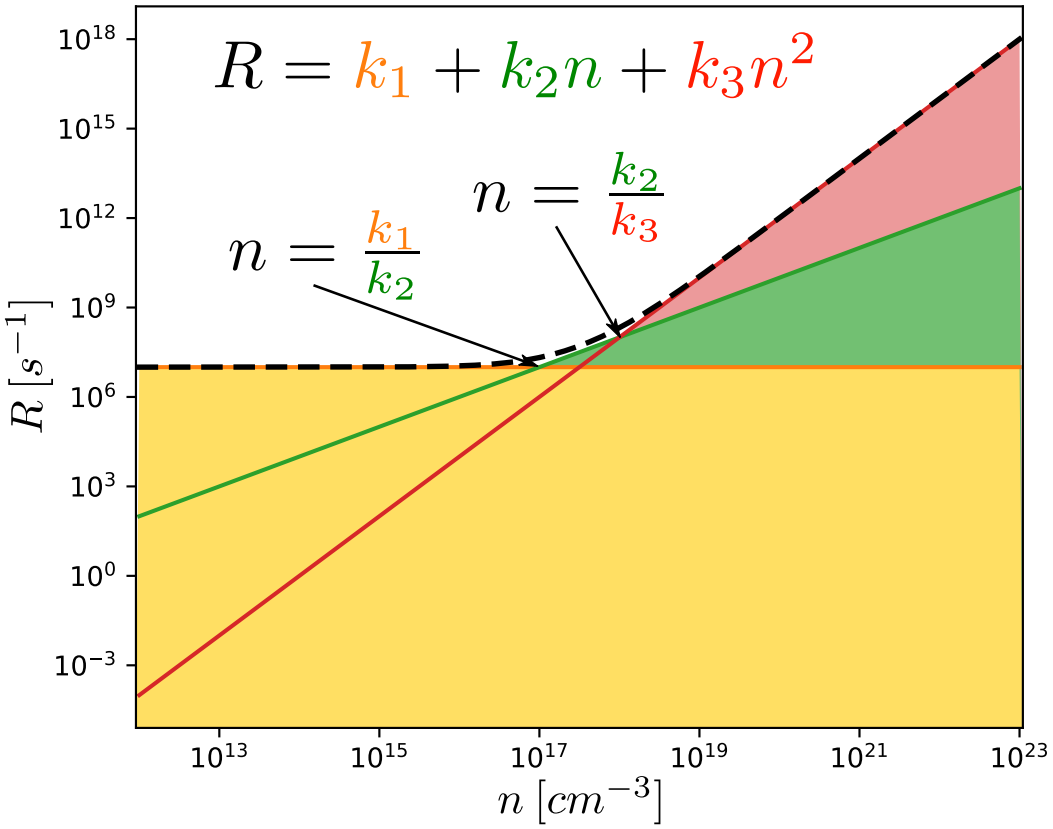


Figure 2.7: The charge-carrier recombination rate for free charge-carrier in a semiconductor, R, as a function of charge-carrier density n. The individual contributions from monomolecular, bimolecular and Auger recombination are shown by the yellow, green and red lines respectively. The two labelled points on the graph mark the crossover into the bimolecular-dominated and Auger-dominated regimes. Values of $k_3 = 10^{-28}\,\mathrm{cm^6 s^{-1}}$, $k_2 = 10^{-10}\,\mathrm{cm^3\,s^{-1}}$ and $k_1 = 10^{-7}\,\mathrm{s^{-1}}$ are assumed.

2.3.4.1 Free-Charge-Carrier Recombination Processes

Monomolecular Recombination. Monomolecular recombination is principally trap mediated, with free carriers falling into defect states located in the band-gap. When a trap state is empty it can capture electrons from the conduction band, and similarly when the trap state is filled it can capture holes from the valance band. This type of recombination is known as Shockley Read Hall (SRH) recombination [106, 107].

In this simplified picture, the rate of monomolecular recombination depends on the density of traps, rather than n, therefore as n increases, SRH recombination increases only linearly. This means, while it will be dominant at the charge-carrier densities of 10^{15}–$10^{16}\,\mathrm{cm^{-3}}$ present in perovskite films under AM 1.5 illumination [108], it will not be

the dominant recombination mechanism at the higher fluences used in OPTP experiments, where $n > 10^{18}\,\mathrm{cm}^{-3}$. Additionally, since $MAPbI_3$ typically displays a monomolecular lifetime of 100s of ns [10], on the timescale of pump-probe experiments (with a maximum time delay of 1-2 ns) monomolecular recombination will be too slow to be observed [94].

A key distinction between SRH recombination and the other recombination mechanisms in 2.4, is that SRH is not an intrinsic loss mechanism. Instead, it is mediated by traps, which are formed by defects and imperfections in the crystal structure [109]. As the density of defects is closely tied to the microstruture of the MHP, the monomolecular recombination rate is therefore highly dependent on the sample fabrication method and a wide range of monomolecular lifetimes has been measured for MHPs, ranging from ns–µs [10].

The nature of monomolecular charge-carrier recombination is further complicated, as even within a given MHP film, defects will not be evenly distributed and lifetimes will show a spatial variation. In particular, grain boundaries [110, 111] and the interfaces of the MHP film with transport layers [112] have been investigated as potential hotspots for SRH recombination. However, as yet a comprehensive understanding of the formation and nature of the traps in $MAPbI_3$ has not been formed.

Even without a complete understanding of the trap states, much effort has been invested into improving material quality to reduce the trap density [113–115]. By lowering the trap density, monomolecular charge-carrier lifetimes in lead-halide perovskites can be extended to more than 1 µs [116, 117] ($k_1 = 10^{-6}\,\mathrm{s}^{-1}$). This is critical to improving device performance, as SRH recombination is currently the dominant mechanism of charge-carrier recombination under AM 1.5 illumination.

Bimolecular Recombination. Bimolecular recombination is the recombination of an electron with a hole, producing either a photon. As can be seen from Figure 2.7, this is a second order process, scaling proportional to n^2, since it requires both a hole and an

electron. Using Equation 2.3, it can be seen that when $n > {}^{k_1}/_{k_2}$, bimolecular recombination will exceed monomolecular recombination, becoming the dominant recombination pathway across the n range of 10^{17}–$10^{19}\,\mathrm{cm}^{-3}$. OPTP spectroscopy principally measures the radiative recombination regime, as charge carriers are generated within a very narrow time-window by an amplified fs laser pulse, resulting in large values of n.

Bimolecular recombination can also be classified into geminate and non-geminate recombination. Geminate recombination occurs in the same spatial location as generation and is typical in organic semiconductors where two polarons formed by the dissociation of an exciton may recombine. Bimolecular recombination can also be non-geminate, as is the case in $MAPbI_3$ at room temperature, where bimolecular recombination is between charge carriers which are unrelated by generation.

The rate of the non-geminate recombination in low charge-carrier mobility semiconductors is often understood in terms of the Langevin model [118, 119], a kinetic theory model which states that, when opposite charges diffusing through a material pass within a capture radius of each other, they recombine. The Langevin model is widely used to describe charge carriers in organic semiconductors [120] and was initially proposed as a model for bimolecular recombination in $MAPbI_3$. However, it has been widely demostrated that bimolecular recombination in $MAPbI_3$ is 2–5 orders of magnitude slower than the Langevin model would suggest [94, 121, 122].

Several possible mechanisms have been proposed to explain this "slow" bimolecular recombination in $MAPbI_3$. One interpretation of the non-Langevin recombination is that the polar nature of $MAPbI_3$ spatially separates the charge carriers [94, 121], reducing the possibility of recombination, as previously postulated for other disordered semiconductors [123]. Ab Initio calculations have also suggested a slightly indirect band-gap [124] or Rashba-splitting [76] may slow charge-carrier recombination. However, no conclusive evidence has been reported to confirm any of these theories.

Another point of view, from the world of inorganic semiconductors, characterises bimolecular recombination in $MAPbI_3$ as a band-to-band transition [125]. In this understanding, the absorption and emission of light by a semi-conductor are inverse processes [16, 126], as both rely on the quantum mechanical matrix element describing transitions between the conduction and valence bands. Recently this picture has been used to experimentally verify the relation between absorption and emission in $MAPbI_3$ [15]. This provides evidence that bimolecular recombination can be explained as a direct-gap, band-to-band transition in $MAPbI_3$.

Finally, in contrast to the other charge-carrier recombination mechanisms discussed, bimolecular recombination in $MAPbI_3$ is radiative, which opens the possibility for the emitted photon to be recaptured by the perovskite, exciting another charge-carrier in a process known as self-absorption, photon re-absorption, or 'photon recycling'. This is a familiar process in gases, where spectral lines are broadened by photon re-absorption as the light travels through the emitting medium [127]. In addition, photon re-absorption features prominently in inorganic semiconductors such as GaAs [128, 129] because of their strong band-edge absorption and weak Stokes shifts of the emission. In these semiconductors, the high probability of photon re-absorption manifests itself by apparent slow charge-carrier decay rates, as carriers can radiatively recombine and be 'recycled' several times before they finally return to the ground state [130, 131]. For hybrid metal halide perovskites such as $MAPbI_3$, photon re-absorption has also recently been reported, with indications that it may support long range charge-carrier transport [132], increase the photoluminescence lifetime [133], and raise open-circuit voltages [134] or short-circuit currents [135] in perovskite solar cells. The role of self-absorption in reducing the apparent rate of radiative charge-carrier recombination in MHPs is a key theme of this thesis.

Auger Recombination. Auger-like recombination in a semiconductor is the solid state equivalent to the Auger process in atomic physics [136]. It is a radiation-less transfer of energy between excited charge carriers in a material, which may, or may not, be trap assisted. Auger recombination involves two electrons and a hole, or two holes and an electron, meaning Auger recombination is $\propto n^3$ and will only be important at very high charge carriers densities and will be the dominant recombination mechanism where $n > {}^{k_2}/_{k_3}$.

During Auger recombination, an electron and hole recombine and the resultant energy is passed to the third charge-carrier, which is excited into a higher-lying energy band, linking k_3 to the band structure. Because of this link, Auger recombination in $MAPbI_3$ has been shown to be highly dependent on the crystal phase [97]. Additionally, in TA studies at very early times, Auger recombination (along with charge-carrier cooling processes) has been identified as a cause of the ultrafast decay [137].

Even at the fluences used in ultrafast pump-probe experiments, bimolecular, not Auger recombination is typically reported as the dominant dynamical process, due to the low Auger rates reported for MHPs (see Table 2.1). The capacity to further reduce this already low Auger rate through varying the halide composition [138], provides hope for the development of MHP based lasers [139, 140]. Finally, an important exception to the slow Auger decay usually observed in MHPs is perovksite nanocrystals, where Auger recombination and other many-body processes are more dominant [141].

2.3.5 Modelling Charge-Carrier Recombination in $MAPbI_3$

The measurement of charge-carrier recombination processes in semiconductors first became of interest as a means of calculating the diffusion length. These first measurements extracted the monomolecular recombination rate by monitoring electroluminescent decays [142] or the turn-on delay time for a semiconductor laser [143]. However, these

techniques were limited by not accounting for higher order recombination processes and by capacitance effects.

A more sophisticated technique for determining recombination rates in LEDs overcame these issues, using a small AC modulation on top of a DC prebias to probe the charge-carrier lifetime across a wide range of charge injection levels [144]. This marked a signifcant step forward in the modelling of the charge-carrier dynamics, introducing a full treatment of first, second and third order recombination processes, in the form used in Equation 2.3. However, these measurements of carrier lifetime were not time-resolved, and with the increasing availibility of ultrafast laser systems, pump-probe and time-resolved PL experiments became the standard techniques used to characterise charge-carrier lifetime [94, 145–147]. The legacy of these early studies which is carried forward into the study of MHPs is the rate equation for free charge-carrier recombination

$$\frac{dn}{dt} = -k_3 n^3 - k_2 n^2 - k_1 n. \tag{2.4}$$

where the various recombination processes are as described above.

Types of Time-Resolved Spectroscopy A range of spectroscopic techniques are used to investigate charge-carrier recombination rates. A summary of studies which have reported values for $MAPbI_3$ are shown in Table 2.1.

These studies can be broadly split into two classifications, those using optically gated pump-probe techniques (TA or OPTP) and those using electrically gated techniques (such as time resolved-single photon-counting experiments). Optically gated experiments have a much higher time resolution (tens of fs) than electronically gated experiments (tens of ps). However, the maximum delay in optically gated experiments is only a few ns, as delays are based on changing the path difference between two laser beams (see Chapter 3.1.2).

As the two classes of experiment consider very different timescales, they are useful for studying different dynamical processes. Broadly, pump-probe techniques are well

k_1 [$\times 10^6\,s^{-1}$]	k_2 [$\times 10^{-10}\,cm^3\,s^{-1}$]	k_3 [$\times 10^{-28}\,cm^6 s^{-1}$]	Technique	Sample Architecture	Reference
4.9	0.9	1	OPTP	Meso*	[94]
14	9.2	1.3	OPTP	Meso	[94]
0.1	1.1	0.2	OPTP	Planar*	[121]
1.5	0.6	1.6	OPTP	Planar	[97]
-	11	-	OPTP	Planar	[151]
0.08	2.5	28	TA	Meso	[152]
-	23	-	TA	Meso	[150]
<0.5	0.8	1.8	TA	Planar*	[133]
0.2	1.7	1.6	TA	Planar	[96]
-	11	3.8	TA	Planar	[95]
5	0.8	1.1	TA	Planar	[133]
-	13	-	TRMC	Meso	[153]
0.04	0.2-0.4	-	TRPL	Meso	[154]
0.04	2.6	4	TRPL	Planar	[155]
7-13	6-37	-	TRPL	Planar	[156]
-	1.7	0.07	TA	GaAs	[157]

Table 2.1: A brief review of the recombination coefficients reported for $MAPbI_3$, using optical-pump THz-probe (OPTP) spectroscopy, transient absorption (TA), time-resolved photoluminescence (TRPL), and time-resolved microwave conductivity (TRMC). Studies labelled by a "*" indicate that $MAPbI_{3-x}Cl_x$, rather than $MAPbI_3$ was used.

suited to monitoring ultrafast processes such as charge-carrier cooling [148, 149] and Auger recombination [150], as well as bimolecular recombination. Conversely, while electrically-gated time-resolved photoluminescence (TRPL) experiments lack the sufficient time-resolution to resolve sub-ps processes, they are useful for determining the bimolecular and monomolecular recombination rates over ns or µs time-scales.

This is reflected in Table 2.1, where Auger recombination rates are reported for TA and OPTP experiments, but usually not for TRPL or time-resolved microwave conductivity (TRMC). Similarly, from the table it can be seen that many pump-probe studies omit the monomolecular recombination rate [95, 150], or determine it separately using TRPL [133], as over the time-window of these experiments monomolecular decay will not be observed [94].

Charge-Carrier Recombination Rates in $MAPbI_3$ Having established some of the background on both the techniques used to study charge-carrier recombination and the rate equation itself, the reported values of charge-carrier recombination in $MAPbI_3$ can now be discussed.

From Table 2.1 it can be seen that there is a wide spread of values, which depends on both the type of sample used in each study, as well as the spectroscopic method, similar to the spread of Auger and bimolecular recombination rates obtained for GaAs [157].

For both the TA and OPTP studies, the largest value of k_2 is reported by a study which has excluded Auger recombination from the dynamical model [150, 151]. Intuitively, if bimolecular recombination is the only available parameter for a dynamical model to fit, then it will be larger, compared with the case where both Auger and bimolecular recombination are fitted. This would explain the larger values of k_2 observed for the cases where Auger recombination is not considered, however, it also raises an important point about the number of parameters to include in the dynamical model. On the one hand, if Auger recombination is included, but the experimental charge-carrier density falls below the regime where significant Auger recombination will occur, the fit will have too many free parameters. conversely, without Auger recombination, at very high fluences all of the charge-carrier decay will be interpreted as bimolecular recombination, resulting in an overestimate of k_2. Therefore judging the correct number of parameters to include in the dynamical model is difficult, and the best results will come from global fits across a wide range of excitation fluences.

Setting aside differences in the fitting procedure, Table 2.1 shows that there is no strong distinction between the bimolecular recombination rates reported for planar samples and those supported by a mesoporous scaffold. This is in contrast to the monomolecular decay rate, which shows a marked increase in planar devices [158]. The lack of a similar pattern

for bimolecular recombination in Table 2.1 suggests that the bimolecular charge-carrier recombination rate is not so strongly affected by the sample architecture.

Another trend evident in the table is that, while there is a narrower distribution in the values given for k_2 from OPTP and TA studies, there is a larger spread of k_2 values reported using TRPL. To some degree this effect may be caused by the lower fluences used in TRPL experiments, as both OPTP and TA use amplified laser pulses. A more likely explanation is that as TRPL experiments measure charge-carrier dynamics over a larger time period. This means that processes such as charge-carrier trapping and de-trapping, will become more important, complicating the dynamical equation [159]. Obtaining an accurate value of k_2 under these circumstances is more challenging than in ultrafast pump-probe studies, which could partly explain the larger spread of results.

Finally, at the bottom of Table 2.1, the charge-carrier recombination rates in GaAs are given as a comparison. Comparing the Auger recombination rates, it can be seen that the average value reported for $MAPbI_3$ is two orders of magnitude greater than for GaAs. On the other hand, the bimolecular recombination rates of $MAPbI_3$ and GaAs are comparable, consistent with the fact that each material is a direct-gap semiconductor. Since the slowest k_2 in Table 2.1 (determined by ultrafast spectroscopy), is less than three times slower than GaAs, reports of "slow" charge-carrier recombination in $MAPbI_3$ must be linked instead with the Langevin model and organic semiconductors. must be understood as being slower than the Langevin-predicted rate, which is not appropriate for MHPs. In any case, Table 2.1 confirms that $MAPbI_3$ has a bimolecular recombination rate comparable to successful inorganic semiconductors, more than sufficient to allow the majority of excited charge carriers to be extracted from the active layer of a solar cell.

3
Experimental Details

Contents

3.1 THz Spectroscopy 34
3.1.1 Time-Domain Terahertz Spectroscopy 34
3.1.2 Optical-Pump-Terahertz-Probe Spectroscopy 35
3.2 Experimental Details of the OPTP System 40
3.2.1 Terahertz Generation 40
3.2.2 Terahertz Detection 41
3.2.3 Extraction of Charge-Carrier THz Mobility 44
3.2.4 Description of the OPTP System 45
3.3 Fourier Transform Infra-Red Spectroscopy 51
3.3.1 Operational Principle of a Michelson Interferometer 51
3.3.2 Referencing an FTIR 54
3.3.3 Description of the FTIR System 55

This chapter outlines the operational principles and experimental details of the instruments used in this thesis, including optical-pump-THz-probe (OPTP) spectroscopy and Fourier transform infrared (FTIR) spectroscopy.

The main focus is on OPTP spectroscopy, which plays a central role in the later chapters, where it is used to monitor the charge-carrier dynamics in thin films of $MAPbI_3$, on a sub ps time-scale.

3.1 THz Spectroscopy

Terahertz (THz) spectroscopy is a powerful non-contact technique, capable of measuring a wide variety of semiconductor properties on an ultra-fast timescale. The terahertz region of the EM spectrum is typically considered to range from around 0.3 to 30 THz [160], sitting between the IR and microwave regions. This region of the EM spectrum is of interest in a number of fields, as the THz band corresponds to processes happening on the scale of 10 to 100 fs, which is the typical time-scale for scattering processes in semiconductors, as well as lattice vibrations. In the field of MHPs, THz spectroscopy has been successfully employed to investigate charge-carrier mobilities [97, 138] and recombination rates [121] as well as background dopant densities [161].

In comparison to other techniques available in the far IR, it has the advantages of being both coherent and offering excellent time resolution. Coherence means that unlike Fourier transform infra-red (FTIR) spectroscopy and temperature dependant microwave conductivity, THz spectroscopy is not limited by thermal background radiation [162]. However, what really sets TRTS apart from other techniques is its ability to provide sub-ps time resolution in the far IR range. This exceeds the resolution managed by free electron lasers (ps), or time resolved microwave conductivity (ns) [163].

3.1.1 Time-Domain Terahertz Spectroscopy

Time-domain Terahertz spectroscopy (TDTS) is a spectroscopic technique for probing the properties of a material in the THz regime. Despite the name, TDTS is not a time-resolved technique, instead, the name refers to the fact that measurements of a THz pulse are made in the time domain. To extract spectral information, these measurements are then Fourier transformed, allowing the determination of various material properties in the frequency domain.

A typical setup for TDTS involves splitting an ultra-short laser pulse into two, with one beam used to generate a THz pulse and the other being used as a gate pulse. The first pulse is used to produce a single cycle THz pulse, which is directed into a sample. The pulse passes through the sample before being focussed into a detection crystal, at the same time as the gate beam. Free space electro-optic sampling (FSEOS), using the fs gate pulse, provides a time domain picture of the THz electric field which is transmitted through the sample. By changing the path length of the THz beam, a different section of the THz pulse will arrive at the detection crystal as the gate beam passes through. This means that by controlling the path length travelled by the THz beam, each part of the THz pulse can be measured in the detection crystal and a time domain picture of the THz electric field can be built up.

By comparing the THz field transmitted through the sample, to the THz field which is measured when the sample is removed from the THz beam path, the THz absorption spectrum of a sample can be determined [164]. This technique has been used to measure the THz absorption of a wide range of samples, including $MAPbI_3$ [165]. Additionally, as both the phase and amplitude of the THz pulse are measured, the complex refractive index can be extracted directly without needing to employ the Kramers-Kronig relations [166, 167].

3.1.2 Optical-Pump-Terahertz-Probe Spectroscopy

Although TDTS is an excellent means of characterising the material properties of a semiconductor, it is not a time resolved technique, and therefore, cannot be used to study dynamical processes. However, a simple extension of TDTS is OPTP, which is able to provide sub-ps time resolution [168].

Achieving Time Resolution. In OPTP spectroscopy the sample is excited by an optical "pump pulse", ahead of the arrival of a THz probe, so that the THz transmission through the photo-excited sample can be measured. By changing the delay between the optical pump and THz probe pulses, the state of the sample at different times after photo-excitation can be measured. The pump-probe delay is controlled by introducing an optical path length difference between the pump and probe pulses, typically using a motorised delay stage. This introduces a practical limit on the maximum delay attainable, as space on an optical table will be restricted and longer delay lines amplify any imperfections in beam alignment, making the system more difficult to set up and maintain. As such, the maximum time delay possible in pump-probe experiments will be on the order of ns.

The time resolution of the experiment will be limited either by the precision with which the path difference can be controlled or by the duration of the laser pulses. Table 3.1 shows how different amounts of delay stage movement translate into optical path difference, presenting the important dimensions of an OPTP experiment as both lengths and light-times. For the OPTP system used in this thesis, the minimum increment of the stage translates into a path length of <7 fs, which is much less than the 35 fs pulse duration of the laser. This means that the time resolution will be limited by the pulse length, and specifically by the duration of the THz pulse, which can be lengthened by imperfections in phase matching and dispersion in the THz generation crystal [169].

Experimental Dimension	Delay Stage Movement (length)	(time)	Beam Path Length (length)	(time)
Minimum Delay Stage Increment	**1 µm**	3.34 fs	2 µm	6.67 fs
Amplifier pulse duration	5.25 µm	17.5 fs	10.5 µm	**35 fs**
1 ps Pump-Probe delay	0.15 mm	0.5 ps	0.3 mm	**1 ps**
Used Delay Stage Increment	**1 mm**	3.34 ps	2 mm	6.67 ps
1 ns Pump-Probe delay	150 mm	0.5 ns	300 mm	**1 ns**
Maximum Delay Stage Delay	**200 mm**	0.67 ns	400 mm	1.33 ns

Table 3.1: Summary of how movement of a delay stage affects the path length, shown in both length and time taken for light to travel the distance in air. For any delay stage movement, double this distance is added to the beam path, as the beam passes along the stage once and is then reflected back parallel to the initial direction of travel.

Applications of OPTP Spectroscopy. In an OPTP experiment, it is possible to adjust the delay of the THz pulse and the pump pulse relative to the gate beam, which remains fixed. The adjustment of these two delay times gives the possibility for three possible types of scan; probe scans, pump scans, and pump-probe scans.

A probe scan involves maintaining a fixed time delay between the pump and the probe, while adjusting the time delay between the THz and gate pulses. As can be seen from Figure 3.1, this allows the electric field of the THz pulse to be measured in the time domain using FSEOS, just as in TDTS, but at a fixed time after photoexcitation. Using this type of scan, photo-induced absorption features in the transmitted THz spectrum can be monitored.

The second type of scan, commonly employed in OPTP spectroscopy is known as a pump scan. In a pump scan the THz-gate delay is adjusted and fixed at the point where the peak of the THz pulse is being measured, while the pump stage is scanned to vary the pump-probe delay. From this type of scan, the percentage change in THz transmission, $\Delta T/T$, can be measured as a function of time after excitation. The aim of this type of scan is to determine the rate of decay of the THz photoconductivity, from which the initial charge-carrier mobility and rate of recombination can be inferred [147]. The pump scan was the first type of OPTP scan [146] to be developed and was initially used to monitor

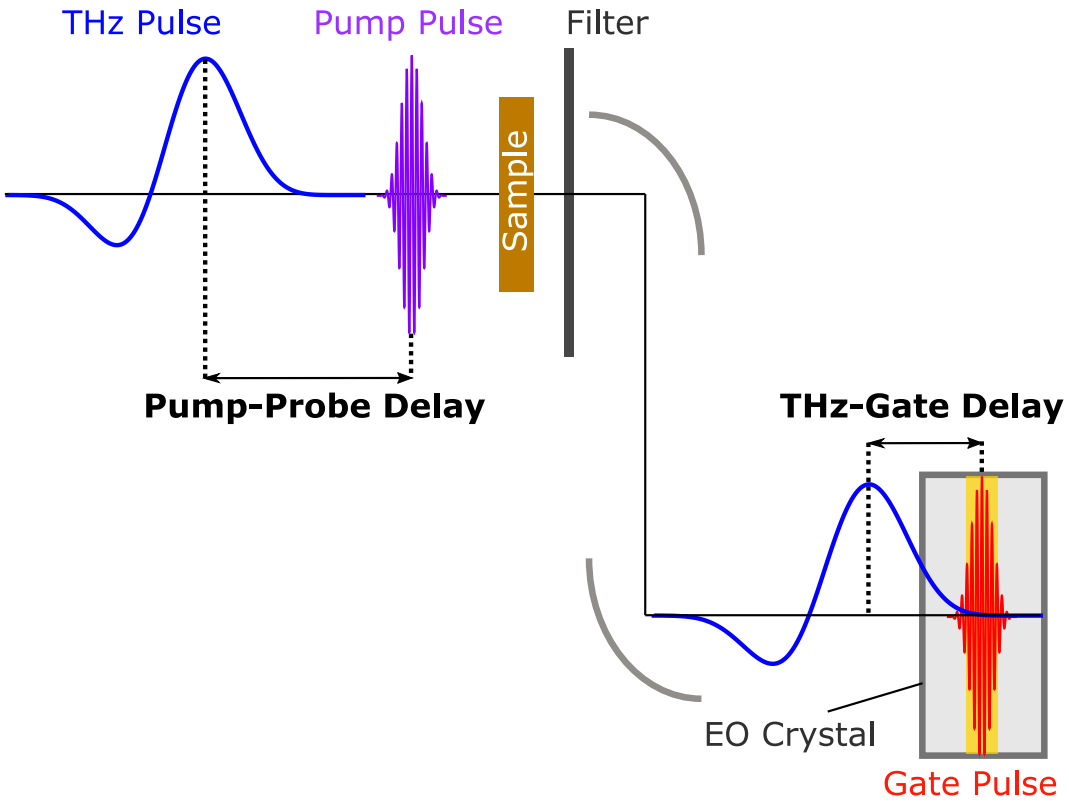


Figure 3.1: Diagram showing the time delays between the different beams in an OPTP experiment. The top of the figure shows the delay between the pump and THz beams; In a pump scan this delay is varied, allowing the transmission of the THz probe to be measured at different times after photo-excitation. The bottom of the figure shows the THz-gate delay, which is altered in a probe scan. As this delay changes, the electric field of different parts of the THz pulse are measured, allowing for the full pulse to be sampled.

inter-valley scattering in GaAs. However, it has since been used to measure the charge-carrier mobility and recombination rates across a wide range of materials; including bulk inorganic and organic semiconductors [170, 171], nanowires [172, 173] and MHPs [94, 138].

The final type of scan used in OPTP studies is a 2D pump-probe scan. This simply involves taking a probe scan at a number of pump delay times, providing a full picture of the THz photoconductivity of the sample as a function of frequency and time. This is important in cases where the refractive index of a sample changes strongly upon photoexcitation, changing the delay between the gate and THz beams. In such a case, unless the THz-gate delay is adjusted for each value of pump-probe delay, it cannot be guaranteed that the peak of the THz pulse is being measured, therefore, a probe scan is

taken to find the THz peak at each pump-probe delay. This allows the changes in refractive index can be differentiated from changes in the THz signal due to photoconductivity [145].

Comparison with Transient Absorption Before continuing, it is useful to make a brief comparison between OPTP and Transient Absorption (TA), another popular pump-probe technique [174]. The basic operating procedure of a TA system is the same as in OPTP, with ultrafast pump and probe beams being directed at a sample and the change in transmission caused by the pump being measured. However, in the case of TA the probe beam is produced by white light generation in a sapphire, and the pump beam can also be a broadband or narrowband optical pulse.

The major differences between TA and OPTP spectroscopy are that, in TA, detection of the signal is in the frequency domain rather than the time domain, and that the sample is probed at optical wavelengths.

As TA probes the absorption of a photoexcited sample in the visible range, it directly measures the wavelengths at which photo-induced bleaches (or absorption) occur. This means that processes such as charge-carrier cooling, refractive index changes, and charge-carrier recombination can all be attributed to specific features in the TA spectrum [77, 175, 176]. However, the sensitivity of TA to such a wide range of processes significantly complicates the interpretation of the TA spectrum, meaning great care must be taken to disentangle the various processes.

In contrast, OPTP probes the photoexcited sample in the THz regime, so is sensitive only to the total THz absorption of all of the photo-excited species, rather than their individual contributions. Since OPTP spectroscopy is not directly sensitive to the wide range of processes measured by TA, the interpretation of THz photoconductivity transients is significantly simplified. As it is only directly sensitive to the number and

mobility of charge carriers in a sample, OPTP provides an excellent tool for recording the charge carriers recombination dynamics in thin-films semiconductors.

3.2 Experimental Details of the OPTP System

3.2.1 Terahertz Generation

Spectroscopy at THz frequencies has only come into use within the last thirty years, as it occupies a gap between traditional optical and electronic frequency ranges, where sources and detectors were not readily available. THz emitters and detectors initially grew out of investigation of transient electrical pulses in transmission lines and the associated EM pulses which they generated, which were in the THz band. These transmission lines were subsequently developed to transmit and receive THz pulses across free space, giving the first THz sources and detectors [163]. From these first experiments on transmission lines, several types of sources have been developed, including air plasma generation, quantum cascade lasers and solid state electronic methods [177, 178]. However, the most commonly implemented generation methods in time-domain spectroscopy rely on non-linear optical processes.

3.2.1.1 Generation using Non-linear Optical Processes

A commonly employed technique for THz pulse generation is to use non-linear processes, such as non-linear optical rectification in crystals of ZnTe or GaP [179, 180]. This process takes two photons and ω_1 and ω_2 and combines them to produce photons with the sum and difference frequencies: $(\omega_1 + \omega_2)$ and $(\omega_1 - \omega_2)$. When the two photons have equal energy the difference is simply zero, but when this process is carried out with a fs laser pulse, the difference frequencies produce a broad THz pulse of up to 100THz [162]. This method of THz generation is widely used in both TDTS and OPTP experiments.

In Chapter 6 THz probe pulses were generated by optical rectification in a 450 µm (110)-GaP crystal.

3.2.1.2 Generation using Spintronic Emitters

A recent advance in the development of broadband THz sources is the inception of spintronic emitters, which provide larger bandwidths and higher THz generation efficiencies than conventional solid state emitters.

A spintronic emitter is composed of a thin ferromagnetic layer joined in a bilayer structure to a thin film of a non-ferromagnetic metal. THz pulses are generated in the following manner [181, 182]; the structure is photo-excited using an ultrafast laser pulse, creating free charge carriers. The difference in the charge-carrier lifetimes and transport properties in the two layers results in the generation of a spin current from the ferromagnetic layer into the non-ferromagnetic layer. As the spin current enters the non-ferromagnetic layer, the inverse spin-Hall effect converts it into an electronic current [183]. This ultrafast electrical transient generates THz radiation with a broad bandwidth from 1 to 30 THz. In contrast to older techniques which rely on non-linear optical processes, the intensity of the THz radiation generated by spintronic emitters increases linearly with laser excitation power.

For the OPTP experiments in Chapter 7, a spintronic emitter was used which was composed of 1.8 nm of $Co_{40}Fe_{40}B_{20}$ sandwiched between 2 nm of Tungsten and 2 nm of Platinum, all supported by a quartz substrate.

3.2.2 Terahertz Detection

There are a range of methods available for the detection of THz pulses, including GaAs photoconductive antennae, superconductor-insulator-superconductor junctions and free-space-electro-optic sampling (FSEOS) [162, 177].

Electro-optic sampling [184] is the most commonly used technique for THz detection in fs spectroscopy experiments. The detector is comprised of a detection crystal, a polarising beam splitter and a pair of balanced photodiodes, typically using a 0.5 to

1 mm ZnTe crystal for detection, as it exhibits a linear electro-optic effect. This means that the refractive index of the crystal along one axis will vary linearly under the electric field of a THz pulse. When a fs gate pulse is passed through at the same time as a THz pulse, the polarisation of the gate pulse is therefore altered linearly by the electric field of the THz pulse.

The gate pulse then continues through a quarter-wave plate and a Wollaston prism. These separate out the two polarisation components, which are directed onto a pair of balanced photodiodes. The quarter-wave plate is aligned such that the photodiodes balance when the THz electric field is zero. Any change in the electric field in the crystal destroys this balance and is detected as a voltage across the photodiodes. A rotation of polarisation in one direction results in a positive voltage, while the opposite change in polarisation gives a negative voltage–providing phase as well as amplitude information about the THz pulse.

By adjusting the time delay between the THz pulse and the gate pulse, the THz electric field as a function of time can be determined. As the detector is sensitive to both the amplitude and phase of the THz electric field, the full complex dielectric constant can be directly determined.

In Chapters 6 and 7, THz probe pulses were detected using electro-optic sampling in a ZnTe crystal (composed of 0.2 mm (110)-ZnTe on 3 mm (100)-ZnTe).

3.2.2.1 Recovery of the Signal

As the voltage produced by the detection photo-diodes is a small periodic signal, it is well suited for lock-in amplification [185]. Lock-in amplifiers are designed to extract a periodic signal by averaging over a specified window. They integrate the product of an input signal and a known sinusoidal carrier signal such that, over a timescale

much longer than the period of the carrier signal, all frequency components except those at the carrier frequency are eliminated.

This technique is used in conjunction with THz detection by mechanically chopping the input beams to provide a modulation in the detected signal. For a laser amplifier with a repetition rate f_{laser}, the THz probe beam is modulated at a frequency of $f_{laser}/2$. This provides a contrast between the THz beam being present and absent, and a lock-in amplifier is used to recover this signal, T.

To recover the modulation of the pump-beam, another lock-in and chopper are used in a double lock-in configuration [186]. In this case a much slower modulation of the laser frequency is used, with the carrier frequency being $f_{laser}/10$ or $f_{laser}/20$. As this modulation is much slower than the integration time of the first lock-in, it provides a slow modulation in the output signal of the first lock-in, which is then fed into a second lock-in. As the output of the first lock-in varies at the frequency of the pump chopper, this modulation, ΔT, can be extracted by the pump lock-in. By providing modulations at two separated timescales, the effect of both the pump and THz beams can be extracted.

Two points are important here. First, in selecting carrier frequencies any multiple of 50 Hz must be avoided. This is the UK mains frequency which adds substantial noise to measurements. Secondly the averaging window of the pump lock-in must be much longer than that of the THz lock-in. This is simple to achieve, but is a drawback of the double lock-in technique as it limits the rate of data acquisition.

An improvement over the double lock-in technique is to use box-car averaging [187]. This technique, also referred to as gated averaging, integrates the signal over a defined time-window. For a periodic signal, the integration window can therefore be selected to be over the region of greatest signal to noise. The greatest advantage however, is that the method does not require a settle-time, as is required by a lock-in amplifier. Because of this, every laser pulse can be measured, resulting in much faster data acquisition.

3.2.3 Extraction of Charge-Carrier THz Mobility

THz mobility of a thin dielectric layer, such as a perovskite thin-film, can be determined using the method described by Wehrenfennig et al [121]. The sheet photo-conductivity, ΔS, of a material with a thickness much less than the wavelength of the THz radiation can be expressed as [188]

$$\Delta S = -\epsilon_0 c(n_a + n_b)(\frac{\Delta T}{T}) \tag{3.1}$$

where n_a and n_b are the THz refractive indices of the materials interfacing the perovskite layer at the front and rear respectively. The quantity $\Delta T/T$ is the ratio of the photo-induced change in THz electric field to the transmitted THz electric field in the dark. The initial number of photo-excited charge carriers N is given by

$$N = \phi\frac{E\lambda}{hc}(1 - R_{pump})(1 - T_{pump}) \tag{3.2}$$

with E being incident pump pulse energy, λ the excitation wavelength, ϕ the ratio of free charges created per photon absorbed, and R_{pump} and T_{pump} being the reflected and transmitted fractions of the pump beam. These two equations can be used to extract the charge carrier mobility μ through

$$\mu = \frac{\Delta S A_{\text{eff}}}{Ne} \tag{3.3}$$

where A_{eff} is the effective area from the overlap of the pump and probe beams and e is the elementary charge. Substituting Equations 3.1 and 3.2 into Equation 3.3 we obtain

$$\phi\mu = -\frac{\epsilon_0 c(n_a + n_b)(A_{\text{eff}})}{e\lambda(1 - R_{pump})(1 - T_{pump})}(\frac{\Delta T}{T}) \tag{3.4}$$

from which the effective charge-carrier mobility $\phi\mu$ may be determined based on the pump beam parameters and the initial measured $\Delta T/T$ of the sample. Here, μ is the charge-carrier mobility, and ϕ is the charge-to-photon branching ratio which is assumed to be unity at room temperature for $MAPbI_3$.

To calculate the charge-carrier mobility of a perovskite film, a number of different excitation fluences are used to photoexcite the film, and a linear fit between N and the initial $\Delta T/T$ allows the calculation of $\phi\mu$. The excitation fluences used must be sufficiently low (typically $< 50\,\mu J\,cm^{-2}$), in order to avoid non-linear effects such as two-photon absorption. For ambipolar materials μ will be the sum mobility of the electrons and holes, as both carriers will interact with the THz radiation.

3.2.4 Description of the OPTP System

This section details the OPTP system used in this thesis, shown in Figure 3.2, also outlining how the system was assembled.

The OPTP experiment relies on ultra-fast laser pulses, which were provided by a laser amplifier. Between Chapters 6 and 7 the laser amplifier was replaced, and the system reconstructed. Figure 3.2 shows the system which was set up after the replacement of the laser amplifier, as used in Chapter 7.

The OPTP measurements in Chapter 6 were performed using a Spectra Physics Mai Tai-Empower-Spitfire Pro Ti:Sapphire regenerative amplifier. The amplifier generated 40 fs pulses with a centre wavelength of 800 nm at a repetition rate of 1.1 kHz. After completion of the work for that Chapter, a new regenerative amplifier system was installed, with an increased rep-rate of 5 kHz and a new average power of 8W. The upgraded amplifier system consists of a Spectra Physics Mai Tai-Ascend-Spitfire Ace Ti:Sapphire regenerative amplifier. This system has a nominal beam diameter of $1/e = 12\,mm$, which is larger than the output mode of the previous amplifier. To accommodate the larger beam size, the beam-lines were refitted with larger 2 inch mirrors.

From this point on, the two systems are functionally equivalent, so the following description is relevant to both, except where noted. The output from the amplifier is

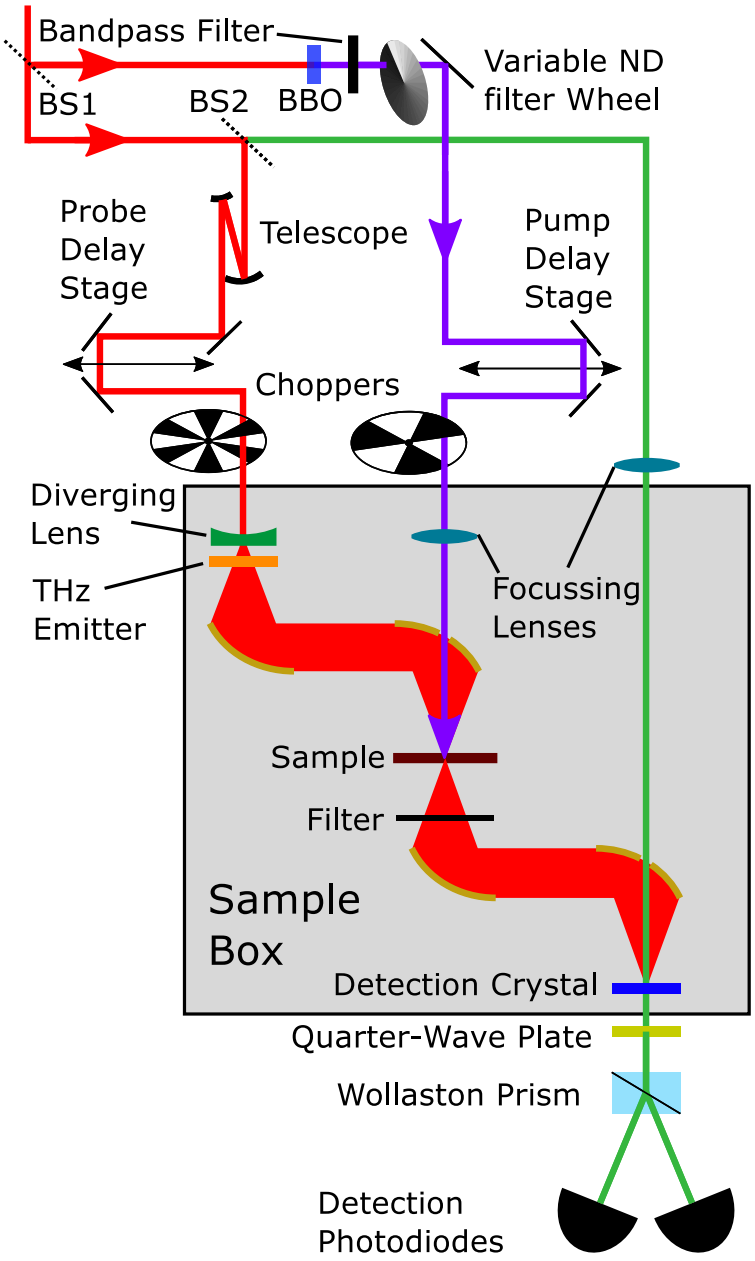


Figure 3.2: Beam diagram of the OPTP system used in this thesis. The different coloured lines indicate the three beams used, with red showing the THz beam, purple showing the pump beam and green showing the gate beam.

first split into two parts using a beam-splitter (BS1), with the pump line being split from the gate and probe beams, using a beam-splitter.

As close as practical to the sample position, the probe and gate beams are separated using a second beam-splitter (BS2). In this case, 95% of the pulse energy is directed into the probe beam, as only a small fraction is required by the gate. The beams are kept together for as long as possible, because, after splitting, twice the amount of optics is required to steer the individual beams. This is problematic as it reduces the available space on the optical bench, which is already densely occupied near the sample box.

After the gate and probe beams are split, the probe beam path passes onto a motorised delay stage, through a telescope and a chopper, before reaching the sample box. The delay stage allows fine control of the arrival time of the probe pulse at the sample, while use of the telescope reduces the beam diameter by $^1/_3$, allowing it to pass through the chopper without clipping.

The path of the gate beam into the sample box is simpler, as it passes along a delay line, equal in path length with to probe beam line, and through a series of neutral-density filters before also entering the box. These filters attenuate the gate beam to protect the THz detection crystal from damage and to avoid saturation of the detection photodiodes.

Inside the sample box, the probe beam is directed onto the THz emitter which generates a short pulse of THz radiation (the emitter was either a ZnTe crystal or spintronic emitter, as detailed in Section 3.2.1). Any unconverted 800 nm light is blocked using a filter placed after the THz emitter, to prevent unintended excitation of the sample. Meanwhile the THz radiation passes through the filter, being expanded outwards by a diverging lens to fill an off axis-parabolic mirror. These gold mirrors steer the THz pulse through the sample box, focussing it first at the sample position, then again on the electro-optic detection crystal.

Meanwhile the gate beam is timed to arrive at the detection crystal concurrently with the THz pulse, passing through a hole in the last off-axis parabolic mirror. To measure

the THz electric field it is crucial that the two pulses are overlapped, temporally as well as spatially, at the point where the THz pulse is focussed. A higher signal will be detected if the gate beam is focussed tightly on the same spot as the THz beam, however, focussing the gate beam too tightly may result in damage to the detection crystal. This overlap also represents the most sensitive point of alignment for the system and the tighter the focus of the gate beam, the more vulnerable the system will be to small drifts in alignment.

In practice, achieving a temporal overlap of the two beams requires a careful measurement of each beam path, while the THz delay stage is in the middle of its travel range. This then allows a full sweep of the THz stage to determine the exact stage position where the two beams overlap. For initial adjustment, of the path difference between the two beam-lines, it is useful to include a manually operated delay stage in the gate beam path. This facilitates small adjustments of the gate beam path, such that it corresponds to the middle of the probe stage range. To spatially overlap the two beams, the THz emitter **and detection crystal**[1] can be removed. This allows the alignment of the 800 nm light from the probe beam line to overlap with the gate pulse, at the detection crystal position.

Once the two beams are correctly overlapped at the detection crystal, the gate beam can be directed out of the THz box, and onto the balanced photodiodes. At this point a quarter-wave plate and a Wollaston prism facilitate the balancing of the photodiodes, which is done in the absence of the THz beam. Together, these two beams constitute a THz time-domain spectroscopy experiment, which is a natural first step towards constructing a full OPTP system.

***

To extend the TDTS system described above into a OPTP system, the addition of an optical pump beam is required. Returning to the point in Figure 3.2 where the

[1]Forgetting to remove the detection crystal along with the THz emitter results in the main 800 nm pulse being focussed onto the detection crystal, which will destroy the crystal!

THz and gate beams were split from the pump pulse, the pump beam is directed along a separate beam line and directed onto the sample.

Before entering the sample box, the pump beam can be frequency-doubled using a β-Barium Borate (BBO) crystal, providing a 400 nm pump excitation which is above the $\sim$780 nm absorption onset of $MAPbI_3$. Any remaining light at 800 nm is removed using a bandpass filter, which admits light only in the region 380–420 nm. To facilitate the automated variation of the pump fluence during experiments, the pump beam is varied using an neutral density (ND) filter wheel, which allows the pump fluence to be attenuated by several orders of magnitude. Similarly to the THz beam, the time delay of the pump pulse is controlled using a delay stage, which provides a total time delay of 1250 ps and the beam is mechanically chopped ahead of entering the sample box. The experimental setup used in Chapter 6 included a retro-reflecting corner cube, which allowed the beam to travel two loops along the pump stage, doubling the maximum possible delay to 2.5 ns. When the system was upgraded the larger beam diameter meant that the retro-reflector could not accommodate the larger beam and so the maximum delay was reduced to 1.25 ns.

Inside the sample box, the pump beam is focussed through a hole in the back of the second off-axis parabolic mirror. After passing through the focal point beam then re-expands before illuminating the sample, which ensures the diameter of the pump beam is much greater than the THz beam at the sample position. The FWHMs (full width at half maximum) of the beams for the pump and THz pulses at the sample were measured to be 3.9 mm and 1.4 mm respectively (For the study in Chapter 6). Any remaining pump-beam light is blocked by a Polytetrafluoroethylene (PTFE) or cellulose-nitrate filter, which are transparent to THz radiation, but block the pump beam and so protect the THz detection crystal.

Ensuring that the pump stage is correctly aligned is much more critical than the alignment of the THz stage, as the entire range of pump stage will routinely be used,

while the THz stage is normally only scanned over a few mm. This means that the pump beam must travel onto and off of the delay stage, horizontally and parallel to the axis of the stage. This can be achieved using irises with matched heights, testing that the beam does not move as the stage is scanned from one positional extreme to the other. Rather than relying on how the beam appears to move across the irises, it can be more effective to judge the movement of the beam by placing a powermeter behind the second iris–thereby judging whether the centre of the beam drifts as the stage moves. The final test of the pump-stage alignment is usually to take a pump scan using a silicon wafer, which has a lifetime $>>1$ ns and so provides a flat THz photoconductivity transient if the stage is correctly aligned. However, care must be taken to keep the pump excitation strength sufficiently low, as the THz refractive index of silicon changes upon photo-excitation. Therefore, to avoid changing the time delay between the THz pulse and the gate beam, the excitation fluence must be kept as low as possible, otherwise the THz photoconductivity will not appear flat as the stage scans.

***

During experiments the sample box, including the sample, THz emitter and THz detector, are evacuated and held under a vacuum of 10^{-2} bar. This means that the path of the THz radiation is completely enclosed in vacuum, which is important to avoid absorption of the THz pulse by water vapour in the air.

Steady state photoluminescence spectra may also be taken, in-situ, during OPTP experiments. A collection lens with a 435 nm longpass filter is placed inside the sample box coupling emitted PL from samples into an optical fibre. The fibre connects to a OceanOptics 2000+ spectrometer which covers a wavelength range of 350–1000 nm.

3.3 Fourier Transform Infra-Red Spectroscopy

Fourier transform infra-red (FTIR) spectroscopy is a technique for measuring the transmission or reflection spectrum of a sample. Rather than separating out different frequencies, as in a dispersive spectrometer, the FTIR uses a Michelson interferometer to measure the entire spectrum at once, separating the signal out later into Fourier components. Compared to dispersive instruments, in an FTIR, light does not need to be attenuated by slits, improving the throughput. It also has the advantage of a better signal to noise ratio, as the entire spectrum is measured at the detector rather than individual spectral components. Together with a rapid scan-time, this makes the FTIR an effective instrument for measuring reflection and transmission spectra.

3.3.1 Operational Principle of a Michelson Interferometer

As shown in Figure 3.3, at the heart of an FTIR is a Michelson interferometer–the operation of which is now described. At the entrance to the interferometer a beam-splitter to evenly split incoming light from a broadband source into two components, which travel along separate beam-paths before being recombined. The path length of one beam is fixed, while the path length of the second beam is controlled by a delay stage. By scanning the delay stage, the path difference, d, between the two beams is varied, causing them to interfere. For a monochromatic source with wavenumber k this causes a variation

$$I(d) = I_0(1 + \cos kd) \tag{3.5}$$

in the measured light intensity as the stage is scanned, where I_0 is the intensity before the beam-splitter.

In the FTIR spectrometer, a broadband, rather than monochromatic, source is passed into a Michelson interferometer, through a sample and onto a detector. This results in a complicated variation in the measured intensity as the stage is scanned, since many

spectral components will be interfering at different frequencies to produce the overall measured intensity. However, by Fourier transforming the detector signal, these individual wavenumber components can be extracted. This is how the FTIR is able to determine the spectrum of transmitted or reflected light through a sample.

The spectral resolution of the FTIR will be limited by the length over which the delay stage in the interferometer can be scanned. Although this may be limited by the length of the stage, the coherence length of source will also be a limiting factor. Additionally, it is necessary to have a sufficiently dense spacing of sampling points along the length being scanned, in order to prevent alising.

The spectral range of the FITR is determined by the convolution of the detector sensitivity and source spectrum. Modern FTIR systems are equipped with a range of sources and solid-state detectors, so a given range from IR to UV can typically be covered with a series of detectors and sources.

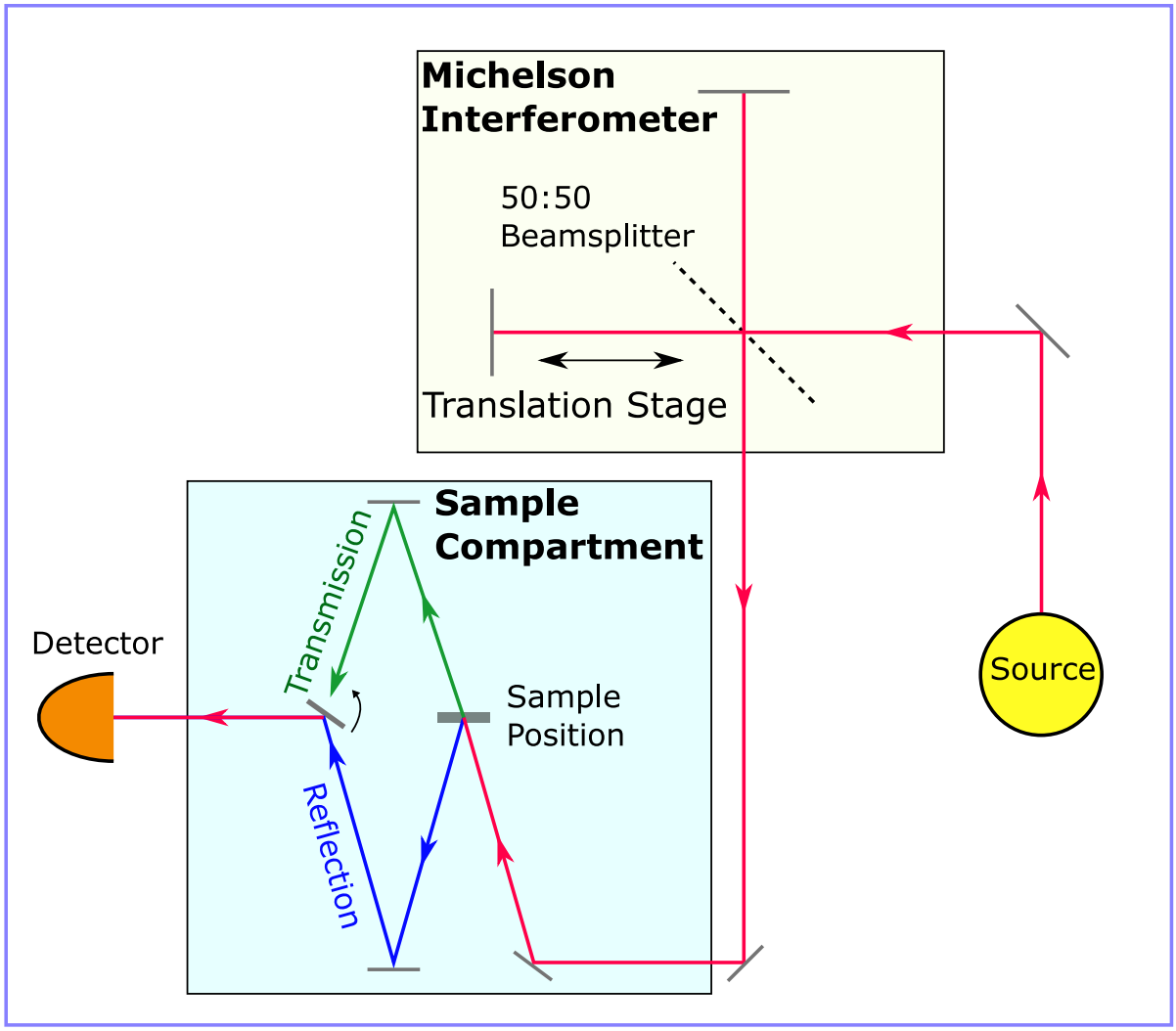


Figure 3.3: Diagram of the FTIR system used in this thesis, shown with the attachment to the system which allows reflection/transmission measurements. Light is emitted from one of a number of interchangeable sources, and directed into a Michelson interferometer. The output from the interferometer is directed to the sample, at which point a mechanically controlled mirror directs either the reflected or transmitted light onto the detector. Movement of the translation stage in the interferometer causes a periodic variations in the detected signal, which are extracted as different frequency components using a Fourier transform.

3.3.2 Referencing an FTIR

With the basic operational principle of the FTIR established, it is necessary to discuss how to reference the signal for both transmission and reflection. Typically, it is not the absolute intensity of transmission or reflection which is of interest, but the percentage as compared with a reference, considered to represent 100%.

For the case of transmission, the 100% reference spectrum can be found by taking the transmission spectrum of an empty sample holder. Alternatively if the multiple reflections inside the quartz substrate which supports the perovskite films are ignored, the transmission through a quartz substrate can be approximated as the 100% transmission reference. In the case of reflection, a silver (in the near infra-red (NIR)/Visible range) or UV-enhanced aluminium (in the UV range) mirror is taken as the 100% reflection reference, with the exact reflectivity usually being specified by the mirror's supplier.

The percentage transmission and reflection spectra for a sample are then given by:

$$\mathrm{T} = \frac{\mathrm{I}^{\mathrm{T}}_{sample} - \mathrm{I}^{\mathrm{T}}_{mirror}}{\mathrm{I}^{\mathrm{T}}_{vacuum} - \mathrm{I}^{\mathrm{T}}_{mirror}} \qquad \mathrm{R} = \frac{\mathrm{I}^{\mathrm{R}}_{sample} - \mathrm{I}^{\mathrm{R}}_{vacuum}}{\mathrm{I}^{\mathrm{R}}_{mirror} - \mathrm{I}^{\mathrm{R}}_{vacuum}}. \tag{3.6}$$

In this case $\mathrm{I}^{\mathrm{T}}_{mirror}$ and $\mathrm{I}^{\mathrm{R}}_{vacuum}$ represent small amounts of background light, which are subtracted from each of the sample and reference signals. In this thesis T and R are measured as a function of wavenumber, but displayed in terms of wavelength, in order to be compared against PL spectra. It should be noted that in general, the conversion of spectra between wavenumber and wavelength is non-trivial. The two scales are inverse of one another, meaning a linearly spaced set of wavenumber data will be unevenly spaced in wavelength, leading to a significant distortion in the spectrum. In converting between them, the signal per unit energy must also be scaled [189]. However, since such a transformation would be applied to both the source and reference, in this case the percentage transmission and reflection can be converted without any transformation.

3.3.3 Description of the FTIR System

The reflection and transmission spectra presented in this thesis were measured using a Bruker 80v Fourier-transform infra-red spectrometer with a tungsten halogen lamp source, a CaF beamsplitter and a silicon diode detector. A UV-protected sliver mirror from Thorlabs was used as the reflection reference and a transmission reference was measured using an empty sample holder (Chapter 6) or a quartz substrate (Chapter 7). Using these references R and T, which are the fractions of reflected and transmitted light, were calculated.

4

Optical and Dynamical Models

Contents

4.1 Transfer Matrix Methods 58
4.1.1 Basic Definitions 58
4.1.2 Derivation of Transfer Matrices 59
4.1.3 Calculation of Reflected and Transmitted Power 64
4.1.4 Inclusion of Incoherent Layers 64
4.1.5 Energy Flow From a Lossy Medium 66
4.1.6 Possible Improvements to the Model 68
4.2 Modelling Charge-Carrier Dynamics 70
4.2.1 Representing Charge-Carrier Density 70
4.2.2 Modelling Charge-Carrier Diffusion 73
4.2.3 Modelling Reabsorption of Emitted PL 79
4.2.4 Models Used for Charge-Carrier Recombination 86

This chapter introduces the self-absorption model which is used in this thesis to describe charge-carrier dynamics in OPTP experiments. The dynamical model is discussed in depth, as the theoretical framework provided here underlies modelling of charge-carrier dynamics presented in the later chapters. The original aspects of the self-absorption model are the incorporation of photon re-absorption and diffusion into the charge-carrier dynamics, implemented here as matrix operations.

Before the introduction of this model, a brief overview of transfer matrices is given,

as this formalism is used to describe light propagation in the MHP samples.

4.1 Transfer Matrix Methods

The MHP samples studied in this thesis are thin films, supported by a glass substrate. To represent the propagation of light through this pair of layers, including multiple reflections, a transfer matrix model is used. This model follows the method of Harbecke [190], and can calculate the reflection and transmission through an arbitrary stack of coherent and incoherent layers. The model is used to extract the refractive index of the $MAPbI_3$ samples in Chapter 6 and is also used by the self-absorption model.

However, the transfer matrix model does not directly describe the power flow out of a lossy material. This is important, as the self-absorption model must determine how much PL is emitted from the absorbing perovskite layer. Therefore expressions for the power transmission out of an absorbing material are also given, following the method of Weber [191].

Although these topics are well established, they form the necessary background to the problem of photon re-absorption, and are used to describe light propagation in the self-absorption model.

4.1.1 Basic Definitions

This section briefly sets out the basic elements of electromagnetic theory which transfer matrices build on. Definitions of the Fresnel equations are presented, along with the complex refractive index. Although this is basic classical electromagnetism, it is important to state how these terms are defined–as several competing definitions exist. In particular, conventions such as the choice of CGS (centimeter-gram-second) or SI units and sign convention for the complex refractive index differ between authors.

The first important definition to make is the complex refractive index, defined here as $\tilde{n} = N + i\kappa$, where N and κ are the real and imaginary parts of the refractive index. The perovskite samples studied in this thesis comprise of one or more thin, homogeneous dielectric layers on top of a substrate, this is modelled as a stack of finite layers, between two infinite layers of air. Layers can be either coherent or incoherent, each having a thickness and (complex) refractive index $\tilde{n}_{layer}$.

To keep track of the propagation direction of the light, one layer in the sample is defined to be the reference layer. In this layer the angle, θ_{ref}, between the direction of propagation and the normal to the layer boundaries, is defined. Using Snell's law,

$$\tilde{n}_i \sin\theta_i = \tilde{n}_{ref} \sin\theta_{ref} \tag{4.1}$$

the direction of propagation in any of the other layers in the stack can then be found. In most situations this reference layer will be air, however this assumption is not made here, to enable light emission from the perovskite layer to be accommodated later.

With these initial definitions made, the Fresnel equations can now be formulated using the above notation. In the current scheme, the amplitude reflection coefficient is given by:

$$\varrho = \begin{cases} (\tilde{n}_a \cos\theta_a - \tilde{n}_b \cos\theta_b)/(\tilde{n}_a \cos\theta_a + \tilde{n}_b \cos\theta_b) & s\text{-polarisation} \\ (\tilde{n}_a \cos\theta_b - \tilde{n}_b \cos\theta_a)/(\tilde{n}_a \cos\theta_b + \tilde{n}_b \cos\theta_a) & p\text{-polarisation} \end{cases} \tag{4.2}$$

and the amplitude transmission coefficient is:

$$\tau = \begin{cases} 2\tilde{n}_a \cos\theta_a/(\tilde{n}_a \cos\theta_a + \tilde{n}_b \cos\theta_b) & s\text{-polarisation} \\ 2\tilde{n}_a \cos\theta_a/(\tilde{n}_a \cos\theta_b + \tilde{n}_b \cos\theta_a) & p\text{-polarisation} \end{cases}. \tag{4.3}$$

These two expressions describe the reflection and transmission of the electric field, rather than the light intensity, which is addressed in Sections 4.1.3 and 4.1.5.

4.1.2 Derivation of Transfer Matrices

This section will introduce transfer matrices, briefly deriving the required transformations of the electric field. The two processes which must be described are: one, the propagation

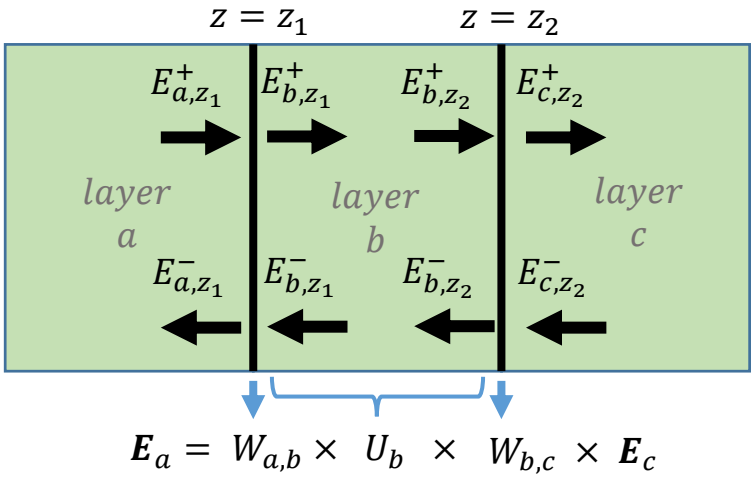


Figure 4.1: Illustration of the transformation of the electric field through a stack of coherent dielectric layers, showing the various transfer matrices used to describe each interface and propagation through the middle layer.

of light through each layer and two, the reflection and transmission of light at the boundaries between layers. In each case the matrix describing the process will be derived using simple physical arguments.

First, an interface matrix W will be derived, to describe the transformation of the electric field between successive layers in a stack. To achieve this, the electric field at the boundary between two layers, a and b is considered. The electric field on each side of the boundary is shown in Figure 4.1. In each layer there is a wave moving left and one moving right, with E_a^+ symbolising the right-moving wave in medium a and E_b^- the left-moving wave in medium b. If the matrix W describes the transformation of the fields at the boundary, from right to left, then

$$\begin{pmatrix} E_a^+ \\ E_a^- \end{pmatrix}_{z_1} = \begin{pmatrix} W_{11} & W_{12} \\ W_{21} & W_{22} \end{pmatrix} \begin{pmatrix} E_b^+ \\ E_b^- \end{pmatrix}_{z_1}, \tag{4.4}$$

where the waves E_a^+ and E_b^- are moving towards the boundary and the other two waves are moving away from it. Equation 4.4 shows the general case, where light is incident from both sides of the boundary, but in this form it is difficult to work out what is

happening. However, by considering the case of light being incident from only one side at a time, the elements of W can be determined.

Taking first the case where light is incident from side a only, $E_b^- = 0$ and E_a^+ is the only incident wave. This means E_a^- will be the reflection from the boundary and E_b^+ will be the transmitted light. Therefore, normalising the input electric field so that $E_a^+ = 1$, the other electric field components in Equation 4.4 will simply be the Fresnel coefficients:

$$\begin{pmatrix} 1 \\ \varrho_{ab} \end{pmatrix} = \begin{pmatrix} W_{11} & W_{12} \\ W_{21} & W_{22} \end{pmatrix} \begin{pmatrix} \tau_{ab} \\ 0 \end{pmatrix} \tag{4.5}$$

This simplified equation allows two elements of W to be determined:

$$W_{21} = \varrho_{ab}/\tau_{ab}, \qquad W_{11} = 1/\tau_{ab}. \tag{4.6}$$

It is entirely appropriate that the elements of W are linked to the Fresnel coefficients, since the change in $\tilde{n}$ at the interface will cause reflections. By repeating this approach, considering illumination from side b only, $E_a^+ = 0$ and $E_b^- = 1$. Equation 4.1 now becomes

$$\begin{pmatrix} 0 \\ \tau_{ba} \end{pmatrix} = \begin{pmatrix} 1/\tau_{ab} & W_{12} \\ \varrho_{ab}/\tau_{ab} & W_{22} \end{pmatrix} \begin{pmatrix} \varrho_{ba} \\ 1 \end{pmatrix} \tag{4.7}$$

where the previously determined values of W_{11} and W_{21} have been substituted in. Using Equation 4.7 the final two elements of W can be obtained

$$W_{12} = -\varrho_{ba}/\tau_{ab}, \qquad W_{22} = (\tau_{ab}\tau_{ba} - \varrho_{ab}\varrho_{ba})/\tau_{ab}. \tag{4.8}$$

The expression for W_{22} can be simplified to $1/\tau_{ab}$, as $(\tau_{ab}\tau_{ba} - \varrho_{ab}\varrho_{ba}) = 1$ (see Appendix A.1).

By considering the cases of light incident from each side of the interface in turn, the matrix has now been determined:

$$W = 1/\tau_{ab} \begin{pmatrix} 1 & -\varrho_{ba} \\ \varrho_{ab} & 1 \end{pmatrix} \tag{4.9}$$

This matrix describes the transformation of the electric field from right to left between two adjacent layers, in terms of their transmission and reflection coefficients. The transformation of the electric field from left to right is given by W^{-1} ($W_{ab}^{-1} = W_{ba}$), as shown in Appendix A.2.

***

The propagation matrix, describing propagation of light through a layer, can be derived even more simply, as there is no coupling of the right and left travelling waves. The only modification of the wave as it travels through a layer will be the accumulation of (complex) phase. The extra phase acquired travelling through layer b is given by

$$\phi_b = \exp\left(\frac{i\omega\tilde{n}_b \cos\theta_b d_b}{c}\right). \tag{4.10}$$

where d is the layer thickness and ω the angular frequency of the light. The phase decreases with increasing angle, as although a single light ray travels further through the material, at a constant x, y point, the wavefront of a plane wave arrives more quickly at the boundary.

To account for the propagation within a single layer, b, a matrix U is needed such that $\mathbf{E}_b|_{z_1} = U_b\mathbf{E}_b|_{z_2}$. As already argued above, this matrix must only alter the right and left travelling waves by adding an extra phase ϕ_b. Therefore,

$$\begin{pmatrix} E_b^+ \\ E_b^-\phi_l \end{pmatrix} = \begin{pmatrix} U_{11} & U_{12} \\ U_{21} & U_{22} \end{pmatrix} \begin{pmatrix} E_b^+\phi_l \\ E_b^- \end{pmatrix}. \tag{4.11}$$

As there is no coupling between the two waves, the off-diagonal elements of U must be zero. With this simplification made, it is then straightforward to determine the diagonal elements, giving the phase matrix:

$$U = \begin{pmatrix} \phi_l^{-1} & 0 \\ 0 & \phi_l \end{pmatrix} \tag{4.12}$$

This propagation matrix accounts for the complex phase accumulated by waves travelling through a layer.

***

Transfer matrices are not meant to be considered in isolation, instead their real benefit is seen only when they are combined. As the operations are linear, they can be combined to account for the transformation of the electric field through many layers at once. This can be seen at the bottom of Figure 4.1 where the transformation between layers a and c is shown. The transformation includes two interfaces and propagation through one layer:

$$E_a = W_{ab} U_b W_{bc} E_c \tag{4.13}$$

However, it is possible to multiply the three matrices together, into a single transfer matrix, $T_{ac} = W_{ab} U_b W_{bc}$. This transfer matrix describes, in one step, the overall transformation of the electric field between the layers a and c

$$\begin{pmatrix} E_a^+ \\ E_a^- \end{pmatrix}_{z_1} = \begin{pmatrix} T_{11} & T_{12} \\ T_{21} & T_{22} \end{pmatrix} \begin{pmatrix} E_c^+ \\ E_c^- \end{pmatrix}_{z_2}, \tag{4.14}$$

which is in the same form as Equation 4.4. The transformationT_{ac} packages the propagation into, through, and out-of layer b as a single 'effective' interface. This means the same arguments used to derive W can now be employed again. However, since the elements of T_{ac} are known, the goal this time is to find the reflection and transmission of the effective interface. Here, ϱ is replaced by r and τ by t, as the reflection is not from a specific interface. Repeating the steps of Equations 4.5 - 4.8, the amplitude coefficients r and t are produced

$$\begin{aligned} r_{ac} &= T_{21}/T_{11}, & t_{ac} &= 1/T_{11} \\ r_{ca} &= -T_{12}/T_{11}, & t_{ca} &= \det(T)/T_{11} \end{aligned} \tag{4.15}$$

In this case, since $T_{ac} = W_{ab} U_b W_{bc}$, r and t describe the total reflection of the two interfaces, separated by layer b. More generally this approach allows any combination of coherent layers and interfaces to be reduced into a single matrix. The only necessary condition for combining successive layer is that they must be coherent. The treatment of non-coherent layers, and the conversion of amplitude coefficients to intensities is dealt with in the next section.

4.1.3 Calculation of Reflected and Transmitted Power

This section details how r and t (the electric field amplitude coefficients) for a stack of coherent layers can be converted into intensity coefficients. This is important not just for finding the reflected and transmitted intensities of a sample, but it will also form the basis for including incoherent layers into the transfer matrix formalism.

Power flow between two materials is determined by the components of the time-averaged Poynting vector normal to the interface. Between two non-absorbing media, the reflected power intensity is related to the amplitude coefficients by $\mathrm{R} = |r|^2$. In the transfer matrix formalism this is equivalent to [190, 192]

$$\mathrm{R} = \frac{T_{21}}{T_{11}} \tag{4.16}$$

The transmitted power from layer i (initial) to f (final) can similarly be expressed as $\mathrm{T} = |t|^2 * (N_f \cos\theta_f)/(N_i \cos\theta_i)$. Here, the expression is complicated by an additional geometrical factor. At normal incidence this factor simply accounts for differences in propagation speeds of the light in each material. Additionally at oblique angles of incidence it will also account for the change in direction of the power flow caused by refraction. Using the matrix notation T is expressed as

$$\mathrm{T} = \frac{1}{T_{11}} \times \left(\frac{N_f \cos\theta_f}{N_i \cos\theta_i} \right) \tag{4.17}$$

Where N is the real part of the refractive index. While absorbing layers can be present between the enclosing layers, these equations are valid only where the outer layers are non-absorbing materials. Power transfer from absorbing media is discussed in Section 4.1.5.

4.1.4 Inclusion of Incoherent Layers

At visible wavelengths the coherence length of many sources will be less than the typical mm thickness of substrates used to support samples. This means that multiple reflections

from the substrate will not interfere with one another, as they will hold no constant phase relation. If these reflections are modelled as coherent they cause a fast and un-physical oscillation in the simulated transmittance and reflection spectra [193].

Several approaches to including incoherent layers into the transfer matrix scheme have been developed. Early methods averaged coherent results over a suitable spectral window, but this is computationally inefficient [194]. More efficient numerical methods have been developed based on matching or eliminating the phase of incoherent reflections [195]. Other approaches are aimed at including partial incoherence, and simulating roughness by the addition of random phases [196, 197]. In this thesis, a flexible system of removing interference developed by Harbecke [190] is used, and will now be described briefly.

Within this scheme, groups of coherent layers are first collapsed together into single transfer matrices, as before. This leaves only incoherent matrices, separated by single effective interfaces.

To combine the effect of these layers incoherently the usual transfer matrices are replaced with their absolute squares

$$U_{incoh} = \begin{pmatrix} |\phi_j|^{-2} & 0 \\ 0 & |\phi_j|^2 \end{pmatrix} \tag{4.18}$$

$$W_{incoh} = 1/|t_{ij}|^2 \begin{pmatrix} 1 & -|r_{ji}|^2 \\ |r_{ij}|^2 & |t_{ij}t_{ij}|^2 - |r_{ij}r_{ji}|^2 \end{pmatrix} \tag{4.19}$$

These incoherent matrices are then combined as in Equation 4.13 and the intensity coefficients are extracted as in Equations 4.16 and 4.17.

This approach allows the calculation of reflected and transmitted intensity through an arbitrary stack of coherent and incoherent layers. This transfer matrix modelling is used in Chapter 6 to fit the complex refractive index of the samples. Additionally, reflections of samples in the self-absorption model are calculated using a transfer matrix approach.

4.1.5 Energy Flow From a Lossy Medium

In the preceding discussion, the assumption has been made that light propagates from an initial layer which is non-absorbing. This will certainly be the case in transmission/reflection experiments, where the sample is bordered on both sides by air. However, in order to properly model photon re-absorption, the emission of light from an absorbing material must be addressed.

The problem of PL emission is tackled as two related problems; propagation of light through the layer is delegated to the ray-tracing model described in Section 4.2.3, meanwhile, this section will address the issue of energy flow at the interface between a lossy and non-lossy material. Together these strategies provide a full picture of PL emission, re-absorption and out-coupling.

Several, in-depth treatments describe the issue of power transmission [198] and formulation of transfer matrices [199] for lossy materials. However, to address the case of PL emission, with minimal mathematical overhead, a simpler treatment by Weber [191] is used. This approach, using the Poynting vector to determine the energy flow between a lossy and non-lossy material, will now be summarised.

The starting point is to decide how much of the previously derived expressions are still valid for absorbing media. Firstly, it should be noted that whether the media are absorbing or not, has no effect on the continuity of the electric field at the boundary, meaning that the Fresnel Equations and Snell's law remain valid. The only change will be that the angles and amplitude coefficients will be complex. Similarly, the transfer matrix formalism developed in Section 4.1.2 also describes the transformation of the electric field through a stack of layers, so will remain valid.

However, the expressions given for power transfer rely not on the electric field, but

on the time averaged Poynting vector

$$\mathbf{S} = \frac{1}{4}(\mathbf{E} \times \mathbf{H}^*) + \frac{1}{4}(\mathbf{E}^* \times \mathbf{H}). \tag{4.20}$$

In an absorbing material, the Poynting vector is not parallel to the direction of propagation of the light. This results in an inhomogeneous wave, and changes the power flow normal to the interface. The effect of this can be clearly seen from the fact that the well known result $\mathrm{R} + \mathrm{T} = 1$ does not hold at the boundary between absorbing media.

Taking the case of normal incidence:

$$I = \mathrm{R} + \mathrm{T} \tag{4.21}$$

$$I = rr^* + tt^* \frac{\tilde{n}_2}{\tilde{n}_1} \tag{4.22}$$

$$I = 1 + \frac{4i(\kappa_1 N_2 - \kappa_2 N_1)}{|\tilde{n}_1 + \tilde{n}_2|^2} \tag{4.23}$$

Where the detailed derivation is given in Appendix A.3. Conservation of energy requires that no energy should be lost at the interface, and so Equations 4.16 and 4.17, are not valid for power flow into or out-of absorbing materials.

The solution is to reconsider the components of the Poynting vector normal to the interface. Without any absorption, Equations 4.16 and 4.17 are the reflected and transmitted components on each side of the boundary. When the first medium is absorbing, an extra cross-term remains in the Poynting vector of the absorbing material– coupling the incident and reflected fields. This extra term arises as $\mathrm{H} = (\mathrm{k} \times \mathrm{E})/\omega\mu_0$ is substituted into Equation 4.20. In an absorbing material the complex conjugate of the wave vector k is no longer perpendicular to E, meaning $\mathrm{E.k}^* \neq 0$, and so an extra term enters the continuity equation at the boundary.

With this extra term, the equation for the energy flow out of an absorbing medium a, into a non-absorbing medium b is given by

$$\mathrm{R} + \mathrm{T} = 1 + \Delta \tag{4.24}$$

where, for each polarisation

$$\Delta_s = [r_s - r_s^*] \frac{\tilde{n}_a^* \cos\theta_a^* - \tilde{n}_a \cos\theta_a}{\tilde{n}_a \cos\theta_a + \tilde{n}_a^* \cos\theta_a^*} \tag{4.25}$$

$$\Delta_p = \left[r_p - r_p^*\right] \frac{\tilde{n}_a^* \cos\theta_a - \tilde{n}_a \cos\theta_a^*}{\tilde{n}_a^* \cos\theta_a + \tilde{n}_a \cos\theta_a^*}. \tag{4.26}$$

Conservation of energy leads to the definition that $\mathrm{R} + \mathcal{T} = 1$, where $\mathcal{T} = \mathrm{T} - \Delta$ is the effective transmission. For the case where medium a is non-absorbing, it can be seen that $\Delta = 0$ and the relation $\mathrm{R} + \mathrm{T} = 1$ is recovered.

This does not describe the full propagation of light through an arbitrary stack of incoherent layers. Rather it describes the reflection and transmission intensities through a single interface, or group of coherent layers. It will be shown in Section 4.2.3 that this is sufficient for the modelling of PL emission in perovskite thin films.

4.1.6 Possible Improvements to the Model

The transfer matrix formalism developed in this chapter is entirely sufficient for the work described in this thesis, there are however several logical ways in which the model could be extended in future. Firstly the two approaches above could be united to provide a single unified model, capable of propagation from a layer with a complex refractive index and through incoherent layers. Secondly, the model assumes that layers are of a well defined thickness, which is appropriate for evaporated perovskite films. Spin-coated films, however, have more variation in thickness across their area [26]. A natural improvement would therefore be to extend the model to fit layers with varying thickness. This could be achieved by using the existing approaches of partial incoherence [196, 197], or through averaging coherent reflections across a distribution of trial thicknesses. Such measures were not introduced, as they were not required for perovskite films studied in the subsequent chapters. Finally, it should be noted that the current model ignores scattering, which may be present at the interfaces between layers or throughout the bulk. The model

could be expanded to support scattering, as a form of incoherence, however, this was not required for the low levels of scattering present in the samples used in this thesis.

4.2 Modelling Charge-Carrier Dynamics

This section outlines how charge-carrier dynamics are simulated in this thesis. First, the geometry of the OPTP experiment is used to show how the charge-carrier density in a sample can be described in a 1D manner, as a stack of slices with different charge-carrier densities. Next, charge-carrier diffusion and photon re-absorption are presented as matrices which transfer charge carriers between the different slices. Finally, two dynamical models are described; the 'standard' recombination model and the 'self-absorption model'.

These models, and their implementations, as described here, form the basis for OPTP simulations in this thesis.

4.2.1 Representing Charge-Carrier Density

The first step towards a model of charge-carrier dynamics is to be able to represent the charge-carrier density, n, within a perovskite film during an OPTP experiment. Two approaches are introduced, one, using an average value of n, and the other considering n as a 1D array, which varies through the sample depth.

First, it will be shown that n can be reduced to being at most 1D, as no areal variation need be considered. In an OPTP experiment, the charge carriers inside a sample will be excited by the absorption of light from a pulse of above-gap light, known as a pump beam. As the pump beam has a Gaussian shape, there will be a spatial variation in the generated charge carriers. However, the OPTP experiment is only sensitive to charge carriers which interact with the THz probe beam. Since the THz beam is much narrower than the pump, only the charge carriers at the very centre of the pump-excited area are important. Within this area, the pump intensity is uniform, and n does not vary. This means that, n in an OPTP experiment will at most only vary through the film depth. Being able to reduce the problem to only one dimension is valuable, as it makes any modelling substantially simpler.

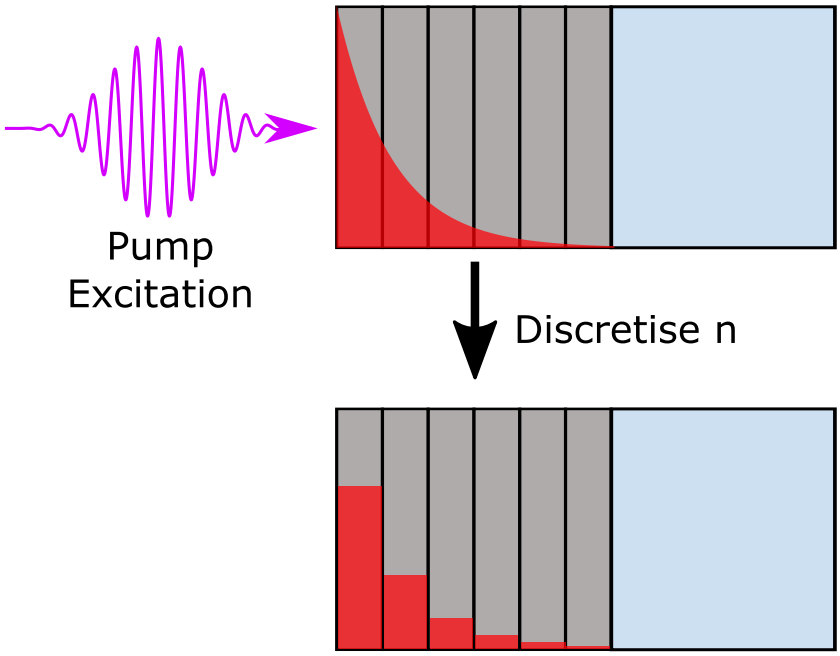


Figure 4.2: Schematic showing the discretisation of charge-carrier density from the Beer profile caused by pump-excitation, into a series of slices with different carrier densities.

Having reduced the system to a 1D model, the absorption of light through the film depth can now be considered. Figure 4.2 shows how light incident on the surface of a perovskite film is absorbed. The absorption follows Beer's law,

$$I(z) = I(0)e^{-\alpha z} \tag{4.27}$$

where z is the direction of travel into the perovskite layer. Different modelling approaches now diverge in the representation of this initial distribution of charge carriers.

As mentioned at the start of the section, there are two available strategies, either taking an average n or treating n as an array, varying through the depth of the film. The majority of previous studies do not consider a variation in n through the film depth [95, 97]. With this approximation, the assumption is typically made that all charge carriers are absorbed within $1/\alpha_{pump}$ of the surface. In this thesis, the resultant charge-carrier density profile is termed a 'step' profile, as when viewed in profile, there is a sharply defined step in n, visible in Figure 4.3. Another possible approach is to assume that charge carriers will be evenly spread across the entire film thickness [153], giving the

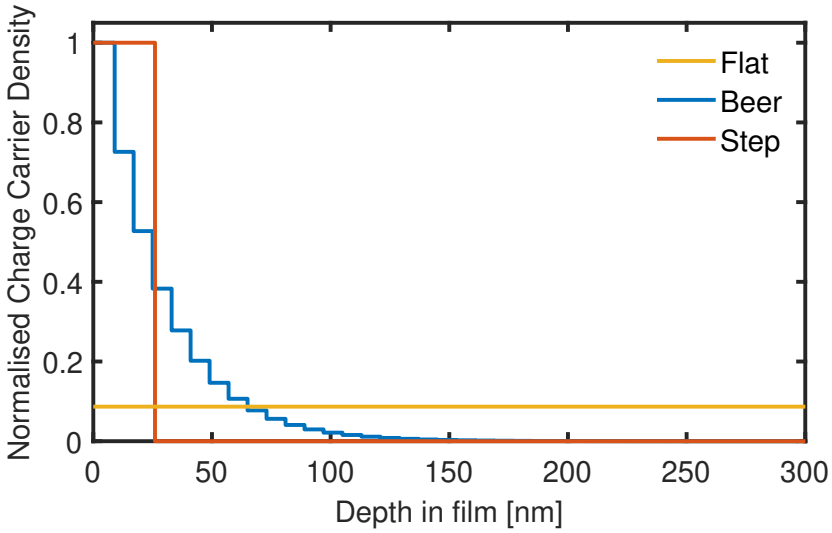


Figure 4.3: Modelled representation of the various n profiles described in the text, with each profile normalised to show the same number of charge-carriers. While the step and flat distributions each use a single average n, the Beer profile separately describes n at each point through the film depth.

'flat' profile in Figure 4.3. These two profiles are computationally simple, as they have only a single n. However, modelling the charge-carrier density in this way neglects the possibility that transport processes such as diffusion or photon re-absorption can alter the spatial distribution of charge carriers.

Alternatively, the initial n profile in a perovskite film can be modelled as an array of charge-carrier densities, using the procedure developed by Wehrenfennig *et al* [121]. In this case, the continuous Beer profile is discretised into a number of slices, as shown in Figure 4.2. In this formulation,

$$n(z) = \begin{pmatrix} n_1 \\ n_2 \\ n_3 \\ \vdots \\ n_{\mathrm{N}} \end{pmatrix} \tag{4.28}$$

where n_i represents the charge carrier density in the i^{th} slice. Comparing this profile to the step and flat profiles, Figure 4.3 shows that this pseudo-Beer profile more closely resembles the actual Beer profile in the sample. Furthermore, this formulation of charge-carrier density naturally supports transport processes transferring charge carriers between the

slices. However, the extra complexity in modelling n as an array means that simulations become more computationally intensive, scaling quadratically with film thickness.

The various n profiles have been introduced here and in Chapter 5 the influence of the choice of profile upon the fitted recombination constants is investigated. In the following chapters, n will always be formulated as an array, unless otherwise stated.

Throughout this thesis the perovskite films are modelled as consisting of 2 nm thick slices. This value was chosen to accurately capture the range of charge-carrier densities produced by the initial Beer profile and provide a fine-grained picture of the charge-carrier distribution within the perovskite films.

As a final point, the initial charge-carrier distribution is generally determined by the ray tracing model in Section 4.2.3, rather than using a simple Beer profile. This means multiple reflections are included, and thin samples are more accurately modelled. Additionally, the in-coupled intensity through arbitrary combinations of other layers in the sample is calculated by the transfer matrix formalism from Section 4.1.

4.2.2 Modelling Charge-Carrier Diffusion

Where the initial charge-carrier density varies through the depth of a film, it is natural to include the effect of diffusion in any simulation of the charge-carrier dynamics. This section will introduce a matrix which describes 1D diffusion into the depth of a perovskite film. Additionally, the matrix will be generalised to support a changing mobility across the sample.

4.2.2.1 Modelling of Diffusion

It is important to include the effect of diffusion when simulating charge-carrier dynamics, as there is a large initial gradient in n, through the film depth. This situation is unstable and, as illustrated in Figure 4.4, diffusion leads to the flattening out of the

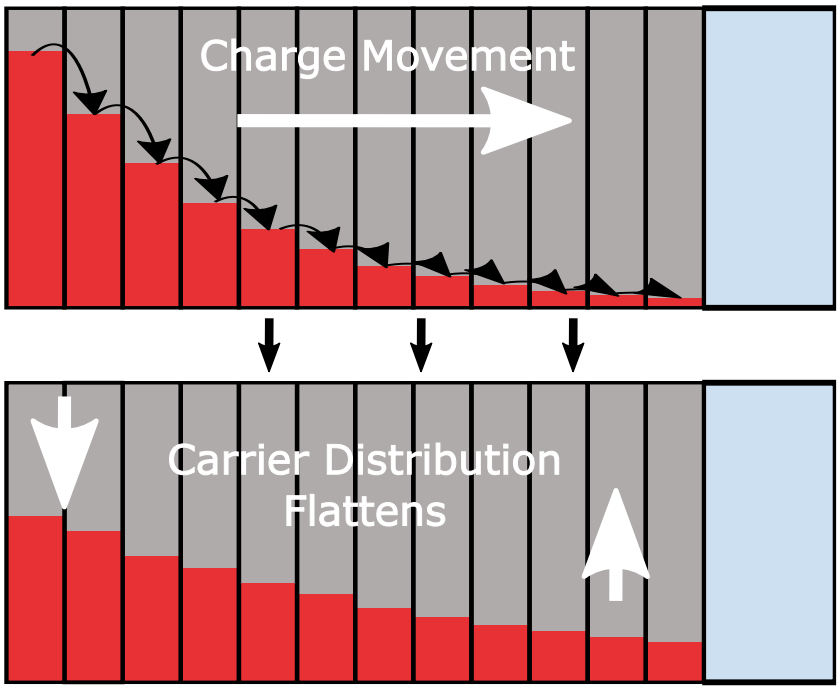


Figure 4.4: Schematic showing the diffusion of charge carriers through the depth of a perovskite film and the resulting flattening out of the initial absorption profile of the pump beam.

initial charge-carrier distribution through the film depth. This is critical to the charge-carrier dynamics, as radiative and Auger recombination are non-linear, meaning they will be suppressed by diffusion.

As the charge-carrier distribution in an OPTP experiment was shown to be 1D in Section 4.2.1, diffusion can also be simulated as a 1D process. The diffusion equation in 1D is given by

$$\frac{\partial n(z,t)}{\partial t} = D\frac{\partial^2 n(z,t)}{\partial z^2} \tag{4.29}$$

with D being the diffusion coefficient. The diffusion coefficient can be determined from the charge carrier mobility μ, using the relation

$$D = \frac{\mu \mathrm{k_B} \Theta}{e}. \tag{4.30}$$

where Θ is the sample temperature. In the subsequent chapters, μ is determined using OPTP spectroscopy, which samples the charge carrier mobility on a length-scale of a few nm [200, 201]. This is on a similar length scale to the 2 nm slice width used in the

model, meaning that the THz mobility can be expected to be constant across a single slice. When considering charge-carrier movement on longer length scales, the diffusion coefficient may be lower than the more local value derived from THz mobility. This is because, when travelling longer distances charge-carriers must cross grain boundaries and in the case of perovskite material embedded within a TiO_2 scaffold charge-carriers must percolate through the mesostructure, resulting in a lower diffusion coefficient. In this thesis, the MHP films which are studied are highly homogeneous. For this reason the THz mobility is used to describe diffusion over length-scales of hundreds of nm, as the local microstructure is taken as representative of the long range structure.

The diffusion equation is solved numerically, using the Forward Euler solution. This solution uses a first-order Taylor expansion of Equation 4.29 to find an updated value of n. A computationally convenient way to represent this solution is as a matrix equation

$$n(t+1) = (M+I)n(t). \tag{4.31}$$

where I is the Identity matrix and M is a matrix which implements diffusion. Using this solution, n is updated at each time-step of the simulation by applying M to the current charge-carrier distribution. In the case where all slices have a uniform mobility, and using a Forward Euler solution with solid boundaries

$$M = F \times \begin{pmatrix} -1 & 1 & 0 & 0 & \dots & 0 & 0 & 0 \\ 1 & -2 & 1 & 0 & \dots & 0 & 0 & 0 \\ 0 & 1 & -2 & 1 & \dots & 0 & 0 & 0 \\ \vdots & \vdots & \vdots & \vdots & \ddots & \vdots & \vdots & \vdots \\ 0 & 0 & 0 & 0 & \dots & 1 & -2 & 1 \\ 0 & 0 & 0 & 0 & \dots & 0 & 1 & -1 \end{pmatrix}. \tag{4.32}$$

The physical interpretation of this matrix is that each slice redistributes charge-carriers to the adjacent slices, represented by the elements in the off-diagonal rows. Charge-carrier density is conserved overall as $\sum_{i,j} M_{i,j} = 0$. Additionally charge-carrier density is conserved locally as the sum of each column of M is also zero, meaning that no more

charge is subtracted from a slice than is placed into the adjacent slices. The magnitude of the diffusion matrix in each step is determined by

$$F = \frac{D\Delta t}{\Delta x^2} \tag{4.33}$$

where Δt is the time-step taken by the model, and Δx is the width of the slices.

The model, as described here and used throughout this thesis, treats electrons and holes as a single entity – making the approximation that they share a common mobility value. This simplification is supported by multiple studies which have shown the electron and hole mobilities in MAPI to be similar, although not identical [15, 77, 101]. In general, the electron mobility and hole mobility of a material can be different, such as in GaAs where the electron mobility is more than 28 times greater than the hole mobility at room temperature [65]. Where there is a difference in the electron and hole mobility each species will diffuse at different rates, leading to a spatial separation of the two types of charge carrier and creating an electric field inside the semiconductor. In this case the dynamics of each species must be accounted for separately and the electric field arising from the space charge also needs to be taken into account. However, as the electron and hole mobilities in MAPI are very similar, throughout the rest of this thesis the electrons and holes in MAPI are approximated as having equal mobility, which greatly simplifies the modelling of the charge-carrier dynamics.

It should be noted that the Forward Euler solution is not the most accurate or elaborate method of solving the Diffusion Equation. However for a typical simulation, lasting 2 ns, with a time-step of 50 fs there will be only 40000 steps made. therefore since the steps are small, and the simulation a short time-window, the model retains sufficient precision. In return, the model is numerically simpler than other solutions, and so fewer computations are required.

4.2.2.2 Stability of the Forward Euler Solution

The Forward Euler solution for diffusion is a numerical solution, not an analytical result. As such, care must be taken to ensure the solution remains stable. Rewriting Equation 4.31 in index notation gives:

$$n_{i,t+1} = n_{i,t} + F(n_{i-1,t} + n_{i+1,t} - 2n_{i,t}).$$

From here, this equation can be rearranged as

$$n_{i,t+1} = n_{i,t}(1 - 2F) + F(n_{i-1,t} + n_{i+1,t}) \tag{4.34}$$

from which it can clearly be seen that if $F > 0.5$ then $n_{i,t+1}$ can be negative, and the solution is unstable. Considering the definition of F in Equation 4.33, this stability criterion places an upper limit on the time-step possible for a given point-spacing and diffusion constant. In simulations, the time-step of the model is set so that F is as large as possible, under the constraint that $F < 0.5$ and that an integer number of steps fit into each ps. This minimised the number of required steps, and ensures the model stays in sync with the recombination steps which occur every ps.

4.2.2.3 Extension for Non-Uniform Charge-Carrier Mobility

In the previous section charge-carrier density was expressed as an array of values, varying throughout the film depth, while the sample itself was considered as homogeneous. However, this scheme can be extended to cases where the mobility varies across the sample depth. If the mobility of a sample is a function of position, diffusion will happen differently across the sample and the matrix presented in Equation 4.32 will not be valid.

In order to correctly simulate a non-uniform mobility across the sample, diffusion between each pair of slices needs to be addressed separately. Instead of using the

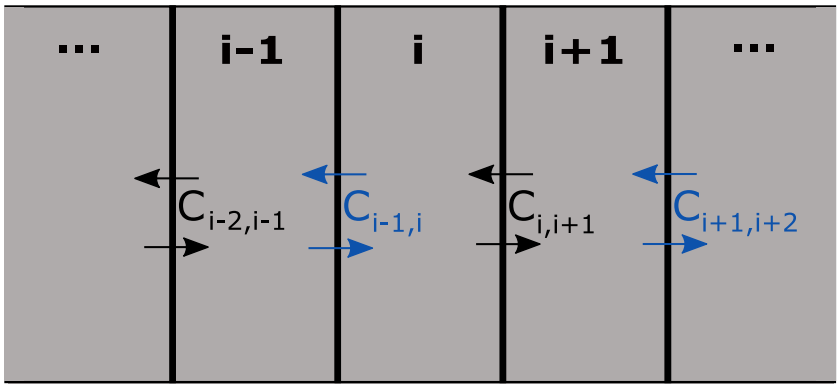


Figure 4.5: Schematic showing coupling between adjacent perovskite slices in the diffusion model, where the coupling between two slices depends on their charge-carrier mobility, which may vary across the sample.

equal coupling between each pair of slices in Equation 4.32, a generalised coupling element is introduced

$$C_{i,i+1} = \frac{F_i + F_{i+1}}{2}. \tag{4.35}$$

Here, the exchange between any two adjacent slices is then simply the mean of their individual F values. This is illustrated in Figure 4.5

The diffusion of charge-carriers through the sample can then be represented in the generalised matrix

$$M = \begin{pmatrix} -C_{1,2} & C_{1,2} & & \dots & 0 & 0 & 0 \\ C_{1,2} & -(C_{1,2}+C_{2,3}) & C_{2,3} & \dots & 0 & 0 & 0 \\ \vdots & \vdots & \vdots & \ddots & \vdots & \vdots & \vdots \\ 0 & 0 & 0 & \dots & C_{n-2,n-1} & -(C_{n-2,n-1}+C_{n-1,n}) & C_{n-1,n} \\ 0 & 0 & 0 & \dots & 0 & C_{n-1,n} & -C_{n-1,n} \end{pmatrix}. \tag{4.36}$$

Again, charge-carrier density is conserved both on the scale of the entire sample (as $\sum_{i,j} M'_{ij} = 0$), as well as locally within each column. For the case where mobility is constant across the sample, the coupling between each of the elements in Equation 4.36 is identical and Equation 4.32 is recovered.

It should also be noted that, in this case, the stability criterion in Section 4.2.2.2 still holds. However, where F holds a range of values, the stability criterion must be fulfilled by all of them, so the time-step for the solution to be stable is limited by the largest value of F.

4.2.2.4 Optimisations of the Model Implementation

The implementation of the above diffusion routine in Matlab has been improved by several optimisations, briefly outlined here.

Firstly, given that M is triagonal matrix typically consisting of several hundred slices many of the elements will simply be zero. Therefore significant performance gains can be achieved by making M sparse.

Secondly, due to the stability criterion of the forward Euler solution ($F < 0.5$) the time-steps for the diffusion matrix are typically on the order of tens or hundreds of fs. This is much faster than the ps time-step used for the recombination model, meaning many steps of the diffusion model are required for each step of recombination. To improve performance, the total diffusion occurring in one ps can be pre-caculated for a one-time cost, if there are r diffusion steps per ps the matrix, $\tilde{M}_r$, describes the diffusion of charge carriers for one ps:

$$n(t+r) = (M+I)^r n(t) \tag{4.37}$$

$$n(t+r) = \tilde{M}_r n(t) \tag{4.38}$$

In many cases this matrix $\tilde{M}_r$ may also remain sparse, meaning that the two optimisations described are complementary.

4.2.3 Modelling Reabsorption of Emitted PL

In direct band-gap semiconductors, any photons emitted by radiative charge-carrier recombination have the potential to be re-absorbed, creating new charge carriers. This process is known as photon re-absorption or photon-recycling, and plays an important role in charge-carrier recombination dynamics. This section shows how photon re-absorption can be simulated in OPTP experiments, as a matrix operation. Ray tracing is used to describe photon re-absorption, and create PL reabsorption matrices, for use in OPTP simulations.

4.2.3.1 Description of Ray Tracing Model

The technique of ray tracing involves following the path of a ray of light as it propagates through a structure. Physicists typically first encounter this technique when tracing the path of light through a lens in classical optics. However, as a numerical method, it is incredibly powerful for calculation of light through complex 3D systems. Indeed, ray tracing has been widely used for the optical modelling of solar cells. In this context, ray tracing is useful as it determines exactly where inside a solar cell light will be absorbed. Previous uses of ray tracing in solar cells span across different materials and scales. At a larger scale, it has been used to refine the surface texturing of silicon cells [202], and to design structures which frustrate light out-coupling in GaAs cells [203]. It has also been applied on microscopic scale, to understand how photon-recycling reduces radiative loss in GaAs [130, 204].

In this thesis, a specialised 1D model of photon re-absorption is used, which specifically describes photon re-absorption in OPTP experiments. More complex models exist, where photon re-absorption is described in more than one dimension [205]. These allow the effect of photon re-absorption on the open circuit voltage and lateral transport of charge carriers to be investigated. However, for the simulation of charge-carrier dynamics in OPTP it is more advantageous to use a simpler 1D model. This simplification greatly reduces the complexity of the simulation, and make it easier to interpret the results.

The ray-tracing program splits the perovskite layer into slices as in Section 4.2.1. Propagation of PL from a given slice is simulated, using Beer's law to determine how much PL is re-absorbed in each of the other slices, as illustrated in Figure 4.6. Reflections at the perovskite boundaries are considered as described in Section 4.1.5. Since the quartz substrate is much thicker than the perovskite film, it is assumed that any light entering the quartz does not return locally to the film and so is lost. Ray tracing continues until either a specified fraction of the emitted light is absorbed, or the maximum propagation distance is

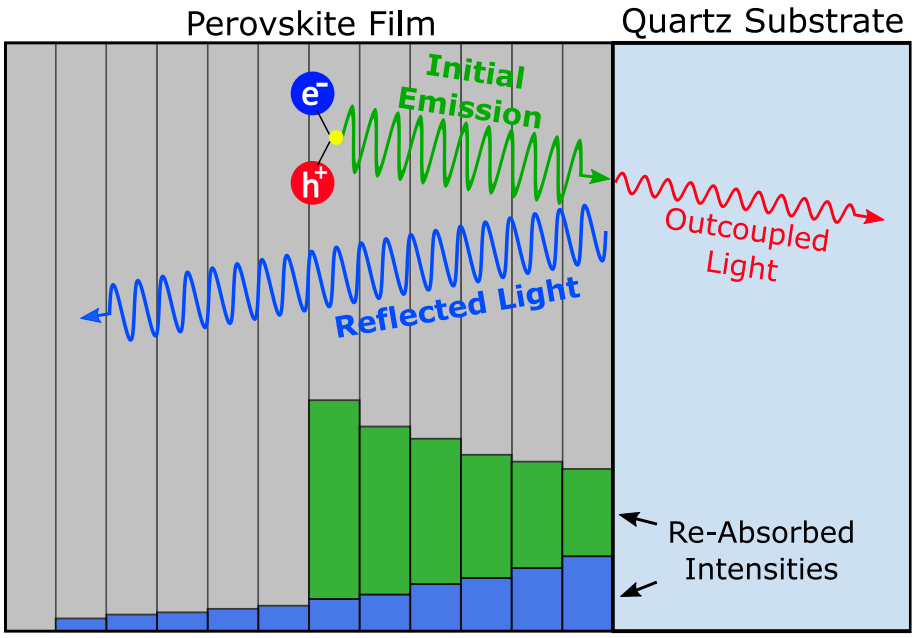


Figure 4.6: An illustration of the ray-tracing model used to model photon re-absorption, showing how emitted light is re-absorbed by a perovskite sample. The top of the figure shows the path of a modelled light ray through the perovskite film, including reflection and out-coupling at the substrate/perovskite boundary. The lower portion of the figure shows how the intensity of the light ray is re-absorbed by each slice in the film, separately displaying the contributions from each stage of the ray's path, to and from the film boundary.

reached. The maximum distance of coherent propagation is limited by scattering, which is experimentally determined for each sample. After this distance is travelled, any remaining intensity is considered lost to scattering and unabsorbed. In this way, emitted intensity is either re-absorbed by a slice, out-coupled through one of the interfaces or unabsorbed.

Although the simulation is 1D, the emission angle of PL in the material is still important. The angle determines the path length travelled by the ray through each slice, as well as the reflection coefficients at the perovskite boundaries. Distance travelled parallel to the film surface is not otherwise important, as the 1D slabs used in the model are uniformly photo-excited across an area much greater than the distance PL can travel in the model, which is typically 1 to 20 µm. This means there is no net flux of photons parallel to the film surface, as any photon travelling laterally in one direction will be compensated by another photon travelling in the opposite direction.

Using this ray tracing procedure, the fraction of PL emitted from a given slice, at

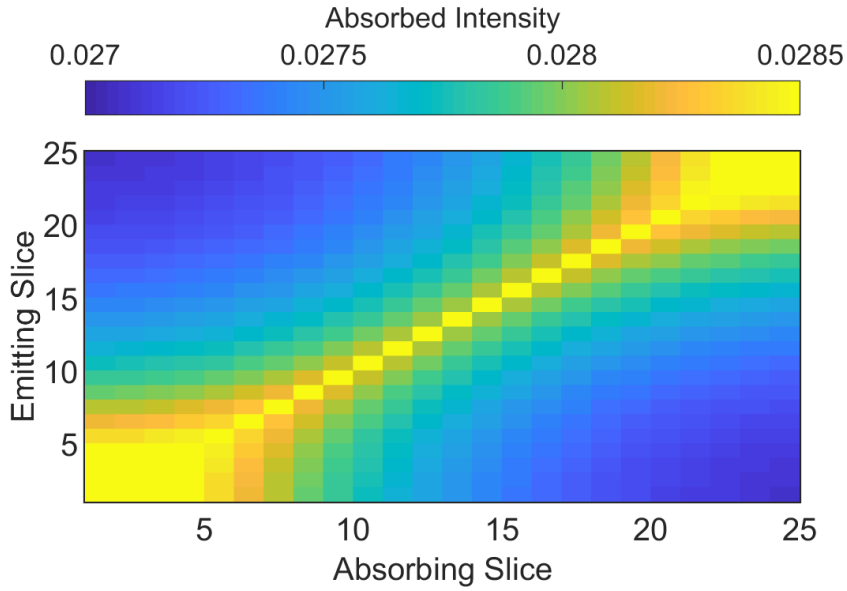


Figure 4.7: Visualisation of a PL redistribution matrix, showing the exchange of PL intensity between 2 nm thick slices in a 50 nm thick MAPI film on quartz. Data was taken from a $MAPbI_3$ film used in Chapter 6. Slices are numbered away from the perovskite/air boundary and elements representing out-coupling and scatter are omitted.

a particular emission angle and wavelength, which ends up being absorbed by each other slice can be determined.

***

Using the basic ray-tracing procedure above, a matrix representing the redistribution of charge carriers by photon re-absorption can be calculated. A typical redistribution matrix for perovskite on quartz is shown in Figure 4.7, with elements representing out-coupling and scatter omitted. Slices are numbered away from the perovskite/air boundary and are 2 nm thick. In the matrix, each row shows how the intensity from an emitting slice is redistributed to the other slices. Similarly, each column shows how much a slice absorbs from the emission of each other slice. When the elements for out-coupling are included, each row of the matrix sums to one, conserving the total number of photons.

The strong diagonal line shows that PL is mostly re-absorbed near to where it is emitted. In fact, looking more closely at any emitting slice in the middle of the film, the exponential absorption profile of Beer's law can be seen, moving away from the

emission point. For the emission near the edges, it can be seen that the bottom-left corner displays higher reabsorption. The higher absorption occurs because air has a lower refractive index than quartz leading to total internal reflection (TIR) at lower angles at the air interface, and so less out-coupling of light.

A redistribution matrix is created by simulating isotropic PL emission at each point in the sample. Typically this process will first be run at each wavelength over which the sample emits PL. The process of creating a redistribution matrix for a single wavelength is illustrated in Figure 4.8. For each slice in the film, isotropic PL emission can be modelled by appropriately averaging the results of the ray tracing model over all possible angles. This determines where the PL emitted isotropically, from one slice, at a given frequency will be re-absorbed. In terms of Figure 4.7, this generates one row at a specific wavelength. Repeating this procedure for each slice, provides a monochromatic redistribution matrix of where the PL emitted by each slice will end up being re-absorbed. This process is then repeated for each wavelength at which PL is emitted. The observer pattern [206] is used to update refractive indices of each layer in the sample as the wavelength is changed, at the same time updating the reflections from the perovskite boundaries. Once the process is complete a series of monochromatic PL redistribution matrices have been generated, describing the sample.

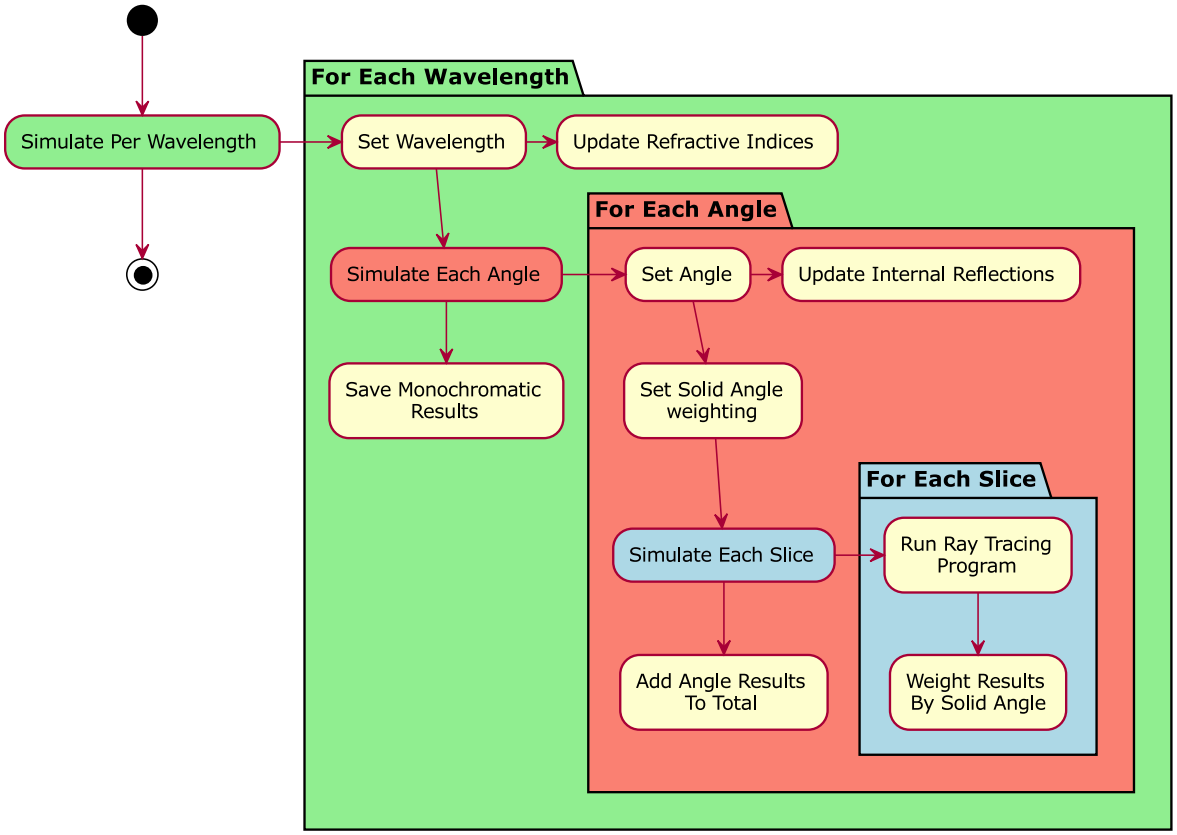


Figure 4.8: Unified modelling language (UML) diagram showing the process of calculating the re-absorption in perovskite films.

4.2.3.2 Relation of Emitted and Measured PL Spectra

Since the photon re-absorption for a single wavelength has been described, the next step is to simulate the reabsorption of a PL spectrum in a single matrix. This matrix will be a sum of the monochromatic PL redistribution matrices, weighted by the normalised PL intensity at each wavelength.

However, the externally measured PL spectrum of a sample is subject to photon re-absorption. It is, therefore, necessary to correct for this and determine the PL spectrum as initially emitted within the material. This can be achieved using the ray tracing model, since it already contains the out-coupled fraction of light, which is the escape probability of emitted PL, P_{escape}. The escape probability, as a function of wavelength,

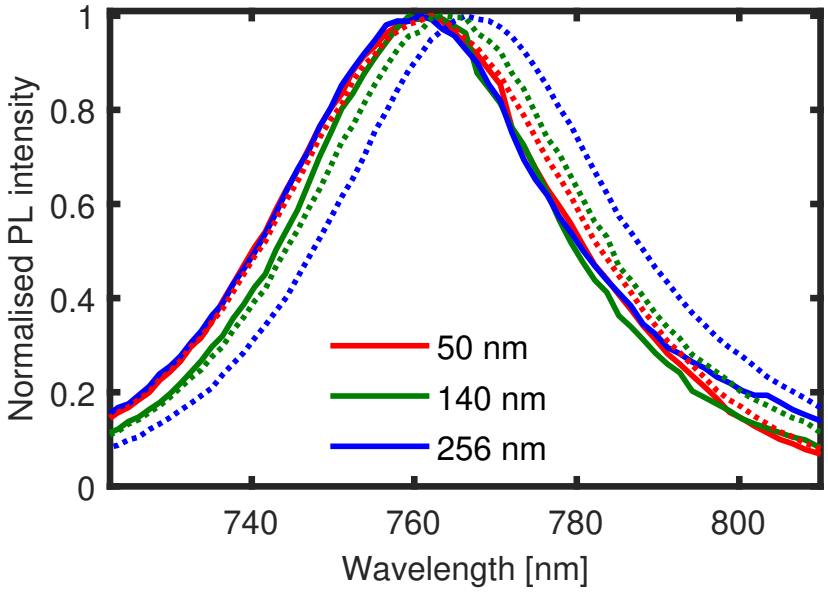


Figure 4.9: PL spectra for three of the $MAPbI_3$ samples used in Chapter 6, shown with (solid lines), and without (dotted lines) a correction for photon re-absorption. While the uncorrected data show a red-shift in centre wavelength as the film thickness increases, this is absent in the corrected data.

relates the internally-emitted and externally-measured PL spectra

$$PL_{measured} = \mathrm{P}_{escape} PL_{emitted}. \tag{4.39}$$

This photon re-absorption correction allows the internal PL spectrum to be obtained from the externally measured PL spectrum.

With the internal PL spectrum determined, the monochromatic PL reallocation matrices described above can then be combined together, weighted by the PL emission intensity at each wavelength, providing a comprehensive PL reallocation matrix for a given perovskite film.

An example of this correction is shown in Figure 4.9, for three $MAPbI_3$ samples from Chapter 6 with different thicknesses. The centre-wavelength of the externally measured PL spectrum red-shifts in the thicker films. This reflects that, as the PL travels through more perovskite to escape, more of the shorter wavelengths are absorbed. However, in the corrected spectra the spread in PL centre-wavelength is visibly reduced, as the shorter wavelengths are recovered.

Using only the externally measured PL spectrum to simulate photon re-absorption would lead to an underestimate of the effects of re-absorption. This is because the wavelengths which will be strongly re-absorbed are, by definition, under-represented in the externally measured spectrum.

In conclusion, the result of this section is that the process of photon re-absorption in an OPTP experiment can be modelled using a single matrix. The ray tracing procedure has also generated a method of correcting measured PL spectra for photon re-absorption. This provides the internally emitted PL spectrum of a sample, unfiltered by self-absorption.

4.2.4 Models Used for Charge-Carrier Recombination

Two models for charge-carrier dynamics are now discussed, with the processes included in each dynamical model and the solution of the governing equations being described. As the models operate in terms of n, while the OPTP experiments measure THz photoconductivity, it is also demonstrated how these two quantities are related.

4.2.4.1 Standard Model For Charge-Carrier Recombination Dynamics

The first dynamical model will be referred to as the 'standard model' of charge-carrier dynamics. This model is widely used in other studies [95, 97, 121, 138, 207, 208], and ignores the effects of self-absorption and charge-carrier diffusion. The free charge-carrier recombination within this standard model is governed by the rate equation:

$$\frac{dn}{dt} = G - k_3 n^3 - k_2^{\text{apparent}} n^2 - k_1 n \tag{4.40}$$

where n is the charge carrier density, G is the charge-density generation rate. k_1, $k_2^{apparent}$ and k_3 are the first, second and third order recombination constants respectively. The second order recombination is denoted $k_2^{apparent}$ as it does not account for any photon re-absorption. This distinction is made to differentiate this rate, from $k_2^{intrinsic}$–which does account for photon re-absorption. This 'standard model' is entirely appropriate

in cases where charge-carrier transport processes are not important, such as when two-photon absorption is used to evenly excite a sample and can be used with either a single average n or an array of n values.

Equation 4.40 is formulated in terms of n, but, the experimentally observed quantity in OPTP experiments is $x = \Delta\mathrm{T}/\mathrm{T}$. To relate the model to experiment, Equation 4.40 is first solved in terms of x, then converted to units of n. Restating the standard model in terms of $\Delta\mathrm{T}/\mathrm{T}$:

$$\frac{dx}{dt} = G - A_3x^3 - A_2x^2 - A_1x \tag{4.41}$$

an ODE solver is then used to determine the A coefficients. These A coefficients relate linearly to the recombination constants, due to the directly proportional relation between n and x, with each pair being related by:

$$A_i = C^{i-1}\phi^{i-1}k_i. \tag{4.42}$$

The proportionality factor, C, which links the absorbed photon density and the initial THz response is defined:

$$C = \frac{E\lambda}{hc \times V \times x(0)}(1 - R_{pump})(1 - T_{pump}), \tag{4.43}$$

where V is the volume in which the charge carriers are contained. Alternatively, if the charge-carrier distribution is modelled as several slices, C can be expressed as the sum of THz photoconductivity from each slice:

$$C = \frac{1}{x(0)}\sum_j \frac{N_j}{V_j}. \tag{4.44}$$

with j being the slice index.

In this way, the recombination coefficients can be extracted from the model. Due to the dependence of the second and third order recombination constants upon the volume occupied by the charge-carriers, the choice of n profile is crucial. The standard

model, is able to describe charge-carrier recombination, but not diffusion or photon re-absorption. It is for this reason that the model has been extended into the self-absorption model, described in the next section.

4.2.4.2 Self-Absorption Model For Charge-Carrier Recombination Dynamics

The second model used to understand the charge-carrier dynamics is the 'self-absorption' model. Unlike the standard model, this model accounts for self-absorption of the emitted PL and charge-carrier diffusion. As these transport processes are included, this model requires that n be considered as an array–otherwise there can be no charge-carrier transport. With the addition of charge diffusion and photon re-absorption, the governing equation for the charge-carrier dynamics is now:

$$\frac{\partial n}{\partial t} = D\frac{\partial^2 n}{\partial z^2} + G - k_3 n^3 - k_2^{intrinsic} n^2 - k_1 n. \tag{4.45}$$

Where the first term accounts for charge-carrier diffusion and the second term is the charge-carrier generation rate, which includes photon re-absorption. The implementation of these processes as matrix operations is described in Sections 4.2.2 and 4.2.3.

Here, the second-order recombination process is denoted $k_2^{intrinsic}$, and represents the rate at which charge carriers recombine radiatively in the perovskite film. This is to make a distinction from the previously defined $k_2^{apparent}$, as some of the emitted photons will later be recaptured by photon re-absorption. Only radiative recombination where the photons are not re-absorbed contributes to $k_2^{apparent}$. This difference between the two definitions of k_2 is addressed in more depth in Chapter 5.

Equation 4.45 is fitted to experimental data using a non-linear least-squares fitting algorithm. This globally fits the recombination constants across several sets of THz photoconductivity transients. At each step in the fitting process, the self-absorption equation is solved numerically, using a finite difference time domain method. The steps

implemented by this simulation are illustrated by the activity diagram in Figure 4.10. After the initial charge-carrier distribution has been loaded into the program, a main loop is entered, which advances the model in 1 ps time-steps. At the start of each cycle, n is allowed to evolve for 1 ps under diffusion. After this, the number of recombining charge carriers in each slice is determined. The radiative fraction of these recombining charge carriers is multiplied by the re-absorption matrix to determine the number and location of recaptured photons. Next, n is updated to reflect the recombination losses, and to add any new charge carriers generated by photon re-absorption.

Before finishing the loop, the program can optionally log the current n. Since the goal is to compare the model to the data, the state of n is stored at the times where experimental data is recorded. The program then returns to the beginning of the loop, until the maximum experimental time-delay has been simulated.

After the simulation has finished, the program converts the stored n values to ΔT/T. This conversion means that the modelled and experimental results are the same units, so the difference between them can be found, and returned to the fitting function.

The necessary conversion factor is determined, by combining Equations 3.1 and 3.3 to give

$$\left(\frac{\Delta T}{T}\right) = -\frac{\mu e}{\epsilon_0 c(\mathrm{n_a} + \mathrm{n_b}) A_{eff}} N. \tag{4.46}$$

This relates the total number of charge carriers in a sample to the induced THz photoconductivity. However, for the self-absorption model it is more useful to express this relation as

$$\left(\frac{\Delta T}{T}\right) = -\sum_j \frac{\mu e d_j}{\epsilon_0 c(\mathrm{n_a} + \mathrm{n_b})} n_j \tag{4.47}$$

where d_j and n_j are the thickness and charge-carrier density of the j^{th} slice.

A major advantage of this approach is that spatial differences in mobility can be accounted for. Since the induced THz photoconductivity is proportional to μ this will

be important in samples which contain regions of differing mobility. This aspect of the model is investigated in Chapter 7.

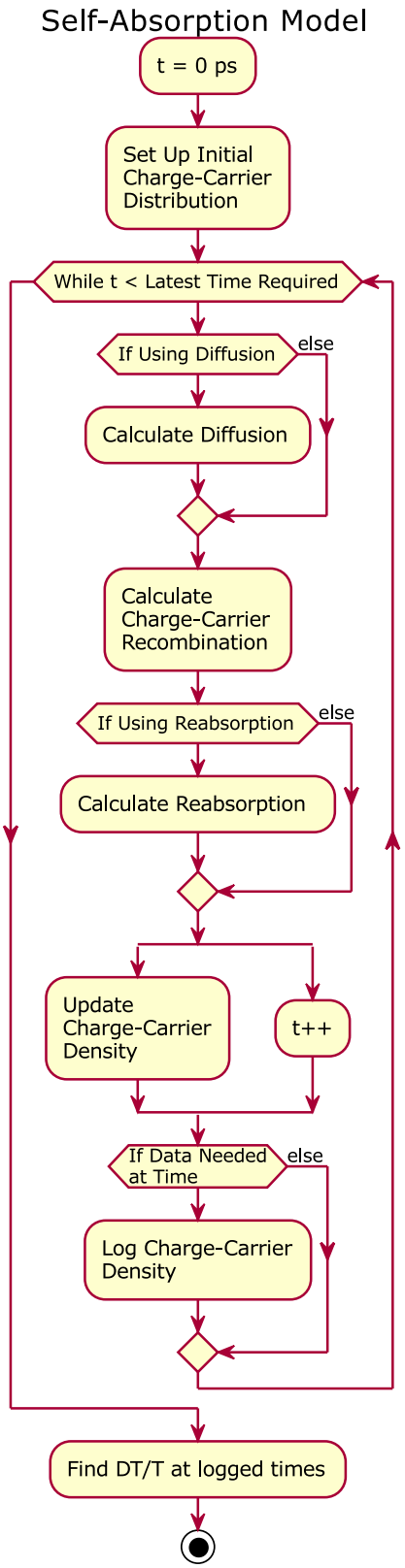


Figure 4.10: UML activity diagram showing the steps taken by the self-absorption model

5

Quantifying the Effects of Charge-Carrier Transport Processes on Bimolecular Recombination in $MAPbI_3$

Contents

5.1 Simulation of charge-carrier dynamics in $MAPbI_3$ Thin Films 95
5.2 Effect of Transport Processes on Charge-Carrier Dynamics 95
5.3 Quantifying the Differences Between Dynamical Models . . 102
5.3.1 Comparing Different Representations of the Initial Charge-Carrier Distribution 104
5.3.2 Comparing the Standard and Self-Absorption Models For a Flat Charge-Carrier Distribution 108
5.3.3 Comparing the Standard and Self-Absorption Models in Pump-Probe Experiments 110
5.4 Questions Addressed in this Chapter 116

Determining the rate of charge-carrier recombination is an essential benchmark for any potential absorbing layer of a solar cell. MHPs are no exception in this regard, with the monomolecular charge-carrier recombination rate, in particular, being used to characterise the material quality of individual perovskite films and place them in the context of other samples [116, 117].

The bimolecular charge-carrier recombination rate, k_2, has also been reported for

a large number of $MAPbI_3$ thin films, as demonstrated by the literature review in Section 2.3.4. Where the monomolecular decay rate is linked to material quality, k_2 is also important to quantify, since bimolecular charge-carrier recombination is an intrinsic process which dictates the ultimate limit on charge-carrier lifetime, once defects have been removed [108].

To determine this bimolecular charge-carrier recombination rate, spectroscopic studies typically monitor the decay of a signal–such as photoluminesence, a transient absorption feature or THz photoconductivity–in order to monitor the rate of decay of charge carriers in a perovskite film. Assuming an average charge-carrier density, a rate equation is then fitted against the decay of this signal, to determine the charge-carrier recombination rate in the sample. Whilst this approach captures the charge-carrier recombination processes happening locally in a perovskite film, it does not account for larger scale movement of charge carriers, which may significantly impact the charge-carrier recombination dynamics [209].

With this context, the current chapter will demonstrate the effect of charge-carrier movement on the rate of charge-carrier recombination in $MAPbI_3$ thin films, using the 'self-absorption model' introduced in Chapter 4. This allows the charge-carrier dynamics to be considered at a device-level scale, accounting for charge-carrier recombination and diffusion, as well as photon re-absorption in a simulated $MAPbI_3$ film. It is demonstrated that both charge-carrier diffusion and photon re-absorption significantly reduce the overall rate of charge-carrier decay in $MAPbI_3$ thin-films, by reducing the rate at which charge carriers are lost to bimolecular recombination.

As the charge-carrier dynamics predicted by the self-absorption model are very different from what is predicted using the standard model, this means each model will determine a different bimolecular recombination rate for a given $MAPbI_3$ sample. Therefore, the second focus of this chapter is on quantifying the difference between the two models. A generalised procedure for comparing the recombination rates, used by two different models

to fit the same charge-carrier decay is presented. Using this procedure, the bimolecular charge-carrier recombination rates which the self-absorption model and standard model fit to the THz photoconductivity decay from the same MHP film are compared. By understanding how the two models are related, the recombination rates determined in previous studies can be corrected for photon re-absorption, to determine the intrinsic bimolecular recombination rate in $MAPbI_3$.

5.1 Simulation of charge-carrier dynamics in $MAPbI_3$ Thin Films

The modelling in this chapter is based around the charge-carrier dynamics within a set of identical modelled $MAPbI_3$ films. These model samples are assumed to have identical material properties and differ only in the thickness of their $MAPbI_3$ layers. The set of model films cover the thickness range from 40 nm to 540 nm, in 10nm steps, thereby spanning the typical thickness range (100–400 nm) used in MHP solar cells.

These modelled $MAPbI_3$ films are bordered on one side by vacuum ($\tilde{n} = 1$) and on the other side a by quartz substrate ($\tilde{n} = 1.55$). Throughout the chapter, the absorption and emission spectra of each simulated MHP film, as well as a diffusion constant of $D = 0.3\,\mathrm{cm^2\,s^{-1}}$, are taken from the average values of the $MAPbI_3$ samples in Chapter 6. Self-absorption, in each of the modelled films, was calculated as described in Section 4.2.3, assuming the emission spectrum, absorption spectrum and refractive indices stated above and a PL propagation distance of 20 µm.

5.2 Effect of Transport Processes on Charge-Carrier Dynamics

The self-absorption model introduces charge-carrier diffusion and photon re-absorption into the governing equation, where typically only charge-carrier recombination is con-

sidered. Therefore, it is important to understand the individual effects of each of these transport processes on the charge-carrier dynamics within a $MAPbI_3$ thin-film, as well as the effect on the total rate of charge-carrier recombination.

In this section, the charge-carrier dynamics in a 300 nm $MAPbI_3$ thin film are simulated, first using the standard model, before including each of the charge-carrier transport processes. By simulating the charge-carrier dynamics with different combinations of charge-carrier diffusion and photon re-absorption, the individual effect of each process can be evaluated. In each case $k_2^{intrinsic} = 6.8 \times 10^{-10}\,\mathrm{cm^3\,s^{-1}}$ and $k_3 = 1 \times 10^{-29}\,\mathrm{cm^6 s^{-1}}$, meaning that the only change in the charge-carrier dynamics comes from the effect of the transport processes.

The Standard Model. The starting point of this comparison is to consider the standard model, which accounts only for charge-carrier recombination (Equation 4.40). Figure 5.1(a) shows the charge-carrier dynamics in this case, where neither diffusion or photon re-absorption are accounted for. The figure shows a slice through the perovskite film, over the first 2.5 ns after photo-excitation. The initial Beer profile of the pump excitation can be seen in the figure at a pump-probe delay of 0 ps, however, as the simulation progresses, the charge-carrier density simply decays away, as no processes other than charge-carrier recombination are considered.

Another way to analyse the simulated charge-carrier dynamics is to consider the total number of charge carriers remaining at each point in time. This is a crucial metric, as the experimentally measured quantity in OPTP experiments is THz photoconductivity, which does not depend on the shape of the charge-carrier distribution inside a $MAPbI_3$ film, but only on the total number of charge carriers (as discussed in Section 3.2.3) The total number of charge carriers remaining as a function of time is shown in Figure 5.2.

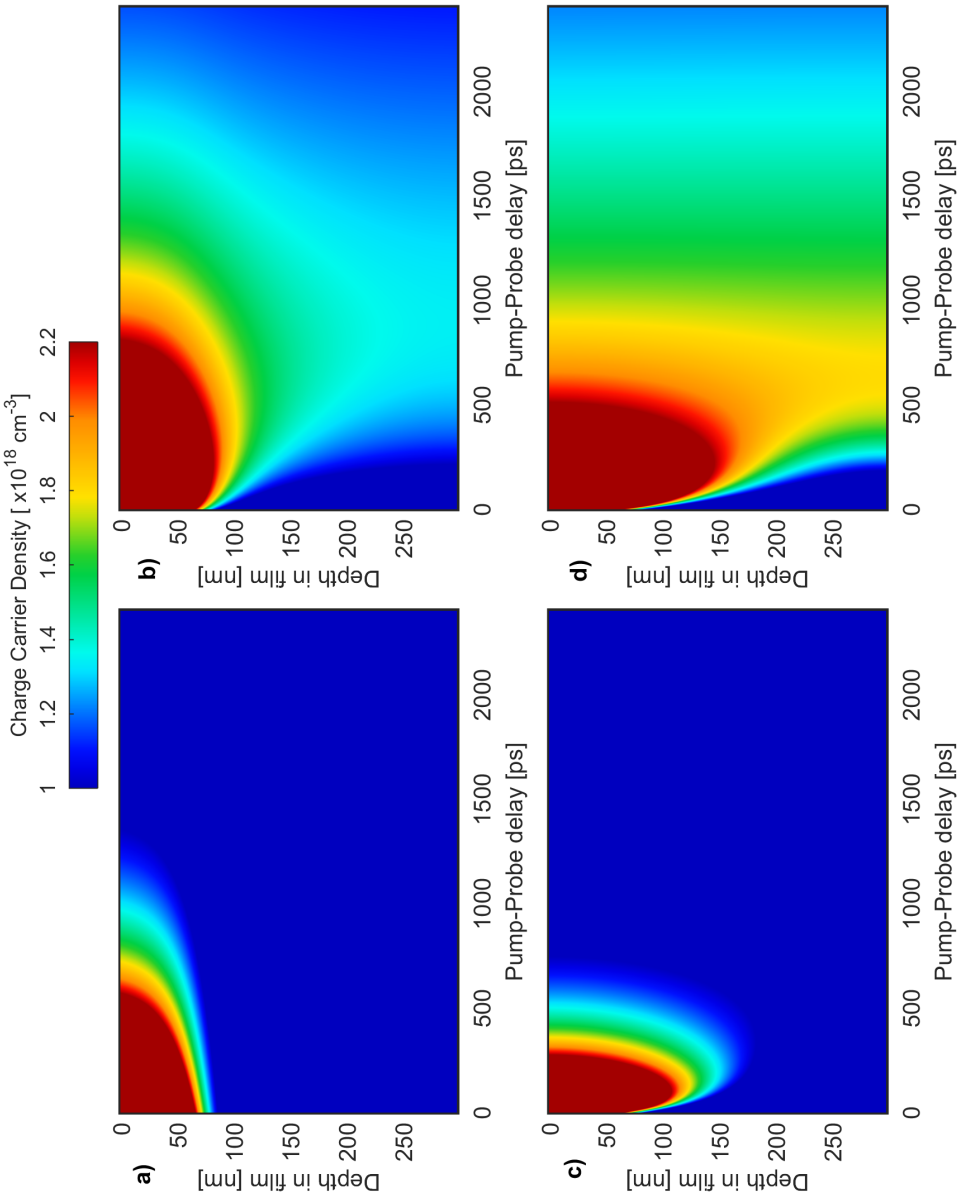


Figure 5.1: Modelled charge-carrier dynamics for the same simulated 300 nm film of $MAPbI_3$ on quartz, where (a) neither diffusion nor self-absorption, (b) only self-absorption, (c) only diffusion and (d) both diffusion and self-absorption are/is accounted for. In each case, the recombination constants used were $k_1 = 1 \times 10^7\,\mathrm{s}^{-1}$, $k_2^{intrinsic} = 6.8 \times 10^{-10}\,\mathrm{cm}^3\,\mathrm{s}^{-1}$ and $k_3 = 1 \times 10^{-29}\,\mathrm{cm}^6\mathrm{s}^{-1}$ and excitation was assumed to be at 400 nm, with an incident pulse energy of $45\,\mu\mathrm{J\,cm}^{-2}$.

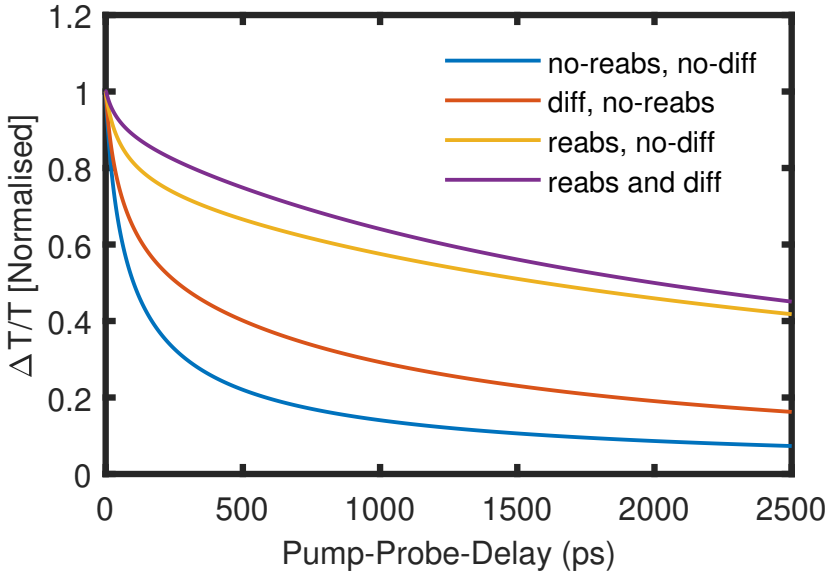


Figure 5.2: Modelled photo-conductivity transients for the simulations shown in Figure 5.1. The THz photoconductivity is directly proportional to the total number of photo-excited charge carriers in the $MAPbI_3$ film. Transients are simulated for a modelled 300 nm film of $MAPbI_3$ on quartz, where charge-carrier diffusion and self-absorption are either included in, or omitted from, the dynamical model as indicated.

As observed in Figure 5.1(a), the total charge-carrier population drops away swiftly, due to bimolecular recombination.

Photon Re-absorption Only. The next case to be considered is when photon re-absorption is included into the dynamical model, but charge-carrier diffusion is still omitted. The evolution of the charge-carrier distribution in this case is shown in Figure 5.1(b). When photon re-absorption is included, there is now a much slower decay in the THz photoconductivity transient, compared to the previous case. This is because only a fraction of bimolecular recombination events now result in the escape of a photon, as illustrated in Figure 5.3. Since the internal recombination rate is the same, but some of the charge carriers are recaptured by photon re-absorption, the THz photoconductivity decay is slower.

However, in Figure 5.1(b) it can be seen that photon re-absorption does not simply result in a slower $k_2^{apparent}$ but also causes a spreading out of charge carriers across the

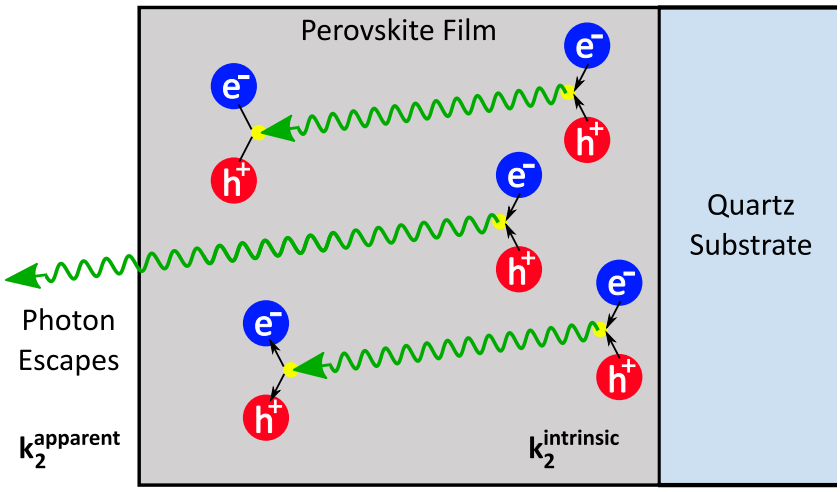


Figure 5.3: Illustration demonstrating the difference between $k_2^{intrinsic}$ and $k_2^{apparent}$. $k_2^{intrinsic}$ is the rate at which charge carriers undergo bimolecular recombination inside a material, generating photons. Some of these emitted photons are re-absorbed by the perovskite, exciting new charge carriers, and leading to no net loss of THz photoconductivity. $k_2^{apparent}$ is the rate at which photons escape the material, which is also the rate at which THz photoconductivity decreases.

film. The spreading out of charge carriers means that, compared to the previous case, the average charge-carrier density in the film is lower. Since bimolecular charge-carrier recombination depends on n^2, this spreading out of charge carriers results in a reduction in bimolecular charge-carrier recombination. Therefore, charge-carrier loss is slowed both by photon re-absorption recapturing emitted photons, but also because the resultant spreading out of charge carriers further reduces bimolecular recombination. This is seen as a slower decay of the charge-carrier population in Figure 5.2.

Charge-Carrier Diffusion Only. Figure 5.1(c) shows the case where, instead of photon re-absorption, charge-carrier diffusion is included in the dynamical model. In this case there is a fast initial spreading out of the charge-carriers, giving the appearance in Figure 5.1(c) that the decay is faster here than when there is no charge-carrier diffusion. In fact, Figure 5.2 shows that the total charge-carrier population actually decays more slowly, as higher-order recombination is made less efficient by the lowering of n from diffusion. The decay only appears faster in Figure 5.1(c) as regions of high

n are being spread out by diffusion. This demonstrates that charge-carrier diffusion is important in slowing recombination, as it locally spreads out the charge carriers, reducing bimolecular recombination.

The Self-Absorption Model. Finally, the charge-carrier dynamics can be simulated using the full self-absorption model, including both charge-carrier diffusion and photon re-absorption. The evolution of the charge-carrier distribution, using the self-absorption model, is in shown in Figure 5.1(d). A similarity can be seen between this case and panels (b) and (c), reflecting that both charge-carrier diffusion and photon re-absorption contribute to the overall charge-carrier dynamics. Importantly, it can be seen in Figure 5.1(d) that after only 1 ns the charge carriers have spread evenly across the film. This minimises higher-order recombination by maximally spreading out the charge carriers. Figure 5.2 also shows that the THz photoconductivity decay in this case is slower than where only photon re-absorption is included. The extra reduction in recombination is seen to come within the first few hundred ps. At these early times, the gradient in n is largest, meaning there will be a rapid diffusion of charge carriers. This helps reduce the fast, initial recombination, caused by the high concentration of charge carriers near the film surface.

The Effect of Each Transport Process on Charge-Carrier Recombination. Comparing the total charge-carrier population decay, in Figure 5.2 it can be clearly seen that each process reduces charge-carrier losses in a different portion of the decay. Most obviously, there is a reduction in bimolecular recombination losses from self-absorption which remains important throughout the decay and will do, so long as a significant fraction of the decay is bimolecular. Additionally, within the first few hundred ps, diffusion slows the rate of charge-carrier recombination, as it will make both bimolecular and Auger recombination less efficient, by spreading out charge carriers and lowering n where it is highest. After this time window, the n profile is much flatter and diffusion becomes less

important, particularly in the case where self-absorption is also redistributing charge-carriers. The combination of these two processes thereby leads to a much slower decay of the total charge-carrier population than when they are omitted.

This section also raises an important point of about the difference between the standard and self-absorption models. Here, the same k_2 has been used in all simulations to produce different THz photoconductivity decays. However, when fitting experimental data, the situation is reversed–in that different recombination constants are trialled to fit a given THz photoconductivity decay. Since each of the four simulations above produce different THz photoconductivity decays for the same values of k_2, this means they will fit the same THz photoconductivity decay using four different values of k_2.

Section 5.3 will describe how the k_2 determined by fitting different dynamical models to the same set of THz photoconductivity transients can be related. From the current discussion, it is already clear that the THz photoconductivity decay alone is not enough to fully understand the charge-carrier dynamics in a sample. The THz photoconductivity reflects only the total number of charge carriers, not how the the charge-carrier distribution is arranged within the sample, or is changing. It has been shown here that changes in the charge-carrier distribution, caused by photon re-absorption and diffusion, will drastically alter the recombination dynamics. By using the self-absorption model to describe these changes, the shape of the resultant THz photoconductivity transient can be interpreted. This is important as, without considering charge-carrier movement, the charge-carrier dynamics can be misinterpreted.

5.3 Quantifying the Differences Between Dynamical Models

The previous section has demonstrated that, when simulating the charge-carrier dynamics of a sample, the shape of the THz photoconductivity transient is strongly influenced by the inclusion of charge-carrier diffusion and photon re-absorption into the dynamical model. This means that fitting different dynamical models to the same THz photoconductivity transient will typically result in different values of the charge-carrier recombination coefficients being obtained.

When comparing charge-carrier recombination rates reported in two separate studies, this effect must, therefore, be taken into consideration. There may be a difference in the reported values of k_2 and k_3, caused by a change in the physical properties of the two samples. However, quite independent of this, if different fitting procedures are used, this will also effect the values reported for each sample. This makes it difficult to quantitatively compare recombination rates reported for $MAPbI_3$ between different studies, as it is unclear how much of the difference in reported values derives from divergent fitting processes and how much is real variation in the material properties.

The solution to this problem is to determine how the different models used in these studies are related and correct any effect caused by the use of different dynamical models. This section will establish how the self-absorption model and standard model are related, and find a correction factor which can be used to understand the results of one model, in terms of the other. This allows the comparison of recombination rates determined using the self-absorption model with previously reported values, which have not accounted for charge-carrier diffusion or photon re-absorption. More importantly, it allows previously published values of k_2 to be corrected for self-absorption, providing information about $k_2^{intrinsic}$, which is the internal rate of photon generation in $MAPbI_3$.

Method for Comparing Dynamical Models. The procedure for quantitatively comparing two different dynamical models mimics the process of fitting experimental THz photoconductivity transients. A first model is used to produce a set of THz photoconductivity decays, across a range of simulated pump fluences, and these are then fitted by a second model, using the recombination constants as free parameters. In this way, the recombination constants used by the two models to fit the same THz photoconductivity transient can be determined. Due to the dominance of bimolecular decay at the excitation fluences used in OPTP spectroscopy, the focus in the following examples will mainly use k_2 as the only free parameter.

The value of k_2 used in the first model is referred to as the 'real' value or k_2^{real}, as this is the value used to simulate the THz photoconductivity transients, which are fitted by the second model. The value of k_2, fitted by the second model, is referred to as k_2^{fitted}, as this is the value which is determined by the model, in the same manner by which experimental THz photoconductivity transients are fitted.

As a means of comparing the 'real' and 'fitted' recombination constants, the ratio

$$\Phi_2 = \frac{k_2^{\text{Model 2}}}{k_2^{\text{Model 1}}} = \frac{k_2^{fitted}}{k_2^{real}}. \tag{5.1}$$

is defined. If there is no significant relation between the two models, then Φ_2 will vary, depending on the value of k_2^{real}. However, if Φ_2 is constant across a range of k_2^{real}, then the factor Φ_2 can be used to relate the two models, even for the case where the actual value of k_2 is unknown. Such a relation is significant, as it allows the comparison of the bimolecular recombination coefficients determined by two separate studies, in terms of the same dynamical model, without knowledge of the actual value of k_2. This removes the problem of confusing real changes in the charge-carrier dynamics of two samples, with differences in the dynamical models used to interpret each set of experimental data.

Before testing this procedure on different models, the same model was initially used, both to generate and then fit the THz photoconductivity transients. Using this procedure, both the self-absorption model, as well as the standard model were able to sucessfully extract the 'real' value of k_2, producing a value of $\Phi_2 = 1$ across a wide range of test values of k_2^{real}. This is a minimum requirement to validate that the fitting procedure could be useful and shows that any variation in Φ_2 away from one is caused by differences in the generating and fitting models.

5.3.1 Comparing Different Representations of the Initial Charge-Carrier Distribution

Before investigating the impact of charge-carrier transport processes, two different ways of representing the charge-carrier density in a perovskite film are first compared.

Although the initially generated n profile in an OPTP experiment will be a Beer-Lambert profile, typically simulations of charge-carrier density represent this in one of two ways. The first approach is to assume that all of the charge carriers are absorbed within one absorption length of the perovskite film surface and model the charge carriers as being spread evenly through this region. This approach is widely used in both OPTP and TA studies [95–97], and is here referred to as a 'step' profile. A second approach is to model n at different points as an array of values, determined by the initial absorption profile [121, 138]. Both representations of the initial charge-carrier distribution in OPTP experiments are fully discussed in Section 4.2.1.

The two n profiles are shown in Figure 5.4, for several values of pump absorption coefficient, α_{pump}. For each value of α_{pump} the area under the curves for the step and Beer profiles is equal, as in each case the same number of charge carriers are being simulated in the film. However, it can be seen that the two n profiles arrange the charge carriers very differently, with the step profile having a higher average charge-carrier density than the Beer profile. Since bimolecular recombination is non-linear, it is expected that the

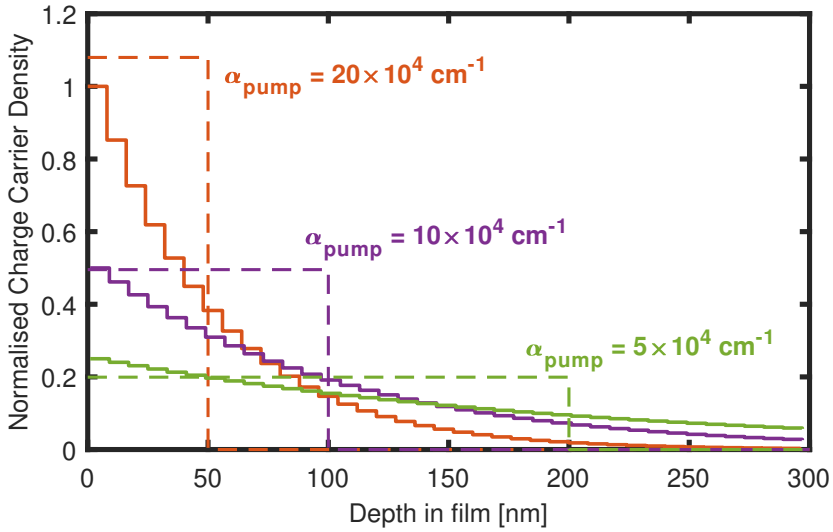


Figure 5.4: Modelled charge-carrier density profiles in a 300-nm perovskite film on quartz shown for different values of pump absorption coefficient. The step profile assumes all charge carriers are absorbed evenly within one absorption length of the film surface, while the Beer profile splits the perovskite film into regions of different n, approximating a Beer absorption profile.

higher average n in the step profile will each lead to faster recombination than if the charge carriers were arranged in a Beer profile.

Although it can be qualitatively reasoned that bimolecular recombination will proceed faster if the charge carriers are arranged in a step profile, the goal here is to quantify the relationship between the two models. Using the procedure outlined above, a dynamical model, with the charge carriers arranged in a Beer profile, was used to create a set of photo-conductivity transients. These transients were then fitted by a second dynamical model, which assumes the charge carriers are arranged in a step profile. Consistent with the definition of Φ_2 in Equation 5.1, the relationship between the two models is given by

$$\Phi_2 = \frac{k_2^{step\ profile}}{k_2^{Beer\ profile}}. \tag{5.2}$$

as the model using a Beer profile generates the THz photoconductivity decay, while the model using a step profile fits the decays. By varying the value of k_2 used in the Beer profile, it can be seen if there is a constant relationship between the bimolecular recombination rates in each model. Throughout this comparison, the underlying dynamical model

remains the standard model (which accounts only for charge-carrier recombination), the only difference between the two simulations is the distribution of charge-carriers.

The relationship which was determined between the two models is shown in Figure 5.5, for a range of absorption coefficients and film thickness, where the film thickness is larger than the absorption length of the pump, $\Phi_2 < 1$. This means that k_2 determined using the step profile is smaller than that predicted when using the Beer profile. This can be understood from the fact that charge-carriers are more spread out in the Beer profile, and so are at a lower charge carrier density. Therefore, to produce the same rate of charge-carrier decay, the recombination constant must be larger.

It should be noted that where the film thickness is less than the absorption length, applying the step profile is unphysical, as the n distribution assumed by the step profile extends further than the film boundary. In this case $\Phi_2 > 1$, as the n predicted by the step profile is lower than that found in the Beer profile. As the step profile is no longer appropriate in this case, it should only be used where the film thickness is greater than the absorption length.

It can be seen in Figure 5.5 that, as the absorption length of the pump increases, Φ_2 becomes closer to one. This is because as the absorption length of the pump increases there is less variation in n across the film. When the charge-carrier distribution is flatter, the average n used in the step profile becomes a better approximation of the Beer profile (demonstrated in Figure 5.4), meaning the distribution of charge carriers and, therefore, the recombination constants in the two models, are more similar.

It is also constructive to consider how the two profiles interpret various aspects of the photo-conductivity decay. Although both profiles can fit the same photo-conductivity decays, they each explain the decays using a different balance of charge-carrier recombination processes. At higher fluences there are two features to the photo-conductivity transients: an initial fast decay process, followed by a slower decay. When using the step

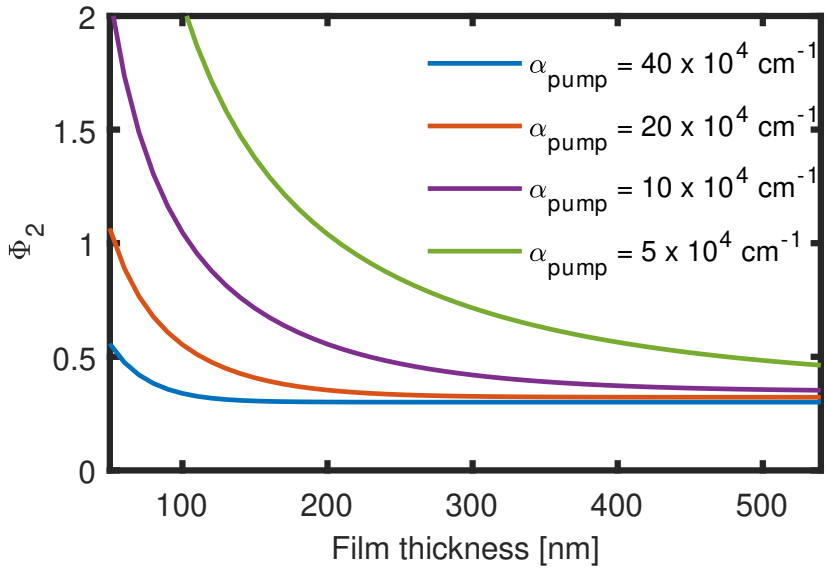


Figure 5.5: a) Φ_2 determined by fitting the modelled photo-conductivity transients from a simulation, with charge carriers arranged in a Beer profile, using a simulation in which the charge carriers are arranged in a step profile. Both dynamical models consider charge-carrier recombination only, with no diffusion or photon re-absorption. The Beer model used the recombination constants $k_2 = 6.4 \times 10^{-10}\,\mathrm{cm^3\,s^{-1}}$ and $k_3 = 1 \times 10^{-29}\,\mathrm{cm^6 s^{-1}}$. The fits had k_3 fixed at 0, as Auger recombination at the pump fluences simulated was minimal.

profile, these decay components are interpreted as Auger and bimolecular recombination respectively. On the other hand, when using the Beer profile, all of this decay is interpreted as bimolecular. The region of high n at the front of the film causes the fast initial recombination, while the low n region deeper in the film decays more slowly. If the Beer profile is taken to be a more accurate representation of the n profile within the film, this means that using the simpler step profile can result in an underestimate of k_2 and an overestimate of k_3.

This example has demonstrated that a useful relationship can be established between two different models for charge-carrier recombination. The relationship between the two models is stable across a wide range of k_2 values, and highlights how each model differently accounts for the shapes of the same THz photoconductivity transients. While this demonstrates the value of the comparison method, it is of more practical interest to now relate the standard and self-absorption models.

5.3.2 Comparing the Standard and Self-Absorption Models For a Flat Charge-Carrier Distribution

The simplest scenario in which the standard and self-absorption models can be compared is the equilibrium case, where charge-carriers are spread evenly across the sample thickness, in a 'flat' profile (shown in Figure 4.3). In this situation there will be no change in the shape of the charge-carrier distribution over time. This means that charge-carrier diffusion is irrelevant and the only difference between the two models will be from self-absorption.

The two models are compared by using the self-absorption model to generate a set of THz photoconductivity transients, which are then fitted by the standard model. The results of this procedure can be seen in Figure 5.6, where, in this case

$$\Phi_2 = \frac{k_2^{\text{standard model}}}{k_2^{\text{self-absorption model}}}. \tag{5.3}$$

It can be seen that Φ_2 varies slowly with sample thickness, but in all cases is less than one, indicating that $k_2^{\text{standard model}} < k_2^{\text{self-absorption model}}$. This difference between the bimolecular recombination rates determined by the two models, actually comes from the fact that in each of the models, k_2 is describing a different processes. In the self-absorption model, k_2 is the rate at which bimolecular recombination occurs inside the perovskite film, which can be called $k_2^{intrinsic}$. However, only a fraction of these emitted photons will escape the film, as the rest will be re-absorbed by the perovskite. This is important, as only those charge carriers which escape the film result in a reduction in the total THz photoconductivity. As the standard model does not include self absorption, the assumption is that any photons produced by bimolecular recombination escape the perovskite. This means that k_2 in the standard model is the rate at which charge carriers are lost from the perovskite film due to bimolecular recombination, $k_2^{apparent}$. These two rates are linked by the escape probability of light from the perovskite film, which in this case is also equivalent to Φ_2, meaning that

$$\Phi_2 = \frac{k_2^{apparent}}{k_2^{intrinsic}}. \tag{5.4}$$

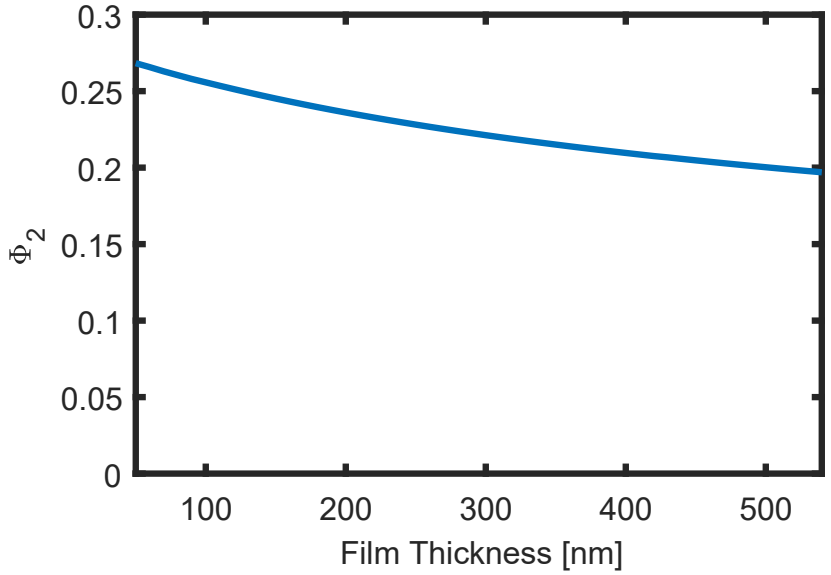


Figure 5.6: Φ_2 modelled as a function of film thickness, for perovskite films on quartz and assuming that the charge carriers are initially spread evenly through the perovskite film. The self-absorption model is used to generate the THz photoconductivity transients, which the standard model then fits. The decay shown uses a value of $k_2^{intrinsic} = 6.8 \times 10^{-10}\,\mathrm{cm^3\,s^{-1}}$ and $k_3 = 1 \times 10^{-29}\,\mathrm{cm^6 s^{-1}}$ for the self-absorption model.

Considering this equation, it is clear that Φ_2 must be less than one, as $k_2^{apparent}$, the rate of photon emission from the perovskite film, cannot be greater than $k_2^{intrinsic}$, the rate of photon generation in the material.

As a final point, it can be seen from Figure 5.6 that Φ_2 displays only a modest variation with film thickness. This slow variation arises as the high refractive index of $MAPbI_3$ (2.5) and long PL absorption length which mean that photon confinement, not film thickness, is the primary factor causing self-absorption. In this case Φ_2 is independent of the particular k_2 values used, as it relies only on the escape probability of photons. The notion of an escape probability has been used in several other studies [132, 210], however, it is only applicable to link $k_2^{intrinsic}$ and $k_2^{apparent}$ in this way when there is a flat charge-carrier distribution.

5.3.3 Comparing the Standard and Self-Absorption Models in Pump-Probe Experiments

Building on the above results, the relationship between the standard and self-absorption models is now tested for the case where there is an initial Beer profile of charge-carriers, as is present in a pump-probe experiment.

As the distribution of charge-carriers through the film is uneven in this case, self-absorption and diffusion will alter the charge-carrier distribution, causing the initial Beer profile to flatten out over time. However, the standard model does not allow the shape of the n profile to change, so the time-varying n profile of the self-absorption model must be approximated by either a Beer or flat charge-carrier profile. Both of these profiles could arguably be used, as the Beer profile matches the initial charge-carrier distribution, while the flat profile matches the final charge-carrier distribution after the charge carriers have spread evenly through the film depth.

Both the 'flat' and the 'Beer' profiles are compared to the self-absorption model, using the same procedure as in the previous examples; the self-absorption model is used to produce a set of THz photoconductivity transients, which the standard model then fits, using each of the n profiles profiles. In each case

$$\Phi_2 = \frac{k_2^{apparent}}{k_2^{intrinsic}}. \tag{5.5}$$

links the internal bimolecular recombination rate $k_2^{intrinsic}$ used to generate the THz photoconductivity decays, with $k_2^{apparent}$, which is the rate the standard model fits to the same THz photoconductivity decays. The degree to which Φ_2 varies, as $k_2^{intrinsic}$ and k_3 in the self-absorption model are changed, determines the how robust the relation between the standard model and the self-absorption model is. If there is a consistent relation between the self-absorption and standard models, independent of the intrinsic recombination constants, then this can be used to link the two models.

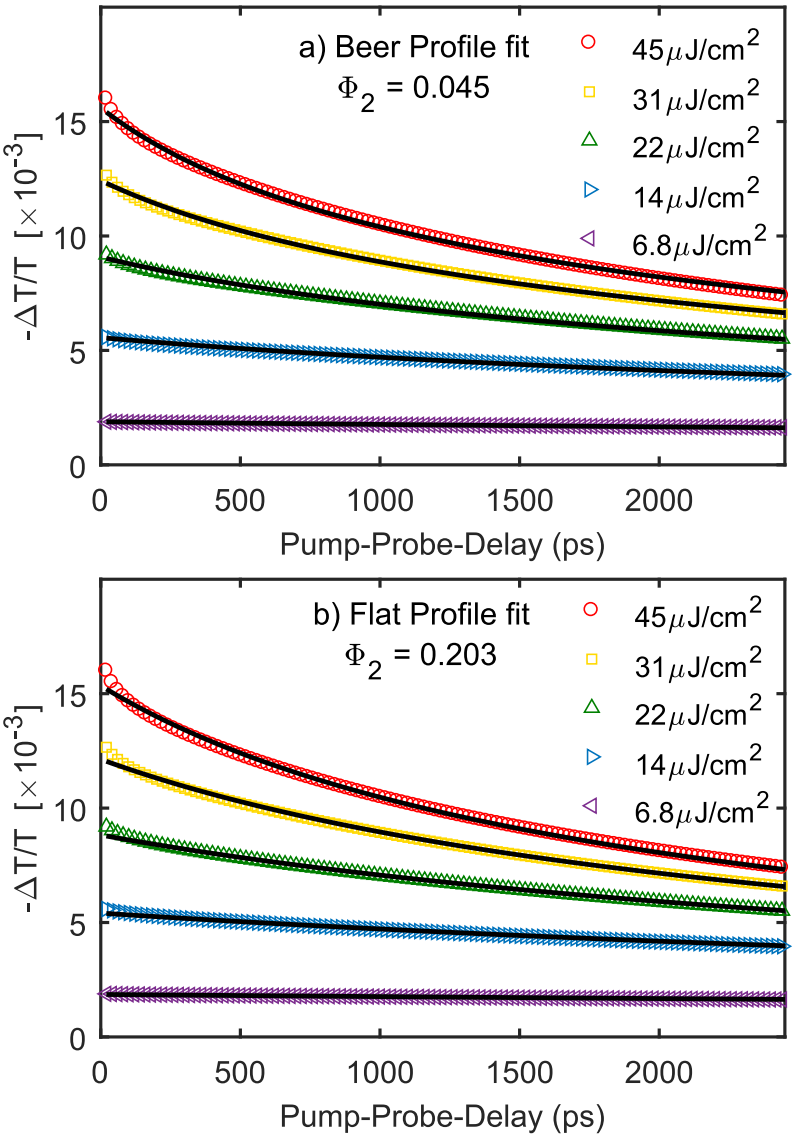


Figure 5.7: Modelled THz photo-conductivity transients in a 300 nm thick film, produced by the self-absorption model and fitted in black lines by the standard model, using (a) a Beer and (b) a flat n profile. The recombination constants $k_2^{intrinsic} = 6.8 \times 10^{-10}\,\mathrm{cm^3\,s^{-1}}$ and $k_3 = 1 \times 10^{-29}\,\mathrm{cm^6 s^{-1}}$ are used in the self-absorption model.

The fits of the standard model (using both the Beer and flat profiles), to the photoconductivity decays created by the self-absorption model are shown in Figure 5.7, where it can be seen that the standard model fits the THz photoconductivity transients well, using either profile. However, the fit alone does not mean that the standard model is properly describing the underlying charge-carrier dynamics, as it was shown in Section 5.2 that the charge-carrier dynamics follow a completely different pattern in the self-absorption model. Indeed it is actually very surprising that the standard model, using a flat n profile, is able to fit the THz photoconductivity decay produced by the self-absorption model. This demonstrates how two very different dynamical models can produce the same THz photoconductivity transient, using different recombination rates, underlining the importance of selecting an appropriate model to determine accurate recombination rates.

Since the two dynamical models make vastly different assumptions about the charge-carrier dynamics it seems unlikely that a strong relation between the models could exist. However, Figure 5.8 shows that a link between the recombination rates in each model can be made. Figure 5.8 shows that using the flat profile results in a Φ_2 which changes only slowly with the thickness of the perovskite film, whereas, when the Beer profile is used, Φ_2 shows a strong decrease as film thickness increases.

For the flat profile Φ_2 varies only slowly and Φ_2 in this case is remarkably similar to the previous section, where the initial charge-carrier distribution in both simulations was already evenly spread across the film. This similarity comes from the fact that in the self-absorption model, the charge carriers are quickly redistributed across the film depth. Therefore, the charge-carrier distribution matches the flat profile after only a few hundred ps and after this point the two simulations only differ due to photon re-absorption slowing charge-carrier recombination. The flat profile is therefore a highly effective way to approximate the self-absorption model using the standard recombination model.

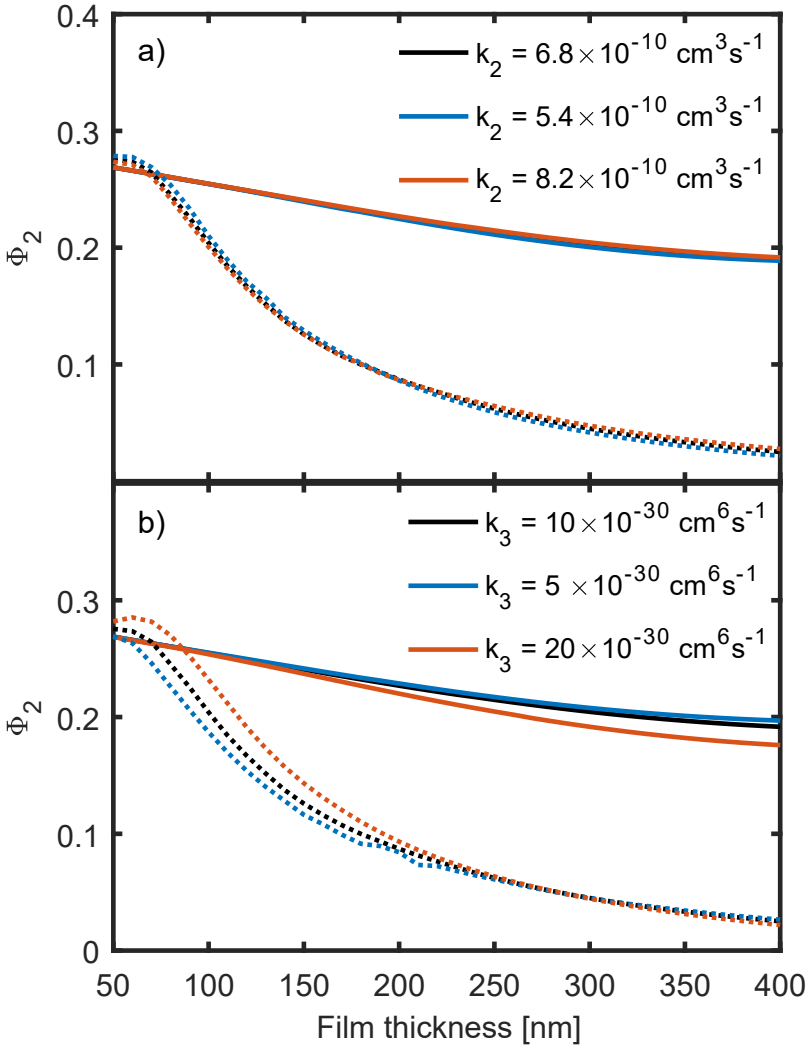


Figure 5.8: Φ_2 modelled as a function of film thickness, relating the standard and self-absorption models for a pump pulse with $\alpha = 4 \times 10^5$ cm^{-1}, incident upon a perovskite film on quartz. The solid lines show Φ_2 for a flat n profile, while dotted lines show the value for a Beer n profile. Panels (a) and (b), respectively show how Φ_2 changes as k_2 and k_3 are varied in the self-absorption model. The recombination constants used by the self-absorption model are $k_2^{intrinsic} = 6.8 \times 10^{-10}\,\mathrm{cm}^3\,\mathrm{s}^{-1}$ and $k_3 = 1 \times 10^{-29}\,\mathrm{cm}^6\mathrm{s}^{-1}$ unless otherwise labelled on the graph.

On the other hand, when the Beer profile is used, although it correctly describes the initial charge-carrier distribution in the self-absorption model, it does not account for charge-carrier movement. This means that over most of the simulation time, the Beer profile does not accurately describe the charge-carrier distribution in the self-absorption model. Additionally, the Beer profile assumes that several different values of n are present at different depths in the perovskite film, whereas in the self-absorption model n quickly equilibrates across the film depth. Consequently, Φ_2 has a more complex form in this case, as it accounts for both a difference in the dynamical equations, as well as in the charge-carrier distribution, between the two models. In more tangible terms, this also means that $k_2^{apparent}$, as determined using the Beer profile, is much further from $k_2^{intrinsic}$ than where the flat profile is assumed.

However, the exact shape of the dependence of Φ_2 on film thickness is not crucial, so long as it changes minimally as $k_2^{intrinsic}$ and k_3 in the self-absorption model vary. As such, the different lines in Figure 5.7(a) and (b) show how Φ_2 depends upon $k_2^{intrinsic}$ and k_3. It can be seen that, using either n profile Φ_2 does not vary significantly as small variations in $k_2^{intrinsic}$ are made[1]. This indicates that there is a strong link between $k_2^{intrinsic}$ and $k_2^{apparent}$, likely arising because the charge carriers are rapidly redistributed throughout the film. Once this flattening out of the initial charge-carrier distribution has occurred, the self-absorption model and standard model can be linked by the PL escape probability, as discussed in the previous section.

Figure 5.7(b) shows that Φ_2 is also sensitive to changes in k_3. In this example, k_3 has been fixed at zero when the standard model is used to fit the THz photoconductivity transients from the self-absorption model. Therefore, it is reasonable that Φ_2 should vary as k_3 in the self-absorption model is changed, as bimolecular recombination is the only free parameter which the standard model can fit. However, this variation is included here to

[1]The variations in $k_2^{intrinsic}$ used here corresponds to one standard deviation of $k_2^{intrinsic}$, as determined for the samples in Chapter 6

demonstrate that Auger recombination in the self-absorption model can be interpreted as bimolecular recombination when fitted by the standard model. This means, that although a robust relation exists between the bimolecular recombination in the two models, it will become less valid at fluences where Auger recombination must also be included.

While the relation between the standard and self-absorption models is here more complex than in the previous section, it has been shown that with careful consideration the two models may be related. It should be noted that this relation requires some knowledge of what self-absorption is likely present in the system and is simplified by a careful choice of n profile. Depending on the absorption length of the pump pulse, and the extent to which charge carriers are redistributed through the film, either a flat or Beer profile could be used to model the charge-carrier distribution in the sample. Ultimately, any profile is an approximation of a changing charge-carrier distribution, and to extract the intrinsic recombination constants of a material the self-absorption model should ideally be used. However, the type of relation shown here could be used to determine $k_2^{intrinsic}$, from a value of $k_2^{apparent}$ reported in another study where the standard model has been used.

5.4 Questions Addressed in this Chapter

What are the effects of charge-carrier diffusion and photon re-absorption on the recombination rate in $MAPbI_3$ thin films?

Section 5.2 demonstrated that both charge-carrier diffusion and photon re-absorption act to spread charge carriers through the depth of a perovskite film, lowering the peak n. As the bimolecular charge-carrier recombination rate increases quadratically with n (see Section 2.3.4), the spreading out of charge carriers dramatically reduces the rate of bimolecular charge-carrier recombination, thereby reducing the overall charge-carrier decay rate. Charge-carrier diffusion has a particular significance in the first 500 ps in evening out the initial charge-carrier distribution, while photon re-absorption not only slows down the loss of charge carriers to bimolecular recombination, but redistributes charge carriers throughout the entire depth of a perovskite film.

When trying to determine the bimolecular recombination rate of a perovskite film, is the spatial distribution of charge carriers important?

Yes, Section 5.3.1 demonstrates that, even in the absence of charge-carrier transport processes, the arrangement of charge carriers in a dynamical model determines n and so affects the bimolecular recombination rate obtained.

Can a quantitative link be made between bimolecular recombination rates reported in previous studies and those predicted by the new self-absorption model?

Yes. It was demonstrated that the bimolecular recombination rates, determined by the self-absorption model and the standard model, maintain a fixed ratio across a range of values of $k_2^{intrinsic}$, allowing the bimolecular recombination rates from previous studies to be corrected for self-absorption (if the spectral overlap between absorption and emission is known).

6

Photon Re-Absorption Masks Intrinsic Bimolecular Charge-Carrier Recombination in $MAPbI_3$ Perovskite

Contents

6.1 Experimental Details 120
6.1.1 Evaporation of $MAPbI_3$ thin Films 120
6.1.2 Structural Characterisation 120
6.1.3 Optical Characterisation 121
6.1.4 Optical-Pump-Terahertz-Probe Spectroscopy 121
6.2 Discussion 122
6.3 Questions Addressed in this Chapter 136

Within the last few years, the performance of solar cells based on hybrid metal halide perovskites has excelled amongst other emerging photovoltaic technologies [25–27], with power-conversion efficiencies (PCEs) now on parity with CdTe and multi-crystalline silicon [211]. However, what sets hybrid perovskites apart from typical inorganic semiconductors is that they allow high efficiency to be achieved in conjunction with low processing and material costs [7]. In parallel with the rise in perovskite solar cell performance, research has focused on unravelling the basic physics underlying this success. Studies focusing on

the prototypical methylammonium lead triiodide ($MAPbI_3$) perovskite have uncovered favourable properties typical of traditional inorganic semiconductors, such as a high charge-carrier mobility [94, 212], low exciton binding energy [213] and the presence of free (uncorrelated) electrons and holes at room-temperature [95, 96].

One issue at the centre of current debate is the extent to which charge-carrier mobilities and recombination mechanisms result from intrinsic (fundamental) properties of the perovskite, or rather from extrinsic factors such as material processing and morphology [212]. In the regime of low charge-carrier density, recombination is mediated by traps and defects [10, 109] leading to non-radiative losses that can be reduced by improved material processing [113–115]. Suppression of such extrinsic charge-carrier recombination channels was found to yield favourable monomolecular (trap-mediated) charge-carrier lifetimes in excess of one μs [116, 117]. These improvements have brought into sharp focus the mechanism governing the radiative bimolecular recombination of free electrons and holes, which will begin to dominate at low charge-carrier densities once most traps have been eliminated [108].

As a first approximation, one would assume the bimolecular recombination between free electrons and holes to be an intrinsic process that is associated with the bandstructure properties of the semiconductor. For classical inorganic semiconductors, bimolecular free-charge recombination is generally viewed as the inverse process of light absorption [16, 126], a relationship that holds across many group IV and III-V semiconductors, such as GaAs [214]. However, adopting such an "intrinsic" view of radiative bimolecular recombination to the case of hybrid perovskites appears to contradict the phenomenally wide range of bimolecular recombination rate constants that have been reported for any given hybrid perovskite. For example, making a survey of the literature [94–97, 121, 150, 153, 156, 215] reveals that values determined from transient spectroscopy vary by more than an order of magnitude for the most commonly examined $MAPbI_3$

perovskite (0.6–23×10^{-10} cm^3s^{-1}, See Table 2.1). Such a wide spread suggests at first sight a dependence on extrinsic parameters, such as material morphology. However, this presumption would be at odds with findings that highlight the similarity of the absorption onset of $MAPbI_3$ with that of GaAs, [216] which, in analogy with GaAs, would result in similarly well-defined intrinsic bimolecular recombination in $MAPbI_3$.

In this chapter, this controversy is resolved, by showing that the apparent bimolecular recombination rate constant k_2^{apparent} in $MAPbI_3$, as perceived in transient spectroscopy, is strongly modified by photon re-absorption, which masks a much larger intrinsic value of $k_2^{\text{intrinsic}}$. As explained in Section 2.3.4, such self-absorption of emitted photons can be moderated by external factors such as film thickness, light scattering or the presence of interfacial material of different refractive index, which can easily account for the huge spread in apparent values reported.

This chapter directly demonstrates that self-absorption of emitted photons can result in a large spread in the apparent value of k_2 in $MAPbI_3$ with film thickness, as perceived in transient spectroscopic experiments. The photo-excited charge-carrier population is recorded as a function of time, using optical-pump-THz-probe (OPTP) spectroscopy for a set of evaporated $MAPbI_3$ films, whose morphology exhibits no systematic variation with film thickness. It is found that the apparent bimolecular recombination rate constant k_2^{apparent} decreases exponentially with increasing film thickness d, from k_2^{apparent} = 1.4×10^{-10} cm^3s^{-1} for d = 50 nm to k_2^{apparent} = 0.2×10^{-10} cm^3s^{-1} for d = 533 nm, indicative of self-absorption that is mediated by Beer's law. However, by use of a model that properly accounts for photon re-absorption and charge-carrier diffusion, it is possible to reveal that all films share a single value of the intrinsic bimolecular recombination rate constant, $k_2^{intrinsic} = 6.8 \pm 1.4 \times 10^{-10}\,cm^3\,s^{-1}$, which is remarkably similar to the value for GaAs [214]. The model is used to show how changes in thin-film architecture can strongly affect photon out-coupling through variation in perovskite layer thickness

or refractive index of the surroundings, which modifies the apparent rate of bimolecular recombination, thus providing an explanation for the wide spread in literature reports.

6.1 Experimental Details

6.1.1 Evaporation of $MAPbI_3$ thin Films

Dual-source vapour deposition [44] was used as an ideal technique to produce a set of highly uniform $MAPbI_3$ films of different thickness (50–533nm) on z-cut quartz substrates[1]. The thickness of the perovskite layers was accurately determined by two different methods that yielded good agreement, that is, through use of a surface profilometer (DekTak) and by optical modelling of reflection and transmission spectra with a transfer matrix model (as described in Section B.4)[2].

6.1.2 Structural Characterisation

To rule out the influence of potential morphological changes, it was first verified that these films exhibit no systematic trends with film thickness, for either structural or optical properties or charge-carrier mobilities. Both scanning electron microscopy (SEM) and grazing incidence wide angle x-ray scattering (GIWAXS)[3] were used to examine the structural properties of these films [217]. SEM images (Figure B.2.1.2 in Appendix B) demonstrate that all samples have a highly uniform thickness and similar surface morphology across the series, with the perovskite layers being composed of a dense network of small grains with ∼100 nm diameter. GIWAXS data (Figure B.2 in Appendix B) show a slight variation in the degree of crystal orientation between individual samples that is, however, uncorrelated with film thickness. Together these results show that the samples share similar surface and bulk morphologies across the full film thickness range.

[1] Samples were fabriacted by Dr Jay Patel

[2] Supplementary information for this chapter is included in Appendix B

[3] GIWAXS measurements were performed by Johannes Schlipf and Peter Müller-Buschbaum, from the Physics department of the Technische Universitat München

6.1.3 Optical Characterisation

In addition to such structural characterisation, the thin-film optical reflection and transmission, as well as photoluminescence (PL) spectra[4] of all films were examined. Reflection and transmission spectra were recorded using Fourier transform infrared (FTIR) spectroscopy and analysed using a transfer matrix model which yields the refractive index and absorption coefficient of the perovskite layers as a function of wavelength (described in Section B.4). Across the set of samples, very similar absorption coefficients were found, with no evident dependence on the film thickness. Steady state PL spectra (Figure B.3) exhibited a slight red-shift in the PL centre wavelength from 762 nm to 766 nm as film thickness increased. However, after the spectra were corrected for photon self-absorption (as described in Section 4.2.3) this red-shift was eliminated, and the corrected PL spectra displayed no trend with thickness.

6.1.4 Optical-Pump-Terahertz-Probe Spectroscopy

To probe further for morphological variations, the charge-carrier mobility at THz frequencies was determined, across the film series, using optical-pump-THz-probe (OPTP) spectroscopy [169, 218, 219]. Here, samples were photo-excited by an optical pump-pulse at 400-nm wavelength, and the initially recorded photoconductivity was extracted from the change in transmitted THz field amplitude $\Delta T/T$ [188, 218]. With knowledge of the absorbed photon density per pulse and the assumption of unit photon-to-charge branching ratio, the value of the charge-carrier mobility can then be determined (see Section 3.2.3). Figure 6.1(d) shows an average charge-carrier mobility value of $(11\pm2)\,\mathrm{cm^2V^{-1}s^{-1}}$ across the series, with no apparent correlation with film thickness. The value is commensurate with the relatively small grain size ($\sim$100 nm) typically encountered in these dual-source evaporated $MAPbI_3$ films [44].

[4]PL spectra were measured by Elizabeth Parrott

Overall, this analysis of structural, optical, photoluminescence and charge-carrier mobility data comprehensively demonstrate that these samples exhibit no morphological trends with film thickness. In the following, it is therefore possible to focus solely on the effect of film thickness on the apparent charge-carrier dynamics, as mediated by the underlying influence of photon re-absorption.

6.2 Discussion

To assess the dynamics of the charge-carrier population, photoconductivity transients were recorded using OPTP following excitation with 400-nm laser pulses over a range of fluences. Figure 6.1 shows example photoconductivity transients for three film thicknesses, with curves for the full range of samples provided in Figure B.9. At the lowest excitation fluence, the decay of the charge-carrier population flattens over the 2.5-ns time window, indicating that mono-molecular trap-mediated charge recombination processes occur over much longer time scale, as typical for these materials [220]. With increasing pump-excitation fluence, the transients become increasingly dominated by higher-order processes such as bimolecular electron-hole and Auger recombination. Strikingly, the transients in Figure 6.1 (and Figure B.9) demonstrate a clear trend towards more prominent higher-order recombination processes for thinner samples. While for a film thickness of 74 nm (Figure. 6.1a) rapid initial decay components are apparent, the photo-conductivity decay in the 533 nm sample is relatively slow. For the given observation window and range of fluences, bimolecular free-charge-carrier recombination was found to be the dominant process depleting the charge-carrier population. Therefore, these two observations suggest a surprising trend of increasing apparent bimolecular recombination with decreasing film thickness.

To provide a more quantitative assessment of the changes in apparent bimolecular recombination with film thickness, the charge-carrier density, n, is initially modelled

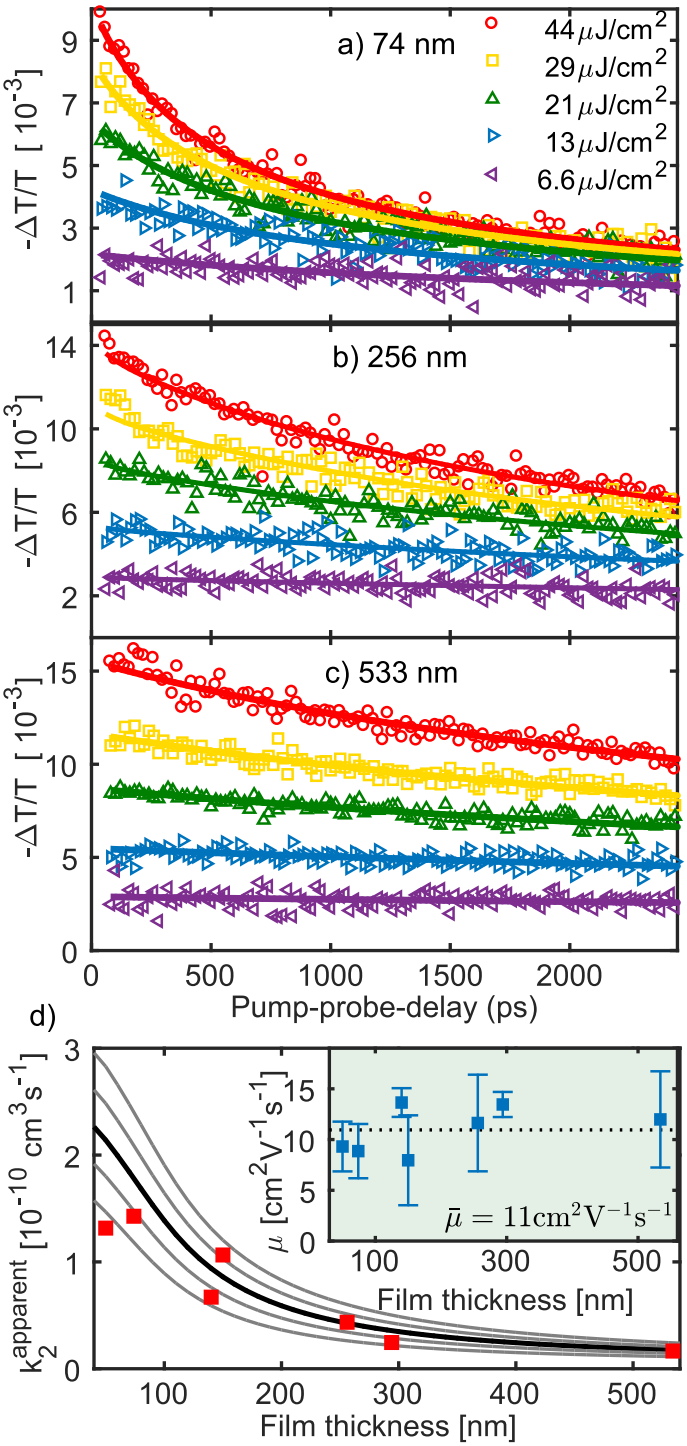


Figure 6.1: Photoinduced THz conductivity transients for thin films of dual-source vapour deposited $MAPbI_3$ with thicknesses of (a) 74 nm (b) 256 nm and (c) 533 nm, following excitation at a wavelength of 400 nm with a range of pulse fluences. Solid lines show global fits to each set, based on the standard model described in the text and Chapter 4.2.4.2. (d) Variation in $k_2^{apparent}$ (red squares) with film thickness, extracted from fits shown in (a)-(c). The lines show the modelled dependence of $k_2^{apparent}$ on film thickness predicted by the self-absorption model, which accounts for photon re-absorption and charge-carrier diffusion. The black line shows the best fits based on a film-thickness independent, $k_2^{intrinsic} = 6.8 \times 10^{-10}\,\mathrm{cm^3\,s^{-1}}$ with the surrounding dashed lines showing the first ($k_2^{intrinsic} = \pm 1.4 \times 10^{-10}\,\mathrm{cm^3\,s^{-1}}$) and second ($k_2^{intrinsic} = \pm 2.8 \times 10^{-10}\,\mathrm{cm^3\,s^{-1}}$) standard deviations. The inset displays the values of the charge-carrier mobility against film thickness, as extracted from OPTP measurements.

with a widely used [94, 95, 138, 221] rate equation,

$$\frac{dn}{dt} = G - k_3 n^3 - k_2^{apparent} n^2 - k_1 n. \tag{6.1}$$

Here, G is the charge-carrier generation rate; k_1 is the trap-related (non-radiative Shockley-Read-Hall [106]) monomolecular charge-recombination rate; $k_2^{apparent}$ is the radiative bimolecular recombination rate constant of free electrons and holes, as apparent from these transients; and k_3 is the rate constant describing non-radiative Auger recombination between electrons and holes that is mediated by a third charge-carrier [108]. Because of the wide-spread use of this rate equation to model such transients, it is referred to in the following as the "standard model" (Discussed in more detail in the previous chapter).

Accurate application of this standard model to the photoconductivity transients still requires the spatial charge-carrier distribution to be taken into account, as described in full detail in Section 4.2.1. A correct evaluation is particularly important since higher-order recombination rates are very sensitive to the charge-carrier density n (see Eqn. 6.1). As the pump pulse travels through the film, its intensity decays exponentially according to Beer's law, which generates a corresponding exponentially decreasing density of charge-carriers through the perovskite film (shown in Figure B.10). To account for this spatial variation along the depth profile, the perovskite film is modelled as a series of slices parallel to the substrate, [220] each of which has a different initial value of n that evolves independently according to Equation 6.1. The contributions from all slices are then summed together to obtain the overall decay of the charge-carrier population, the result of which is fitted globally to each set of experimental photo-conductivity transients obtained for the given range of excitation fluences. Variations in charge-carrier distribution across the lateral dimension of the film can be neglected, because the full-width-at-half-maximum of the pump pulse is much larger (3.9 mm) than that of the THz probe pulse (1.4 mm).

Figure 6.1(d) shows that the apparent value $k_2^{apparent}$ of the bimolecular recombination rate constant decreases by roughly one order of magnitude with increasing film thickness, from $1.4\times10^{-10}\,\mathrm{cm^3s^{-1}}$ for d=50 nm to $0.2\times10^{-10}\,\mathrm{cm^3s^{-1}}$ for d=533 nm. This variation cannot be caused by differences in material quality or morphology as the measurements discussed above found that there were no correlations between these parameters and film thickness. Therefore, the observed trends in k_2^{apparent} with film thickness suggest that Eqn. 6.1 does not fully capture the charge-carrier dynamics in these samples. An insight into the problem can be gained by noting that k_2^{apparent} decreases roughly exponentially with film thickness, on a similar length scale to the absorption length of the PL (vide infra). This observation indicates that self-absorption of photons following radiative bimolecular recombination may be responsible for the trend in $k_2^{apparent}$ with film thickness.

To account for such effects a new model was developed, which more accurately describes the charge-carrier dynamics in these films and which incorporates both charge-carrier diffusion and PL self-absorption. This "self-absorption model" (See Chapters 5 and 4 for further details) follows the treatment of PL self-absorption as successfully implemented for GaAs [130, 222] and also includes a diffusion term to account for the effect of charge-carrier motion on levelling the charge-carrier distribution along the film depth profile. Incorporating these two processes, the rate equation governing the density n of free charge-carriers now becomes:

$$\frac{\partial n}{\partial t} = D\frac{\partial^2 n}{\partial z^2} \; + \; G \; - \; k_3 n^3 \; - \; k_2 n^2 \; - \; k_1 n. \tag{6.2}$$

Here, z is the position in the direction normal to the substrate (film depth), and the diffusion coefficient D is set by using the charge-carrier mobility of each sample (shown in Figure 6.1d). G is again the charge-carrier generation rate, but importantly it now includes not only charge-carrier creation by the initial laser pulse (at zero time) but also charge generation via the re-absorption of photons produced by radiative bimolecular

charge-carrier recombination. Photon re-absorption in the perovskite is accounted for by using explicit ray tracing [130] which tracks the propagation of each emitted photon and accounts for possible absorption by the perovskite and reflections at the film boundaries to determine if, and where, photons are re-absorbed in the film. Full details of the self-absorption model are provided in Section4.2.4.2.

Fits based on the self-absorption model to the photoconductivity transients displayed in Figure B.9 again yield a value of the bimolecular recombination constant k_2 for each film thickness. However, when fitting with the self-absorption model there is no longer any systematic variation with film thickness (see Figure B.9) but rather a single value of $k_2^{intrinsic} = 6.8 \pm 1.4 \times 10^{-10}\,\mathrm{cm^3\,s^{-1}}$ is found to be common to all samples. The self-absorption model therefore reveals that once photon re-absorption is accounted for, these $MAPbI_3$ films display an intrinsic mechanism of bimolecular charge-carrier recombination that is characterized by a single rate constant, despite the apparent changes in the shape of the photoconductivity transients. It is interesting to note that the absolute value of $k_2^{intrinsic}$ extracted for $MAPbI_3$ is remarkably close to that for GaAs ($7.2 \times 10^{-10}\,\mathrm{cm^3\,s^{-1}}$ [214]). Given that the absorption onsets of $MAPbI_3$ and GaAs have also been found to be very similar, [216] this finding suggests that bimolecular free-charge recombination may be directly related to the inverse process of light absorption [15, 16, 126] in $MAPbI_3$. These phenomena are analogous to what has been observed in inorganic semiconductors such as GaAs [129] and InP [223] for which photon re-absorption has been found to result in a similar reduction of apparent bimolecular recombination with respect to the intrinsic expectation.

Figure 6.2 further illustrates how self-absorption masks the intrinsic bimolecular recombination dynamics, by showing the charge-carrier density decay as a function of depth in the film and time after photo-excitation, as determined by the self-absorption

model. Figure 6.2a examines the case that applies to the current transient photoconductivity study, i.e. a $MAPbI_3$ film in a "spectroscopic" configuration on a quartz disk and under vacuum. The colour plot indicates that initially after photo-excitation, charge-carriers are mostly concentrated at the front of the film, which directly results from the short absorption length of only 25 nm at the excitation wavelength of 400 nm (see absorption spectrum in Figure B.6). Over time, charge-carriers rapidly spread through the film, until after ∼1 ns a flat charge-carrier density profile is present across the full depth profile. This redistribution is driven jointly by diffusion and self-absorption and lowers the peak charge-carrier densities, thereby reducing the efficiency of higher-order recombination processes such as bimolecular and Auger recombination [94]. As a result, the charge-carrier population experiences a fast initial decay rate governed by the initially uneven charge-carrier distribution, which is then substantially lowered when the population spreads out. Self-absorption and charge diffusion therefore lead to an apparent lowering of the bimolecular recombination rate constant k_2^{apparent} that masks a much higher intrinsic value $k_2^{\text{intrinsic}}$.

Based on these arguments, the apparent thickness dependence of the photoconductivity transients can therefore be explained by the propensity of charge carriers to spread out further in thicker films, which lowers peak charge-carrier densities and slows bimolecular recombination. The self-absorption model shows that indeed, even for the thickest sample examined in the current study, photon re-absorption will occur over a sufficient length scale to result in an even spread of charge-carriers through the depth of the film (see Figure B.10). To illustrate this further, the solution to Equation 6.1 within the standard model can be fitted to modelled photoconductivity transients obtained from the self-absorption model, in order to obtain the apparent value of $k_2^{apparent}$ as a function of film thickness (using the procedure discussed in Chapter 5). The resulting dependence is shown as lines in Figure 6.1d for different values of $k_2^{intrinsic}$, showing

good agreement with the values of $k_2^{apparent}$ extracted by fits of the standard model to the experimental transients (red squares). Hence the model incorporating photon re-absorption and charge-carrier diffusion can fully explain the apparent changes in the shape of the transients with film thickness.

The influence of photon re-absorption on the apparent bimolecular recombination rate raises the question of how such processes will be affected by out-coupling of photons from the film. Since hybrid perovskites exhibit a relatively large refractive index at optical frequencies (e.g. $n_{per} = 2.5$ for $MAPbI_3$, see Figure B.6b), strong dependencies can be expected on the refractive index of the surrounding layers. To illustrate such effects, Figure 6.2 shows the time-dependent charge-carrier density distributions also for the cases of (b) an $MAPbI_3$ film surrounded by infinitely thick layers of silicon on one side and a typical organic transport layer on the other, such as may be encountered in a perovskite-silicon tandem cell, and (c) an $MAPbI_3$ film index-matched to its surroundings. This modelling of photon out-coupling does not include thin-film interference effects, which would modify the effect somewhat [134], but would give a specific dependence on overall layer architecture which is neglected at this point to allow for a better qualitative comparison.

Figure 6.2 hence illustrates the evolution of the charge-carrier distribution inside a $MAPbI_3$ film with (a) high, (b) intermediate, and (c) no photon confinement. The stark changes between the three scenarios are directly attributable to the large absorption length of the emitted PL in $MAPbI_3$, which is a multiple of the typical film thickness. As a result, the extent of photon re-absorption is mostly determined by the strength of the photon confinement within the perovskite layer, which is influenced by the refractive index of the surrounding layers through the modification of total internal reflection. Figure 6.2c illustrates that for fully index-matched surroundings, when most photons leave the film without being re-absorbed, the charge-carrier density decays swiftly and with only minor

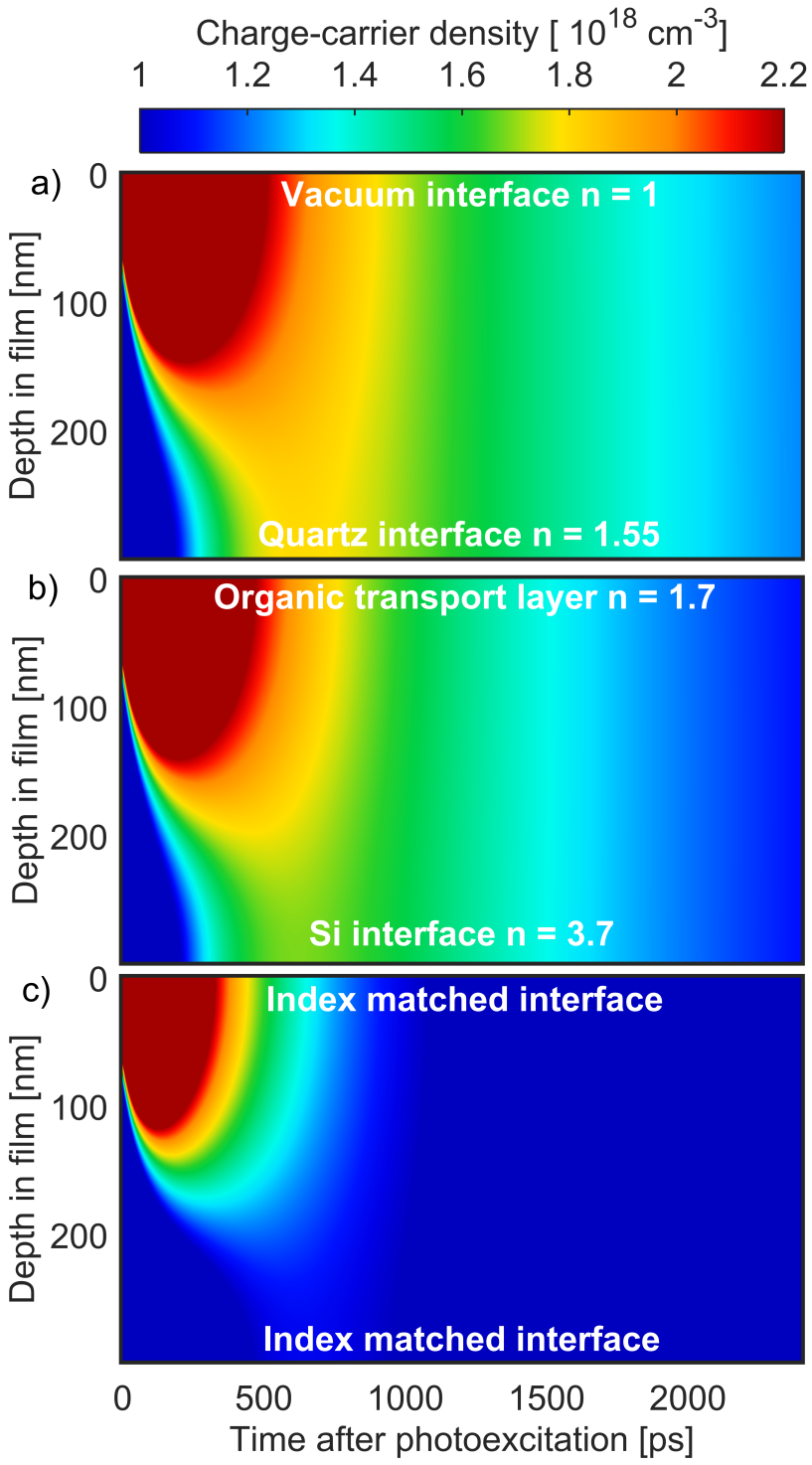


Figure 6.2: Colour plots showing the charge-carrier density evolution with time after excitation and along the film depth profile, as simulated with the self-absorption model which accounts for charge-carrier recombination, diffusion and photon re-absorption. Simulations are shown over a 2.5-ns time window for (a) an $MAPbI_3$ film on a z-cut quartz disk in vacuum (spectroscopic configuration) (b) a film between an organic hole-transporting layer and monolithic silicon (tandem configuration) and (c) a film between two layers that are index-matched to $MAPbI_3$ (refractive index n=2.5). The model uses the fitted value of $k_2^{intrinsic} = 6.8 \times 10^{-10}\,\mathrm{cm^3\,s^{-1}}$ and $k_3 = 1 \times 10^{-29}\,\mathrm{cm^6 s^{-1}}$ and assumes a pump excitation fluence of $45\,\mu\mathrm{J\,cm^{-2}}$

re-distribution caused by charge-carrier diffusion, which is a weak effect over this time interval (see also Chapter 5.2 for a discussion on the relative effects of charge-carrier diffusion and photon re-absorption). As a result, the apparent bimolecular recombination rate increases, meaning that $k_2^{apparent}$ becomes closer to the value of $k_2^{intrinsic}$.

This evaluation of photon out-coupling effects has important consequences for the analysis of spectroscopic transients recorded for these materials. First, it has been shown that the closer the apparently observed bimolecular recombination rate constants are to the intrinsic values, the more photons are allowed the leave the film. This can be facilitated e.g. through index-matching with the surrounding layers, or light scattering effects. Second, it can be noted that the dependence of photon out-coupling on the refractive index of the surrounding layers means that the addition of a charge-extraction layer on top of a perovskite film will modify the shape of the observed transients even in the absence of charge-transfer across that interface. Therefore, such transients require careful analysis before quantitative deductions on the charge-transfer efficiencies can be made.

To further characterise the effects of photon out-coupling the correction factor Φ_2 that is required in order to obtain intrinsic values $k_2^{\text{intrinsic}}$ from the apparent values k_2^{apparent} is calculated. This is determined using the procedure detailed in Chapter 5 and the relation between the two models is defined here as

$$\Phi_2 = \frac{k_2^{\text{apparent}}}{k_2^{\text{intrinsic}}}, \tag{6.3}$$

such that lower values of Φ_2 denote slower charge-carrier recombination in a system. To determine Φ_2, the self-absorption model is used to generate a set of photo-conductivity transients based on the intrinsic value $k_2^{\text{intrinsic}}$, which are then globally fitted using the standard model to determine the apparent value k_2^{apparent} (see Section 5.3). These calculations are conducted for an assumed even charge-carrier distribution through the film. The effect of photon confinement can be explored by calculating the correction

factor Φ_2 for a 300-nm thick perovskite layer sandwiched between two infinitely thick layers with a range of refractive indices, shown in Figure 6.3(a). When at least one of the interfacial layers has a higher refractive index than the perovskite (2.5), Φ_2 is always greater than 50%, as there is no total internal reflection to enhance the photon confinement. When both of the surrounding layers are lower in refractive index than the perovskite, Φ_2 decreases sharply as photon confinement is boosted. The wide range of values encountered for Φ_2 show the sensitivity of charge-carrier retention on the type of surroundings the film is embedded in.

Figure 6.3(a) clearly highlights the potential downside of incorporating perovskites into indexed-matched surrounds. For example, for the configurations selected in Figure 6.2 the probability of photon re-absorption falls from 78% for layers on quartz substrates, to 47% in the simplified silicon-tandem configuration, and only 34% for indexed matched interfaces. These scenarios indicate real losses since the apparent value k_2^{apparent} reflects the rate with which charge-carriers are lost from the system, while the value of $k_2^{\text{intrinsic}}$ represents only the intrinsic loss through bimolecular charge-carrier recombination and therefore photon generation inside the material. As pointed out in recent studies [132–134], such losses become more important as parasitic non-radiative recombination via traps is reduced. In high-quality thin films of $MAPbI_3$, trap-related recombination rates on the order of μs are already becoming reality [116, 117, 224, 225]. These advances thus highlight the need for enhanced photon confinement to further reduce charge-carrier losses from the perovskite. Such photon management may for example be achieved through placing light-trapping structures around solar cells [226] or texturing of the cell surface [133, 227]. Ultimately the correct management of radiative losses determines the maximum efficiency of a solar cell [228], and as light management is already a limiting factor in perovskite devices [229], further consideration of photon management will become an important element in device design.

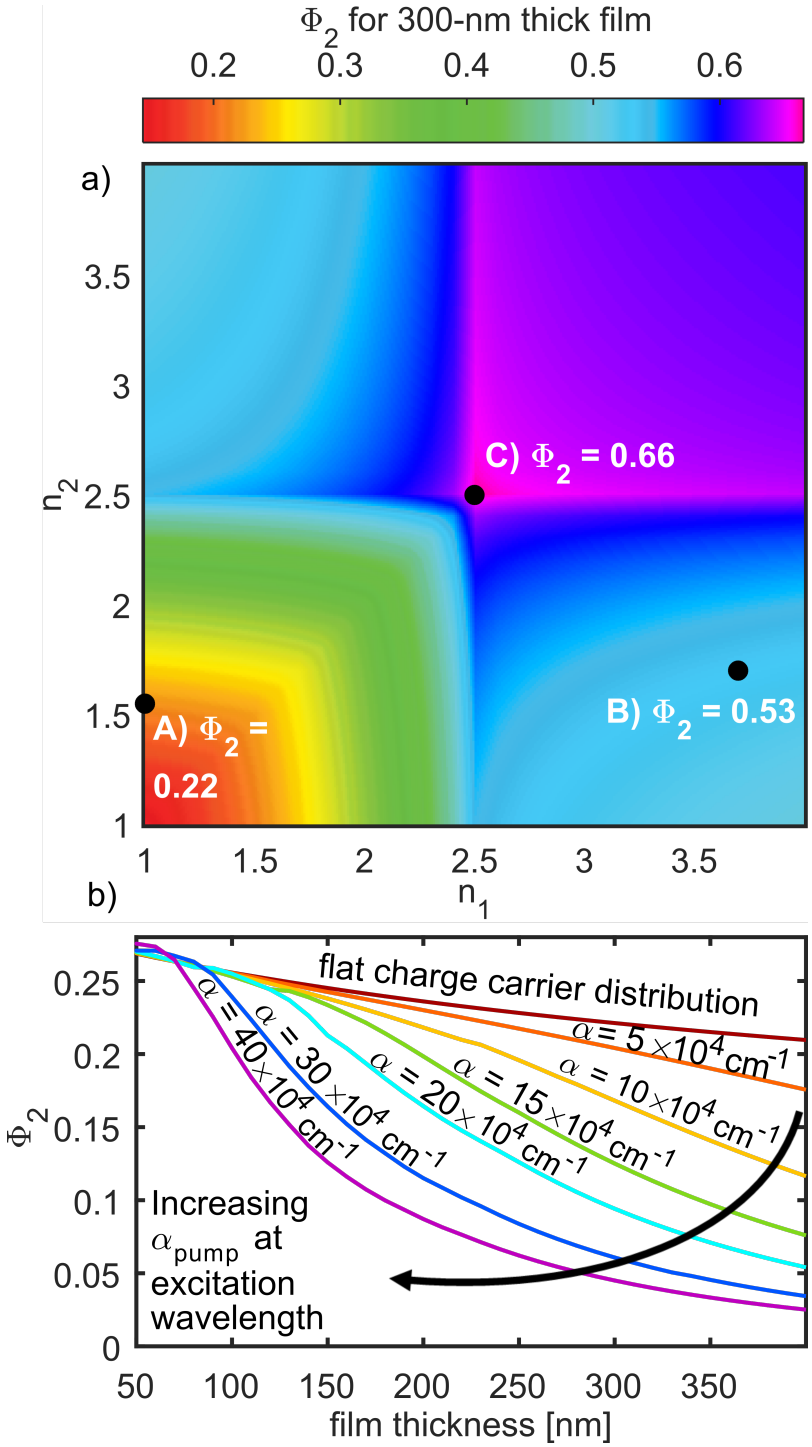


Figure 6.3: (a) Simulated ratio $\Phi_2 = k_2^{\text{apparent}}/k_2^{\text{intrinsic}}$ of the apparent to the intrinsic bimolecular recombination rate, with $k_2^{\text{intrinsic}} = 6.8{\times}10^{-10}\,\text{cm}^3\text{s}^{-1}$. Φ_2 was evaluated using the self-absorption model described in the text for an even initial distribution of charge-carriers along the film depth profile. The model assumes a 300-nm-thick layer of perovskite (n = 2.5), sandwiched between two infinitely thick interfacing layers. The points A-C represent the modelled examples in Figure 6.2(a-c). (b) Simulated variation of Φ_2 as a function of thickness shown for different values of the absorption coefficient experienced at a given excitation (pump) wavelength by a $MAPbI_3$ perovskite film on a quartz substrate. Higher absorption coefficients lead to a less even initial charge-carrier distribution through the film depth profile.

Finally, the findings presented above can be used to highlight some of the potential causes for the wide spread in apparent values of k_2 reported in the literature for a range of different hybrid metal perovskites. First variations in material morphology that may affect light re-absorption through scattering are addressed, followed by a comment on the effect of compositional changes such as halide substitution.

A number of independent studies have reported that bimolecular recombination constants appeared to be higher for lead iodide perovskite films with smaller grain size [94, 156, 230]. Such effects are surprising at first sight. Extrinsic trap-mediated recombination may well be affected by grain size because of a potential propensity of traps to accumulate at grain boundaries [110]. However, the bimolecular recombination between free electrons and holes is normally governed by the band-edge density of states that is intrinsic to the semiconductor, which should be largely unaffected by grain size given that $MAPbI_3$ exhibits an energetically sharp absorption onset [216]. To explain the dependence of the apparent bimolecular recombination rate constant on grain size it is noted that in these films, the lateral extent of the grains is typically on a length scale comparable to the PL wavelength. Hence changes in grain size will strongly affect the extent of Rayleigh scattering from crystal defects in both the bulk and surface of the material, which is known to limit the free path length of PL [134, 227]. A scattering event can alter the direction of a travelling photons, allowing photons previously confined by total internal reflection to escape [134]. As shown above, the lowered photon confinement will result in an increase in the apparent bimolecular recombination rate constant k_2^{apparent} that is perceived in transient spectroscopy. These considerations can thus not only explain the dependence of k_2^{apparent} on grain size, but also the faster bimolecular recombination reported for hybrid perovskites infused into mesoporous oxide scaffolds [94, 230, 231] which scatter strongly, leading to reduced photon retention. While a full consideration of scattering mechanism involved [227] is beyond this study, it is proposed that the wide range in

bimolecular recombination rates reported for $MAPbI_3$ in the literature may largely derive from an indirect impact of the film morphology and thickness, which mask the underlying existence of a single, intrinsic value $k_2^{\text{intrinsic}}$ of the bimolecular rate constant.

In addition, the impact of halide substitution on the apparent bimolecular rate constant perceived in transient spectroscopy can also be considered. Several literature studies have reported bimolecular charge-carrier recombination dynamics to be more rapid in bromide lead perovskites compared to the equivalent iodide lead perovskites [138, 207, 232]. Rehman *et al.* found k_2^{apparent} to increase steadily by about one order of magnitude with increasing bromide fraction x in thin films of $FAPb(Br_xI_{1-x})_3$ [138] and $Cs_yFA_{1-y}Pb(Br_xI_{1-x})_3$ [232] which they attributed to gradual changes in the bandstructure. It is noted here that the associated increase in band-gap with increasing bromide content will lead to a decrease in the density of the absorbing states at the fixed laser excitation typically employed by these experiments (the excitation in effect moves closer in energy to the band-gap). As a result, the absorption length for photons inside the material increases, giving rise to a more even initial distribution of charge-carriers across the depth profile which may, in turn, affect the subsequent charge-carrier dynamics.

To exemplify such effects, Figure 6.3(b) shows how the ratio Φ_2 between the apparent bimolecular recombination rate constant, $k_2^{apparent}$, and the intrinsic value $k_2^{intrinsic}$ changes as a function of film thickness, for a range of different absorption coefficient values α experienced at the excitation wavelength. Since $k_2^{intrinsic}$ is independent of film thickness and photon wavelength, these curves in essence chart the change in the apparent rate constant k_2^{apparent} that is perceived in transient spectroscopy following pulsed excitation. These curves show that for high absorption coefficient or short penetration depth (purple curve) at the excitation wavelength, the bimolecular recombination appears to be particularly severely suppressed for large film thickness. This effect results from the rapid re-distribution of charge-carriers induced by photon re-absorption that flattens

the charge-carrier profile soon after excitation (see Figure 6.2a). As a consequence, fits to the transients using the standard model return a particularly low value of the bimolecular recombination constant with respect to the intrinsic value. It is noted that even for an initially flat (even) charge-carrier distribution (red curve) photon re-absorption will still reduce the apparent rate constant k_2^{apparent} below the intrinsic value, because re-absorbed photons re-generate charge-carriers at later stages, thus maintaining a high charge-carrier density over longer times. However, the factor Φ_2 is particularly low for large film thicknesses and uneven initial charge-carrier density profiles, for which photon re-absorption has the strongest redistributive influence. With relevance to the influence of halide substitution, one has to consider that for the $MAPbX_3$ system, the absorption coefficient for a given excitation wavelength of 400 nm falls by a factor 4 when X is changed from I to Br [233]. Figure 6.3(b) shows that, for a 300-nm thick film, this change alone would introduce a reduction by a factor 4.2 in k_2^{apparent} as measured following pulsed excitation. Therefore, changes in photon re-absorption with changing band-gap energy are partly to blame for the observed order-of-magnitude difference in k_2^{apparent}, with changes in the band-edge density of states the most likely cause for the remaining trend.

6.3 Questions Addressed in this Chapter

Why does the charge-carrier recombination rate in the $MAPbI_3$ films studied show a dependence on the film thickness?

The self-absorption model shows that charge-carrier diffusion and photon re-absorption cause charge carriers to be spread evenly across each of the $MAPbI_3$ films studied. As charge carriers will be spread out across a larger volume in thicker films n will be lower. Since the rate of bimolecular charge-carrier recombination depends on the square of the charge-carrier density, charge carriers will, therefore, decay more slowly in thicker $MAPbI_3$ films where n is smaller, despite $k_2^{intrinsic}$ being the same in all $MAPbI_3$ films.

If bimolecular recombination in $MAPbI_3$ is intrinsic, how can this be reconciled with the wide range of values reported in literature?

Whilst it has been claimed here that $MAPbI_3$ samples should share a single intrinsic value of k_2, it has also been pointed out that this value will be hidden by effects such as photon re-absorption and charge-carrier diffusion. Therefore, a range of $k_2^{apparent}$ can be reported for samples with differences in film thickness or other extrinsic factors. A key factor will be the level of scattering present in each sample, which significantly reduces the level of photon confinement and so increases the loss of charge carriers to radiative recombination. Although the external or apparent recombination rate will be different between samples, this is not incompatible with the idea of a single $k_2^{intrinsic}$.

How do the transport layers in a MHP device affect radiative losses?

This chapter has demonstrated that radiative losses from a $MAPbI_3$ layer are strongly affected by the refractive index of the adjacent layers. In a solar cell, if a MHP layer is surrounded by lower refractive index materials, this will limit the solid angle of light which can be emitted and so increase the fraction of emitted photons which are recaptured by the MHP. Conversely, transport layers with a higher refractive index will reduce

photon confinement, leading to more of the emitted photons being lost, and a faster overall decay of the charge-carrier population.

7

Charge-Carrier Dynamics in Mixed 2D/3D Perovskite Films

Contents

7.1 Sample Preparation 141
7.2 Initial Sample Characterisation 142
7.2.1 Steady State and Time-Resolved Photoluminescence 142
7.2.2 Steady-State Absorption 145
7.2.3 Optical-Pump-Terahertz-Probe Spectroscopy 145
7.3 Modelling Charge-Carrier Dynamics in the Quasi-2D/3D Perovskite 146
7.3.1 Model Used for the Perovskite Film 146
7.3.2 Description of Dynamical Model 150
7.3.3 Correction of the PL Spectrum for Self-Absorption 151
7.4 Fits to THz Photoconductivity Data 154
7.5 Analysis of the Shape of the THz Photoconductivity Transients 158
7.5.1 Impact of Charge-Carrier Diffusion 159
7.5.2 Impact of Photon-Reabsorption 165
7.5.3 Impact of the Thickness of the Quasi-2D Region 172
7.5.4 Summary 176
7.6 Questions Addressed in this Chapter 178

Although MHP solar cells have now reported photo-conversion efficiencies (PCEs) of over 23% [71], the long term stability and sensitivity of these devices to moisture still poses a serious challenge for real-world use [40]. A potential means of overcoming this

barrier is the incorporation of large organic cations into the perovskite structure, which have been demonstrated to both protect the perovskite against moisture and provide improved structural stability [50]. However, this improved stability comes at a cost, as the resulting layered-2D perovskite structures have unfavourable properties for use in solar cells, having large exciton binding energies [49], reduced charge-carrier mobility and increased monomolecular recombination rates [221].

Instead, a mixed 2D/3D perovskite blend has been employed, to take advantage of the increased stability of the 2D perovskite while still maintaining the excellent optoelectronic properties characteristic of 3D perovskites. By mixing small and large organic cations a structure consisting of m layers of semiconducting 3D perovskite, separated by insulating planes of the larger cations, can be formed. Varying the ratio of the two cations allows the width of the 3D regions, and therefore, the degree of quantum confinement, to be modulated [49]. Quasi-2D perovskite films typically include domains with a range of m values, arranged either randomly, or vertically ordered from low to high m [234].

Such quasi-2D structures have been demonstrated to produce efficient solar cells, as well as bright LEDs [53, 56, 60]. However, despite several studies which have reported on short-range charge-carrier transfer between domains exhibiting different degrees of confinement [60, 235–237], the larger-scale picture of charge-carrier transport in quasi-2D perovskites is still poorly understood.

In this chapter, optical pump THz probe (OPTP) spectroscopy and time-resolved photoluminescence (TRPL) are used to analyse the charge-carrier dynamics of a mixed 2D/3D perovskite film. The formation of quasi-2D domains is observed at the back of the mixed 2D/3D perovskite film, next to the substrate, while predominantly 3D domains are formed on the front side of the perovskite film. Compared to the front side, the back (quasi-2D) side displays both a blue-shifted PL spectrum as well as a lower charge-carrier mobility. However, when the mixed 2D/3D perovskite film is excited from the back side a

rise in THz photoconductivity is observed, indicating that charge carriers are not inhibited from moving into the higher mobility 3D region. By modelling the charge-carrier dynamics in the mixed 2D/3D perovskite film, it is demonstrated that charge-carrier diffusion causes this rise in THz photoconductivity when the back side of the sample is photo-excited, suggesting an efficient transfer of charge carriers into 3D domains. It is also shown that the blue-shift in the PL emission from the quasi-2D domains, with respect to the 3D phase absorption onset, allows an increased rate of photon re-absorption which prolongs the charge-carrier lifetime. These results demonstrate that mixed 2D/3D structures are not constrained by the unfavourable optoelectronic properties of 2D perovskites and also help advance the understanding of the physics underlying these already successful materials.

7.1 Sample Preparation

The mixed 2D/3D perovskite film was prepared by Rong Yang and Jianpu Wang from Nanjing Tech, from a solution of 3-bromobenzylammonium iodide (3BBAI), MACl and PbI_2, dissolved in DMF with molar ratio of 1.8:2.5:3 at a weight concentration of 20% and stirred overnight in a nitrogen-filled glovebox before use.

A quartz substrate was placed on a hotplate at 140 °C for 2 – 3 minutes, then 40 μL of the perovskite precursor solution was immediately deposited onto the substrate and spin-coated at 5000 rpm for 20 seconds. The perovskite film was then post-annealed for 15 minutes on a hotplate maintained at 90 °C.

This fabrication route has previously been employed to create moisture tolerant solar cells with a PCE > 18% [238]. The resulting mixed 2D/3D perovskite film is composed of regions of $MAPbI_3$, separated by planes of the large cation $3BBA^+$.

7.2 Initial Sample Characterisation

7.2.1 Steady State and Time-Resolved Photoluminescence

The photoluminescence spectra[1] and lifetimes of the mixed 2D/3D perovskite film were measured using pulsed excitation from a 398 nm diode laser operating at 500 kHz (A full description of the PL system used is given in Appendix C.1).

Time-resolved photoluminescence spectra were fitted as two Gaussian components with distinct lifetimes. The PL as a function of time (t) and wavelength (λ) was modelled as:

$$I_{PL}(t,\lambda) = A_1 \cdot e^{-\frac{(\lambda-\lambda_1)^2}{2w_1^2}} \cdot e^{-t/\tau_1} + A_2 \cdot e^{-\frac{(\lambda-\lambda_2)^2}{2w_2^2}} \cdot e^{-t/\tau_2} \tag{7.1}$$

where A_1 and A_2 are the amplitudes, w_1 and w_2 the bandwidths, λ_1 and λ_2 the central wavelengths and τ_1 and τ_2 the lifetimes of each component in the emission.

Experimental data, together with fits produced by the model, can be seen in Figures 7.1 and 7.2. It can be seen from the fits in Figures 7.1 and 7.2 that excitation of either side of the film results in PL lifetimes on the order of one µs at the 771 nm peak of the 3D phase PL emission. However, when the film is excited from the back side, most of the PL emission occurs very rapidly at the shorter wavelength of 711 nm.

From the PL spectra in Figure 7.2(d), it can be seen that there is a higher energy component associated with quasi-2D domains, which is absent from the spectrum in Figure 7.1(d). This indicates a concentration of quasi-2D perovskite domains near the quartz substrate, while the front side of the film is composed of only 3D perovskite domains. Additionally, from the modest (60 nm) shift in the emission peak, it can be concluded that the quasi-2D domains in the mixed 2D/3D perovskite film exhibit only a mild degree of quantum confinement.

[1] Photoluminesence data was collected and fits to the PL data were made by Dr S. G. Motti

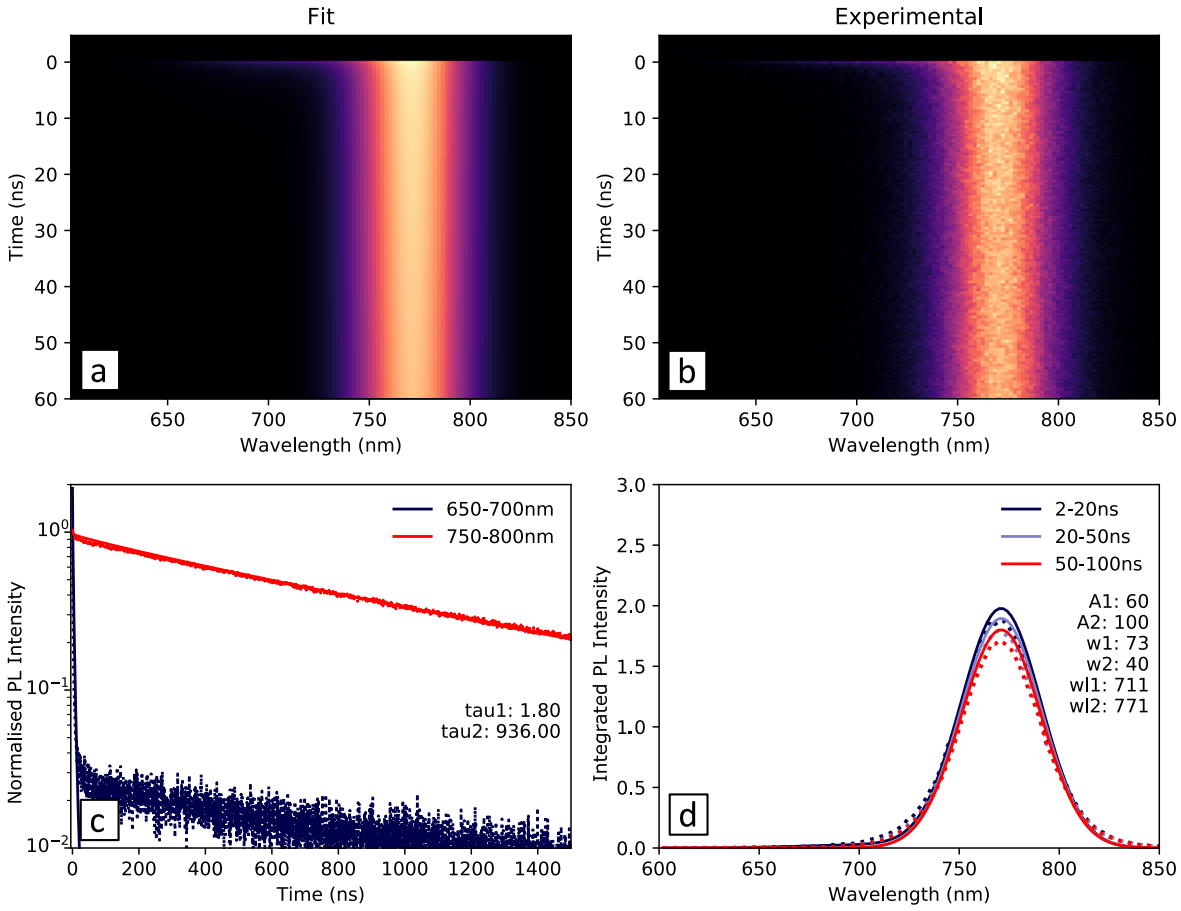


Figure 7.1: (a), (b) Modelled and experimental data of TRPL spectra, measured for the excitation of the front side of the mixed 2D/3D perovskite film at a wavelength of 398 nm; (c) Time resolved PL dynamics integrated in the spectral ranges 650-700 nm (dark blue) and 750-800 nm (red), the dotted lines show experimental data, while solid lines are fitted curves; (d) PL Spectra integrated over three different time windows, dotted lines show experimental data, while solid lines are fitted curves. Data was collected and fits were calculated by Dr S.G. Motti.

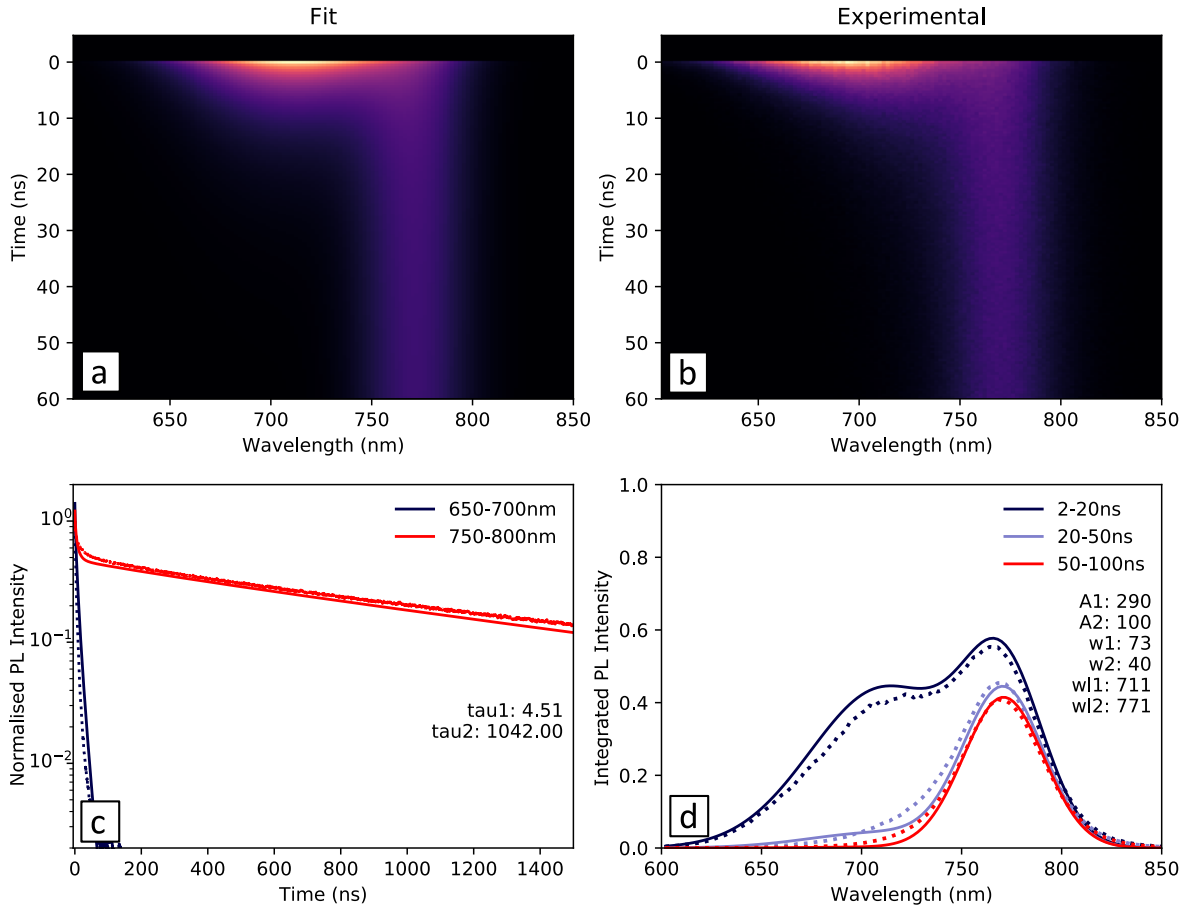


Figure 7.2: (a), (b) Modelled and experimental data of TRPL spectra, measured for the excitation of the back side of the mixed 2D/3D perovskite film at a wavelength of 398 nm; (c) Time resolved PL dynamics integrated in the spectral ranges 650-700 nm (dark blue) and 750-800 nm (red), the dotted lines show experimental data, while solid lines are fitted curves; (d) PL Spectra integrated over three different time windows, dotted lines show experimental data, while solid lines are fitted curves. Data was collected and fits were calculated by Dr S.G. Motti.

7.2.2 Steady-State Absorption

Reflection and transmission spectra[2] of the mixed 2D/3D perovskite film were measured using a Bruker 80v Fourier-transform infrared spectrometer with a tungsten halogen lamp source, a CaF beamsplitter and a silicon diode detector.

Figure 7.3 shows the absorption spectrum of the mixed 2D/3D perovskite film, both with and without a correction for background scatter. The level of background scattering was calculated based on the average sub-gap absorption in the range 850 to 950 nm. This value was subtracted from the entire spectrum to obtain a scatter-corrected absorption spectrum.

From the figure, it can be seen that the dominant features in the absorption spectrum are consistent with the 3D $MAPbI_3$ perovskite, suggesting that it comprises the bulk of the perovskite film. This is in contrast to other previously reported mixed 2D/3D perovskite samples, which have included strong absorption features from quasi-2D domains [234].

7.2.3 Optical-Pump-Terahertz-Probe Spectroscopy

OPTP spectroscopy[3] was employed to characterise the charge-carrier mobility and recombination dynamics in the mixed 2D/3D perovskite film, using the OPTP system described in Chapter 3. When exciting the mixed 2D/3D perovskite film at 400 nm from the back side, a charge-carrier mobility of $17.6\,cm^2\,V^{-1}\,s^{-1}$ was obtained, while the charge-carrier mobility was $23.3\,cm^2\,V^{-1}\,s^{-1}$ when exciting from the front side. This lower charge-carrier mobility of the quasi-2D domains on the back side of the film is consistent with previous THz measurements of 2D perovskite films [221] and stems from the higher dielectric confinement of charge carriers in the quasi-2D domains. Time-resolved THz photoconductivity decays were also measured for the mixed 2D/3D perovskite film, but are described separately in Section 7.4.

[2]Reflection/Transmission data was collected by Dr S. G. Motti
[3]THz photoconductivity measurements were made by Dr S. G. Motti

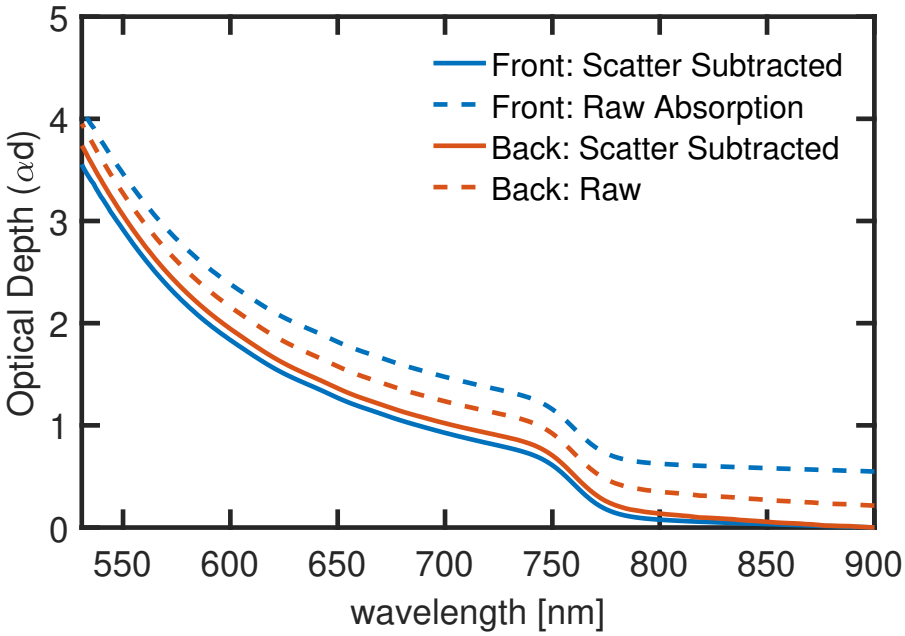


Figure 7.3: Absorption spectrum of the mixed 2D/3D perovskite film. Dotted lines show the raw data while solid lines show the same data with a baseline correction removing subgap absorption as described in the text. Data was collected by Dr S.G. Motti.

7.3 Modelling Charge-Carrier Dynamics in the Quasi-2D/3D Perovskite

7.3.1 Model Used for the Perovskite Film

The initial characterisation of the mixed 2D/3D perovskite film has indicated the presence of quasi-2D and 3D perovskite domains, at different points in the perovskite layer. In order to model the charge-carrier dynamics in the mixed 2D/3D perovskite film, a simplified model of the perovskite film is now developed.

Modelling the Mixed 2D/3D film as Two Regions Figure 7.4 shows a cross-sectional scanning transmission electron microscope (STEM) image of the mixed 2D/3D perovskite film, where both 3D and quasi-2D domains can be seen. Close to the substrate the sample contains large fractions of quasi-2D domains, while near the surface it has only 3D perovskite domains.

For the purposes of modelling the charge-carrier dynamics, the film is considered as

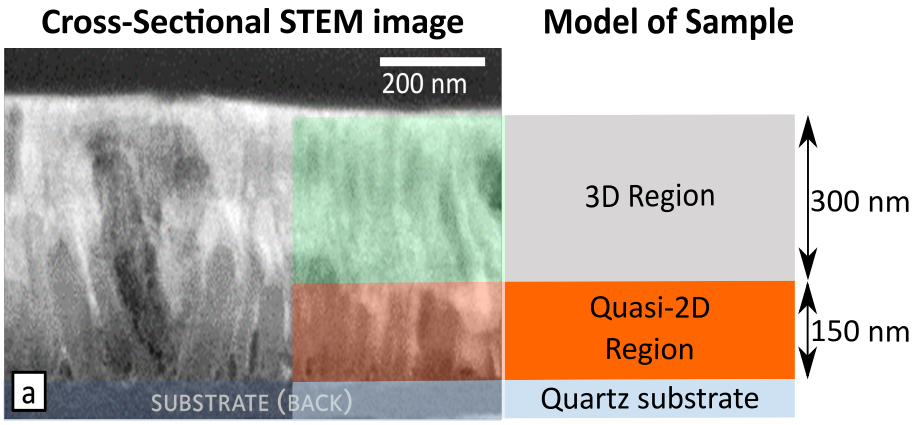


Figure 7.4: Schematic representation of the mixed 2D/3D perovskite film; the left part of the figure shows the STEM image of a mixed 2D/3D perovskite film prepared using the same procedure as the one studied in this chapter, while the right side shows the simplified model of the film used for simulating the charge-carrier dynamics. It can be seen in the STEM image how the film is divided into two regions with different morphologies and how the thickness of each region in the model derives from the STEM image. STEM image taken by R. Yang and J. Wang from Nanjing Tech.

two layers (representing the quasi-2D and 3D regions), stacked on top of one another. Figure 7.4 shows how the STEM image of the perovskite film is used to build this simplified model. The bottom of the film is modelled as a quasi-2D region, representing the mix of quasi-2D and 3D perovskite domains seen at the bottom of the STEM image. The rest of the film is represented as a capping layer of pure 3D perovskite. The thickness of each region is taken from the STEM image, based on the average thickness of the quasi-2D domains. The values used for the thickness of each layer are: 150 nm for the quasi-2D region and 300 nm for the 3D region. In this way, the mixed 2D/3D perovskite film can be represented by the simplified model on the left of Figure 7.4, consisting of a quasi-2D and 3D region.

Properties of the Two Regions Having split the sample into two regions, the next issue is to decide how the material properties of each region differ. Although, in reality, there is no sharp distinction between the regions, using short-wavelength light, the volume of the mixed 2D/3D perovskite film corresponding to each region can be independently

probed. This means that separate properties can be assigned to each of the modelled regions, namely the charge-carrier mobility and PL spectrum.

Both of these measurements are made by exciting either the front or back of the mixed 2D/3D perovskite film with a laser at 400 nm. Due to the strong absorption of the perovskite film, the absorption depth at this wavelength could not be determined, however, even at 550 nm excitation, the perovskite absorbs light strongly enough such that $1/\alpha_{pump} < 100\,\text{nm}$. Instead, the previously reported [239] value of $\alpha_{pump} = 2 \times 10^5\,\text{cm}^{-1}$ was used, giving $1/\alpha_{pump} < 50\,\text{nm}$. This value was measured for a $MAPbI_3$ film and is appropriate here since the 3D phase perovskite is dominant in the absorption spectrum of the mixed 2D/3D perovskite film. Therefore, for an excitation at a wavelength of 400 nm, all of the light will be absorbed before reaching the modelled boundary between the two regions and so the properties of each region can be measured individually. For this reason, when the front side of the mixed 2D/3D perovskite film is excited, the measurement is associated with the 3D region, and when the back side is excited, the measurement associated with the quasi-2D region.

Using the values reported in Section 7.3, the 3D region of the model was assigned a charge-carrier mobility of $23.9\,\text{cm}^2\,\text{V}^{-1}\,\text{s}^{-1}$ and the quasi-2D region a charge-carrier mobility of $17.4\,\text{cm}^2\,\text{V}^{-1}\,\text{s}^{-1}$, as these, respectively, were the values measured for front and back side excitation of the mixed 2D/3D perovskite film.

Similarly, using the PL spectra described in Section 7.2.1, the quasi-2D region is modelled as emitting the PL spectrum measured for excitation of the sample back, while the 3D region is considered to emit the spectrum measured when exciting the front side of the mixed 2D/3D perovskite film, subject to the photon re-absorption correction discussed in Section 7.3.3.

As the quasi-2D domains have a wider band-gap than the 3D domains, at the interface between the two there will be an offset in the band alignment. A type 2 alignment

would lead to the separation of charge carriers at the interface between the 2D and 3D domains, resulting in the separation of electrons and holes, as reported by Lui *et al* [235]. This would lead to much slower recombination which is not observed from TRPL. The presence of a type 2 alignment would allow charge-carriers to move in only one direction across the interface – from the quasi-2D to the 3D material – as proposed by Wang *et al* [237]. Either arrangement will clearly have a strong impact on the charge-carrier dynamics, however, in the mixed 2D/3D perovskite film being studied, quasi-2D and 3D domains are mixed together throughout the quasi-2D region. The model therefore treats the quasi-2D region as an effective medium, composed largely of 3D domains, with a minority of quasi-2D domains. Within this picture, the presence of the quasi-2D domains serves only to lower the mobility and charge-carrier transfer between the 3D and quasi-2D domains is not directly addressed. Rather, the focus of the model is on longer-scale movement of charge carriers through 3D domains within the 3D and the quasi-2D regions. With a clearer picture as to the nature of the band alignment at the interface, the model could be improved by resolving the quasi-2D region into quasi-2D and 3D domains and appropriately modelling the movement of charge carriers between the two types of domains. However, as there remains no consensus within the surrounding literature, the quasi-2D region is for now modelled as a composite of the two types of domain. Additionally, due to the mixing of the quasi-2D and 3D domains, only the total mobility of the quasi-2D region can be resolved by OPTP spectroscopy so it is more appropriate to model the quasi-2D region as a mix of the two domains. Diffusion of charge-carriers to be modelled as diffusing through the composite with a lower effective mobility, which is expected to represent mainly sampling the fraction of charge carriers in 3D domains.

In summary, the film is modelled as two layers of perovskite, with the top being composed of 3D perovskite domains and the bottom as a mixture of quasi-2D and

3D perovskite domains. The model assumes that, with the exception of the thickness, charge-carrier mobility and PL emission spectrum, each region is identical.

7.3.2 Description of Dynamical Model

With a model of the mixed 2D/3D perovskite film structure developed, a dynamical model, which accounts for the variation in charge-carrier mobility and PL spectrum across the film is needed, in order to simulate the THz photoconductivity decays measured for the mixed 2D/3D perovskite film using OPTP spectroscopy.

It is required that the model accounts not only for charge-carrier recombination, but additionally for charge-carrier transport by diffusion and photon re-absorption, as it has been previously reported that exchange of charge carriers between the quasi-2D and 3D domains is an important aspect of the charge-carrier dynamics [60, 235, 236].

To model the charge-carrier dynamics, including these transport processes, the self-absorption model described in Chapter 4.2.4.2 is used. In the previous chapters, the self-absorption model has been used to simulate the charge-carrier dynamics in uniform perovskite films, in order to model the charge-carrier dynamics in the mixed 2D/3D perovskite film, the dynamical model has been extended to allow the charge-carrier mobility, recombination rates and PL emission spectra to vary through the film.

Extensions to the self-absorption model for the Mixed 2D/3D Perovskite. The self-absorption model, as previously used in the last two chapters is shown in Figure 7.5. In this model, the charge-carrier density across the film is broken into a series of slabs, with each slab having identical material properties. For this chapter the model was extended, as shown on the right side of Figure 7.5, so that each slab in the model can now have a different charge-carrier mobility and PL emission spectrum, allowing the two regions identified in the mixed 2D/3D perovskite film to be simulated with different properties. As the original self-absorption model is based around matrix

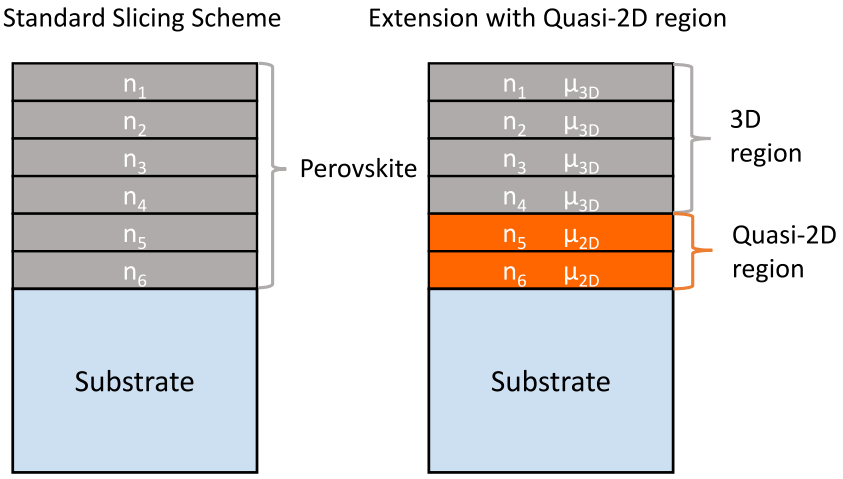


Figure 7.5: A schematic showing the slicing scheme used to split a perovskite layer into slabs with independent charge-carrier density. Also shown is the extension of this scheme to include a separate quasi-2D region with a different charge-carrier mobility to the 3D region.

operations, these changes can be supported in a straightforward manner, for example, by replacing a single value of charge-carrier mobility with an array of the mobilities for each slice (See Chapter 4.2.2.3 for details of the implementations).

Although only simple changes were made to the code, they open the possibility for several interesting effects. The obvious effect of having a changing charge-carrier mobility throughout the sample is that charge-carrier diffusion will happen at different rates in different locations. The more subtle effect is that since the THz photoconductivity (Equation 4.47) depends on the charge-carrier mobility, if charge carriers move from a low to high mobility region, the THz photoconductivity will increase. These diffusion-related effects are explored in more detail in Section 7.5.1.

Having a different PL spectrum for each region will mean that the photons emitted from each region have different probabilities of being re-absorbed. The effects of this heterogeneous PL spectrum on the charge-carrier dynamics are discussed in Section 7.5.2.

7.3.3 Correction of the PL Spectrum for Self-Absorption

In order to simulate photon re-absorption within the mixed 2D/3D perovskite film, the ray tracing program described in Chapter 4.2.3 was first used to calculate the

amount of light re-absorbed by the sample, for wavelengths between 600 nm and 850 nm. This calculation used the absorption coefficient measured for the sample using FTIR spectroscopy, shown in Section 7.2.2.

For each wavelength, the ray-tracing model was used to simulate isotropic emission from each slice of the model in order to determine the amount of photon re-absorption at each wavelength, as well as the probability that PL will escape from the film.

Using this wavelength dependent probability that an emitted photon will escape the film, the externally measured PL spectra can be corrected for self-absorption.

Figure 7.6 shows this correction for the PL spectrum measured for excitation of each side of the mixed 2D/3D perovskite film. It can be seen that after the correction, both spectra are blue-shifted and that the shorter-wavelength component of the quasi-2D PL is much stronger.

This can be understood from the fact that the 700 nm component of the quasi-2D PL is above the absorption edge, it is more strongly re-absorbed, whereas the longer-wavelength component is not. This means that, when considering how much of each component was emitted, the 700 nm component must initially be much more dominant. After accounting for this re-absorption, the 700 nm component is seen to be the most prominent peak in the PL spectrum of the quasi-2D region. It is noted that the appearance of shorter wavelength PL components when exciting the substrate-side of the film has been observed in other sources [235, 236], but without the correction for photon re-absorption the relative intensity of the internally emitted components cannot be compared.

Modelling Photon-Reabsorption in the mixed 2D/3D perovskite Using the internal PL spectra for each region, a re-absorption matrix for the mixed 2D/3D perovskite film was created. This matrix describes how the photons emitted in each slice of the film are re-absorbed by each other slice, as described in Chapter 4.2.3. In the following

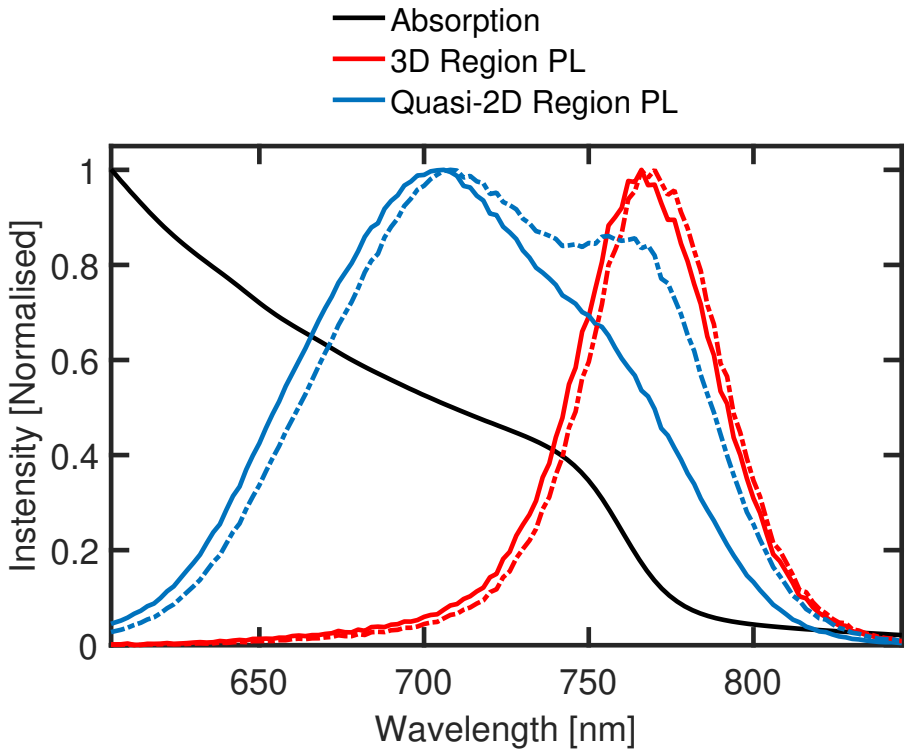


Figure 7.6: The PL spectrum measured for front and back excitation of the mixed 2D/3D perovskite film, shown with the normalised absorption spectrum. Dashed lines show the uncorrected PL spectra data, while solid lines show the PL spectra after correcting for photon re-absorption, as described in the text. Details of how the PL spectra were collected are given in Section 7.5.2. Data was collected by Dr S.G. Motti.

simulations the PL emitted from the 3D region of the model is the corrected emission spectrum from the excitation of the front of the mixed 2D/3D perovskite film, while the quasi-2D region is modelled as emitting the PL spectrum measured for the excitation of the back of the perovskite sample. As the PL varies between the two regions, this model of the mixed 2D/3D perovskite film PL is referred to as 'heterogeneous' PL.

7.4 Fits to THz Photoconductivity Data

The time-resolved THz photoconductivity of the mixed 2D/3D perovskite film was measured using OPTP spectroscopy (as described in Chapter 3), exciting the perovskite film from both the front and the back. The resulting THz photoconductivity transients are shown in Figures 7.7 and 7.8, along with fits made using the self-absorption model. To demonstrate the respective roles of charge-carrier diffusion and photon re-absorption, each set of THz photoconductivity transients are fitted; a) without either transport process, (b) and (c), with only diffusion or photon re-absorption and, (d) with both processes. Across each of the dynamical models, k_2 and the amplitude of initial THz photoconductivity transients were the only free parameters in the fits (full details of the fitting process are given in C.2).

Excitation from the Front of the Perovskite Sample Figure 7.7 shows the measured THz photoconductivity transients, for excitation from the front side of the mixed 2D/3D perovskite film, together with the four different dynamical models as described above and as indicated in the figure. As each model either includes or omits charge-carrier diffusion and photon re-absorption, the individual effects of each transport process on the shape of the modelled THz photoconductivity transients can be seen.

The THz photoconductivity transients, measured for excitation of the front side of the mixed 2D/3D perovskite film, show a simple decay of THz photoconductivity over time. The rate of this decay increases with excitation fluence, consistent with there being more bimolecular recombination at higher charge-carrier densities. All of the simulations can fit the THz photoconductivity decays well, however, each fits the same curve using a different value for the bimolecular recombination rate, k_2. This reflects that although the models all fit the data, they make different assumptions about the charge-carrier

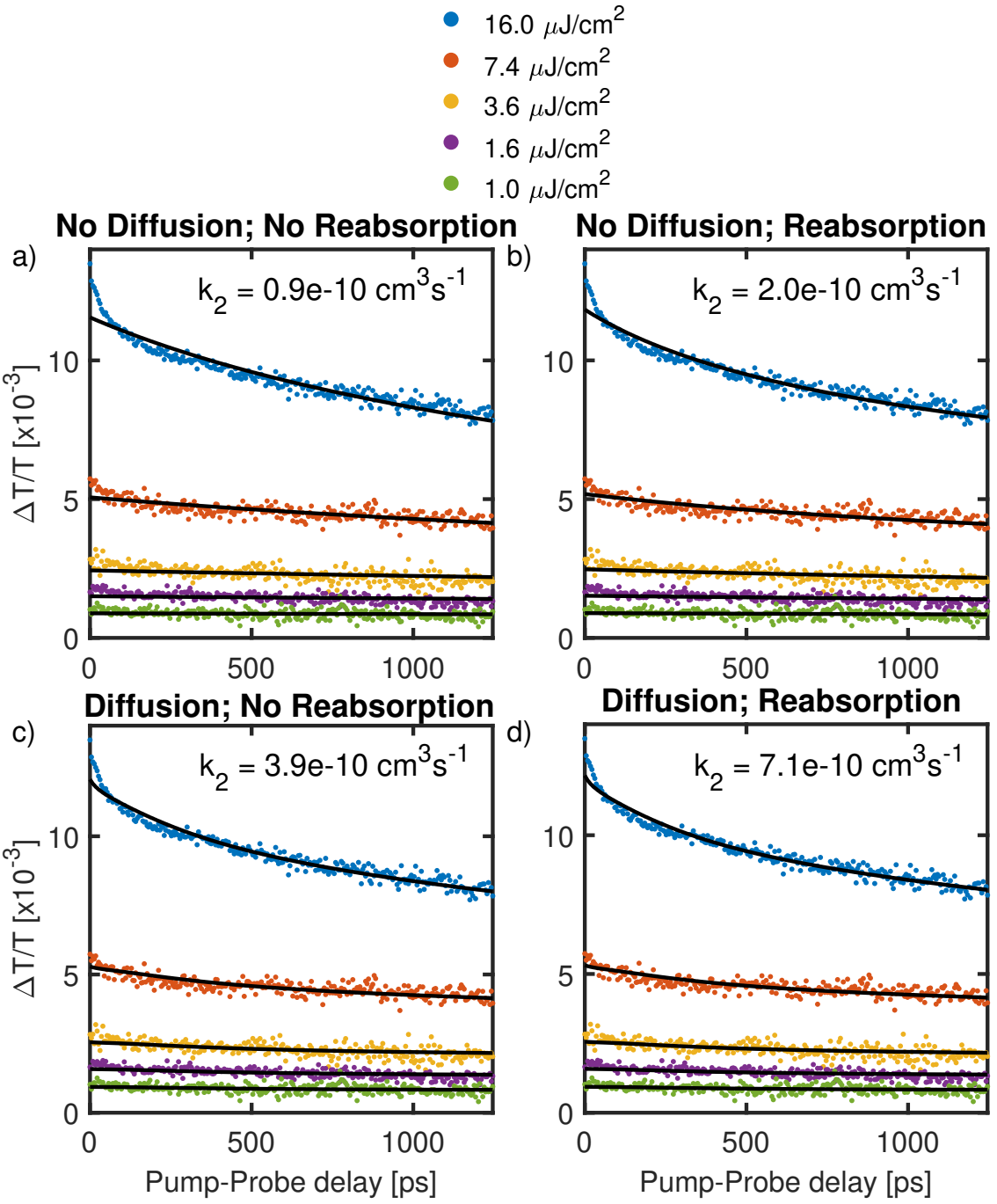


Figure 7.7: THz Photoconductivity transients measured for excitation from the front side of the mixed 2D/3D perovskite film with a pump wavelength of 400 nm. Shown with global fits using the self-absorption model (black lines). In each panel, charge-carrier diffusion and photon re-absorption are included or omitted from the dynamical model, as indicated. THz photoconductivity transients were measured by Dr S.G. Motti.

dynamics. It can also be seen that the faster initial decay within the first 100 ps is fitted more closely only by the models which include charge-carrier diffusion.

Excitation from the Back of the Perovskite Sample The THz photoconductivity transients, for excitation from the back side of the mixed 2D/3D perovskite film, are shown in Figure 7.8. As before, the THz photoconductivity transients in each panel of Figure 7.8 show the same data, but in each case a different dynamical model is used.

Unusually, Figure 7.8 shows that several of the THz photoconductivity transients rise, rather than decay, within the first 500 ps. After this initial rise the THz photoconductivity transients decay, in the same manner as the transients for front-side excitation. Once again, the THz photoconductivity transients for higher excitation fluences decay faster than those where the excitation fluence was lower.

By comparing panels (a) – (d) in Figure 7.8 it can be seen that charge-carrier diffusion must be included in the dynamical model to simulate the experimentally observed rise in THz photoconductivity. The top row of Figure 7.8 shows the two simulations which do not include charge-carrier diffusion (where one model includes and the other omits photon re-absorption). It can be seen that none of the transients produced by these dynamical models show any rise in THz photoconductivity. In contrast, the bottom two simulations in Figure 7.8 both include charge-carrier diffusion and each set of simulated transients reproduce the rise in THz photoconductivity seen in the experimental data.

The exact shape of the transients and the role of each of the transport processes is fully discussed in Section 7.5, but from Figure 7.8 it is already clear that diffusion is chiefly responsible for the rise in THz photoconductivity seen when the back of the mixed 2D/3D perovskite film is excited.

***

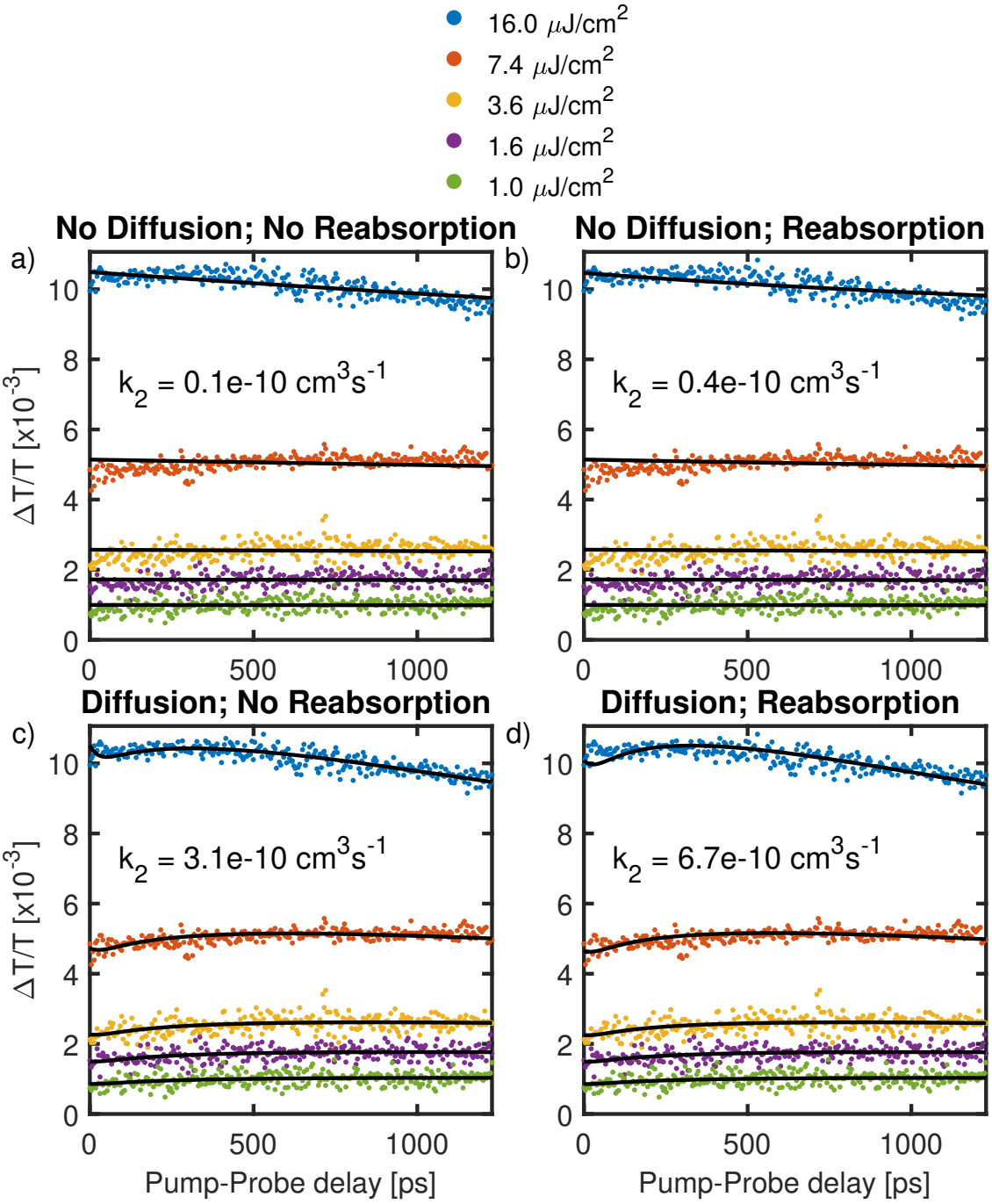


Figure 7.8: THz Photoconductivity transients measured for excitation from the back side of the mixed 2D/3D perovskite film with a pump wavelength of 400 nm. Shown with global fits using the self-absorption model (black lines). In each panel, charge-carrier diffusion and photon re-absorption are included or omitted from the dynamical model, as indicated. THz photoconductivity transients were measured by Dr S.G. Motti.

The values of k_2 obtained for the mixed 2D/3D perovskite film using the self-absorption model are, $k_2 = 7.1 \times 10^{-10}\,\mathrm{cm^3\,s^{-1}}$ for excitation from the front side and $k_2 = 6.7 \times 10^{-10}\,\mathrm{cm^3\,s^{-1}}$ for excitation from the back side. It is interesting to note that the average of these two values ($6.9 \times 10^{-10}\,\mathrm{cm^3\,s^{-1}}$) is remarkably close to the value of $k_2 = 6.8 \times 10^{-10}\,\mathrm{cm^3\,s^{-1}}$ determined for a conventional $MAPbI_3$ film in Chapter 6. The fact that the same bimolecular recombination rate can describe the charge-carrier dynamics in both the mixed 2D/3D perovskite film and a conventional $MAPbI_3$ film highlights the intrinsic nature of bimolecular recombination in lead-halide perovskites. For the rest of the modelling work undertaken around the mixed 2D/3D perovskite film, this average value of $k_2 = 6.9 \times 10^{-10}\,\mathrm{cm^3\,s^{-1}}$ is used as the bimolecular recombination rate throughout both regions of the modelled perovskite film.

7.5 Analysis of the Shape of the THz Photoconductivity Transients

Having demonstrated that charge-carrier recombination in the mixed 2D/3D perovskite film can be described using the self-absorption model, it is now possible to further study the shape of the modelled THz photoconductivity transients, to untangle the details of the charge-carrier dynamics. With this in mind, the influence of charge-carrier diffusion, photon re-absorption and the thickness of the quasi-2D region on the shape of the THz photoconductivity transients is now discussed.

In each of the following subsections reflection losses of the optical pump pulse, as it enters the sample, are not considered. This allows the charge-carrier dynamics for back and front side excitation to be analysed under identical pump-excitation, without any in-coupling effects. Internal reflections of emitted PL are still considered as part of the ray tracing model.

Additionally, all simulations nominally assume $k_2 = 6.9 \times 10^{-10}\,\mathrm{cm^3\,s^{-1}}$ across both regions of the modelled film and use the simplified model of the mixed 2D/3D perovskite film, developed in Section 7.3.1.

7.5.1 Impact of Charge-Carrier Diffusion

Although the rise in THz photoconductivity has already been attributed to charge-carrier diffusion in Section 7.4, the mechanism behind this rise will now be explained using a set of simulated THz photoconductivity transients, which include different combinations of charge-carrier transport processes. This approach allows the individual effects of charge-carrier diffusion, photon re-absorption and charge-carrier recombination to be understood in isolation from each other. To understand charge-carrier diffusion, the discussion here will focus on the simulations involving charge-carrier diffusion, with and without charge-carrier recombination.

Under Which Circumstances Is There a Rise in THz Photoconductivity? Figure 7.9 shows simulated THz photoconductivity transients for the lowest excitation fluence utilised in OPTP spectroscopy ($1.0\,\mu\mathrm{J\,cm^{-2}}$). The simulations use the same model parameters, but different combinations of charge transport processes are included in each. The blue, orange and black curves in Figure 7.9 represent simulations that all include charge-carrier diffusion and it can be seen that in these cases a rise in THz photoconductivity is seen, when the perovskite film is excited from the back side. Conversely, in the simulations represented by the purple and green curves, which do not account for charge-carrier diffusion, no initial rise in THz photoconductivity can be seen. This is consistent with the dynamical models presented in Section 7.4, where no rise in the simulated THz photoconductivity was seen, except where diffusion was included. Therefore, the rise in THz photoconductivity appears only in simulations where charge-carrier diffusion is accounted for. Additionally, since this rise is seen

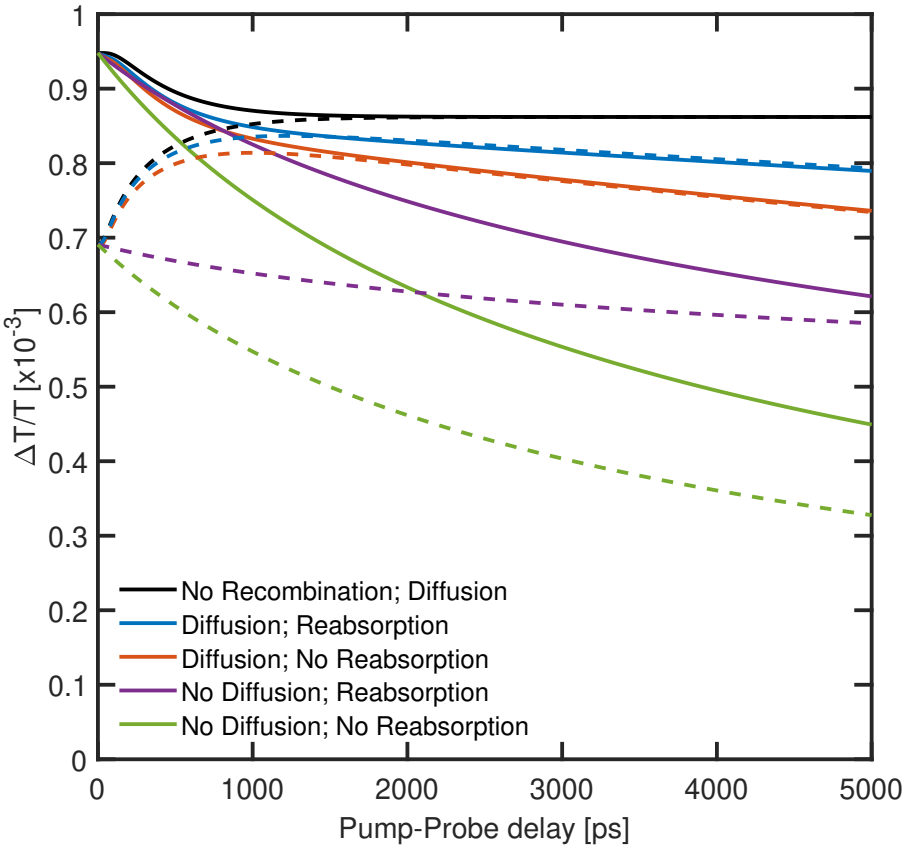


Figure 7.9: Simulated THz photoconductivity transients for the mixed 2D/3D perovskite film, showing the effect of including different combinations of charge-carrier diffusion, photon re-absorption, and recombination in the dynamical model. Solid lines indicate the perovskite film is excited from the front side, while dotted lines indicate excitation from the back side. All simulations are modelled using an incident fluence of $1.0\,\mu J\,cm^{-2}$ and with $k_2 = 6.9 \times 10^{-10}\,cm^3\,s^{-1}$. Reabsorption simulations use heterogeneous PL as described in Section 7.3.1.

in the experimental THz photoconductivity transients, it is clear that diffusion plays some role in the charge-carrier dynamics.

The Cause of the THz Photoconductivity Rise. By considering the charge-carrier dynamics in the absence of recombination, the mechanism behind the THz photoconductivity rise can be more clearly understood. Figure 7.10 shows a simulated THz photoconductivity transient, for excitation from the back side of the sample. The THz photoconductivity is simulated accounting for charge-carrier diffusion, but assuming no recombination (identical to the dotted black line in Figure 7.9). In this case, along

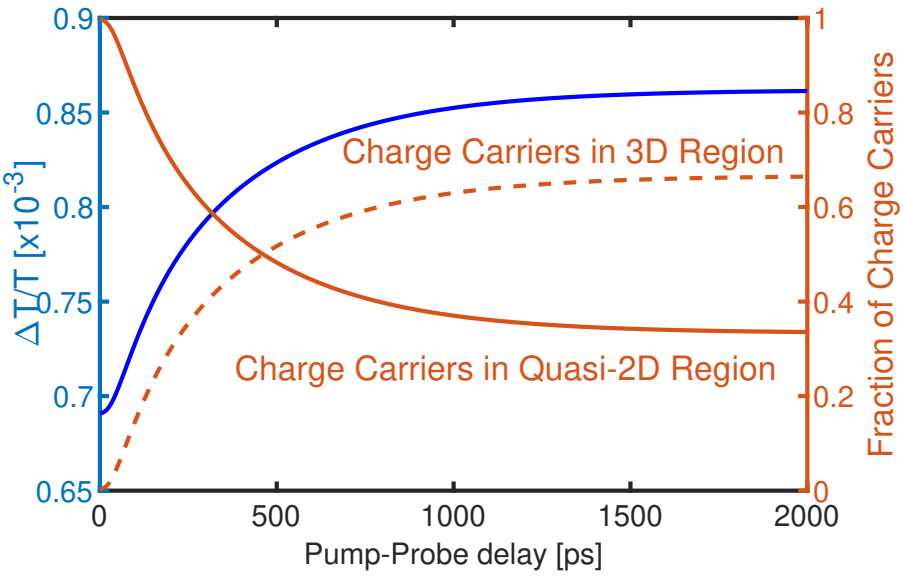


Figure 7.10: Simulated THz photoconductivity transient for excitation from the back of the mixed 2D/3D perovskite film, at an excitation fluence of $1.0\,\mu J\,cm^{-2}$, modelled assuming charge-carrier diffusion and no recombination.. Shown with the fraction of charge carriers present in each region of the model. It can be seen that the increase in THz photoconductivity correlates exactly with the number of charge carriers in the 3D region.

with the simulated THz photoconductivity, the fraction of charge carriers present in each region of the film is also shown. It can be seen that, in parallel with the rise in THz photoconductivity, there is an identical rise in the number of charge carriers which have diffused into the 3D region of the sample. This clearly indicates that diffusion of charge carriers out of the quasi-2D region and into the 3D region is the source of the rise in THz photoconductivity.

The reason that diffusion of charge carriers between the quasi-2D and 3D regions produces a change in THz photoconductivity is that the charge-carrier mobility of the quasi-2D region is lower than that of the 3D region. In an OPTP experiment, the THz photoconductivity produced by a sample is proportional to both the number and mobility of the charge carriers [218]. For the mixed 2D/3D perovskite film, the charge-carrier mobility of the quasi-2D region is less than that of the 3D region. This means that charge carriers in the quasi-2D region produce a smaller THz photoconductivity signal than those in the 3D region. Movement of charge carriers between the two regions, therefore,

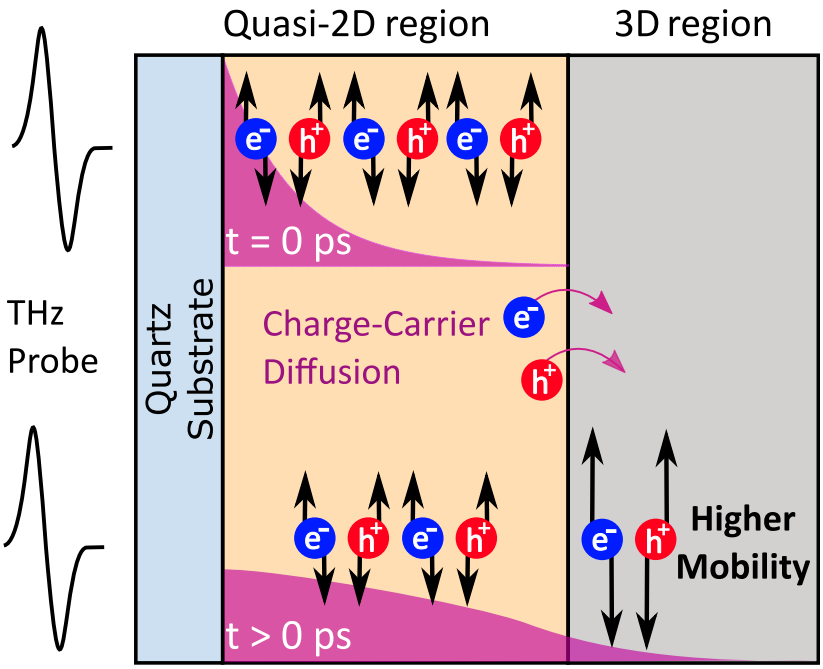


Figure 7.11: Illustration showing how the movement of charge carriers, from the lower charge-carrier mobility quasi-2D region into the higher mobility 3D region, causes an increase in the total THz photoconductivity of the mixed 2D/3D perovskite film.

results in a change in the total THz photoconductivity.

The case where the mixed 2D/3D perovskite film is excited from the back is illustrated in Figure 7.11. Initially, the charge carriers are generated in the quasi-2D region and have a low charge-carrier mobility. However, over time, diffusion causes some of the charge carriers to transfer from the quasi-2D region into the 3D region, raising their mobility. This increase in charge-carrier mobility results in the experimentally measured rise in THz photoconductivity.

Charge-Carrier Diffusion and the Shape of the THz Photoconductivity Transients In the context of the modelled transients in Figure 7.9, the effects of charge-carrier diffusion can now be explained. When the back side of the sample is excited, the initial rise in THz photoconductivity comes from the increase in charge-carrier mobility as diffusion moves charge carriers from the quasi-2D region into the 3D region. This is consistent with previous TA reports of movement of charge carriers into the lower band-gap regions

[60, 235, 236] but now modelled at a device-scale level. This rise is seen only in the simulations involving diffusion, as otherwise the charge carriers are not transferred into the 3D region. The reasons why photon re-absorption cannot cause a similar rise in THz photoconductivity, are discussed in Section C.3.

For the case where the sample is excited from the front, diffusion of charge carriers causes a drop in THz photoconductivity over the first ns, rather than a rise. This is because charge carriers now diffuse from the 3D region to the quasi-2D region, where their mobility is lower. The drop in charge-carrier mobility adds to any recombination losses and gives an initial fast decrease in THz photoconductivity for simulations including diffusion.

By comparing the simulated THz photoconductivity transients for the simulations which account for charge-carrier diffusion and recombination to those where there is no recombination, it can now be seen that much of the change in THz photoconductivity within the first ns is caused by movement of charge carriers between the two regions, rather than by recombination. Distinguishing between the change in THz photoconductivity caused by charge-carrier diffusion and that caused by recombination is important. Otherwise, the charge-carrier recombination rate (k_2) is overestimated when the sample is excited from the front and underestimated when it is excited from the back.

An additional effect of diffusion on the charge-carrier dynamics is the supression of higher-order recombination processes. At the charge-carrier densities being studied, the principal recombination mechanism is bimolecular recombination, the rate of which is proportional to n^2. Initially, as the absorption length of the pump beam is short, the charge carriers are highly concentrated on one side of the perovskite film (depending on the side from which the perovskite was excited). This means that n^2 is large and the rate of bimolecular recombination is initially very fast. However, as diffusion spreads the charge carriers out over more of the film, the average n is reduced, and so the rate of bimolecular recombination slows.

Figure 7.9 shows that when diffusion is omitted from a simulation, charge carriers are lost much faster than when diffusion is included. It can also be seen that the THz photoconductivity transients for back and front excitation rejoin by $\approx 2\,\text{ns}$. This indicates that regardless of which side the perovskite film was excited from, by this time there are now the same number of charge carriers in each region. After the initial charge-carrier distribution has flattened, diffusion plays no further role and the THz photoconductivity transients continue to decay.

Conclusions. In summary, charge-carrier diffusion shapes the THz photoconductivity transients in two ways. Firstly it has been shown that the initial rise in THz photoconductivity, when the samples are excited from the back, is caused by diffusion. As the charge carriers diffuse from a lower to higher mobility, the THz photoconductivity increases, which produces the observed rise, seen experimentally. Without accounting for diffusion there is no way to simulate such a rise in THz photoconductivity. Secondly diffusion also lowers the charge-carrier density, which reduces the amount of bimolecular charge-carrier recombination in the sample.

Accounting for the movement of charge carriers between regions of different charge-carrier mobility gives a clear physical explanation for the rise in THz photoconductivity measured for the mixed 2D/3D perovskite film. This highlights the importance of including charge-carrier movement when modelling their dynamics, as otherwise the shape of the THz photoconductivity transients cannot be understood. The simulations have also shown that, despite the sharp fall in THz photoconductivity when exciting from the front, charge carriers are not being lost, but are still present with a reduced mobility. As the charge carriers have not recombined they could potentially still be extracted. Based on this interpretation of the charge-carrier dynamics, it can be seen

that the rise in THz photoconductivity provides evidence of charge-carrier transfer from the quasi-2D to the 3D region.

7.5.2 Impact of Photon-Reabsorption

Photon-reabsorption refers to a semiconductor's absorption of its own emitted photons, exciting new charge carriers. This process is important in normal 3D perovskite films [132, 133], as it reduces the number of charge carriers lost through radiative recombination. In the mixed 2D/3D perovskite film photon re-absorption is particularly important as the quasi-2D region emits PL above the band-gap of the 3D phase, meaning it will be strongly re-absorbed.

In this section the role of photon re-absorption in the charge-carrier dynamics of the mixed 2D/3D perovskite film is considered. It will be shown that photon re-absorption slows the rate of charge-carrier recombination throughout the entire film. However, it will also be shown that the blue-shifted PL emitted from the quasi-2D region is re-absorbed more strongly than the PL emitted from the 3D region. Separately, in Appendix C, an analytical expression is derived showing the conditions under which photon re-absorption could give a rise in THz photoconductivity.

7.5.2.1 Influence of Photon-Reabsorption on Charge-Carrier Dynamics

In discussing photon re-absorption, the most important factor is how strongly a perovskite film absorbs light at the wavelength where PL is emitted. Stronger absorption will lead to a higher fraction of the emitted photons being recaptured. This excites new charge carriers, effectively slowing the rate of radiative recombination in the perovskite film.

The novel aspect of the mixed 2D/3D perovskite film is that it is composed of two different regions, which are modelled as having two different PL spectra. Although the quasi-2D and 3D regions are simulated as having separate PL spectra, because the 3D phase absorption profile is dominant in Figure 7.3, this absorption spectrum

is taken to apply throughout the perovskite film. This is important, as it means the quasi-2D PL, which is blue-shifted by quantum confinement, is much more strongly re-absorbed than PL emitted by the 3D region.

Here, the effects of photon re-absorption on the charge-carrier dynamics of the mixed 2D/3D perovskite film will be discussed, as two separate points. First, the role of photon re-absorption in slowing the charge-carrier recombination, across the entire perovskite film, is addressed. Secondly, the effect of the enhanced photon re-absorption of the PL emitted from the quasi-2D region is discussed.

As in the analysis of charge-carrier diffusion in Section 7.5.1, the discussion will rely on a set of simulated THz photoconductivity transients, shown in Figure 7.12. The THz photoconductivity transients are simulated for back and front side excitation of the mixed 2D/3D perovskite film, in all cases using the same excitation fluence. Across the different simulations, charge-carrier diffusion, recombination and photon re-absorption are either included in, or omitted from, the dynamical model. This allows the effect of photon re-absorption on the shape of the THz photoconductivity transients to be separated from the effects of charge-carrier diffusion and recombination.

The details of the ray-tracing model used to simulate photon re-absorption are discussed in Section 7.3.3. Unless otherwise specified, the quasi-2D and 3D regions are modelled as having separate PL spectra, termed 'Heterogeneous PL', as described in Section 7.3.1.

Effect one: Reduction in Bimolecular Recombination Losses. The first trend which can be established from Figure 7.12 is that photon re-absorption slows down charge-carrier decay. This trend can be seen in the solid lines shown in Figure 7.12, which are the THz photoconductivity transients for the case where the front side of the sample is excited. It can be seen that compared to the simulation where neither

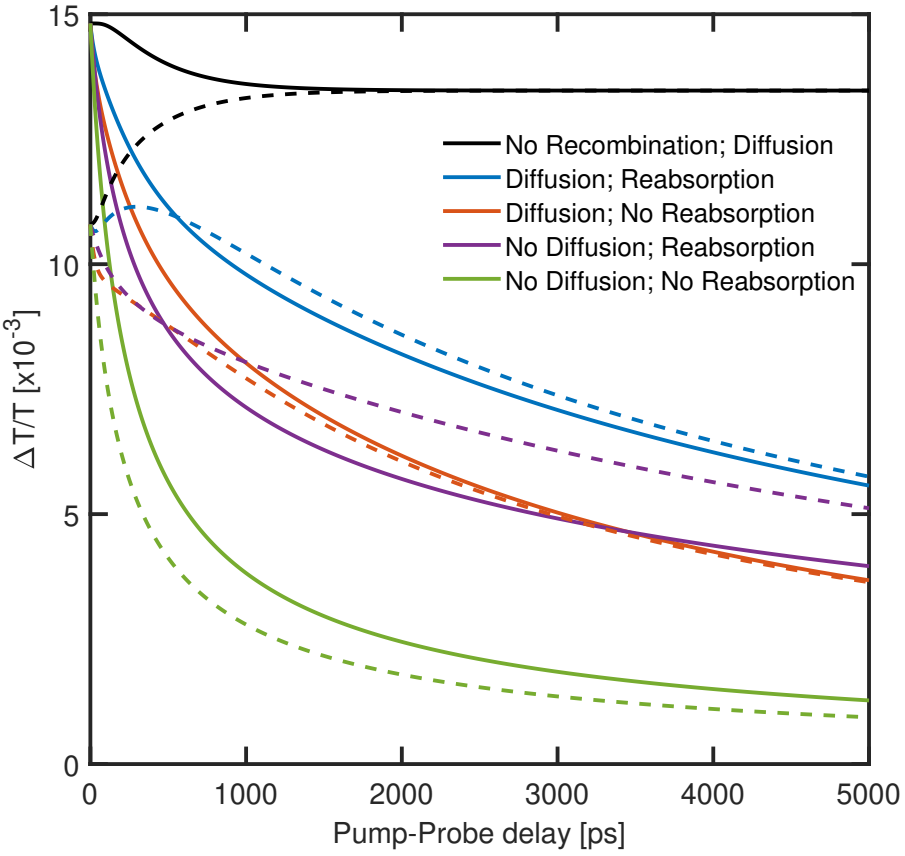


Figure 7.12: Simulated THz photoconductivity transients for the mixed 2D/3D perovskite film, showing the effect of including different combinations of charge-carrier diffusion, photon re-absorption, and recombination in the dynamical model. Solid lines indicate the perovskite film is excited from the front side, while dotted lines indicate excitation from the back side. All simulations are modelled using an incident fluence of $16\,\mu J\,cm^{-2}$ and with $k_2 = 6.9 \times 10^{-10}\,cm^3\,s^{-1}$. Reabsorption simulations use heterogeneous PL as described in Section 7.3.1.

charge-carrier diffusion nor photon re-absorption is accounted for (green lines), adding photon re-absorption to the model (purple lines) drastically slows the decay of THz photoconductivity. The explanation for this is that just as many charge carriers decay as before, however, photon re-absorption causes some of the photons emitted by bimolecular recombination to be recovered again as charge carriers. The suppression of bimolecular recombination by photon re-absorption in a similar fashion has been seen before in MAPI and GaAs [131, 239].

When charge-carrier diffusion is also accounted for, the same slowing down of THz photoconductivity decay is observed, as can be seen from the orange and blue lines in

Figure 7.12. Both simulations account for charge-carrier diffusion, but since the blue line also includes photon re-absorption, it shows a much slower THz photoconductivity decay than the orange line.

Figure 7.12 shows that charge-carrier diffusion and photon re-absorption both act to reduce the decay of charge carriers in the mixed 2D/3D perovskite film. Although charge-carrier diffusion alone can produce the experimentally observed rise in THz photoconductivity, both charge-carrier diffusion and photon re-absorption act to reduce charge-carrier decay and so it is important to consider both processes. Unless photon re-absorption is included in the dynamical model, it will wrongly be concluded that bimolecular recombination is slower than it really is and k_2 will be underestimated [239].

Effect Two: Slower Charge-Carrier Recombination in the Quasi-2D Region. The second and more subtle effect of photon re-absorption is that it causes more charge carriers to be retained if they are excited into the quasi-2D region rather than the 3D region. This effect can be seen in Figure 7.12, where the the dotted lines show THz photoconductivity transients when the back of the sample is excited, while solid lines show front excitation. Although the lower charge-carrier mobility of the quasi-2D region means the THz photoconductivity will initially be lower when the back side of the sample is excited, diffusion of charge carriers should mean that the two lines eventually meet as the charge carriers spread evenly across the sample. However, Figure 7.12 shows that where photon re-absorption is present, the lines cross over and the THz photoconductivity at the end of the simulation is higher for back excitation than front excitation. As the THz photoconductivity is higher when the mixed 2D/3D perovskite film is excited from the back, even after the charge carriers have diffused across the sample, this means that the charge carriers must decay more slowly in the quasi-2D region.

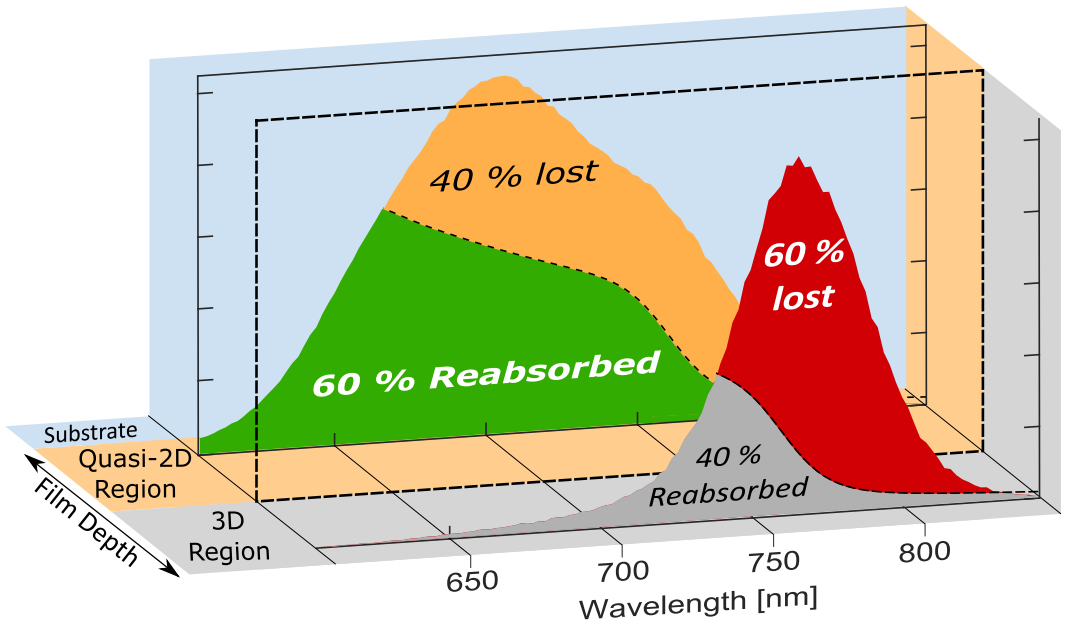


Figure 7.13: An illustration of how the PL emitted from the quasi-2D region is absorbed more strongly by the mixed 2D/3D perovskite film than the PL emitted from the 3D region. PL spectra are taken from Figure 7.6 and reabsorption probabilites are taken from Figure 7.14.

The model has shown that in the quasi-2D region, charge carriers decay more slowly overall; now the mechanism for this slower recombination will be investigated. As the quasi-2D region in the model differs from the 3D region only in charge-carrier mobility and PL spectrum, the higher charge-carrier retention for back side excitation must arise from one or both of these two features. However, the lower mobility of charge carriers in the quasi-2D region will slow down charge-carrier diffusion, resulting in higher charge-carrier densities being present for longer times. If this was the only difference between the two regions, it would, therefore, result in faster bimolecular recombination when the sample is excited from the back, the opposite of what is observed experimentally. This rules out the difference in charge-carrier mobility between the two regions as the cause of the slower charge-carrier recombination in the quasi-2D region.

On the other hand, although having a different PL spectrum will not impact the number of charges recombining, it will cause a difference in how they are re-absorbed. As the quasi-2D PL spectrum is blue-shifted compared to the absorption onset of the

3D phase, the sample will absorb the emission from the quasi-2D region much more strongly than that of the 3D region PL, as shown in Figure 7.13. The protective effect which reduces charge-carrier losses in the quasi-2D region can therefore be attributed to enhanced photon re-absorption of the quasi-2D PL, rather than a charge diffusion effect.

Having identified that the difference in the PL spectrum between the quasi-2D and 3D regions impacts the charge-carrier dynamics, it is helpful to look in detail at what happens to PL emitted from both regions. Figure 7.14 shows what happens to PL which is emitted from each point in the model, as calculated by the ray-tracing model described in Section 7.3.3. The potential fates of an emitted photon are that it will either be absorbed in one of the quasi-2D or 3D regions, or else escape from the perovskite film – by being out-coupled from the sample or lost to scattering processes.

It can be seen that although at least 60% of the light emitted from the quasi-2D region is recaptured by the sample, this number is only 40% for emission from the 3D region. This reflects the higher absorption coefficient of the sample at the quasi-2D PL wavelengths, whereas much of the 3D PL is emitted below the band-gap of the material and so not re-absorbed (see Figure 7.6). As the probability of recapturing a photon emitted from the quasi-2D region is higher, this will mean that over time there will be more charges remaining if the back of the sample is excited, compared with the front.

A further demonstration of how the heterogeneous nature of the sample PL causes slower THz photoconductivity decay can be made by modelling the quasi-2D region as having the same PL spectrum as the 3D region. Figure 7.15 shows THz photoconductivity transients from two simulations, identical except for the simulated PL spectrum used in the quasi-2D region. The 'homogeneous PL' simulation uses the spectrum associated with the 3D phase to model the PL spectrum in both regions of the modelled film. The 'Heterogeneous' case uses the blue shifted PL spectrum, associated with the quasi-2D phase, as the PL spectrum emitted from the quasi-2D region (as described in Section 7.3.1).

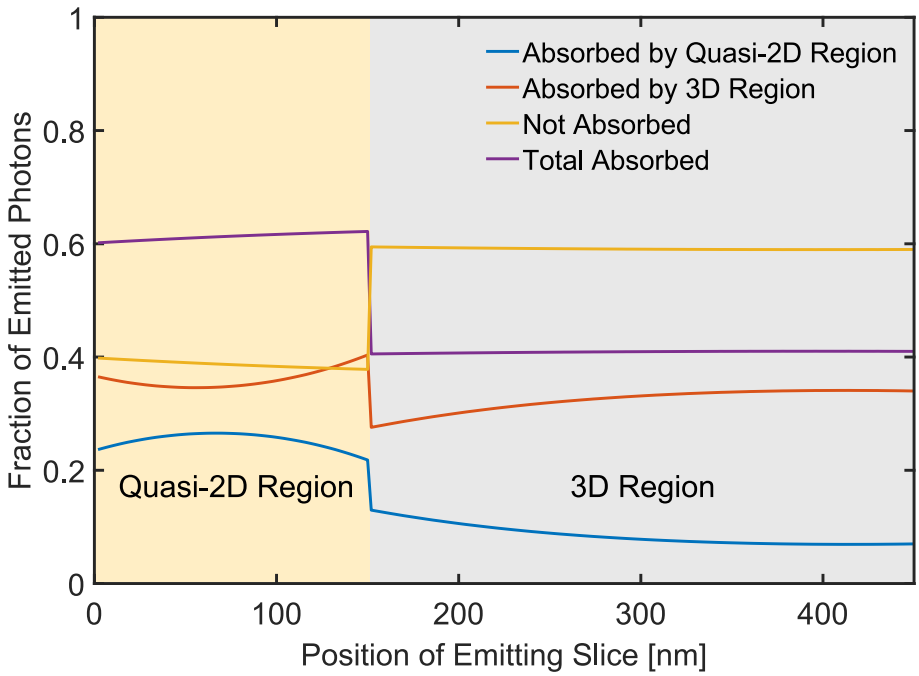


Figure 7.14: The probability of recapturing an emitted photon, calculated using the ray-tracing model in Section 7.3.3, shown as a function of the position of the emitting slice from the substrate. Due to the higher-energy PL spectrum, the probability of photon re-absorption is higher for PL emitted from the quasi-2D region.

.

It can be seen that when the PL is homogeneous across the perovskite film, the two THz photoconductivity transients meet and no advantage is conferred by the presence of the quasi-2D region. Only when the PL is heterogeneous does exciting the back of the sample cause more charge carriers to be retained and the THz photoconductivity transients to cross. This confirms that the crossing of the THz photoconductivity is only caused by the PL spectrum in the quasi-2D region being different.

Conclusions. In summary, it has been shown that the unique composition of the quasi-2D region allows enhanced levels of photon re-absorption. This is because the inclusion of both 2D and 3D domains allows the PL emission to be significantly blue-shifted from the absorption edge and so more strongly recaptured. This enhanced recapture of the quasi-2D PL is especially important, as it has been reported elsewhere [60] that some 2D perovskites can show increased luminosity, compared with 3D perovskites. However, the

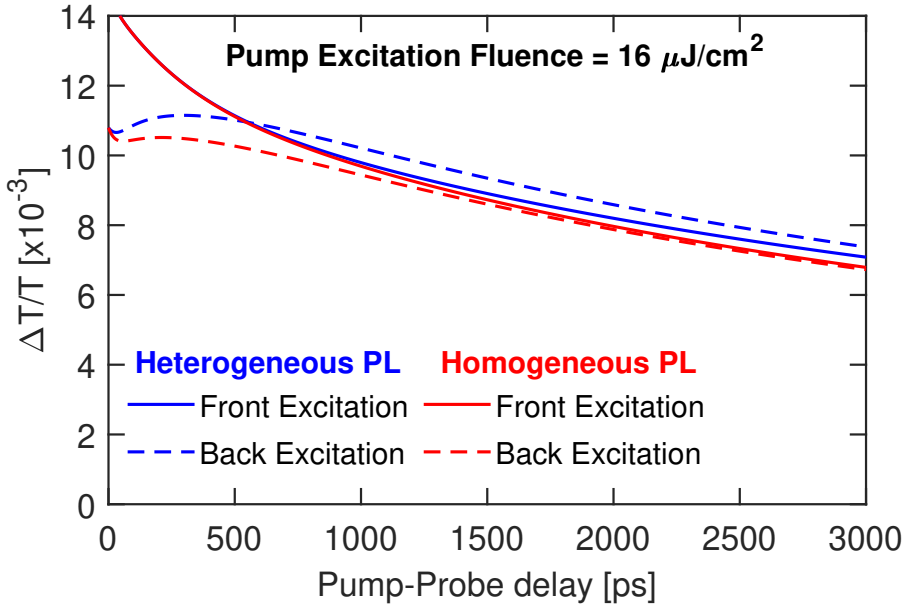


Figure 7.15: Modelled THz photoconductivity transients demonstrating the boost in photon re-absorption caused by the blue-shift of the quasi-2D PL, using $k_2 = 6.9 \times 10^{-10}\,\mathrm{cm^3\,s^{-1}}$. Heterogeneous PL indicates the quasi-2D region and 3D region are modelled with different PL spectra, as described in Section 7.3.1, Homogeneous PL indicates that the spectrum associated with the 3D-phase perovskite is used throughout the whole sample.

enhanced reabsorption of the mixed 2D/3D perovskite film will go some way to offsetting these increased radiative losses, as the surrounding 3D region can efficiently absorb the PL from the 2D material. This more efficient recapture of emitted quasi-2D PL by the surrounding 3D material when the two are mixed together is a useful symbiosis, as it allows the structural stability of the 2D material to be taken advantage of without losing charge carriers to the increased bimolecular recombination rate.

7.5.3 Impact of the Thickness of the Quasi-2D Region

The final model parameter which will be examined is the thickness of the quasi-2D region. Both the rise in THz photoconductivity and the crossing of the transients from back and front excitation, rely on differences in the charge-carrier mobility and PL emission spectra between the two sample regions. Therefore, it is instructive to vary the size of the two regions and see how these trends are affected.

In order to investigate how the thickness of the quasi-2D region will impact the charge-carrier dynamics, a series of simulations is used, where the size of the quasi-2D region is varied. In these simulations, the total width of the sample remains constant at 450 nm, so that as the quasi-2D region increases, the 3D region becomes smaller. The results of the simulations are shown in Figure 7.16, which shows both the modelled THz photoconductivity as well as charge-carrier density. It is helpful to look directly at the charge-carrier density in this case, because as the width of the quasi-2D region decreases, this raises the average charge-carrier mobility of the sample, increasing the THz photoconductivity.

Variation in the Final THz Photoconductivity. From Figure 7.16, one clear trend is that the final THz photoconductivity decreases as the width of the quasi-2D region increases. This drop in THz photoconductivity can be principally explained by a lower average charge-carrier mobility, rather than faster charge-carrier recombination. Comparing the two parts of Figure 7.16, the top panel shows a decrease in THz photoconductivity as the thickness of the quasi-2D region increases. Conversely the bottom panel shows an increase in the number of remaining charge carriers. Therefore, as the quasi-2D region grows thicker, there is no dramatic change in charge-carrier recombination. Instead, the reason for the large change in THz photoconductivity can be explained by the lower mobility of charge carriers in the quasi-2D region. In the simulation the charge carriers will diffuse evenly across the sample, so that when the quasi-2D region is thicker, it holds more of the charge carriers. This moves the final THz photoconductivity closer to the initial value for back excitation, as more charge carriers are in the low mobility quasi-2D region.

Variation in the THz-Photoconductivity Rise. As the thickness of the quasi-2D region increases, THz photoconductivity transients for back excitation can also be seen to

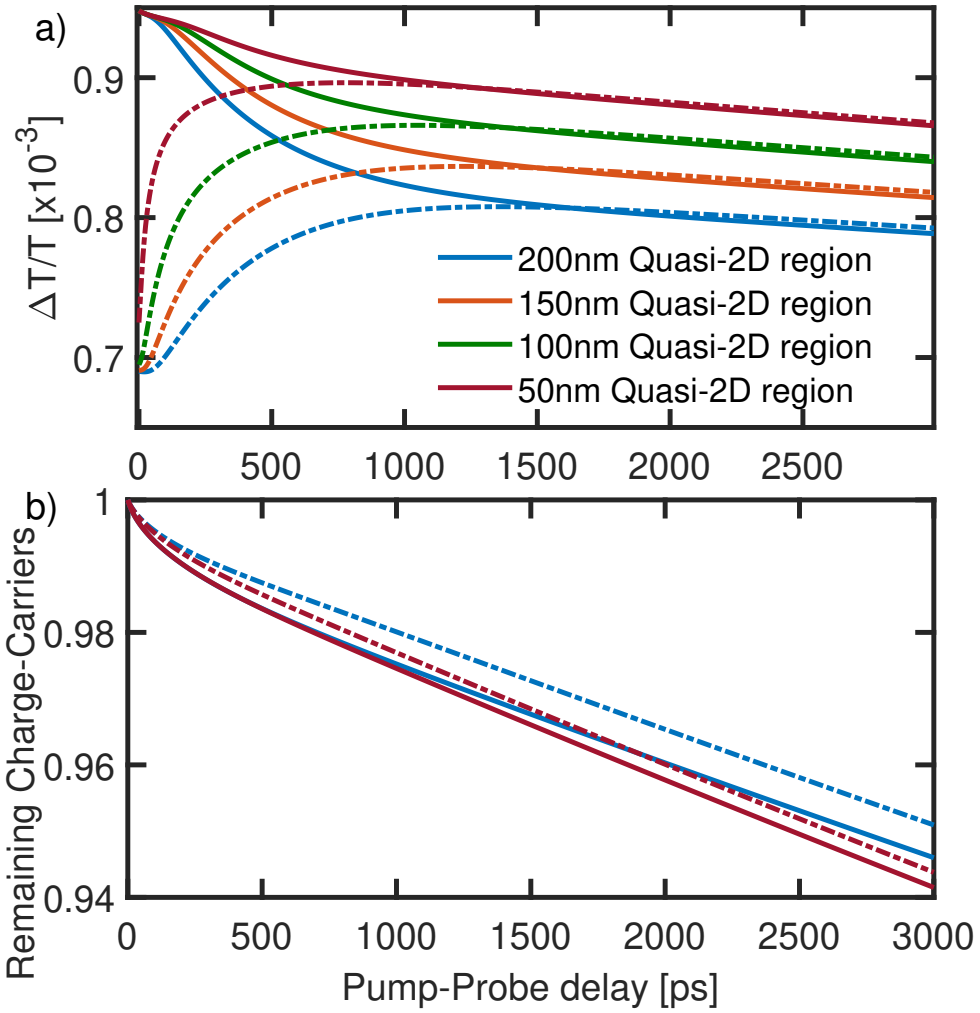


Figure 7.16: (a) THz photoconductivity transients and (b) charge-carrier density, simulated for mixed 2D/3D perovskite films which have quasi-2D regions of different thickness (the total sample thickness in all cases is 450 nm and the charge-carrier mobilities of the 3D and quasi-2D regions remain 23.9 $\mathrm{cm^2\,V^{-1}\,s^{-1}}$ and 17.4 $\mathrm{cm^2\,V^{-1}\,s^{-1}}$, respectively). Solid lines show excitation from the front side of the perovskite film, while dashed lines show excitation from the back side. The PL spectrum of the sample is Heterogeneous as described in Section 7.3.3. In each case the excitation fluence used is 1.0 $\mathrm{\mu J\,cm^{-2}}$ and $k_2 = 6.9 \times 10^{-10}\,\mathrm{cm^3\,s^{-1}}$.

rise more quickly. The THz photoconductivity rise indicates charge carriers diffusing from the quasi-2D region into the 3D region, and increasing in mobility. When the quasi-2D region is thicker, the charge carriers must diffuse further, so take longer to reach the 3D region. This is reflected in the THz photoconductivity transient taking longer to increase as the quasi-2D region becomes thicker. The THz photoconductivity rise can also seen to become less sharp where the width of the quasi-2D region is thicker.

The rise in THz photoconductivity does not only start at earlier times, but is sharper when the quasi-2D region is thinner. The speed of the THz photoconductivity rise reflects the rate at which charge carriers cross between the two regions of the film. This movement of charge carriers into the 3D region is mainly by diffusion, which is faster where the gradient in n is larger. Initially, the gradient in n is large and the charge carriers diffuse quickly through the film. Further into the film, the gradient in n is smaller, so charge-carrier diffusion slows down. When the boundary between the layers is close to the surface, the fast initial spreading out of charge carriers across the film is seen as the sharp rise. However, as the thickness of the quasi-2D region increases, the boundary between the two regions moves deeper into the film. This means that charge-carrier diffusion will have slowed down and the flux of charge carriers into the 3D region is slower, giving a less sharp rise in THz photoconductivity.

The speed and sharpness of the THz photoconductivity rise are linked with charge-carrier diffusion, and can be seen to decrease as the thickness of the quasi-2D region increases.

Variation in Photon Reabsorption. The photon re-absorption related effects are also altered by the width of the quasi-2D region, as this increases the amount of high-energy PL being emitted within the sample. Figure 7.16 shows that when there is a wider quasi-2D region, although the THz photoconductivity transients for the back and front of the sample take longer to cross, the transient for excitation from the back rises higher above the transient for front side excitation. This indicates that the overall decay of charge carriers is slower, when more of the sample is composed of the quasi-2D material. From Figure 7.16(b) it can be seen that indeed more charge carriers are retained when the quasi-2D region is thicker. The difference is particularly pronounced when the sample is excited

from the back. This trend can be explained as, when more of the sample is composed of the quasi-2D material, more of the PL released will be strongly re-absorbed by the sample.

It has been shown that a larger quasi-2D region will allow more of the PL to be reabsorbed more efficiently. However it would not be valid to extend the quasi-2D region indefinitely to allow more efficient photon re-absorption, as this would invalidate the assumption that the emitted PL is absorbed predominately by the 3D-phase perovskite. Instead, it is beyond the scope of the current model to determine the correct fraction of quasi-2D material to include.

7.5.4 Summary

In this section the shape of the simulated THz photoconductivity transients modelled for the mixed 2D/3D perovskite film have been discussed.

Charge-carrier diffusion between regions of different charge-carrier mobility was shown to be the driving force behind the experimentally observed THz photoconductivity rise. Additionally, by spreading out the charge carriers, diffusion also reduces the charge-carrier density and so acts to reduce bimolecular recombination.

Excitation of the back of the sample was demonstrated to result in more charge carriers being retained than when the front is excited. This was linked to increased photon re-absorption of the blue-shifted quasi-2D PL, which is efficiently recaptured by the lower bandgap 3D perovskite. This demonstrates a symbiosis of the quasi-2D and 3D materials. The quasi-2D material provides structural stability and the 3D material strongly reabsorbs the PL emission from the quasi-2D domains.

Finally the thickness of the quasi-2D region was shown to determine the timing, height and sharpness of the rise in THz photoconductivity. A larger quasi-2D region is also predicted by the model to improve photon retention. However, this will be

limited by the necessity of including sufficient 3D perovskite to efficiently recapture emitted PL from the quasi-2D region.

In conclusion, by including charge-carrier diffusion and photon re-absorption in the dynamical model, the charge-carrier dynamics in the mixed 2D/3D perovskite film have been accurately modelled. Both the observed rise in THz photoconductivity, as well as the crossing of the transients for back and front side excitation are reproduced by the dynamical model. The same approach could be used to model other systems which display non-uniform mobilities or PL characteristics. One such candidate system could be a perovskite single-crystal, with a surface region, which has a low charge-carrier mobility, and a higher-mobility bulk region.

7.6 Questions Addressed in this Chapter

Is charge-carrier transfer between the quasi-2D and 3D domains in the mixed 2D/3D perovskite film mediated by charge-carrier diffusion or photon re-absorption?

For the mixed 2D/3D perovskite film studied in this chapter, OPTP spectroscopy and modelling have identified that charge-carrier diffusion dominates transfer between the quasi-2D and 3D domains.

Does the current study provide evidence for charge-carrier transfer from the quasi-2D region into the 3D region and/or from the 3D region into the quasi-2D region?

The THz photoconductivity rise seen when exciting the back of the mixed 2D/3D perovskite film shows charge-carrier transfer from the quasi-2D region into 3D region. Also, a faster THz photoconductivity decay when the front of the perovskite film is excited, indicates some level of charge-carrier transfer in the opposite direction. However, as neither OPTP spectroscopy nor the dynamical model make a distinction between electrons and holes, further work is needed to look into the separate dynamics of each charge carrier.

How do the charge-carrier dynamics in the mixed 2D/3D perovskite film compare with those of regular 3D $MAPbI_3$?

Remarkably, the charge-carrier dynamics of the mixed 2D/3D perovskite film have been described using the same self-absorption model used for the $MAPbI_3$ samples in Chapter 6. In the previous chapter, $k_2^{intrinsic}$ was calculated to be $6.8 \times 10^{-10}\,\mathrm{cm^3\,s^{-1}}$, while for the mixed 2D/3D perovskite film, the average value was $6.9 \times 10^{-10}\,\mathrm{cm^3\,s^{-1}}$, highlighting the intrinsic nature of bimolecular recombination. A key difference in the mixed 2D/3D perovskite film is that, due to the variation in charge-carrier mobility between the two modelled regions, THz photoconductivity can no longer be directly

equated with the number of remaining charge carriers, requiring extra care in the interpretation of the transients.

How does the blue-shifting of the quasi-2D perovskite PL affect the charge-carrier dynamics in these samples?

As the quasi-2D domains have a PL emission spectrum which is blue-shifted with respect to the 3D perovskite absorption onset, photons emitted from quasi-2D domains have a much higher probability of being re-absorbed by the mixed 2D/3D perovskite film. This goes some way towards offsetting the faster radiative recombination typically reported for these materials.

8
Conclusion

In this thesis, a device-scale model of charge-carrier dynamics has been presented and successfully applied to describe the charge-carrier dynamics in both conventional $MAPbI_3$ films and a mixed 2D/3D perovskite film.

Chapter 5 showed an initial demonstration of the new dynamical model (referred to as the self-absorption model), comparing it to previous simulations of charge-carrier dynamics. It was demonstrated that both charge-carrier diffusion and photon re-absorption act to spread charge carriers through the depth of a perovskite film. Since the rate of bimolecular charge-carrier recombination increases quadratically with n, it is slowed down by the spreading out of the charge carriers. Charge-carrier diffusion has a particular significance in the first 500 ps, where it spreads out the initial charge-carrier distribution. Meanwhile photon re-absorption not only slows down the loss of charge carriers to bimolecular recombination, but redistributes charge carriers throughout the entire depth of a perovskite film. Since the inclusion of charge-carrier transport processes so strongly affects the charge-carrier recombination rate of a sample, the chapter also presented a way to quantify the difference in recombination rates which different dynamical models will fit to a given sample. It was shown that a consistent relationship exists between the

bimolecular recombination rates used by the self-absorption model and the dynamical model used by previous studies. Using this relationship, it was shown that, for typical 300-nm $MAPbI_3$ film, photon re-absorption and charge-carrier diffusion cause a reduction in the rate of charge-carrier recombination, equivalent to an order of magnitude decrease in k_2. These findings demonstrate the benefit of considering charge-carrier dynamics on the scale of the whole perovskite film, to more fully understand how the charge-carrier recombination rate changes over the first few ns. Additionally, the insight gained from comparing different modelling approaches is useful for relating previously published values of k_2, with the results determined by the self-absorption model.

In **Chapter 6**, the charge-carrier recombination in a set of $MAPbI_3$ films, with a range of thickness was investigated, demonstrating that re-absorption of emitted photons masks a much higher underlying intrinsic rate of bimolecular recombination of electrons with holes. It was found that such self-absorption is particularly prominent in thick films, where it leads to a pronounced reduction in the apparent bimolecular rate constant associated with the charge-carrier density transients. By accounting for photon re-absorption and charge-carrier diffusion, it was demonstrated that all films share a common intrinsic value of the bimolecular recombination rate constant of $k_2^{intrinsic} = 6.8 \pm 1.4 \times 10^{-10}\,\mathrm{cm^3\,s^{-1}}$, irrespective of film thickness. These results suggest that the wide range of values reported in the literature for $MAPbI_3$ are most likely caused by variations in film thickness and light out-coupling, with the latter resulting e.g. from scattering caused by crystal grains with different nanoscale sizes, or an underlying mesoscopic metal-oxide structure. These findings further link the apparent bimolecular recombination constants perceived in transient spectroscopy with the overall charge-carrier retention strategies achieved through photon management. Since k_2^{apparent} in essence captures the real dynamics of the bimolecular charge-carrier density decay, which includes radiative recombination and photon re-absorption effects, it can serve as an indicator of the extent to which the photon

retention has been achieved. Hence the success of photon management strategies can be conveniently evaluated in a contactless manner by recording spectroscopic transients for full solar cell device structures and comparing extracted values of k_2^{apparent} against the intrinsic value $k_2^{\text{intrinsic}}$ determined here. It was shown that for typical layer structures surrounding lead halide perovskite in a photovoltaic device, photon retention is clearly suppressed, highlighting the need for additional photon management strategies as these devices approach the Shockley-Queisser limit.

Chapter 7 built upon the work of the previous chapter, investigating the charge-carrier dynamics of a mixed 2D/3D perovskite film. It was shown that the blending of quasi-2D and 3D perovskite domains allow the increased stability of quasi-2D perovskite structures to be harnessed, while maintaining the exemplary optoelectronic properties of $MAPbI_3$. By using OPTP spectroscopy, a rise in THz photoconductivity was measured after the back side of the mixed 2D/3D perovskite film, containing a high proportion of quasi-2D domains, was photo-excited. This rise was linked with charge-carrier diffusion out of the quasi-2D domains and into the 3D perovskite, demonstrating that charge carriers do not remain confined in the quasi-2D region but could be extracted from the perovskite layer. It was also shown that quantum confinement in the quasi-2D domains leads to a blue-shift in the PL emission peak, meaning that radiative recombination in quasi-2D domains is efficiently recaptured by the surrounding 3D phase perovskite. In a further validation of the self-absorption model, the average bimolecular recombination rate in the mixed 2D/3D perovskite film was determined to be $6.9 \times 10^{-10}\,\text{cm}^3\,\text{s}^{-1}$, which is extremely close to the value of $6.8 \times 10^{-10}\,\text{cm}^3\,\text{s}^{-1}$ determined in Chapter 6. These findings help explain the success of mixed 2D/3D perovskite films, demonstrating the symbiosis between quasi-2D and 3D domains, with the quasi-2D providing structural stability and the 3D perovskite efficiently harvesting the increased radiative emission from the quasi-2D domains.

Future Outlook. MHP solar cells are still a hot topic for research, in both the 3D and mixed 2D/3D forms. As material processing of perovskite films improves, and extrinsic defects are removed, the bimolecular recombination and photon re-absorption processes discussed in this thesis will become increasingly relevant, even at the lower fluences present in solar cells.

To support this advance, further fundamental studies will be needed to understand the charge-carrier dynamics, particularly in regard to the more complex mixed 2D/3D perovskite films. In this light the dynamical model presented here offers a powerful approach to understanding the ultra-fast charge-carrier recombination and transport in these systems.

In fact, this self-absorption model has recently been used to help unveil the link between the absorption coefficient and bimolecular recombination rate of $MAPbI_3$, in a study led by Dr Chris Davies [15], which demonstrated that bimolecular recombination in $MAPbI_3$ is the inverse of absorption. However, the model could also be applied to determine the intrinsic recombination in different MHPs, or other thin-film semiconductors.

List of Abbreviations

E_B . . . . . Exciton Binding Energy

(J_{sc}) . . . . . Short-circuit Current

k_B . . . . . Boltzmann Constant

L_d . . . . . Charge-Carrier Diffusion Length

n . . . . . Charge-Carrier Density.

$\tilde{n}$ . . . . . Complex Refractive Index ($\tilde{n} = N + i\kappa$)

Θ . . . . . Temperature

R . . . . . Percentage of Reflected Light (in reference to FTIR)

T . . . . . Percentage of Transmitted Light (in reference to FTIR)

1D . . . . . one-dimensional

2D . . . . . two-dimensional

3D . . . . . three-dimensional

Al_2O_3 . . . . . Aluminium Oxide (a.k.a. Alumina)

AM 1.5 . . . . Air Mass 1.5

BBO . . . . . β-Barium Borate (frequency doubling crystal)

CdTe . . . . . Cadmium telluride

CGS . . . . . Centimetre-Gram-Second (system of units)

DFT . . . . . Density Functional Theory.

DSSC . . . . . Dye Sensitised Solar Cell

FSEOS . . . . Free-Space-Electro-Optic Sampling

FWHM . . . . Full width at Half Maximum

ITO . . . . . Indium Tin Oxide

$MAPbI_3$ . . . Methylammonium Lead Iodide

MHP . . . . . Metal Halide Perovskite

ND . . . . . Neutral Density (filter)

NIR . . . . . Near Infra-Red

V_{oc} . . . . . Open-Circuit Voltage

OPTP . . . . . Optical-Pump-Terahertz-Probe (spectroscopy).

PCE . . . . . Power-Conversion Efficiencies

PL . . . . . Photoluminescence.

PTFE . . . . . Polytetrafluoroethylene (a.k.a. Teflon)

PbI_2 . . . . . Lead Iodide

PV . . . . . Photovoltaic

Si . . . . . Silicon

Spiro-OMeTAD 2,2',7,7'-Tetrakis(N,N-di-p-Methoxyphenylamine)-9,9'-Spirobifluorene

SRH . . . . . Shockley Read Hall (recombination)

STEM . . . . . Scanning Transmission Electron Microscope

TA . . . . . Transient Absorption (spectroscopy)

TDTS . . . . . Time-Domain Terahertz Spectroscopy

TiO_2 . . . . . Titanium Oxide

TIR . . . . . Total Internal Reflection

TRMC . . . . Time-Resolved Microwave Conductivity

TRPL . . . . . Time-Resolved Photoluminescence

TRTS . . . . . Time-Resolved Terahertz Spectroscopy

THz . . . . . Terahertz

UML . . . . . Unified Modelling Language

UV . . . . . Ultra Violet

Appendices

A

Supplementary Derivations for Transfer Matrix Formalism

A.1 Supporting Argument for Derivation of Interface Matrix

In Equation 4.8, the claim was made that

$$1 = \tau_{ab}\tau_{ba} - \varrho_{ab}\varrho_{ba}. \tag{A.1}$$

This will now be demonstrated for each polarisation state. for the s polarisation:

$$\varrho_{ab}\varrho_{ba} = \frac{\tilde{n}_a\cos\theta_a - \tilde{n}_b\cos\theta_b}{\tilde{n}_a\cos\theta_a + \tilde{n}_b\cos\theta_b} \times \frac{\tilde{n}_b\cos\theta_b - \tilde{n}_a\cos\theta_a}{\tilde{n}_a\cos\theta_a + \tilde{n}_b\cos\theta_b} \tag{A.2}$$

$$\varrho_{ab}\varrho_{ba} = -\frac{\tilde{n}_a^2\cos^2\theta_a + \tilde{n}_b^2\cos^2\theta_b - 2\tilde{n}_b\tilde{n}_a\cos\theta_a\cos\theta_b}{\left(\tilde{n}_a\cos\theta_a + \tilde{n}_b\cos\theta_b\right)^2} \tag{A.3}$$

$$\tau_{ab}\tau_{ba} - \varrho_{ab}\varrho_{ba} = \frac{4\tilde{n}_b\tilde{n}_a\cos\theta_a\cos\theta_b}{\left(\tilde{n}_a\cos\theta_a + \tilde{n}_b\cos\theta_b\right)^2} \tag{A.4}$$

$$+ \frac{\tilde{n}_a^2\cos^2\theta_a + \tilde{n}_b^2\cos^2\theta_b - 2\tilde{n}_b\tilde{n}_a\cos\theta_a\cos\theta_b}{\left(\tilde{n}_a\cos\theta_a + \tilde{n}_b\cos\theta_b\right)^2} \tag{A.5}$$

$$\tau_{ab}\tau_{ba} - \varrho_{ab}\varrho_{ba} = \frac{\left(\tilde{n}_a\cos\theta_a + \tilde{n}_b\cos\theta_b\right)^2}{\left(\tilde{n}_a\cos\theta_a + \tilde{n}_b\cos\theta_b\right)^2} \tag{A.6}$$

$$\tau_{ab}\tau_{ba} - \varrho_{ab}\varrho_{ba} = 1 \tag{A.7}$$

For the p polarisation:

$$\varrho_{ab}\varrho_{ba} = \frac{\tilde{n}_a\cos\theta_b - \tilde{n}_b\cos\theta_a}{\tilde{n}_a\cos\theta_b + \tilde{n}_b\cos\theta_a} \times \frac{\tilde{n}_b\cos\theta_a - \tilde{n}_a\cos\theta_b}{\tilde{n}_a\cos\theta_b + \tilde{n}_b\cos\theta_a} \tag{A.8}$$

$$\varrho_{ab}\varrho_{ba} = -\frac{\tilde{n}_a^2\cos^2\theta_b + \tilde{n}_b^2\cos^2\theta_a - 2\tilde{n}_b\tilde{n}_a\cos\theta_a\cos\theta_b}{\left(\tilde{n}_a\cos\theta_b + \tilde{n}_b\cos\theta_a\right)^2} \tag{A.9}$$

$$\tau_{ab}\tau_{ba} - \varrho_{ab}\varrho_{ba} = \frac{4\tilde{n}_b\tilde{n}_a\cos\theta_a\cos\theta_b}{\left(\tilde{n}_a\cos\theta_b + \tilde{n}_b\cos\theta_a\right)^2} \tag{A.10}$$

$$+\frac{\tilde{n}_a^2\cos^2\theta_b + \tilde{n}_b^2\cos^2\theta_a - 2\tilde{n}_b\tilde{n}_a\cos\theta_a\cos\theta_b}{\left(\tilde{n}_a\cos\theta_b + \tilde{n}_b\cos\theta_a\right)^2} \tag{A.11}$$

$$\tau_{ab}\tau_{ba} - \varrho_{ab}\varrho_{ba} = \frac{\left(\tilde{n}_a\cos\theta_b + \tilde{n}_b\cos\theta_a\right)^2}{\left(\tilde{n}_a\cos\theta_b + \tilde{n}_b\cos\theta_a\right)^2} \tag{A.12}$$

$$\tau_{ab}\tau_{ba} - \varrho_{ab}\varrho_{ba} = 1 \tag{A.13}$$

A.2 The Inverse of the Interface Matrix

The transfer matrix $W_{a,b}$ shown in the main text shows the transformation of the electric field from the right to left side of the boundary. The transformation of the electric field from left to right is given by the inverse:

$$\det(W) = \frac{1 + \varrho_{ab}\varrho_{ba}}{\tau_{ab}^2} \tag{A.14}$$

using the result, $1 = \tau_{ab}\tau_{ba} - \varrho_{ab}\varrho_{ba}$, from the previous section

$$\det(W) = \frac{\tau_{ab}\tau_{ba}}{\tau_{ab}^2} \tag{A.15}$$

$$\det(W) = \frac{\tau_{ba}}{\tau_{ab}} \tag{A.16}$$

This can then be used to show:

$$W^{-1} = \frac{1}{\det(W)} \times \frac{1}{\tau_{ab}}\begin{pmatrix} 1 & -\varrho_{a,b} \\ \varrho_{b,a} & 1 \end{pmatrix} \tag{A.17}$$

$$W^{-1} = \frac{1}{\tau_{ba}}\begin{pmatrix} 1 & -\varrho_{a,b} \\ \varrho_{b,a} & 1 \end{pmatrix}, \tag{A.18}$$

demonstrating that the matrix $W_{a,b}^{-1} = W_{b,a}$.

A.3 Energy Flow Between Two Lossy Media at Normal Incidence

Assuming the power relations in Section 4.1.3, at normal incidence between two lossy materials the total reflected and transmitted intensity is:

$$I = \mathrm{R} + \mathrm{T} \tag{A.19}$$

$$I = rr^* + tt^* \frac{\tilde{n}_2}{\tilde{n}_1} \tag{A.20}$$

$$= \frac{|\tilde{n}_1|^2 + |\tilde{n}_2|^2 - \tilde{n}_1\tilde{n}_2^* - \tilde{n}_1^*\tilde{n}_2}{|\tilde{n}_1 + \tilde{n}_2|^2} + \frac{2\tilde{n}_1^*\tilde{n}_2}{|\tilde{n}_1 + \tilde{n}_2|^2} \tag{A.21}$$

$$= 1 + \frac{2\tilde{n}_1^*\tilde{n}_2 - 2\tilde{n}_1\tilde{n}_2^*}{|\tilde{n}_1 + \tilde{n}_2|^2} \tag{A.22}$$

$$= 1 + \frac{4i(\kappa_1 N_2 - \kappa_2 N_1)}{|\tilde{n}_1 + \tilde{n}_2|^2} \tag{A.23}$$

$$\implies \mathrm{R} + \mathrm{T} \neq 1 \tag{A.24}$$

B

Supporting Information and Methods for Chapter 6

B.1 Material Preparation

B.1.1 Cleaning of Substrates

Z-cut quartz substrates were cleaned with Hellmanex solution, followed by a rinse with distilled water. The substrate was then twice washed with acetone, isopropanol, and ethanol. Thereafter the substrates were plasma etched in O_2 for 10 minutes. Sample preparation was performed by Dr Jay Patel.

B.1.2 Thermal Co-Evaporation of $MAPbI_3$

Thin films of $MAPbI_3$ were fabricated by Dr Jay Patel using thermal evaporation as reported previously [44]. In brief, the tooling factor was determined by depositing the starting powders, PbI_2 and methylammonium iodide (MAI), separately on glass, then the achieved film thicknesses were measured using a Dektak surface profilometer. MAI was purchased from Oxford Photovoltaics and lead (II) iodide, ultradry 99.999% (metals basis), was purchased from Alfa Aesar. MAI and PbI_2 (500mg of each) were placed in separate crucibles, and the substrates were mounted on a rotating substrate holder to

ensure that a uniform film was deposited. The temperature of the substrates was kept at 21 throughout the deposition. The chamber was allowed to reach a high vacuum (10^{-6} mbar), before the PbI_2 and the MAI were heated to reach a deposition rate of $0.4\,\text{Å}s^{-1}$. Once the deposition rate had stabilized along with the pressure (3×10^{-6} mbar), the substrates were exposed to the vapour. The rates of both MAI and PbI_2 deposition were monitored using a quartz crystal microbalance (QCM). The final deposition rate was $0.8\,\text{Å}s^{-1}$. The thickness of the samples was controlled by varying the exposure time of the substrates to the vapour. Thereafter the thicknesses of the films were accurately determined by using a Dektak surface profilometer, an FTIR transfer matrix method, and by capturing scanning electron microscopy images of the cross sections as detailed below.

B.2 Initial Material Characterisation

B.2.1 Scanning Electron Microscopy

B.2.1.1 Sample Preparation

Samples for scanning electron microscopy (SEM) were prepared[1] on a quartz substrate as detailed above. All samples were cleaned using a nitrogen gun, and a sputter coater was used to deposit a 3 nm coating of platinum to improve conductivity. Carbon tape was applied to secure the samples and prevent charge build-up by further increasing the conductivity. Samples for cross-sectional SEM were cleaved in two halves, using a diamond scribe, before the deposition of the platinum.

B.2.1.2 Experimental Details and Results

A Hitachi S-4300 scanning electron microscope with an accelerating voltage of 3 keV was used to capture cross-sectional and top view images of the samples, as shown in Figure B.1. The top view images show a slight increase in the grain size with thickness, but this is a very weak trend, and the average grain size remains ∼100 nm. This demonstrates that each of the samples share a similar surface morphology, with no evidence of any significant trend with thickness. The large-scale images (Figures B.1(h) & (i)) highlight the homogeneity of the films across several microns. This high degree of uniformity enables us to define a single film thickness across the full extent of the sample. This uniformity is further shown in the cross-sectional images displayed in Figures B.1(j), (k) and (l), which confirm the consistency of the film thickness across the substrate.

[1] Dr Jay Patel assisted with SEM sample preparation and image acquisition.

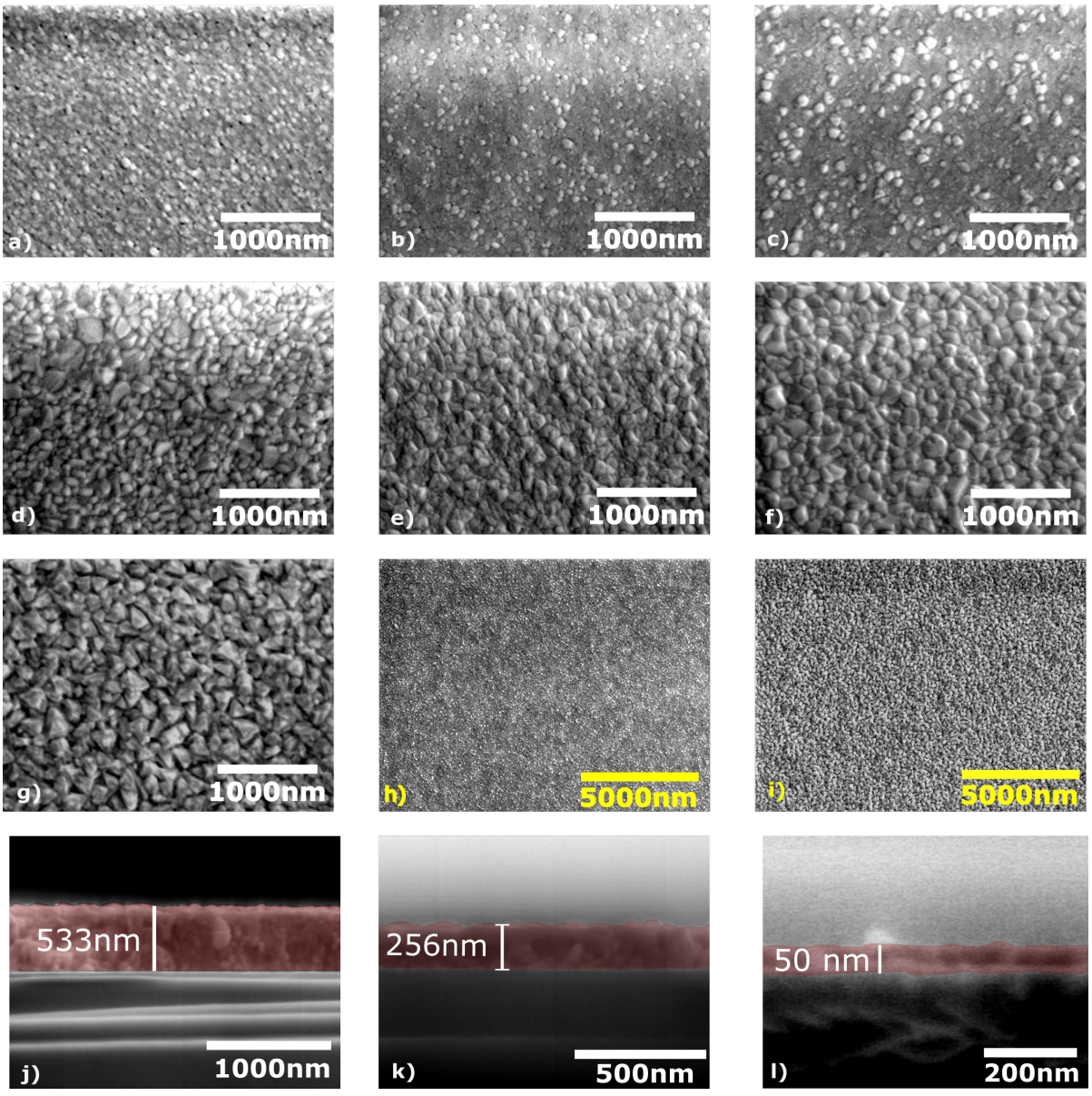
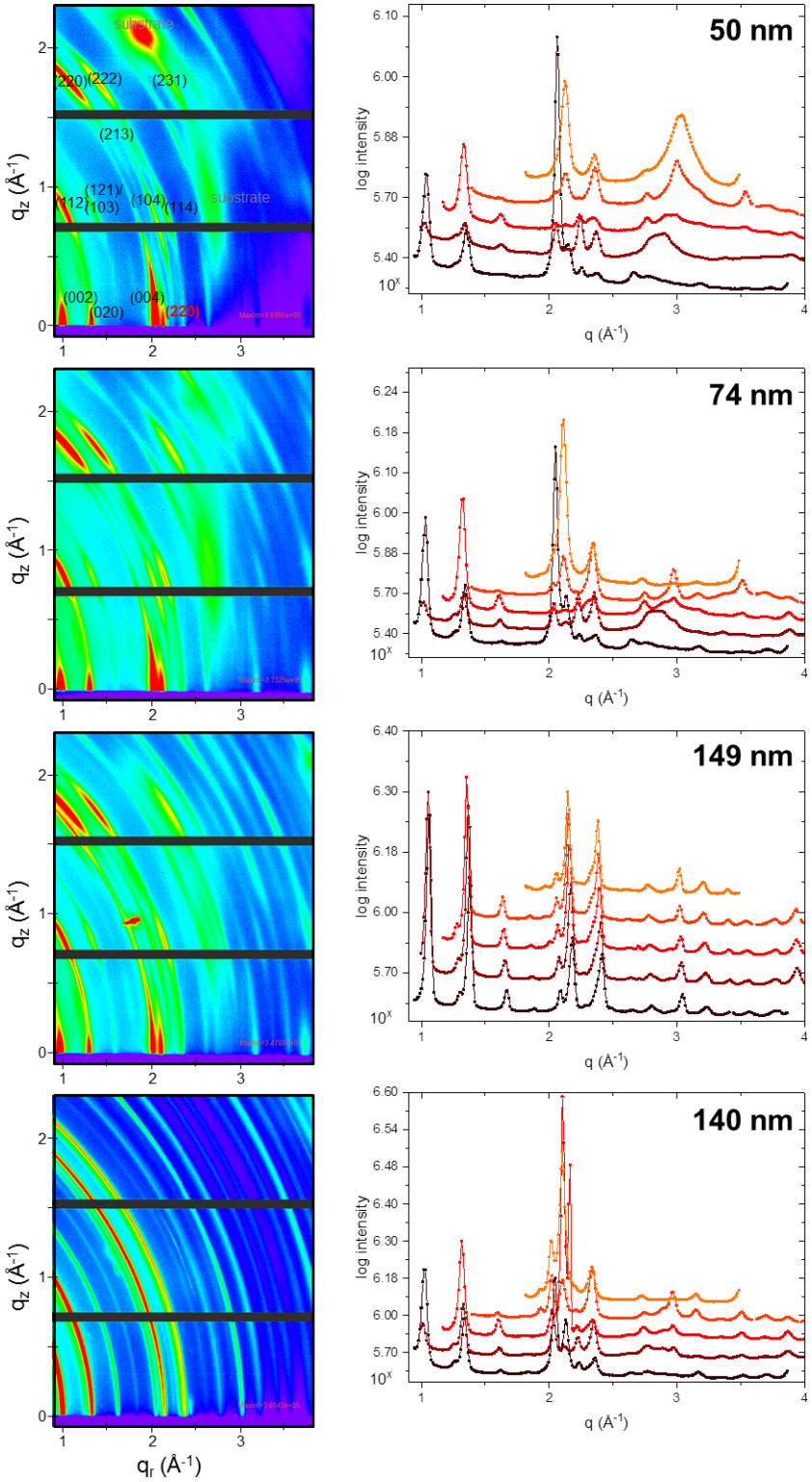


Figure B.1: Scanning electron microscope images of samples showing ×35 000 magnification for films of thickness (a) 50 nm (b) 74 nm (c) 150 nm (d) 140 nm (e) 256 nm (f) 295 nm (g) 534 nm as well as ×8 000 magnification for (h) 50 nm and (i) 534 nm thick films. The images (j) - (l) show cross sectional images of films whose thickness is indicated by the labels. Images taken with assistance from Dr Jay Patel

B.2.2 Grazing Incidence Wide Angle X-Ray Scattering (GIWAXS)

Johannes Schlipf and Peter Müller-Buschbaum, from the Physics department of the Technische Universitat München, performed the grazing-incidence wide angle X-ray scattering (GIWAXS) measurements. GIWAXS probes length scales in the crystallographic range. Random crystal orientation produces Debye-Scherrer rings with equal intensity distribution. For oriented samples higher intensities are visible depending on the orientation of the specific crystal plane. GIWAXS measurements were conducted at the beamline P03 of the German Electron-Synchrotron (DESY), Hamburg. The beam energy was 13 keV, the incident angle 0.4° and the sample-detector distance 279.6 mm. The raw detector images taken with a Pilatus 300k pixel detector are reduced and corrected with the software Igor Pro. For evaluation of crystal orientation we take five sector cuts and integrate the intensity over the azimuthal angle. The 2D GIWAXS patterns with corresponding sector cuts are shown in Figure S2, with the full treatment of the GIWAXS data being as previously reported[217, 240].

Some samples show a high degree of crystal orientation, e.g. for film thicknesses of 50 nm, 74 nm and 149 nm. The presence of the (220) reflections at two positions shows that two preferred orientations are present, respectively with the (002) and the (200) planes parallel to the substrate which is also apparent from different peak intensities in the sector cuts. Dominant is the (200) orientation. On the other hand, samples 140 nm and 295 nm do not show any preferred crystal orientations.


substrate
(220)
(222)
(231)
(213)
(121)/
(112)
(103)
(104)
(114)
substrate
(002)
(020)
(004)
(220)
qz (Å-1)
qr (Å-1)
log intensity
q (Å-1)
50 nm
74 nm
149 nm
140 nm

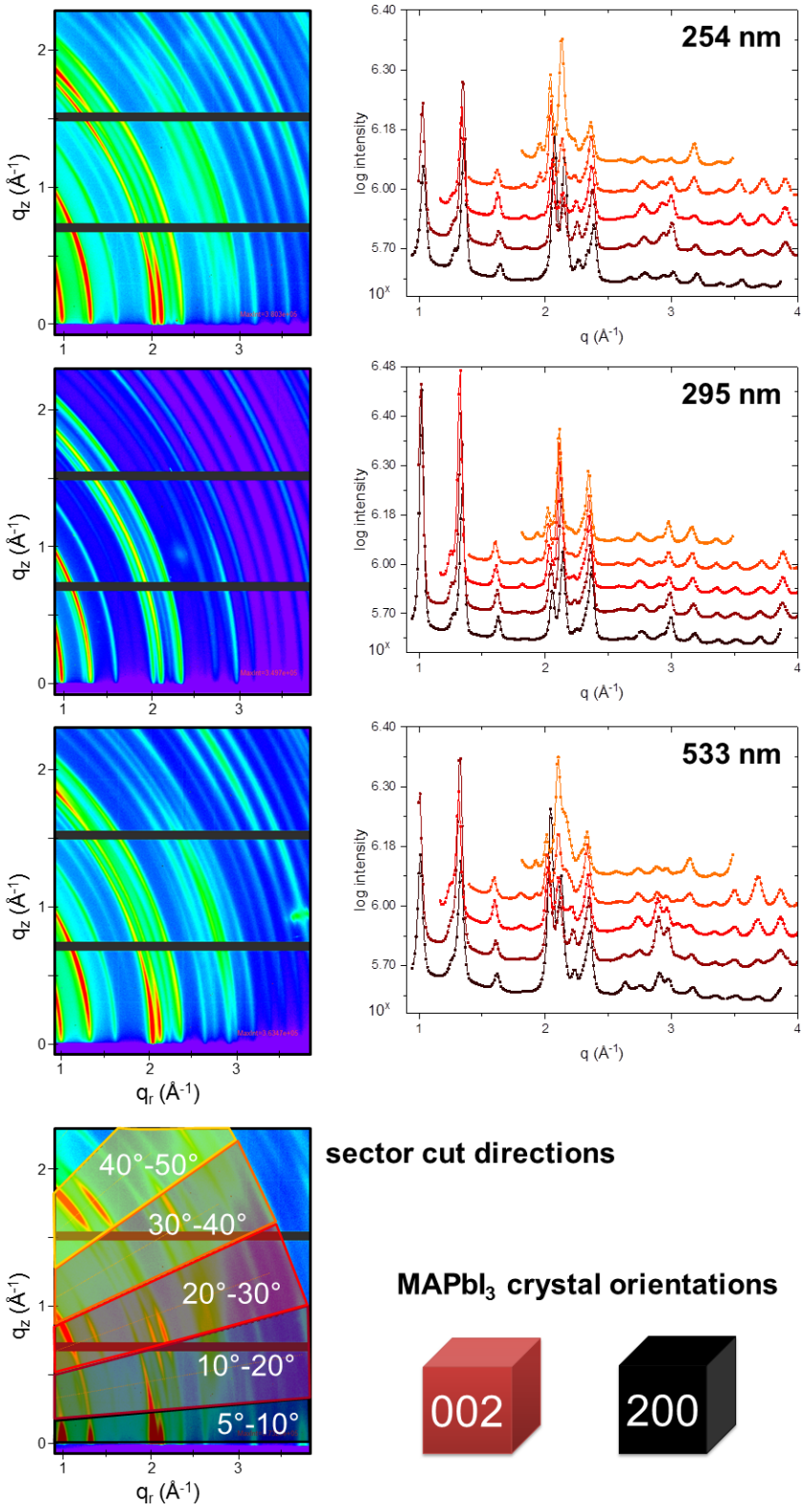


Figure B.2: Grazing incidence wide angle x-ray scattering patterns and sector cuts for each sample. The results show slight variations in crystal orientation across the samples, however this does not follow any trend with thickness. Taken by Johannes Schlipf and Peter Müller-Buschbaum.

B.3 Photoluminescence Spectra

The externally measured PL spectra collected for each of the samples are shown in Figure(S3)b, where a clear red-shift in the centre wavelength of the emitted PL with increasing film thickness can be observed. This red-shift arises because PL typically has to travel further to escape thicker films, meaning the shorter wavelength components will be attenuated more strongly, and the external PL peak is red-shifted.

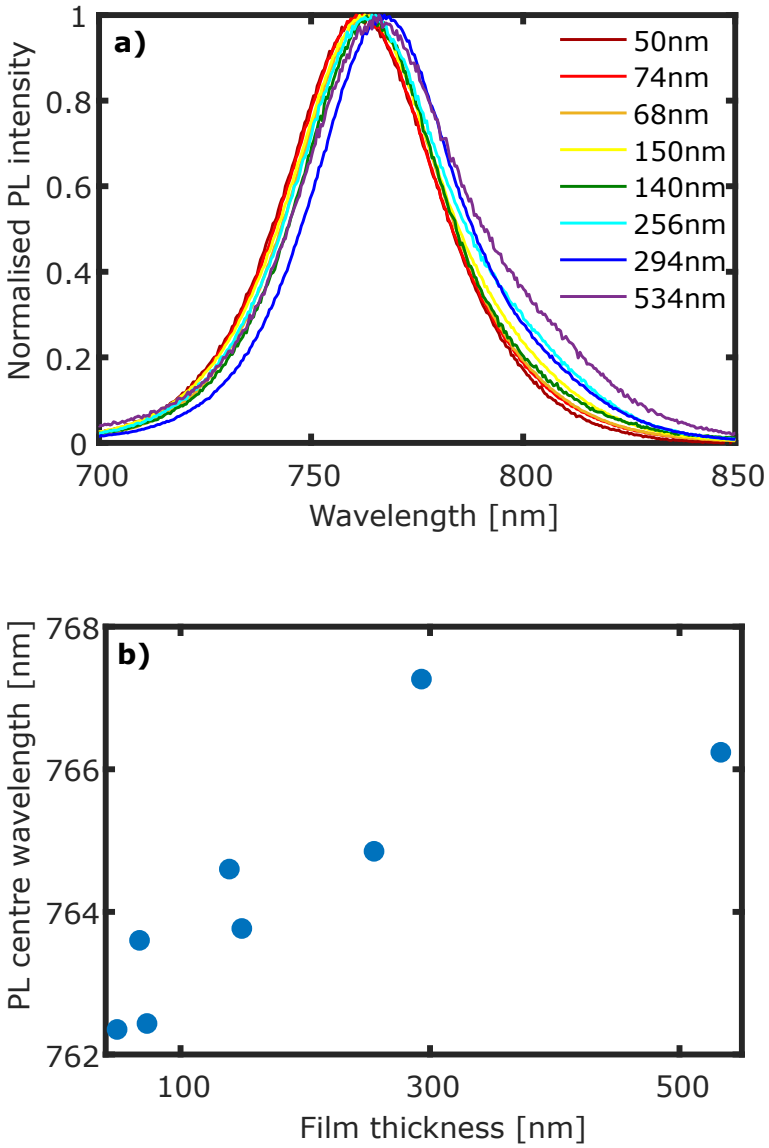


Figure B.3: (a) Photoluminescence spectra obtained for each sample whose film thicknesses are indicated in the legend. Excitation was provided by a 400-nm picosecond pulsed laser diode (PicoHarp LDH-D-C-405M), and the emitted PL spectra was collected using a Princeton Instruments SP-2558 grating spectrometer and a PI-MAX4 Princeton Instruments iCCD. (b) Variation in centre wavelength of the PL spectra as a function of film thickness. Data was collected by Elizabeth Parrott.

B.4 FTIR

B.4.1 FTIR Transfer Matrix Model

The complex refractive index, $\tilde{n} = N + i\kappa$, of each sample was determined using the generalised transfer matrix approach described in Section 4.1 The model determines the R and T from the combined film and substrate system, accounting for coherent multiple reflections within the perovskite layer (50-530 nm thick), and incoherent reflections from the quartz substrate (2 mm thick). As the reflections within the perovskite are coherent, the reflected and transmitted intensities are highly sensitive to the film thickness. This allows the model to determine the thickness of the perovskite layer, as discussed below.

B.4.2 Extraction of Quartz Complex Refractive Index

The transfer matrix model was first used to extract the complex refractive index, N_{qu}, of the quartz substrate. By fitting the model to the experimentally obtained R and T for a blank quartz substrate, n_{qu} and κ_{qu} were extracted, as shown in Figure B.4. The transfer matrix model fits the data well across the whole wavelength range, and the extracted value of refractive index is as expected for quartz. This value for $\tilde{n}_{qu}$ was then used for the substrate when the properties of each perovskite layer were extracted.

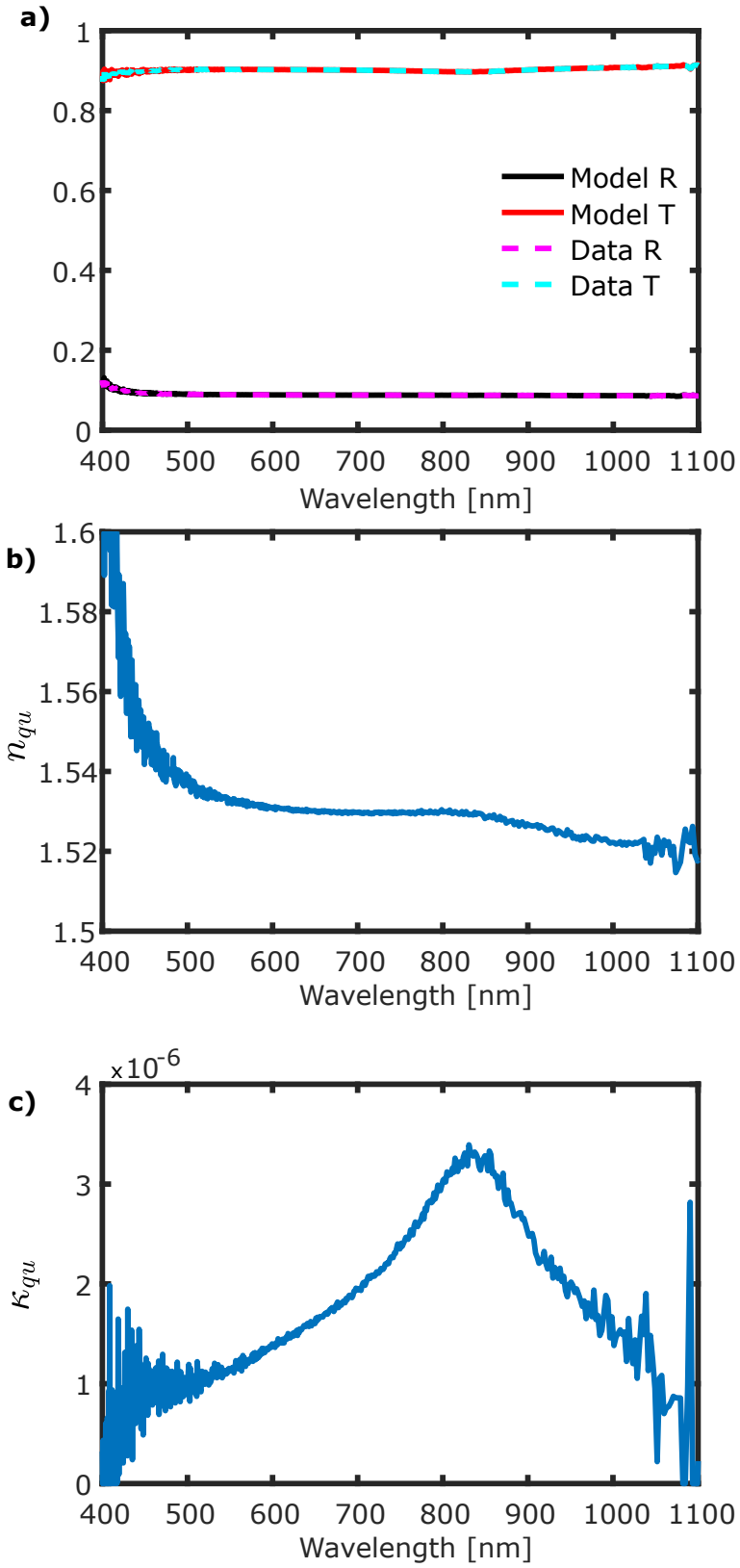


Figure B.4: (a) Fits of transfer matrix model to the experimental R and T data for a blank quartz substrate. The real and imaginary parts of the extracted complex refractive index are shown in (b) and (c), respectively.

B.4.3 Extraction of Perovskite Complex Refractive Index

With the complex refractive index for the quartz substrate determined, the transfer matrix model was then applied to the perovskite layer. As reflections within the perovskite layer are coherent, the model is highly sensitive to the film thickness. This means that both the thickness and complex refractive index $\tilde{n}_{per}$ of each sample can be determined. Initial estimates of film thickness were obtained from a Dektak 150 surface profilometer, these values were then refined by the transfer matrix model, with the results shown in Table B.1. Comparing the two measurements, there is a strong agreement between the DekTak and transfer matrix model, both of which differ in several cases from the thickness predicted by the quartz crystal microbalance (QCM) during evaporation. The values determined by the DekTak and transfer matrix model are also in agreement with the SEM cross-sections in Section B.2.1.2, suggesting the error is in the QCM prediction. The QCM thickness estimates provide only a rough guide to film thickness based on the evaporation protocol for a 300-nm thick film, so it acceptable that this should disagree with the actual direct measurements of film thickness. Throughout this study, the sample thickness is taken to be that extracted by our FTIR transfer matrix model (shown in bold in Table B.1) as this is the method most sensitive to the sample thickness.

The fits of the transfer matrix model to the experimental R and T values for each sample are shown in Figure B.5, where it can be seen that the model provides a good fit to the data. For the model to accurately fit the data, it is important that the thickness is highly uniform, as a variation in sample thickness will result in a range of interference patterns in the overall sample R and T. Therefore, the close agreement between the

QCM Nominal thickness [nm]	45	60	110	150	220	300	400
Dektak profilometer thickness [nm]	60	80	152	144	274	310	540
Thickness from fit to R, T data [nm]	**50**	**74**	**149**	**140**	**256**	**295**	**533**

Table B.1: Perovskite film thickness for each sample as determined by determined by different methods

data and the transfer matrix model highlights the highly planar nature of these vapour-deposited samples. The samples also display minimal scattering as shown by the very weak absorption below the bandgap, discussed further in Section B.4.5.

Figure B.6 shows the extracted values of κ_{per} and n_{per} for each sample, as well as the average of the entire sample set. Our samples all have very similar refractive indices and absorption coefficients, α, showing that the absorption coefficient spectra of the samples display no dependence on film thickness. At shorter wavelengths, the thicker films do not transmit sufficient light, making the extraction of the refractive index less accurate, however, to model self-absorption we only require a knowledge of N_{per} at the PL wavelengths.

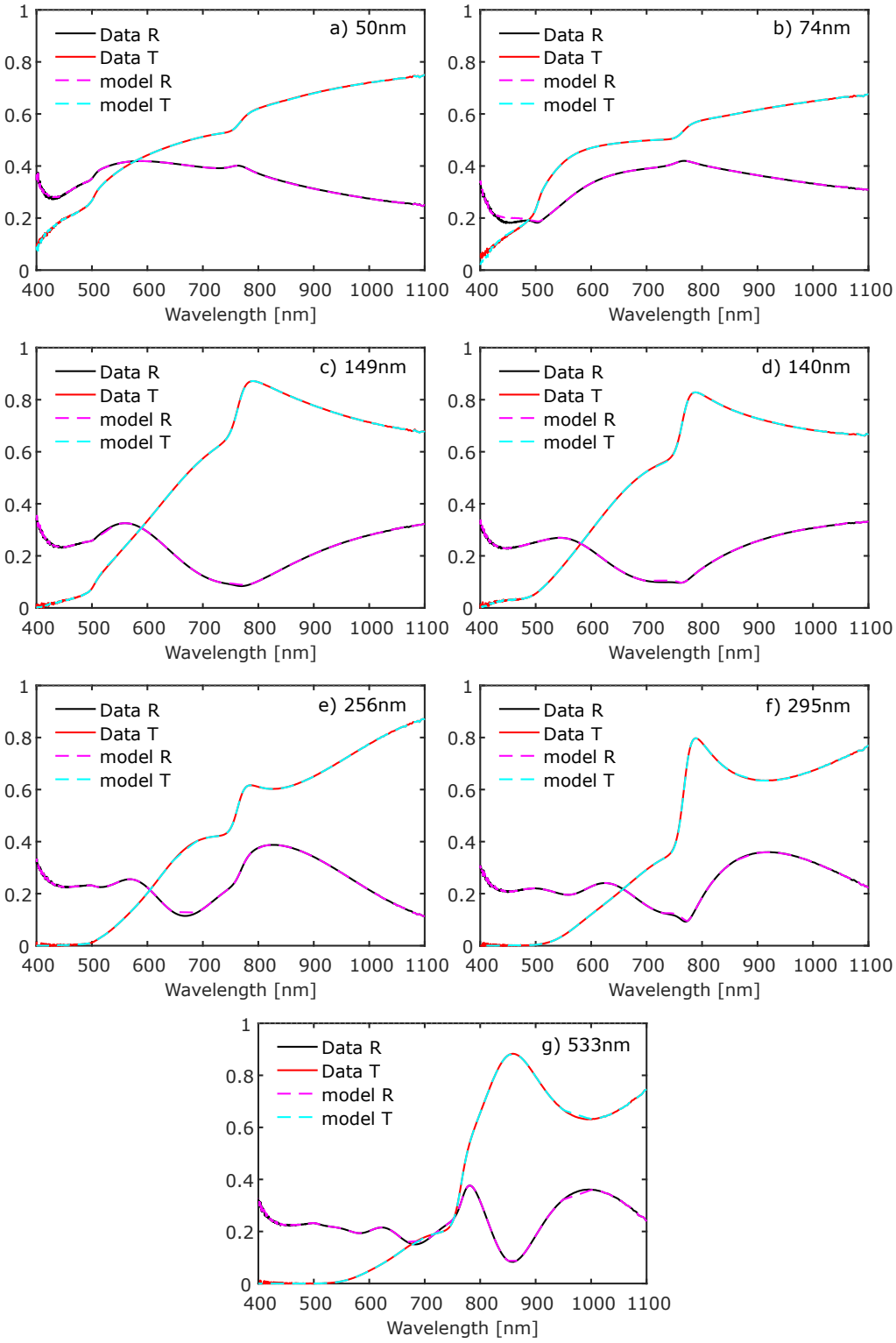


Figure B.5: Individual fits of the transfer matrix model to the experimentally measured R and T of each perovskite sample.

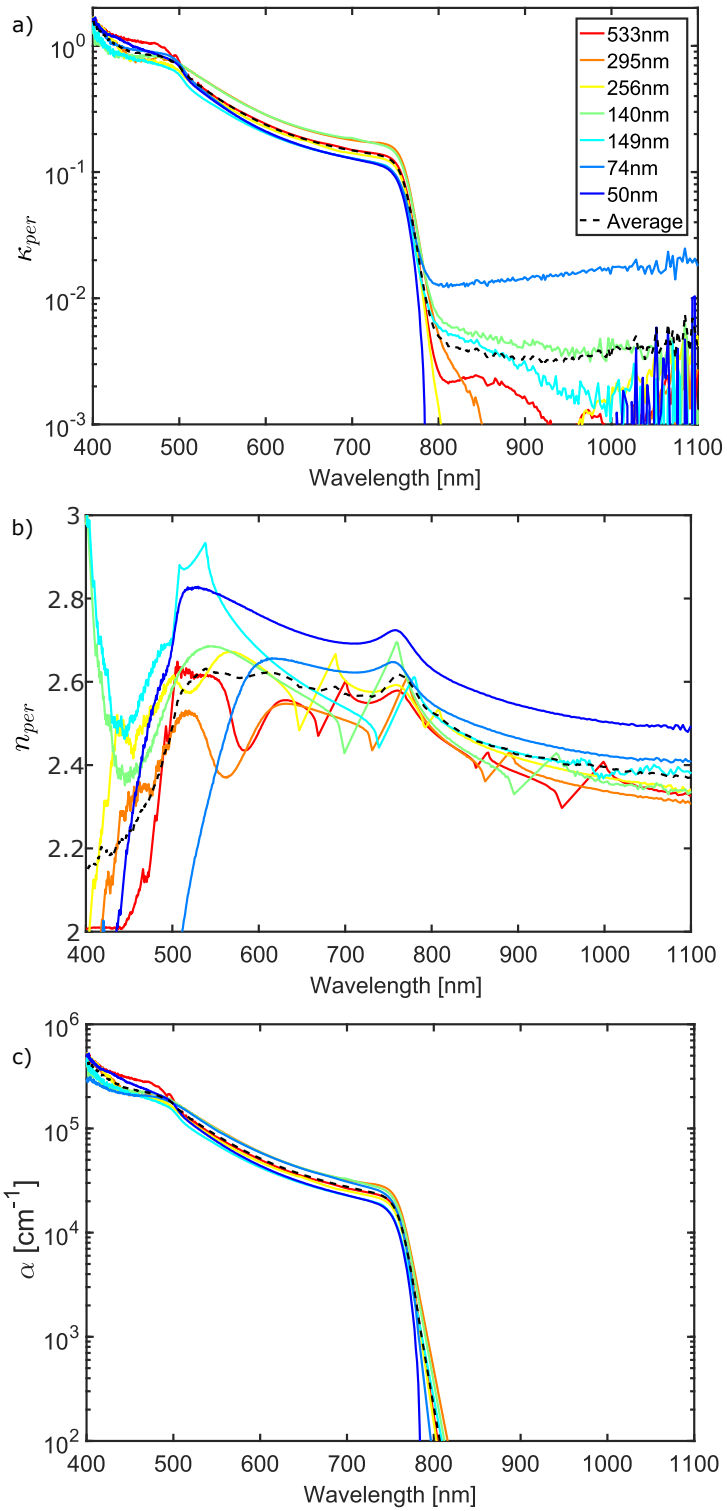


Figure B.6: Extracted parameters for the complex refractive index of each of the perovskite samples using a transfer matrix model. (a) and (b) show the imaginary and real elements of the refractive index as directly extracted from the model. (c) shows the absorption coefficient, $\alpha = (4\pi\kappa)/\lambda$, corrected for scattering, as discussed in Section B.4.5.

B.4.4 Comparison of Methods Used to Extract Absorption Coefficient

The absorption coefficient, α, of the perovskite samples has been calculated here using a transfer matrix method, but another common technique is to determine α from the optical density (OD). This approach uses Beer's law and the fractions of light transmitted and reflected by the sample to obtain:

$$\alpha = -\frac{1}{d}\ln(\frac{T}{1-R}), \tag{B.1}$$

where d is the film thickness. Figure B.7 compares the raw value of α determined by each approach, before any corrections are applied. It can be seen that the two methods produce a very similar absorption spectrum, however, there are some differences, particularly at the absorption edge where the transfer matrix method provides a clearer rise in α. One reason for this disagreement is that the OD method produces an effective α for the combined perovskite and substrate stack, whereas the transfer matrix method accounts for the effect of the substrate and isolates the absorption of the perovskite layer. When the absorption of the perovskite is strong, very little light is transmitted through the film and there is little effect from the substrate. However, at the absorption edge, or in thinner films, the absorption is weaker and multiple reflections from the substrate are more significant. This leads to the differences in the absorption spectra produced by each approach, shown in Figure B.7, which are most clearly seen in the 50 nm film. For this reason, the transfer matrix method is employed in this study to decouple the effect of the substrate from that of the film, and obtain α, independent of any substrate effects.

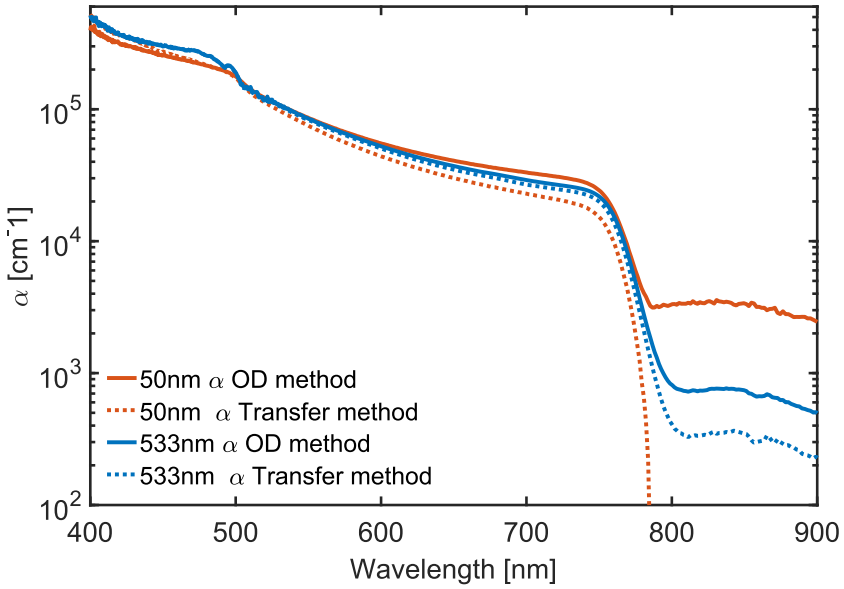


Figure B.7: Comparison of absorption coefficient spectrum extracted using the transfer matrix approach to that produced by using the optical density method of Equation B.1, for both a thick and a thin film. All data are shown without correction for scattering.

B.4.5 Correction of Absorption Data for Scattering

The raw absorption data in Figure B.6(a) contains contributions from both scattering and absorption, as the FTIR could only detect coherent transmission or reflection from a sample. This means scattered light will not be detected, and is not directly distinguished from actual absorption. As this light is not actually absorbed by the perovskite to produce charge-carriers, it is important to differentiate scattering and absorption when modelling self-absorption.

The two processes are separated by assuming that the absorption below the bandgap arises only from scattering, and taking the average α in this region to be the strength of scattering in the sample. The samples all displayed very low levels of scattering, occurring on a length scale of $1/\alpha_{scatter} \approx 20\,\mu$m for the most strongly scattering sample, much longer than the absorption lengths of a few hundred nanometers typical for the PL. In relation to the ray tracing model (Section 4.2.3) this means that most of the self-absorption takes place on a length scale where scattering can be discounted. However,

the scattering length scale of 20 µm is used as an upper limit on the coherent propagation distance of PL within the samples.

To extract a scattering-corrected absorption spectrum, the average below band-gap scattering amplitude was first subtracted from the raw absorption spectrum. This process produces the corrected α (Figure B.6(c)), which are then used in the ray tracing model, described in Section 4.2.3.

B.5 THz Spectroscopy

B.5.1 THz Mobility

The charge carrier mobility as a function of thickness is shown in Figure B.8. It can be seen that although there is a spread in values, there is no systematic variation with film thickness.

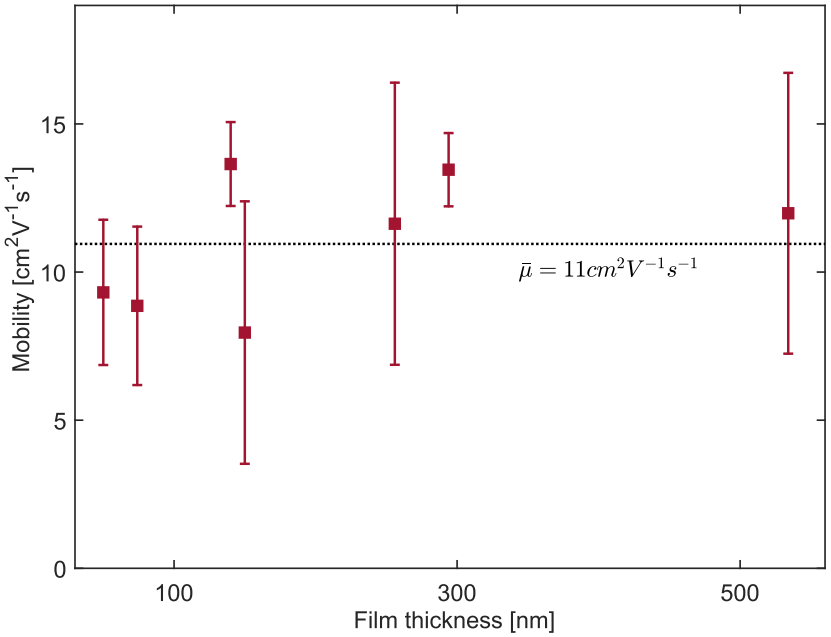


Figure B.8: Charge-carrier mobility shown against $MAPbI_3$ film thickness determined using OPTP spectroscopy as described in Section 3.2.3.

B.5.2 Global Fits to Photoconductivity Transients

The intrinsic bimolecular recombination constant $k_2^{intrinsic}$ was determined by global fits of the Self-Absorption Model to the OPTP photo-conductivity decays for each sample. The monomolecular decay was too slow to be noticeable within the 2.5-ns time window of the experiment, and so was fixed at $1 \times 10^{-7}\,\mathrm{s}^{-1}$. Additionally, from the modelling in Chapter 5 it was determined that the fluences used were too low to result in noticeable contributions from Auger recombination, so k_3 was also fixed at zero. A set of photo-conductivity decays for excitation fluences in the range 6.6 to $45\,\mu\mathrm{J\,cm}^{-2}$ were globally

fitted to provide an optimised value of $k_2^{intrinsic}$ for each sample, using the self-absorption model. The fits associated with the self-absorption model to the photo-conductivity transients of each sample are shown in Figure B.9. Also shown is the variation in $k_2^{intrinsic}$ with film thickness, as determined by the self-absorption model.

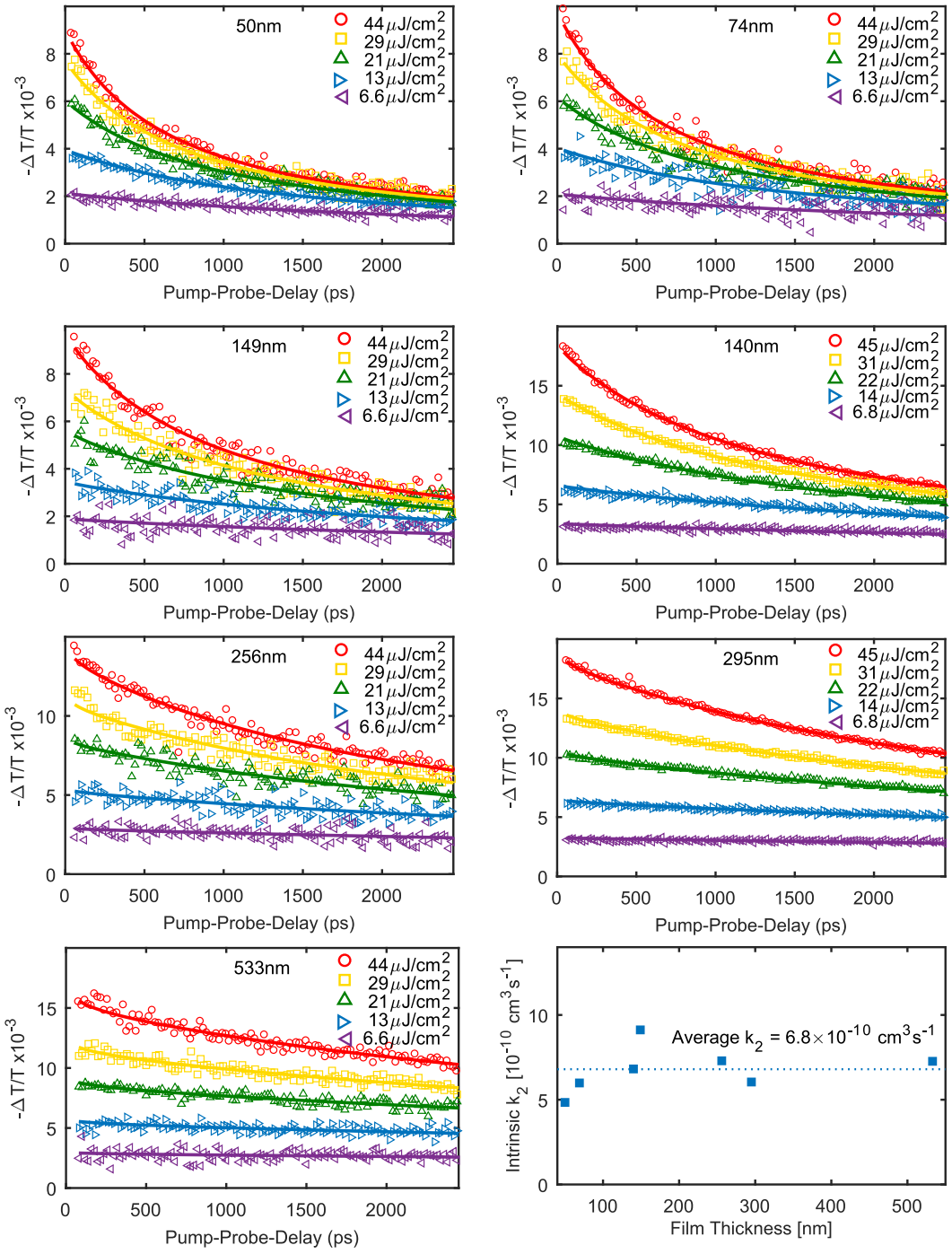


Figure B.9: THz photoconductivity transients for samples of different thickness as indicated in the figure panels shown together with global fits for all fluences based on the Self-Absorption Model. Also shown is the trend in intrinsic value of the extracted bimolecular recombination constant $k_2^{intrinsic}$ across the thickness range, showing a single, average value as indicated.

B.5.3 PL Redistribution Matrices

For the samples in Chapter 6 monochromatic redistribution matrices were generated for wavelengths between 651 to 830 nm, as described in Section 4.2.3. The absorption coefficient for each sample was taken from the values extracted by the transfer matrix model in Section B.4. The PL spectra used in the modelling came from the spectra presented in Section B.3, which were corrected for photon re-absorption before being used. The diffusion in each sample was modelled using the average mobility of $11\,\mathrm{cm^2\,V^{-1}\,s^{-1}}$, determined in Section B.5.1. This provided a value of D =$0.3\,\mathrm{cm^2\,s^{-1}}$.

Additionally, PL reallocation maps were produced for a perovskite film between interfacing media with different refractive indices, to investigate the effect of out-coupling on PL re-absorption and charge-carrier recombination. In this case the average absorption and emission spectra, and average mobility of the individual samples was used. These maps are used in Figures 6.2 and 6.3, and are based on 20 µm photon propagation in a 300nm thick perovskite film located between two semi-infinite media.

B.6 Charge carrier decay for Thick and Thin Films

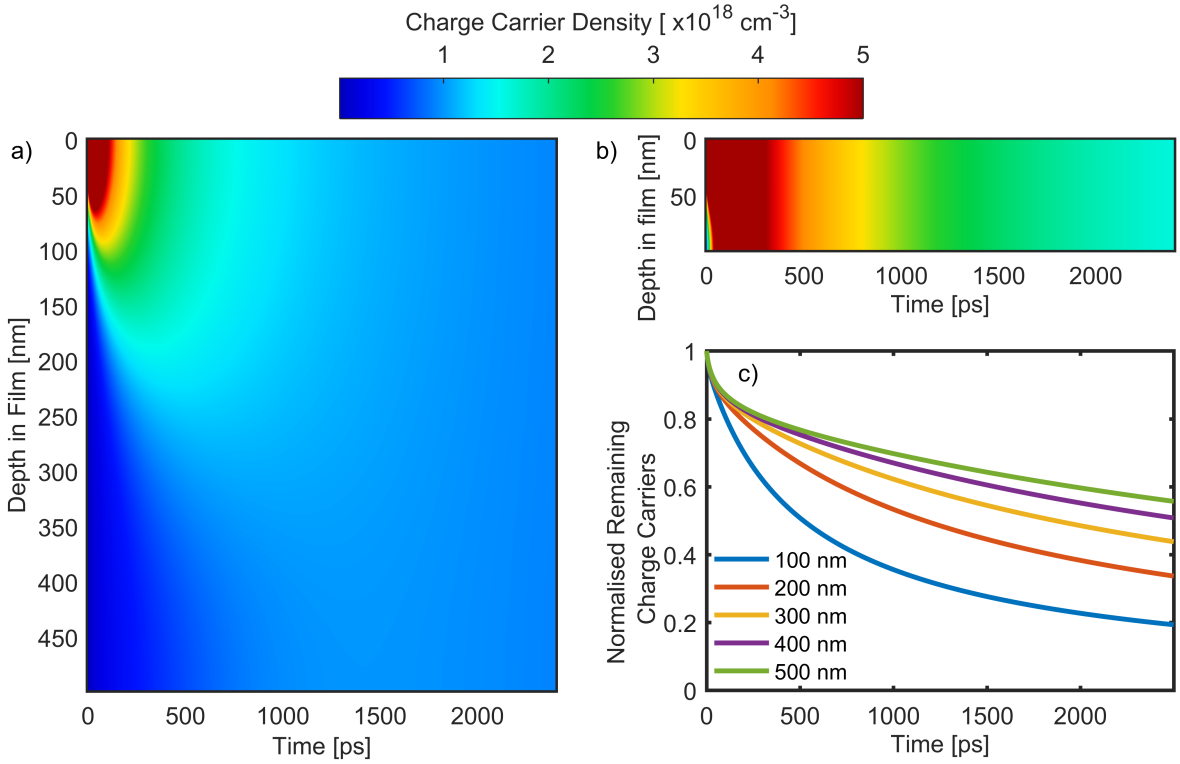


Figure B.10: Modelled charge-carrier dynamics in a (a) 500-nm and (b) 100-nm perovskite film on quartz, for excitation at a wavelength of 400 nm with an incident pulse energy of 44 µJ cm^{-2} using the self-absorption model. (c) The normalised remaining charge-carrier populations for perovskite films with thickness range 100-500 nm, under the excitation conditions described above. The recombination constants used in each case are $k_2^{intrinsic} = 6.8 \times 10^{-10}$ cm^3 s^{-1} and $k_3 = 1 \times 10^{-29}$ cm^{6}s^{-1}.

C

Supporting Information and Methods for Chapter 7

C.1 Steady-State and Time-Resolved Photoluminescence

The excitation source was a 398 nm pulsed diode laser (PicoHarp, LDH-D-C-405M) operating at 500 kHz, which has a pulse duration of 68 ps[1].

The PL was collected in reflection geometry and coupled into a grating spectrometer (Princeton Instruments, SP-2558). Steady-state spectra were acquired with an iCCD iCCD (PI-MAX4, Prineton Instruments) and time-resolved measurements were acquired in a Time Correlated Single Photon Counting (TCSPC) system (Picoharp300). The measurements were performed under vacuum (pressure $< 10^{-1}$ mbar).

C.2 Description of the Fitting of THz Photoconductivity Transients

For excitation from each side of the mixed 2D/3D perovskite film, four different simulations of the charge-carrier dynamics were globally fitted against the experimental

[1] Although the laser has a 68 ps FWHM, at the power used in Chapter 7 the pulse also possesses a longer tail – lasting up to 1 ns after the initial pulse

THz photoconductivity transients. Each simulation uses the self-absorption model from Section 7.3.2, but across the different simulations charge-carrier diffusion and photon re-absorption are included or excluded from the model, as indicated in Figures 7.7 and 7.8. This highlights how diffusion and photon re-absorption individually contribute to the charge-carrier dynamics.

The maximum pump-excitation fluence used was $16\,\mu J\,cm^{-2}$. This was sufficiently low that any Auger-like recombination processes were not considered in the fitting, with k_3 being fixed at zero. Additionally, monomolecular decay is not considered and k_1 is fixed at zero. This is because the PL lifetime of the mixed 2D/3D perovskite film (in the range 750 to 800 nm) was determined to be $\approx$1 µs (Section 7.2.1), while the maximum time delay in the experiment was 1.2 ns. Since the monomolecular lifetime far exceeds the experimental time window, mono-molecular decay will not be observed. This means the only free parameter in the model was k_2, as Auger and monomolecular recombination are not considered.

Excitation from the front and back sides of the mixed 2D/3D perovskite film were considered separately. In each case, k_2 was globally fitted across a set THz photoconductivity transients measured for a range of pump-excitation fluences. The fitting routine also made small adjustments to the values of the pump powers used in the dynamical model, to allow the model to fit the experimental data. This accounts for small errors in the measurement of the pump beam power.

C.3 Can Photon Re-absorption Cause a Photoconductivity Rise?

It has been previously demonstrated in Section 7.5.1 that diffusion of charge carriers can cause a rise in THz photoconductivity, now the circumstances under which photon re-absorption may cause such a rise will be discussed.

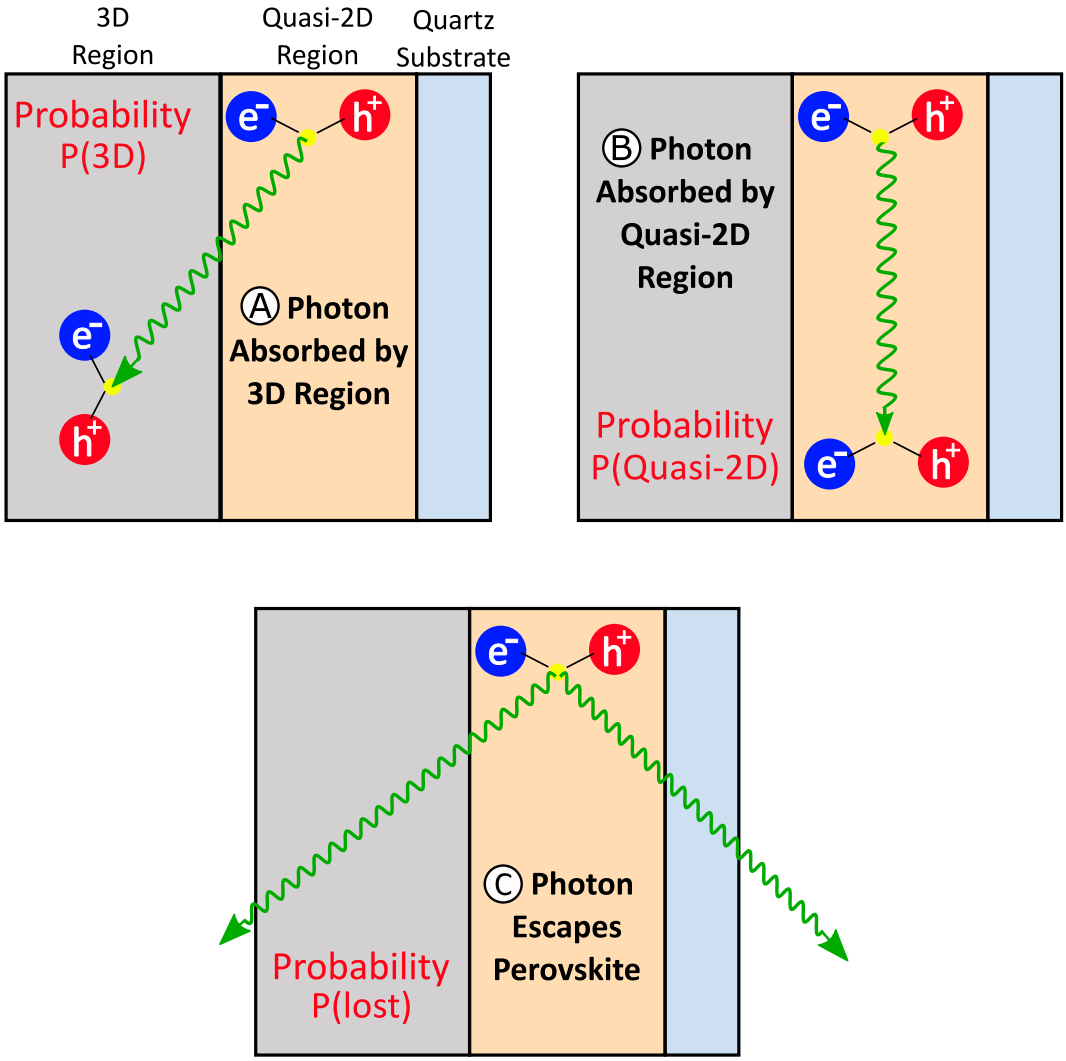


Figure C.1: Illustration of the three possible outcomes of PL emission from the quasi-2D region. The emitted photon can be reabsorbed by, (a), the 3D region, or (b), the quasi-2D region. If it is not reabsorbed, the photon is considered lost from the sample as in case (c).

First it is good to summarise why charge-carrier diffusion causes a rise in THz photoconductivity. When the mixed 2D/3D perovskite film is excited from the back side, charge carriers are initially generated in the quasi-2D region. Over time, diffusion spreads charge carriers evenly across the film, meaning that some charge carriers are transferred into the 3D region, which has a higher charge-carrier mobility. Since THz photoconductivity is proportional to charge-carrier mobility, it is the transfer of charge carriers from the quasi-2D region into the 3D region which leads to the observed rise in THz photoconductivity.

Since photon re-absorption also transports charge carriers across the sample, it is possible that it could also contribute to the rise in THz photoconductivity, when the sample is excited from the back. For photon re-absorption to cause a rise in THz photoconductivity, charge carriers which decay radiatively in the quasi-2D region must be transferred efficiently into the 3D region, by being reabsorbed there. However, not all of the photons in the quasi-2D region will be reabsorbed in the 3D region.

Figure C.1 shows the three possible outcomes of PL emission from the quasi-2D region. Firstly, the emitted photon can be reabsorbed inside the 3D region, with a probability P(3D). Secondly, the photon could be recaptured by the quasi-2D region, with a probability P(quasi-2D). Finally, there is the possibility that the photon is not reabsorbed by any part of the perovskite layer, but is instead lost through scattering or out-coupling. The probability that the photon is lost in this way is given by P(lost). If a charge-carrier is not reabsorbed in either the quasi-2D or 3D regions then it must be lost from the perovskite film. Therefore these three scenarios describe all the possible outcomes of photon emission from the quasi-2D region.

With the possible outcomes of PL emission from the quasi-2D region determined, the next step is to consider how each scenario affects the THz photoconductivity. In the first case, where the emitted photon is recaptured by the 3D region, there will be an increase in THz photoconductivity. This is because one charge-carrier is lost from the quasi-2D region and another is added to the 3D region. The change in THz photoconductivity is proportional to $(\mu_{3D} - \mu_{quasi-2D})$. For the case where the emitted photon is reabsorbed by the quasi-2D region, the charge-carrier which is lost to recombination is replaced by a charge-carrier with an identical mobility. This means that there is no net change in THz photoconductivity. For the third case, where the photon is lost, there will be a reduction in THz photoconductivity, proportional to $\mu_{quasi-2D}$. This is because a charge-carrier is lost from the quasi-2D region, and not replaced. Therefore, if a

charge-carrier is reabsorbed in the 3D region, THz photoconductivity will increase and if it escapes the film, THz photoconductivity will decrease.

The average effect of photon re-absorption across many recombination events can now be calculated. The absorption of charge carriers by the 3D region happens at a probability P(3D), and increases THz photoconductivity $\propto$ $(\mu_{3D} - \mu_{quasi-2D})$. The loss of charge carriers by scattering or out-coupling occurs with probability P(lost) and results in a decrease in THz photoconductivity $\propto$ $\mu_{quasi-2D}$. If the increase in THz photoconductivity, from transfer into the 3D region, outweighs the loss from charge carriers not being reabsorbed, there will be a net rise in THz photoconductivity caused by photon re-absorption. This criterion can be stated as

$$\mathrm{P(3D)} \times (\mu_{3D} - \mu_{quasi-2D}) > \mathrm{P(lost)} \times \mu_{quasi-2D}. \tag{C.1}$$

If this equation is satisfied there will be a net rise in THz photoconductivity, caused by photon re-absorption.

In the mixed 2D/3D perovskite film, Figure 7.14 shows that $P(3D)$ and $P(lost)$ will both be around 0.4. This means there will only be a rise in THz photoconductivity if the difference in charge-carrier mobility between the two regions is greater than the charge-carrier mobility of the quasi-2D region. Since this is not the case, it can, therefore, be concluded that only charge-carrier diffusion will contribute towards a rise in THz photoconductivity in the mixed 2D/3D perovskite film.

In general, Equation C.1 shows the relation which must be fulfilled if photon re-absorption is to cause a rise in THz photoconductivity. This happens only in cases where there are extremely low radiative losses, or where the high-mobility phase has a much greater charge-carrier mobility than the low-mobility phase. This can be understood, as, although it does redistribute charge carriers, photon re-absorption is an intrinsically lossy process, which reduces but does not completely stop the loss of charge carriers.

C.4 Comparing the Simulations with Real Data

The modelling work in the previous section represents an idealised situation, where excitation of the mixed 2D/3D perovskite film, from the back or front, results in exactly the same number of charge carriers being generated. However, under real conditions, reflection losses make it difficult to equally excite the front and back of a perovskite film, as illustrated in Figure C.2. Using FTIR spectroscopy (see Section 7.2.2), a reflection loss of 20% was measured for the front side of the mixed 2D/3D perovskite film at 400 nm, but this was only 6% when the excitation is from the front side, due to increased in-coupling through the quartz substrate. This means that the THz photoconductivity transients for excitation of the back and front of the film cannot be directly compared, as different numbers of charge carriers are present in each case.

This section will investigate the extent to which reflection losses influence the comparison of the charge-carrier dynamics for front and back excitation of the mixed 2D/3D perovskite film and show that a linear rescaling of the THz photoconductivity transients can be used to minimise the effects of the reflection losses from each side. With this correction, the THz photoconductivity transients for excitation of the back and front of the mixed 2D/3D perovskite film can be more accurately compared.

Before including reflection losses, THz photoconductivity transients for excitation from each side of the mixed 2D/3D perovskite film were simulated, assuming no reflection losses. These THz photoconductivity transients will then serve as a benchmark, to determine how the reflection losses affect the charge-carrier dynamics.

Without reflection losses, for a given pump fluence, there is no difference in the number of charge carriers injected into the back and front of the film. This allows a direct comparison of the differences in charge-carrier dynamics caused by the intrinsic material properties, rather than the in-coupling of different light intensities. Figure C.3

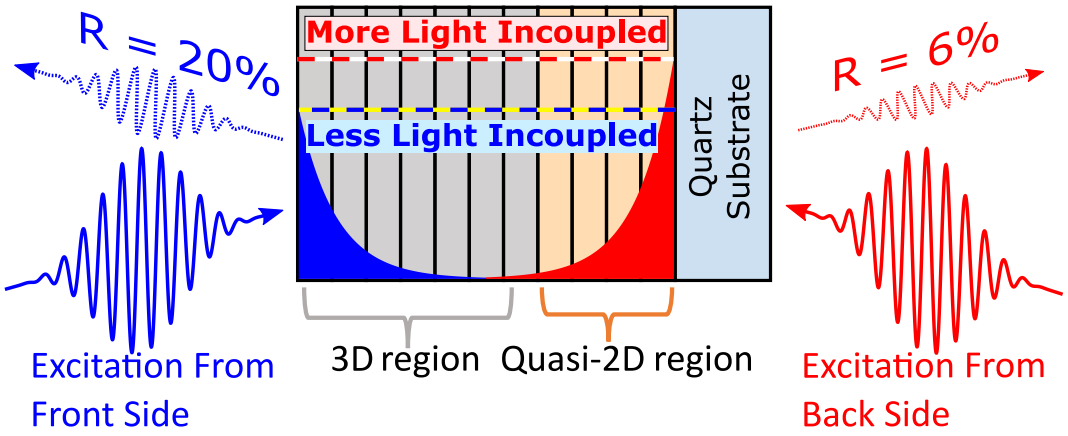


Figure C.2: Illustration of how different amounts of the pump beam being reflected by each side of the sample leads to a different number of charge carriers being generated, depending on which side the mixed 2D/3D perovskite film is excited from. The values of the reflection coefficients are taken from FTIR measurements of the mixed 2D/3D perovskite film (Section 7.2.2).

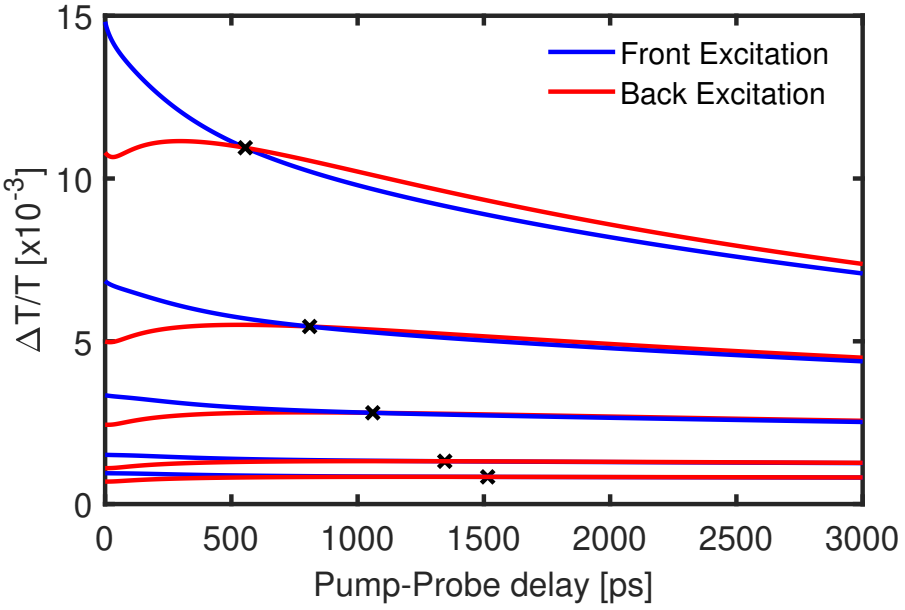


Figure C.3: THz photoconductivity transients modelled for the mixed 2D/3D perovskite film, ignoring any reflection losses on either side of the sample and with $k_2 = 6.9 \times 10^{-10}\,\mathrm{cm^3\,s^{-1}}$. The excitation fluences are $16.0\,\mu\mathrm{J\,cm^{-2}}$, $7.4\,\mu\mathrm{J\,cm^{-2}}$, $3.6\,\mu\mathrm{J\,cm^{-2}}$, $1.6\,\mu\mathrm{J\,cm^{-2}}$ and $1.0\,\mu\mathrm{J\,cm^{-2}}$. For each excitation fluence a black cross indicates the time when the THz photoconductivity transients for back and front side excitation are equal (due to the heterogeneous PL, as described in 7.3.1).

shows the THz photoconductivity decays produced by the model in this case. The excitation fluences used are the same as those set in the OPTP study in Section 7.4, and transients are modelled for excitation from the front and back of the film, assuming no reflection losses. A clear pattern can be observed in the time taken for the THz photoconductivity transients for back and front excitation to cross. Each of the pairs of lines cross, with lower fluence lines taking longer to cross. This provides an idealised set of THz photoconductivity decays for equal excitation of the back and front side of the sample, against which further simulations, which include reflection losses, can be compared.

In the simulations above, the number of charge carriers injected into the back and front of the sample is the same. However, in OPTP experiments, usually only the incident laser power is kept constant between back and front excitations, while the reflection of each side will vary. Comparing the THz photoconductivity dynamics of the two sides is therefore complicated by the fact that the number of charge carriers injected into each side will be slightly different, due to the different reflection losses. At 400 nm the mixed 2D/3D perovskite film, reflected 20% of incident light from the front side and only 6% from the back, as determined using FTIR spectroscopy. What is now required is a means of correcting for these differing reflection losses, so that the dynamics of the two sides can be compared.

In order to determine the effect of the reflection losses for the mixed 2D/3D perovskite film, THz photoconductivity decays were again simulated, using the excitation fluences used in the OPTP study, and accounting for reflection losses. In the model, these reflection losses lower the number of charge carriers initially generated by the pump-pulse. The dotted lines in Figure C.4 show the raw THz photoconductivity decays for the top two fluences used in OPTP, accounting for reflection losses. However, as the simulations for back and front excitation initially contain different numbers of charge carriers, it does not make sense to directly compare these raw THz photoconductivity transients.

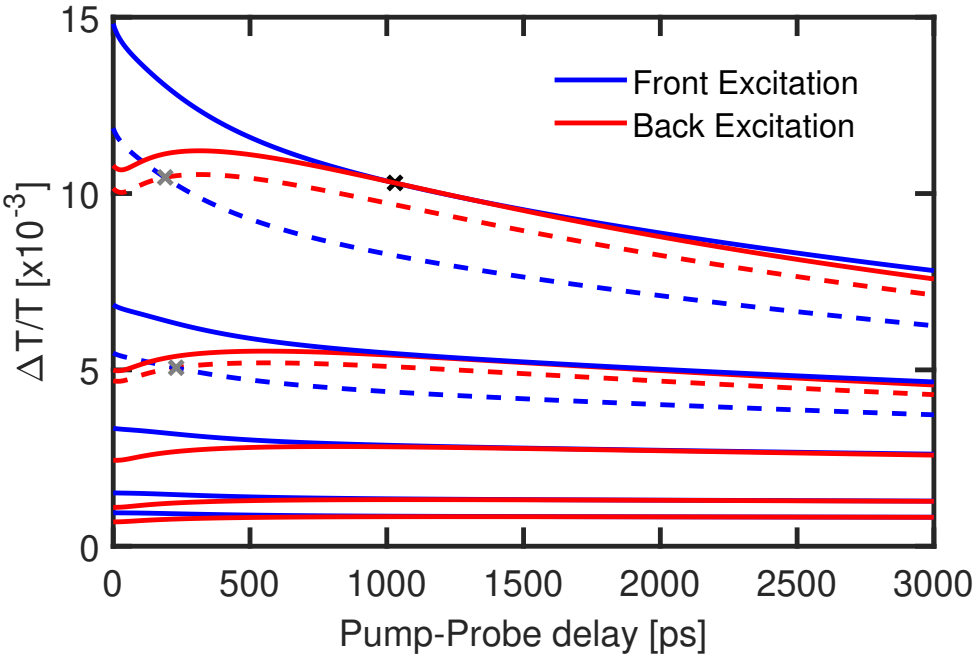


Figure C.4: THz photoconductivity transients modelled for the mixed 2D/3D perovskite film, accounting for the reflection losses from each side of the sample and with $k_2 = 6.9 \times 10^{-10}\,\mathrm{cm^3\,s^{-1}}$. At 400 nm, the reflection losses are 0.2 from the front side, and 0.06 from the back side. Dotted lines show the raw THz photoconductivity transients, while the solid lines are scaled by scaled up by a factor of $1/(1-\mathrm{R})$ to correct for the reflection losses. The excitation fluences are 16.0 µJ cm^{-2}, 7.4 µJ cm^{-2}, 3.6 µJ cm^{-2}, 1.6 µJ cm^{-2} and 1.0 µJ cm^{-2}. For each fluence, a black cross indicates the time when the corrected THz photoconductivity transients for back and front side excitation are equal, while grey crosses show the crossing points of the raw lines.

Instead, the solid lines in Figure C.4 show each transient scaled up by a factor of $1/(1-\mathrm{R})$, where R is the pump beam reflection loss off each side. This linear correction for the small difference in excited charge carriers rescales each THz photoconductivity transient to have the same initial value as in Figure C.3, where there are no reflection losses. This scaling is equivalent to normalising each THz photoconductivity transient by the number of injected charge carriers. When the scaling is made, the data can be seen to more closely resemble Figure C.3 and the trend in crossing times is partially recovered.

The validity of rescaling the reflection-corrected THz photoconductivity transients can be ascertained by directly comparing them with the transients modelled without any reflections. This determines how close rescaled experimental THz photoconductivity transients will be to the case where equal numbers of charge carriers are incoupled

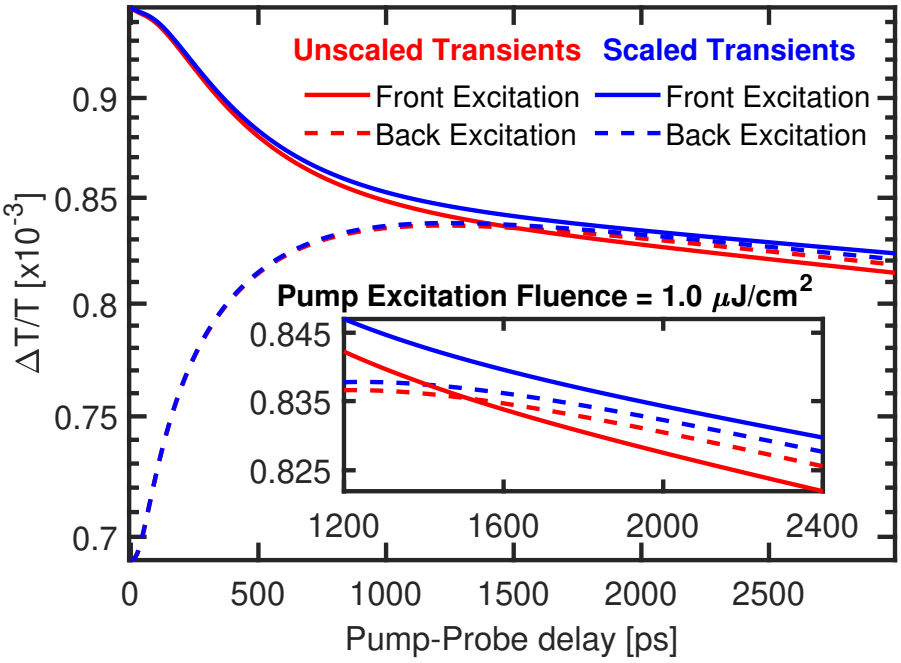


Figure C.5: A comparison of THz photoconductivity transients modelled for the mixed 2D/3D perovskite film, for excitation from the back and front sides, with an incident fluence of 1.0 µJ cm^{-2}. Unscaled lines are simulated assuming no reflection losses. The scaled lines account for reflection losses, but in the figure, the simulated THz photoconductivity is shown scaled by a factor of 1/1 − R), to correct for the reflection losses. The scaling means that both sets of THz photoconductivity transients have the same initial value of ΔT/T. Note that in both cases the scaling has recovered the initial value of ΔT/T.

into the back and front of the sample. Figure C.5 shows a comparison of the THz photoconductivity decays for the lowest excitation fluence shown in Figures C.3 and C.4. The 'unscaled' transients are modelled with no reflections considered, while the 'scaled' transients consider reflection losses, and are linearly scaled up by $1/(1-R)$ as described above. Because of this rescaling, both the scaled and unscaled THz photoconductivity transients start at the same value. However, in the scaled transients, fewer charge carriers are present in the simulations, as reflection losses are considered. As there are fewer charge carriers, n is lower and the bimolecular recombination is slower than in the unscaled case. This means that when the THz photoconductivity transients are scaled up, they decay more slowly than the equivalent unscaled transients.

In Figure C.5, it can be seen that the scaled THz photoconductivity transients (which have been corrected for reflection loss) decay more slowly than the unscaled transients

(which are modelled in the absence of any reflection losses). While there is little difference between the scaled and unscaled transients for back excitation, there is a much larger discrepancy for front excitation. This can be explained by the different reflection losses, which were measured as 0.20 for the front side but only 0.06 for the back. As the reflection loss from the front side is larger, so is the difference in the charge-carrier density away from the unscaled case. This larger difference makes the linear correction less accurate for the case of front side excitation.

Although the scaling does not recover the exact shape of the transients, it does closely resemble the unscaled decays. The absolute differences in $\Delta T/T$ for the case shown are $O(10^5)$, which is an error of around 2.5%. This is within the noise of the OPTP experiment, and so rescaling the experimental THz photoconductivity transients will not produce a measurable error. At higher fluences bimolecular losses are larger, so the correction will be less accurate, especially for the case of front side excitation. However making a linear correction to the data is still a considerable improvement, especially since the maximum time-delay used in the OPTP experiment is 1.25 ns, rather than the 3 ns time-window shown here. Therefore, the linear correction procedure outlined here is a valid approximation, which can be used to correct the experimental OPTP transients shown in Figures C.6 and C.7.

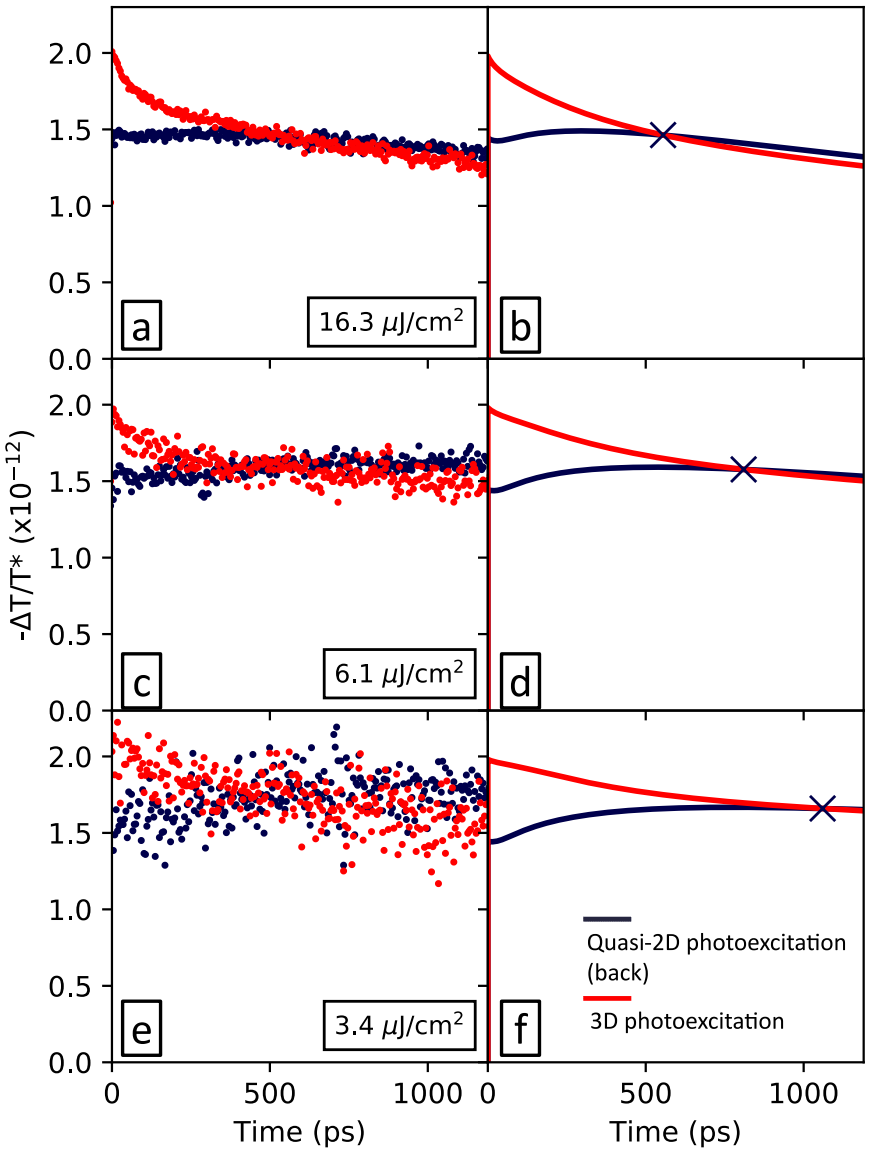


Figure C.6: Panels (a), (c) and (e) show a comparison of the corrected OPTP dynamics for excitation from the front (red) and back (dark blue) sides of the mixed 2D/3D perovskite film. The data in each panel is scaled as $\Delta T/T/T^* = (\Delta T/T)/N_0$, where N_0 is the predicted initial density of photoexcited carriers. Panels (b), (d) and (f) show simulated THz photoconductivity transients assuming no reflection losses from either side of the film. Comparing the simulations with the corrected data, it can be seen there is good agreement between the two. THz photoconductivity transients were measured by Dr S. G. Motti.

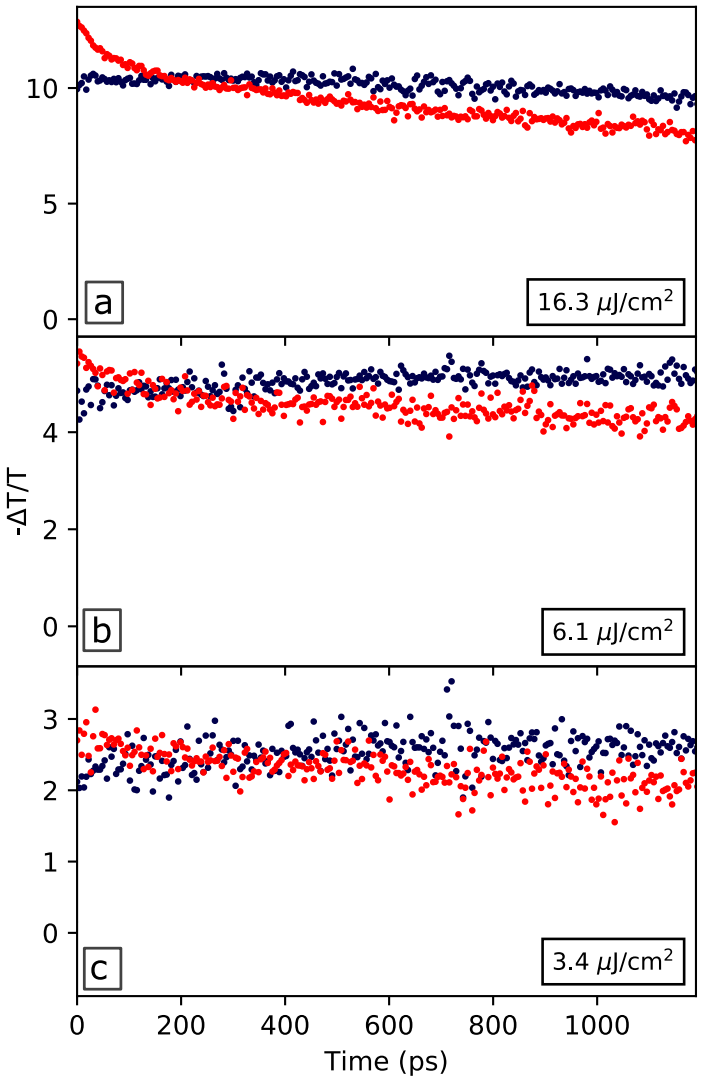


Figure C.7: A comparison of the uncorrected OPTP dynamics for excitation from the front (red) and back (dark blue) sides of the mixed 2D/3D perovskite film. THz photoconductivity transients were measured by Dr S. G. Motti.

References

[1] Gerland, P.; Raftery, A. E.; Ševčíková, H.; Li, N.; Gu, D.; Spoorenberg, T.; Alkema, L.; Fosdick, B. K.; Chunn, J.; Lalic, N. *et al.* 'World population stabilization unlikely this century'. *Science*, 2014, **346**, 234–237.

[2] International Energy Agency. *World Energy Outlook 2018*. IEA, 2018.

[3] Breyer, C.; Bogdanov, D.; Aghahosseini, A.; Gulagi, A.; Child, M.; Oyewo, A. S.; Farfan, J.; Sadovskaia, K. and Vainikka, P. 'Solar photovoltaics demand for the global energy transition in the power sector'. *Prog. Photovoltaics*, 2018, **26**, 505–523.

[4] Jäger-Waldau, A. 'Snapshot of Photovoltaics—February 2019'. *Energies*, 2019, **12**, 769.

[5] Sivaram, V. *Taming the sun: Innovations to harness solar energy and power the planet.* MIT Press, 2018.

[6] Cai, M.; Wu, Y.; Chen, H.; Yang, X.; Qiang, Y. and Han, L. 'Cost-performance analysis of perovskite solar modules'. *Adv. Sci.* 2017, **4**, 1600269.

[7] Snaith, H. J. 'Perovskites: The Emergence of a New Era for Low-Cost , High-Efficiency Solar Cells'. *J. Phys. Chem. Lett*, 2013, **4**, 3623–3630.

[8] Green, M. A.; Hishikawa, Y.; Dunlop, E. D.; Levi, D. H.; Hohl-Ebinger, J. and Ho-Baillie, A. W. 'Solar cell efficiency tables (version 52)'. *Prog. Photovoltaics*, 2018, **26**.

[9] Hou, Y.; Du, X.; Scheiner, S.; McMeekin, D. P.; Wang, Z.; Li, N.; Killian, M. S.; Chen, H.; Richter, M.; Levchuk, I. *et al.* 'A generic interface to reduce the efficiency-stability-cost gap of perovskite solar cells'. *Science*, 2017, **358**, 1192–1197.

[10] Herz, L. M. 'Charge-carrier dynamics in organic-inorganic metal halide perovskites'. *Annu. Rev. Phys. Chem.* 2016, **67**, 65–89.

[11] Brenner, T. M.; Egger, D. A.; Kronik, L.; Hodes, G. and Cahen, D. 'Hybrid organic—inorganic perovskites: low-cost semiconductors with intriguing charge-transport properties'. *Nat. Mater.* 2016, **1**, 15007.

[12] Zhou, D.; Zhou, T.; Tian, Y.; Zhu, X. and Tu, Y. 'Perovskite-based solar cells: materials, methods, and future perspectives'. *J. Nanomater*, 2018, **2018**.

[13] Sha, W. E.; Ren, X.; Chen, L. and Choy, W. C. 'The efficiency limit of $CH_3NH_3PbI_3$ perovskite solar cells'. *Appl. Phys. Lett.* 2015, **106**, 221104.

[14] Shockley, W. and Queisser, H. J. 'Detailed Balance Limit of Efficiency of p-n Junction Solar Cells'. *J. Appl. Phys.* 1961, **32**, 510.

[15] Davies, C. L.; Filip, M. R.; Patel, J. B.; Crothers, T. W.; Verdi, C.; Wright, A. D.; Milot, R. L.; Giustino, F.; Johnston, M. B. and Herz, L. M. 'Bimolecular recombination in methylammonium lead triiodide perovskite is an inverse absorption process'. *Nat. Commun.* 2018, **9**, 293.

[16] Van Roosbroeck, W. and Shockley, W. 'Photon-radiative recombination of electrons and holes in germanium'. *Phys. Rev.* 1954, **94**, 1558–1560.

[17] De Wolf, S.; Holovsky, J.; Moon, S.-J.; Löper, P.; Niesen, B.; Ledinsky, M.; Haug, F.-J.; Yum, J.-H. and Ballif, C. 'Organometallic halide perovskites: sharp optical absorption edge and its relation to photovoltaic performance'. *J. Phys. Chem. Lett.* 2014, **5**, 1035–1039.

[18] Goldschmidt, V. 'Die gesetze der krystallochemie'. *Naturwissenschaften*, 1926, **14**, 477–485.

[19] Kieslich, G.; Sun, S. and Cheetham, A. K. 'An extended tolerance factor approach for organic–inorganic perovskites'. *Chem. Sci.* 2015, **6**, 3430–3433.

[20] Bednorz, J. G. and Müller, K. A. 'Perovskite-type oxides—the new approach to high-T c superconductivity'. *Rev. Mod. Phys.* 1988, **60**, 585.

[21] Zhang, Z.; Wei, D.; Xie, B.; Yue, X.; Li, M.; Song, D. and Li, Y. 'High reproducibility of perovskite solar cells via a complete spin-coating sequential solution deposition process'. *Sol. Energy*, 2015, **122**, 97–103.

[22] Borchert, J.; Milot, R. L.; Patel, J. B.; Davies, C. L.; Wright, A. D.; Martínez Maestro, L.; Snaith, H. J.; Herz, L. M. and Johnston, M. B. 'Large-Area, Highly Uniform Evaporated Formamidinium Lead Triiodide Thin Films for Solar Cells'. *ACS Energy Lett.* 2017, **2**, 2799–2804.

[23] Hwang, K.; Jung, Y.-S.; Heo, Y.-J.; Scholes, F. H.; Watkins, S. E.; Subbiah, J.; Jones, D. J.; Kim, D.-Y. and Vak, D. 'Toward large scale roll-to-roll production of fully printed perovskite solar cells'. *Adv. Mater.* 2015, **27**, 1241–1247.

[24] Deng, Y.; Peng, E.; Shao, Y.; Xiao, Z.; Dong, Q. and Huang, J. 'Scalable fabrication of efficient organolead trihalide perovskite solar cells with doctor-bladed active layers'. *Energy Environ. Sci.* 2015, **8**, 1544–1550.

[25] Lee, M. M.; Teuscher, J.; Miyasaka, T.; Murakami, T. N. and Snaith, H. J. 'Efficient hybrid solar cells based on meso-superstructured organometal halide perovskites.' *Science*, 2012, **338**, 643–647.

[26] Liu, M.; Johnston, M. B. and Snaith, H. J. 'Efficient planar heterojunction perovskite solar cells by vapour deposition.' *Nature*, 2013, **501**, 395–398.

[27] Li, X.; Bi, D.; Yi, C.; Decoppet, J.-D.; Luo, J.; Zakeeruddin, S. M.; Hagfeldt, A. and Gratzel, M. 'A vacuum flash-assisted solution process for high-efficiency large-area perovskite solar cells'. *Science*, 2016, **353**, 58–62.

[28] Park, N.-G. 'Organometal perovskite light absorbers toward a 20% efficiency low-cost solid-state mesoscopic solar cell'. *J. Phys. Chem. Lett.* 2013, **4**, 2423–2429.

[29] Kagan, C. R. 'Organic-Inorganic Hybrid Materials as Semiconducting Channels in Thin-Film Field-Effect Transistors'. *Science*, 1999, **286**, 945–947.

[30] Grätzel, M. 'Dye-sensitized solar cells'. *J. Photochem. Photobiol. C*, 2003, **4**, 145–153.

[31] Kojima, A.; Teshima, K.; Shirai, Y. and Miyasaka, T. 'Organometal halide perovskites as visible-light sensitizers for photovoltaic cells.' *Journal of the American Chemical Society*, 2009, **131**, 6050–1.

[32] Hagfeldt, A.; Boschloo, G.; Sun, L.; Kloo, L. and Pettersson, H. 'Dye-sensitized solar cells'. *Chem. Rev.* 2010, **110**, 6595–6663.

[33] Kim, H.-S.; Lee, C.-R.; Im, J.-H.; Lee, K.-B.; Moehl, T.; Marchioro, A.; Moon, S.-J.; Humphry-Baker, R.; Yum, J.-H.; Moser, J. E. *et al.* 'Lead iodide perovskite sensitized all-solid-state submicron thin film mesoscopic solar cell with efficiency exceeding 9%'. *Sci. Rep.* 2012, **2**, 591.

[34] Nakade, S; Saito, Y; Kubo, W; Kitamura, T; Wada, Y and Yanagida, S. 'Influence of TiO_2 nanoparticle size on electron diffusion and recombination in dye-sensitized TiO_2 solar cells'. *J. Phys. Chem. B*, 2003, **107**, 8607–8611.

[35] Ball, J. M.; Lee, M. M.; Hey, A. and Snaith, H. J. *Energy Environ. Sci.* 2013, **6**, 1739.

[36] Qiu, W.; Merckx, T; Jaysankar, M.; Huerta, C. M. de la; Rakocevic, L.; Zhang, W.; Paetzold, U.; Gehlhaar, R; Froyen, L.; Poortmans, J. *et al.* 'Pinhole-free perovskite films for efficient solar modules'. *Energy & Environmental Science*, 2016, **9**, 484–489.

[37] Nie, W.; Tsai, H.; Asadpour, R.; Blancon, J.-C.; Neukirch, A. J.; Gupta, G.; Crochet, J. J.; Chhowalla, M.; Tretiak, S.; Alam, M. A. *et al.* 'High-efficiency solution-processed perovskite solar cells with millimeter-scale grains'. *Science*, 2015, **347**, 522–525.

[38] Yang, W.; Yao, Y. and Wu, C.-Q. 'Origin of the high open circuit voltage in planar heterojunction perovskite solar cells: Role of the reduced bimolecular recombination'. *J. Appl. Phys.* 2015, **117**, 095502.

[39] Habibi, M.; Zabihi, F.; Ahmadian-Yazdi, M. R. and Eslamian, M. 'Progress in emerging solution-processed thin film solar cells - Part II: Perovskite solar cells'. *Renew. Sust. Energ. Rev.* 2016, **62**, 1012 –1031.

[40] Petrus, M. L.; Schlipf, J.; Li, C.; Gujar, T. P.; Giesbrecht, N.; Müller-Buschbaum, P.; Thelakkat, M.; Bein, T.; Hüttner, S. and Docampo, P. 'Capturing the sun: A review of the challenges and perspectives of perovskite solar cells'. *Adv. Energy Mater.* 2017, **7**, 1700264.

[41] Correa-Baena, J.-P.; Saliba, M.; Buonassisi, T.; Grätzel, M.; Abate, A.; Tress, W. and Hagfeldt, A. 'Promises and challenges of perovskite solar cells'. *Science*, 2017, **358**, 739–744.

[42] Tress, W.; Marinova, N.; Moehl, T.; Zakeeruddin, S. M.; Nazeeruddin, M. K. and Grätzel, M. 'Understanding the rate-dependent J–V hysteresis, slow time component, and aging in $CH_3NH_3PbI_3$ perovskite solar cells: the role of a compensated electric field'. *Energy Environ. Sci.* 2015, **8**, 995–1004.

[43] Reenen, S. van; Kemerink, M. and Snaith, H. J. 'Modeling anomalous hysteresis in perovskite solar cells'. *J. Phys. Chem. Lett.* 2015, **6**, 3808–3814.

[44] Patel, J. B.; Wong-Leung, J.; Van Reenen, S.; Sakai, N.; Wang, J. T. W.; Parrott, E. S.; Liu, M.; Snaith, H. J.; Herz, L. M. and Johnston, M. B. 'Influence of Interface Morphology on Hysteresis in Vapor-Deposited Perovskite Solar Cells'. *Adv. Electron. Mater.* 2017, **3**, 1600470.

[45] Snaith, H. J.; Abate, A.; Ball, J. M.; Eperon, G. E.; Leijtens, T.; Noel, N. K.; Stranks, S. D.; Wang, J. T.-W.; Wojciechowski, K. and Zhang, W. 'Anomalous hysteresis in perovskite solar cells'. *J. Phys. Chem. Lett*, 2014, **5**, 1511–1515.

[46] Rajagopal, A.; Yao, K. and Jen, A. K.-Y. 'Toward perovskite solar cell commercialization: a perspective and research roadmap based on interfacial engineering'. *Adv. Mater.* 2018, **30**, 1800455.

[47] Braly, I. L.; deQuilettes, D. W.; Pazos-Outón, L. M.; Burke, S.; Ziffer, M. E.; Ginger, D. S. and Hillhouse, H. W. 'Hybrid perovskite films approaching the radiative limit with over 90% photoluminescence quantum efficiency'. *Nat. Photon.* 2018, **12**, 355–361.

[48] Wang, D.-L.; Cui, H.-J.; Hou, G.-J.; Zhu, Z.-G.; Yan, Q.-B. and Su, G. 'Highly efficient light management for perovskite solar cells'. *Sci. Rep.* 2016, **6**, 18922.

[49] Hong, X.; Ishihara, T. and Nurmikko, A. V. 'Dielectric confinement effect on excitons in PbI_4-based layered semiconductors'. *Phys. Rev. B*, 12 1992, **45**, 6961–6964.

[50] Smith, I. C.; Hoke, E. T.; Solis-Ibarra, D.; McGehee, M. D. and Karunadasa, H. I. 'A layered hybrid perovskite solar-cell absorber with enhanced moisture stability'. *Angew. Chem.* 2014, **126**, 11414–11417.

[51] Zhang, X.; Ren, X.; Liu, B.; Munir, R.; Zhu, X.; Yang, D.; Li, J.; Liu, Y.; Smilgies, D.-M.; Li, R. *et al.* 'Stable high efficiency two-dimensional perovskite solar cells via cesium doping'. *Energy Environ Sci*, 2017, **10**, 2095–2102.

[52] Mitzi, D.; Wang, S; Feild, C.; Chess, C. and Guloy, A. 'Conducting layered organic-inorganic halides containing $< 110 >$-oriented perovskite sheets'. *Science*, 1995, **267**, 1473–1476.

[53] Cao, D. H.; Stoumpos, C. C.; Farha, O. K.; Hupp, J. T. and Kanatzidis, M. G. '2D homologous perovskites as light-absorbing materials for solar cell applications'. *J. Am. Chem. Soc.* 2015, **137**, 7843–7850.

[54] Grancini, G; Roldán-Carmona, C; Zimmermann, I; Mosconi, E; Lee, X; Martineau, D; Narbey, S; Oswald, F; De Angelis, F; Graetzel, M *et al.* 'One-year stable perovskite solar cells by 2D/3D interface engineering'. *Nat. Commun.* 2017, **8**, 15684.

[55] Tsai, H.; Nie, W.; Blancon, J.-C.; Stoumpos, C. C.; Asadpour, R.; Harutyunyan, B.; Neukirch, A. J.; Verduzco, R.; Crochet, J. J.; Tretiak, S. *et al.* 'High-efficiency two-dimensional Ruddlesden–Popper perovskite solar cells'. *Nature*, 2016, **536**, 312.

[56] Bai, Y.; Xiao, S.; Hu, C.; Zhang, T.; Meng, X.; Lin, H.; Yang, Y. and Yang, S. 'Dimensional Engineering of a Graded 3D–2D Halide Perovskite Interface Enables Ultrahigh Voc Enhanced Stability in the p-i-n Photovoltaics'. *Adv. Energy Mater.* 2017, **7**, 1701038.

[57] Li, M.; Gao, Q.; Liu, P.; Liao, Q.; Zhang, H.; Yao, J.; Hu, W.; Wu, Y. and Fu, H. 'Amplified Spontaneous Emission Based on 2D Ruddlesden–Popper Perovskites'. *Adv. Funct. Mater.* 2018, **28**, 1707006.

[58] Matsushima, T.; Mathevet, F.; Heinrich, B.; Terakawa, S.; Fujihara, T.; Qin, C.; Sandanayaka, A. S.; Ribierre, J.-C. and Adachi, C. 'N-channel field-effect transistors with an organic-inorganic layered perovskite semiconductor'. *Appl. Phys. Lett.* 2016, **109**, 253301.

[59] Zhang, H.; Liao, Q.; Wu, Y.; Zhang, Z.; Gao, Q.; Liu, P.; Li, M.; Yao, J. and Fu, H. '2D Ruddlesden–Popper perovskites microring laser array'. *Adv. Mater.* 2018, **30**, 1706186.

[60] Yuan, M.; Quan, L. N.; Comin, R.; Walters, G.; Sabatini, R.; Voznyy, O.; Hoogland, S.; Zhao, Y.; Beauregard, E. M.; Kanjanaboos, P. *et al.* 'Perovskite energy funnels for efficient light-emitting diodes'. *Nat. Nanotechnol.* 2016, **11**, 872.

[61] Chen, Z.; Guo, Y.; Wertz, E. and Shi, J. 'Merits and Challenges of Ruddlesden–Popper Soft Halide Perovskites in Electro-Optics and Optoelectronics'. *Adv. Mater.* 2019, **31**, 1803514.

[62] Nelson, J. *The physics of solar cells*. World Scientific Publishing Company, 2003.

[63] Gueymard, C.; Myers, D and Emery, K. 'Proposed reference irradiance spectra for solar energy systems testing'. *Solar energy*, 2002, **73**, 443–467.

[64] Rühle, S. 'Tabulated values of the Shockley–Queisser limit for single junction solar cells'. *Solar Energy*, 2016, **130**, 139–147.

[65] Sze, S. M. and Ng, K. K. *Physics of semiconductor devices*. John Wiley & Sons, 2006.

[66] Wang, C.; Liu, X.; Wang, C.; Xiao, Z.; Bi, C.; Shao, Y.; Huang, J. and Gao, Y. 'Surface analytical investigation on organometal triiodide perovskite'. *J. Vac. Sci. Technol. B*, 2015, **33**, 032401.

[67] Yamada, Y.; Nakamura, T.; Endo, M.; Wakamiya, A. and Kanemitsu, Y. 'Photoelectronic Responses in Solution-Processed Perovskite solar cells from PL and PA spec'. *IEEE Journal of Photovoltaics*, 2015, **5**, 401–405.

[68] Futscher, M. H. and Ehrler, B. 'Efficiency limit of perovskite/Si tandem solar cells'. *ACS Energy Lett.* 2016, **1**, 863–868.

[69] Bush, K. A.; Palmstrom, A. F.; Zhengshan, J. Y.; Boccard, M.; Cheacharoen, R.; Mailoa, J. P.; McMeekin, D. P.; Hoye, R. L.; Bailie, C. D.; Leijtens, T. *et al.* '23.6%-efficient monolithic perovskite/silicon tandem solar cells with improved stability'. *Nat. Energy*, 2017, **2**, 17009.

[70] Jaysankar, M.; Filipič, M.; Zielinski, B.; Schmager, R.; Song, W.; Qiu, W.; Paetzold, U. W.; Aernouts, T.; Debucquoy, M.; Gehlhaar, R. *et al.* 'Perovskite–silicon tandem solar modules with optimised light harvesting'. *Energy Environ. Sci.* 2018, **11**, 1489–1498.

[71] NREL. *Best Research-Cell Efficiencies*. 2019. `https://www.nrel.gov/pv/assets/pdfs/best-reserch-cell-efficiencies.pdf` (visited on 14/03/2019).

[72] Chang, N. L.; Yi Ho-Baillie, A. W.; Basore, P. A.; Young, T. L.; Evans, R. and Egan, R. J. 'A manufacturing cost estimation method with uncertainty analysis and its application to perovskite on glass photovoltaic modules'. *Prog. Photovoltaics*, 2017, **25**, 390–405.

[73] Kegel, J.; Angermann, H.; Stürzebecher, U.; Conrad, E.; Mews, M.; Korte, L. and Stegemann, B. 'Over 20% conversion efficiency on silicon heterojunction solar cells by IPA-free substrate texturization'. *Appl. Surf. Sci.* 2014, **301**, 56–62.

[74] Tsunomura, Y.; Yoshimine, Y.; Taguchi, M.; Baba, T.; Kinoshita, T.; Kanno, H.; Sakata, H.; Maruyama, E. and Tanaka, M. 'Twenty-two percent efficiency HIT solar cell'. *Sol. Energy Mater Sol. Cells*, 2009, **93**, 670–673.

[75] Motta, C.; El-Mellouhi, F.; Kais, S.; Tabet, N.; Alharbi, F. and Sanvito, S. 'Revealing the role of organic cations in hybrid halide perovskite $CH_3NH_3PbI_3$'. *Nat. Commun.* 2015, **6**, 7026.

[76] Kim, M.; Im, J.; Freeman, A. J.; Ihm, J. and Jin, H. 'Switchable S= 1/2 and J= 1/2 Rashba bands in ferroelectric halide perovskites'. *Proc. Natl. Acad. Sci. U.S.A.* 2014, **111**, 6900–6904.

[77] Xing, G.; Mathews, N.; Sun, S.; Lim, S. S.; Lam, Y. M.; Grätzel, M.; Mhaisalkar, S. and Sum, T. C. 'Long-range balanced electron- and hole-transport lengths in organic-inorganic $CH_3NH_3PbI_3$.' *Science*, 2013, **342**, 344–7.

[78] Kurik, M. 'Urbach rule'. *Phys. Status Solidi A*, 1971, **8**, 9–45.

[79] Urbach, F. 'The long-wavelength edge of photographic sensitivity and of the electronic absorption of solids'. *Phys. Rev.* 1953, **92**, 1324.

[80] Ledinsky, M.; Schönfeldová, T.; Holovsky, J.; Aydin, E.; Hájková, Z.; Landová, L.; Neykova, N.; Fejfar, A. and De Wolf, S. 'Temperature Dependence of the Urbach Energy in Lead Iodide Perovskites'. *J. Phys. Chem. Lett.* 2019, **10**, 1368–1373.

[81] Patel, J. B.; Lin, Q.; Zadvorna, O.; Davies, C. L.; Herz, L. M. and Johnston, M. B. 'Photocurrent Spectroscopy of Perovskite Solar Cells Over a Wide Temperature Range from 15 to 350 K'. *J. Phys. Chem. Lett.* 2017, **9**, 263–268.

[82] Fujiwara, H.; Fujimoto, S.; Tamakoshi, M.; Kato, M.; Kadowaki, H.; Miyadera, T.; Tampo, H.; Chikamatsu, M. and Shibata, H. 'Determination and interpretation of the optical constants for solar cell materials'. *Appl. Surf. Sci.* 2017, **421**, 276–282.

[83] Fujiwara, H.; Kato, M.; Tamakoshi, M.; Miyadera, T. and Chikamatsu, M. 'Optical Characteristics and Operational Principles of Hybrid Perovskite Solar Cells'. *Phys. Status Solidi A*, 2018, **215**, 1700730.

[84] Bogardus, E. H. and Bebb, H. B. 'Bound-exciton, free-exciton, band-acceptor, donor-acceptor, and Auger recombination in GaAs'. *Phys. Rev.* 1968, **176**, 993.

[85] Thomas, D. 'Excitons and band splitting produced by uniaxial stress in CdTe'. *J. Appl. Phys.* 1961, **32**, 2298–2304.

[86] Knupfer, M. 'Exciton binding energies in organic semiconductors'. *Appl. Phys. A*, 2003, **77**, 623–626.

[87] Dennler, G.; Scharber, M. C. and Brabec, C. J. 'Polymer-fullerene bulk-heterojunction solar cells'. *Adv. Mater.* 2009, **21**, 1323–1338.

[88] Scharber, M. C. and Sariciftci, N. S. 'Efficiency of bulk-heterojunction organic solar cells'. *Prog. Polym. Sci.* 2013, **38**, 1929–1940.

[89] Peumans, P.; Yakimov, A. and Forrest, S. R. 'Small molecular weight organic thin-film photodetectors and solar cells'. *J. Appl. Phys.* 2003, **93**, 3693–3723.

[90] Forrest, S. R. 'The limits to organic photovoltaic cell efficiency'. *MRS bull.* 2005, **30**, 28–32.

[91] D'innocenzo, V.; Grancini, G.; Alcocer, M. J.; Kandada, A. R. S.; Stranks, S. D.; Lee, M. M.; Lanzani, G.; Snaith, H. J. and Petrozza, A. 'Excitons versus free charges in organo-lead tri-halide perovskites'. *Nat. Commun.* 2014, **5**, 3586.

[92] Sestu, N.; Cadelano, M.; Sarritzu, V.; Chen, F.; Marongiu, D.; Piras, R.; Mainas, M.; Quochi, F.; Saba, M.; Mura, A. *et al.* 'Absorption F-sum rule for the exciton binding energy in methylammonium lead halide perovskites'. *J. Phys. Chem. Lett.* 2015, **6**, 4566–4572.

[93] Miyata, A.; Mitioglu, A.; Plochocka, P.; Portugall, O.; Wang, J. T.-W.; Stranks, S. D.; Snaith, H. J. and Nicholas, R. J. 'Direct measurement of the exciton binding energy and effective masses for charge carriers in organic–inorganic tri-halide perovskites'. *Nat. Phys.* 2015, **11**, 582.

[94] Wehrenfennig, C.; Eperon, G. E.; Johnston, M. B.; Snaith, H. J. and Herz, L. M. 'High charge carrier mobilities and lifetimes in organolead trihalide perovskites'. *Adv. Mater.* 2014, **26**, 1584–1589.

[95] Trinh, M. T.; Wu, X.; Niesner, D. and Zhu, X. 'Many-Body Interactions in Photo-Excited Lead Iodide Perovskite'. *J. Mater. Chem. A*, 2015, **3**, 9285–9290.

[96] Yamada, Y.; Nakamura, T.; Endo, M.; Wakamiya, A. and Kanemitsu, Y. 'Photocarrier Recombination Dynamics in Perovskite $CH_3NH_3PbI_3$ for Solar Cell Applications'. *J. Am. Chem. Soc.* 2014, **136**, 11610–11613.

[97] Milot, R. L.; Eperon, G. E.; Snaith, H. J.; Johnston, M. B. and Herz, L. M. 'Temperature-Dependent Charge-Carrier Dynamics in $CH_3NH_3PbI_3$ Perovskite Thin Films'. *Adv. Funct. Mater.* 2015, **25**, 6218–6227.

[98] Motta, C.; El-Mellouhi, F. and Sanvito, S. 'Charge carrier mobility in hybrid halide perovskites'. *Sci. Rep.* 2015, **5**, 12746.

[99] Parkinson, P.; Lloyd-Hughes, J.; Johnston, M. B. and Herz, L. M. 'Efficient generation of charges via below-gap photoexcitation of polymer-fullerene blend films investigated by terahertz spectroscopy'. *Phys. Rev. B*, 11 2008, **78**, 115321.

[100] Sze, S. and Irvin, J. 'Resistivity, mobility and impurity levels in GaAs, Ge, and Si at 300 K'. *Solid-State Electron.* 1968, **11**, 599–602.

[101] Stranks, S. D.; Eperon, G. E.; Grancini, G.; Menelaou, C.; Alcocer, M. J. P.; Leijtens, T.; Herz, L. M.; Petrozza, A. and Snaith, H. J. 'Electron-hole diffusion lengths exceeding 1 micrometer in an organometal trihalide perovskite absorber'. *Science*, 2013, **342**, 341–344.

[102] Shi, D.; Adinolfi, V.; Comin, R.; Yuan, M.; Alarousu, E.; Buin, A.; Chen, Y.; Hoogland, S.; Rothenberger, A.; Katsiev, K. *et al.* 'Low trap-state density and long carrier diffusion in organolead trihalide perovskite single crystals'. *Science*, 2015, **347**, 519–522.

[103] Chen, Y.; Yi, H.; Wu, X; Haroldson, R; Gartstein, Y.; Rodionov, Y.; Tikhonov, K.; Zakhidov, A; Zhu, X.-Y. and Podzorov, V. 'Extended carrier lifetimes and diffusion in hybrid perovskites revealed by Hall effect and photoconductivity measurements'. *Nat. Commun.* 2016, **7**, 12253.

[104] Chernyak, L.; Osinsky, A.; Temkin, H.; Yang, J.; Chen, Q and Asif Khan, M. 'Electron beam induced current measurements of minority carrier diffusion length in gallium nitride'. *Appl. Phys. Lett.* 1996, **69**, 2531–2533.

[105] Hodes, G. and Kamat, P. V. 'Understanding the implication of carrier diffusion length in photovoltaic cells'. *J. Phys. Chem. Lett.* 2015, **6**, 4090–4092.

[106] Shockley, W. and Read Jr, W. 'Statistics of the recombinations of holes and electrons'. *Phys. Rev.* 1952, **87**, 835.

[107] Hall, R. N. 'Electron-hole recombination in germanium'. *Phys. Rev.* 1952, **87**, 387.

[108] Johnston, M. B. and Herz, L. M. 'Hybrid perovskites for photovoltaics: charge-carrier recombination, diffusion, and radiative efficiencies'. *Acc. Chem. Res.* 2015, **49**, 146–154.

[109] Draguta, S.; Thakur, S.; Morozov, Y. V.; Wang, Y.; Manser, J. S.; Kamat, P. V. and Kuno, M. 'Spatially Non-uniform Trap State Densities in Solution-Processed Hybrid Perovskite Thin Films.' EN. *J. Phys. Chem. Lett.* 2016, **7**, 715–721.

[110] DeQuilettes, D. W.; Vorpahl, S. M.; Stranks, S. D.; Nagaoka, H.; Eperon, G. E.; Ziffer, M. E.; Snaith, H. J. and Ginger, D. S. 'Impact of microstructure on local carrier lifetime in perovskite solar cells'. *Science*, 2015, **348**, 683–686.

[111] Sherkar, T. S.; Momblona, C.; Gil-Escrig, L.; Ávila, J.; Sessolo, M.; Bolink, H. J. and Koster, L. J. A. 'Recombination in perovskite solar cells: significance of grain boundaries, interface traps, and defect ions'. *ACS Energy Lett.* 2017, **2**, 1214–1222.

[112] Yang, M.; Zeng, Y.; Li, Z.; Kim, D. H.; Jiang, C.-S.; Lagemaat, J. van de and Zhu, K. 'Do grain boundaries dominate non-radiative recombination in $CH_3NH_3PbI_3$ perovskite thin films?' *Phys. Chem. Chem. Phys.* 2017, **19**, 5043–5050.

[113] Stewart, R. J.; Grieco, C.; Larsen, A. V.; Maier, J. J. and Asbury, J. B. 'Approaching Bulk Carrier Dynamics in Organo-Halide Perovskite Nanocrystalline Films by Surface Passivation.' *J. Phys. Chem. Lett.* 2016, **7**, 1148–1153.

[114] Ham, S.; Choi, Y. J.; Lee, J.-W.; Park, N.-G. and Kim, D. 'Impact of Excess CH_3NH_3I on Free Carrier Dynamics in High-Performance Non-Stoichiometric Perovskites'. *J. Phys. Chem. C*, 2017, **121**, 3143–3148.

[115] Ziang, X.; Shifeng, L.; Laixiang, Q.; Shuping, P.; Wei, W.; Yu, Y.; Li, Y.; Zhijian, C.; Shufeng, W.; Honglin, D. *et al.* 'Refractive index and extinction coefficient of $CH_3NH_3PbI_3$ studied by spectroscopic ellipsometry'. *Opt. Mater. Express*, 2015, **5**, 29–43.

[116] DeQuilettes, D. W.; Koch, S.; Burke, S.; Paranji, R. K.; Shropshire, A. J.; Ziffer, M. E. and Ginger, D. S. 'Photoluminescence Lifetimes Exceeding 8 μs and Quantum Yields Exceeding 30% in Hybrid Perovskite Thin Films by Ligand Passivation'. *ACS Energy Lett.* 2016, **1**, 438–444.

[117] Zhumekenov, A. A.; Saidaminov, M. I.; Haque, M. A.; Alarousu, E.; Sarmah, S. P.; Murali, B.; Dursun, I.; Miao, X.-H.; Abdelhady, A. L.; Wu, T. *et al.* 'Formamidinium Lead Halide Perovskite Crystals with Unprecedented Long Carrier Dynamics and Diffusion Length'. *ACS Energy Lett.* 2016, **1**, 32–37.

[118] Langevin, P. 'L'ionization des gaz'. *Ann. Chim. Phys*, 1903, **28**, 289–384.

[119] Köhler, A. and Bässler, H. *Electronic and Optical Processes of Organic Semiconductors.* Wiley-VCH Weinheim, Germany, 2015. Chap. 3.

[120] Heiber, M. C.; Baumbach, C.; Dyakonov, V. and Deibel, C. 'Encounter-limited charge-carrier recombination in phase-separated organic semiconductor blends'. *Phys. Rev. Lett.* 2015, **114**, 136602.

[121] Wehrenfennig, C.; Liu, M.; Snaith, H. J.; Johnston, M. B. and Herz, L. M. 'Charge-carrier dynamics in vapour-deposited films of the organolead halide perovskite $CH_3NH_3PbI_{3-x}Cl_x$'. *Energy Environ Sci*, 2014, **7**, 2269–2275.

[122] Blancon, J.-C.; Nie, W.; Neukirch, A. J.; Gupta, G.; Tretiak, S.; Cognet, L.; Mohite, A. D. and Crochet, J. J. 'The Effects of Electronic Impurities and Electron-Hole Recombination Dynamics on Large-Grain Organic-Inorganic Perovskite Photovoltaic Efficiencies'. *Adv. Funct. Mater.* 2016, **26**, 4283–4292.

[123] Adriaenssens, G. and Arkhipov, V. 'Non-Langevin recombination in disordered materials with random potential distributions'. *Solid State Commun.* 1997, **103**, 541–543.

[124] Azarhoosh, P.; McKechnie, S.; Frost, J. M.; Walsh, A. and Van Schilfgaarde, M. 'Research Update: Relativistic origin of slow electron-hole recombination in hybrid halide perovskite solar cells'. *APL Mater.* 2016, **4**, 091501.

[125] Filippetti, A.; Delugas, P. and Mattoni, A. 'Radiative recombination and photoconversion of methylammonium lead iodide perovskite by first principles: properties of an inorganic semiconductor within a hybrid body'. *J. Phys. Chem. C*, 2014, **118**, 24843–24853.

[126] Bhattacharya, R.; Pal, B. and Bansal, B. 'On conversion of luminescence into absorption and the van Roosbroeck-Shockley relation'. *Appl. Phys. Lett.* 2012, **100**, 1–4.

[127] Bonner, T. 'The Luminosity of a Flame Containing Sodium Vapor'. *Phys. Rev.* 1932, **40**, 105.

[128] Ettenberg, M and Kressel, H. 'Interfacial recombination at (AlGa) As/GaAs heterojunction structures'. *J. Appl. Phys.* 1976, **47**, 1538–1544.

[129] Asbeck, P. 'Self-absorption effects on the radiative lifetime in GaAs-GaAlAs double heterostructures'. *J. Appl. Phys.* 1977, **48**, 820–822.

[130] Steiner, M.; Geisz, J.; Garcia, I; Friedman, D.; Duda, A and Kurtz, S. 'Optical enhancement of the open-circuit voltage in high quality GaAs solar cells'. *J. Appl. Phys.* 2013, **113**, 123109.

[131] Ahrenkiel, R. K.; Dunlavy, D. J.; Keyes, B.; Vernon, S. M.; Dixon, T. M.; Tobin, S. P.; Miller, K. L.; Hayes, R. E.; Ahrenkie, R. K.; Dunlavy, D. J. *et al.* 'Ultralong minority carrier lifetime epitaxial GaAs by photon recycling Ufetime epitaxial GaAs by photon recycling'. *Appl. Phys. Lett.* 1989, **55**, 1088–1090.

[132] Pazos-Outon, L. M.; Szumilo, M.; Lamboll, R.; Richter, J. M.; Crespo-Quesada, M.; Abdi-Jalebi, M.; Beeson, H. J.; Vrucinic, M.; Alsari, M.; Snaith, H. J. *et al.* 'Photon recycling in lead iodide perovskite solar cells'. *Science*, 2016, **351**, 1430–1433.

[133] Richter, J. M.; Abdi-Jalebi, M.; Sadhanala, A.; Tabachnyk, M.; Rivett, J. P.; Pazos-Outón, L. M.; Gödel, K. C.; Price, M.; Deschler, F. and Friend, R. H. 'Enhancing photoluminescence yields in lead halide perovskites by photon recycling and light out-coupling'. *Nat. Commun.* 2016, **7**, 13941.

[134] Kirchartz, T.; Staub, F. and Rau, U. 'Impact of Photon-Recycling on the Open-Circuit Voltage of Metal Halide Perovskite Solar Cells'. *ACS Energy Lett.* 2016, **1**, 731–739.

[135] Saliba, M.; Zhang, W.; Burlakov, V. M.; Stranks, S. D.; Sun, Y.; Ball, J. M.; Johnston, M. B.; Goriely, A.; Wiesner, U. and Snaith, H. J. 'Plasmonic-Induced Photon Recycling in Metal Halide Perovskite Solar Cells'. *Adv. Funct. Mater.* 2015, **25**, 5038–5046.

[136] Burhop, E. H. S. *The Auger effect and other radiationless transitions.* Cambridge University Press, 2014.

[137] Flender, O.; Klein, J. R.; Lenzer, T. and Oum, K. 'Ultrafast photoinduced dynamics of the organolead trihalide perovskite $CH_3NH_3PbI_3$ on mesoporous TiO_2 scaffolds in the 320-920 nm range'. *Phys. Chem. Chem. Phys.* 2015, **17**, 19238–19246.

[138] Rehman, W.; Milot, R. L.; Eperon, G. E.; Wehrenfennig, C.; Boland, J. L.; Snaith, H. J.; Johnston, M. B. and Herz, L. M. 'Charge-carrier dynamics and mobilities in formamidinium lead mixed-halide perovskites'. *Adv. Mater.* 2015, **27**, 7938–7944.

[139] Sutherland, B. R. and Sargent, E. H. 'Perovskite photonic sources'. *Nat. Photon.* 2016, **10**, 295.

[140] Saliba, M.; Wood, S. M.; Patel, J. B.; Nayak, P. K.; Huang, J.; Alexander-Webber, J. A.; Wenger, B.; Stranks, S. D.; Hörantner, M. T.; Wang, J. T.-W. *et al.* 'Structured organic–inorganic perovskite toward a distributed feedback laser'. *Adv. Mater.* 2016, **28**, 923–929.

[141] Aneesh, J; Swarnkar, A.; Kumar Ravi, V.; Sharma, R.; Nag, A. and Adarsh, K. 'Ultrafast exciton dynamics in colloidal $CsPbBr_3$ perovskite nanocrystals: Biexciton effect and Auger recombination'. *J. Phys. Chem. C*, 2017, **121**, 4734–4739.

[142] Ettenberg, M; Kressel, H and Gilbert, S. 'Minority carrier diffusion length and recombination lifetime in GaAs: Ge prepared by liquid-phase epitaxy'. *J. Appl. Phys.* 1973, **44**, 827–831.

[143] Dixon, R. and Joyce, W. 'Generalized expressions for the turn-on delay in semiconductor lasers'. *J. Appl. Phys.* 1979, **50**, 4591–4595.

[144] Su, C. and Olshansky, R. 'Carrier lifetime measurement for determination of recombination rates and doping levels of III-V semiconductor light sources'. *Appl. Phys. Lett.* 1982, **41**, 833–835.

[145] Zielbauer, J. and Wegener, M. 'Ultrafast optical pump THz-probe spectroscopy on silicon'. *Appl. Phys. Lett.* 1996, **68**, 1223–1225.

[146] Saeta, P. N.; Federici, J. F.; Greene, B. I. and Dykaar, D. R. 'Intervalley scattering in GaAs and InP probed by pulsed far-infrared transmission spectroscopy'. *Appl. Phys. Lett.* 1992, **60**, 1477–1479.

[147] Beard, M. C.; Turner, G. M. and Schmuttenmaer, C. A. 'Transient photoconductivity in GaAs as measured by time-resolved terahertz spectroscopy'. *Phys. Rev. B*, 23 2000, **62**, 15764–15777.

[148] Fu, J.; Xu, Q.; Han, G.; Wu, B.; Huan, C. H. A.; Leek, M. L. and Sum, T. C. 'Hot carrier cooling mechanisms in halide perovskites'. *Nat. Commun.* 2017, **8**, 1300.

[149] Price, M. B.; Butkus, J.; Jellicoe, T. C.; Sadhanala, A.; Briane, A.; Halpert, J. E.; Broch, K.; Hodgkiss, J. M.; Friend, R. H. and Deschler, F. 'Hot-carrier cooling and photoinduced refractive index changes in organic–inorganic lead halide perovskites'. *Nat. Commun.* 2015, **6**, 8420.

[150] Manser, J. S. and Kamat, P. V. 'Band filling with free charge carriers in organometal halide perovskites'. *Nat. Photon.* 2014, **8**, 737–743.

[151] Salim, T.; Kadro, J.; Khuc, M.-T.; Haselsberger, R.; Cheng, L.; Xia, H.; Gurzadyan, G. G.; Su, H.; Lam, Y. M.; Marcus, R. A. *et al.* 'Elucidating the role of disorder and free-carrier recombination kinetics in $CH_3NH_3PbI_3$ perovskite films'. *Nat. Commun*, 2015, **6**, 7903.

[152] Piatkowski, P.; Cohen, B.; Ramos, F. J.; Di Nunzio, M.; Nazeeruddin, M. K.; Grätzel, M.; Ahmad, S. and Douhal, A. 'Direct monitoring of ultrafast electron and hole dynamics in perovskite solar cells'. *Phys. Chem. Chem. Phys.* 2015, **17**, 14674–14684.

[153] Savenije, T. J.; Ponseca, C. S.; Kunneman, L.; Abdellah, M.; Zheng, K.; Tian, Y.; Zhu, Q.; Canton, S. E.; Scheblykin, I. G.; Pullerits, T. *et al.* 'Thermally activated exciton dissociation and recombination control the carrier dynamics in organometal halide perovskite'. *J. Phys. Chem. Lett.* 2014, **5**, 2189–2194.

[154] Bi, D.; Tress, W.; Dar, M. I.; Gao, P.; Luo, J.; Renevier, C.; Schenk, K.; Abate, A.; Giordano, F.; Baena, J.-P. C. *et al.* 'Efficient luminescent solar cells based on tailored mixed-cation perovskites'. *Sci. Adv.* 2016, **2**, e1501170.

[155] Saba, M.; Cadelano, M.; Marongiu, D.; Chen, F.; Sarritzu, V.; Sestu, N.; Figus, C.; Aresti, M.; Piras, R.; Geddo Lehmann, A. *et al.* 'Correlated electron-hole plasma in organometal perovskites.' *Nat. Commun.* 2014, **5**, 5049.

[156] D'Innocenzo, V.; Srimath Kandada, A. R.; De Bastiani, M.; Gandini, M. and Petrozza, A. 'Tuning the light emission properties by band gap engineering in hybrid lead halide perovskite'. *J. Am. Chem. Soc.* 2014, **136**, 17730–17733.

[157] Strauss, U; Rühle, W. and Köhler, K. 'Auger recombination in intrinsic GaAs'. *Appl. Physi. Lett.* 1993, **62**, 55–57.

[158] Leijtens, T.; Stranks, S. D.; Eperon, G. E.; Lindblad, R.; Johansson, E. M.; McPherson, I. J.; Rensmo, H.; Ball, J. M.; Lee, M. M. and Snaith, H. J. 'Electronic properties of meso-superstructured and planar organometal halide perovskite films: charge trapping, photodoping, and carrier mobility'. *ACS Nano*, 2014, **8**, 7147–7155.

[159] Stranks, S. D.; Burlakov, V. M.; Leijtens, T.; Ball, J. M.; Goriely, A. and Snaith, H. J. 'Recombination kinetics in organic-inorganic perovskites: excitons, free charge, and subgap states'. *Phys. Rev. Appl.* 2014, **2**, 034007.

[160] Murakami, H.; Serita, K.; Maekawa, Y.; Fujiwara, S.; Matsuda, E.; Kim, S.; Kawayama, I. and Tonouchi, M. 'Scanning laser THz imaging system'. *J. Phys. D*, 2014, **47**, 374007.

[161] Milot, R. L.; Klug, M. T.; Davies, C. L.; Wang, Z.; Kraus, H.; Snaith, H. J.; Johnston, M. B. and Herz, L. M. 'The Effects of Doping Density and Temperature on the Optoelectronic Properties of Formamidinium Tin Triiodide Thin Films'. *Adv. Mater.* 2018, **30**, 1804506.

[162] Schmuttenmaer, C. a. 'Exploring dynamics in the far-infrared with terahertz spectroscopy'. *Chem. Rev.* 2004, **104**, 1759–1779.

[163] Beard, M. C.; Turner, G. M. and Schmuttenmaer, C. A. 'Terahertz Spectroscopy'. *J. Phys. Chem. A*, 2002, **106**, 6427–6444.

[164] Van Exter, M.; Fattinger, C. and Grischkowsky, D. 'Terahertz time-domain spectroscopy of water vapor'. *Opt. Lett.* 1989, **14**, 1128–1130.

[165] Pérez-Osorio, M. A.; Milot, R. L.; Filip, M. R.; Patel, J. B.; Herz, L. M.; Johnston, M. B. and Giustino, F. 'Vibrational properties of the organic–inorganic halide perovskite $CH_3NH_3PbI_3$ from theory and experiment: factor group analysis, first-principles calculations, and low-temperature infrared spectra'. *J. Phys. Chem. C*, 2015, **119**, 25703–25718.

[166] Dorney, T. D.; Baraniuk, R. G. and Mittleman, D. M. 'Material parameter estimation with terahertz time-domain spectroscopy'. *JOSA A*, 2001, **18**, 1562–1571.

[167] Duvillaret, L.; Garet, F. and Coutaz, J.-L. 'A reliable method for extraction of material parameters in terahertz time-domain spectroscopy'. *IEEE J. Sel. Top. Quantum Electron.* 1996, **2**, 739–746.

[168] Němec, H; Kadlec, F and Kužel, P. 'Methodology of an optical pump-terahertz probe experiment: An analytical frequency-domain approach'. *J. Chem. Phys.* 2002, **117**, 8454–8466.

[169] Ulbricht, R.; Hendry, E.; Shan, J.; Heinz, T. F. and Bonn, M. 'Carrier dynamics in semiconductors studied with time-resolved terahertz spectroscopy'. *Rev. Mod. Phys.* 2011, **83**, 543–586.

[170] Lui, K. and Hegmann, F. 'Ultrafast carrier relaxation in radiation-damaged silicon on sapphire studied by optical-pump–terahertz-probe experiments'. *Appl. Phys. Lett.* 2001, **78**, 3478–3480.

[171] Cunningham, P. D. and Hayden, L. M. 'Carrier dynamics resulting from above and below gap excitation of P3HT and P3HT/PCBM investigated by optical-pump terahertz-probe spectroscopy'. *J Phys. Chem. C*, 2008, **112**, 7928–7935.

[172] Parkinson, P.; Joyce, H. J.; Gao, Q.; Tan, H. H.; Zhang, X.; Zou, J.; Jagadish, C.; Herz, L. M. and Johnston, M. B. 'Carrier lifetime and mobility enhancement in nearly defect-free core- shell nanowires measured using time-resolved terahertz spectroscopy'. *Nano Lett.* 2009, **9**, 3349–3353.

[173] Boland, J. L.; Conesa-Boj, S.; Parkinson, P.; Tötöncöoglu, G.; Matteini, F.; Röffer, D.; Casadei, A.; Amaduzzi, F.; Jabeen, F.; Davies, C. L. *et al.* 'Modulation doping of GaAs/AlGaAs core–shell nanowires with effective defect passivation and high electron mobility'. *Nano Lett.* 2015, **15**, 1336–1342.

[174] Berera, R.; Grondelle, R. van and Kennis, J. T. M. 'Ultrafast transient absorption spectroscopy: principles and application to photosynthetic systems'. *Photosynth. Res.* 2009, **101**, 105–118.

[175] Sheng, C.; Zhang, C.; Zhai, Y.; Mielczarek, K.; Wang, W.; Ma, W.; Zakhidov, A. and Vardeny, Z. V. 'Exciton versus Free Carrier Photogeneration in Organometal Trihalide Perovskites Probed by Broadband Ultrafast Polarization Memory Dynamics'. *Phys. Rev. Lett.* 11 2015, **114**, 116601.

[176] Anand, B.; Sampat, S.; Danilov, E. O.; Peng, W.; Rupich, S. M.; Chabal, Y. J.; Gartstein, Y. N. and Malko, A. V. 'Broadband transient absorption study of photoexcitations in lead halide perovskites: Towards a multiband picture'. *Phys. Rev. B*, 16 2016, **93**, 161205.

[177] Tonouchi, M. 'Cutting-edge terahertz technology'. *Nat. Photonics*, 2007, **1**, 97–105.

[178] Lewis, R. A. 'A review of terahertz sources'. *J. Phys. D*, 2014, **47**, 374001.

[179] Chang, G.; Divin, C. J.; Liu, C.-H.; Williamson, S. L.; Galvanauskas, A. and Norris, T. B. 'Power scalable compact THz system based on an ultrafast Yb-doped fiber amplifier'. *Optics Express*, 2006, **14**, 7909–7913.

[180] Rice, A; Jin, Y; Ma, X.; Zhang, X.-C.; Bliss, D; Larkin, J and Alexander, M. 'Terahertz optical rectification from $< 110 >$ zinc-blende crystals'. *Appl. Phys. Lett.* 1994, **64**, 1324–1326.

[181] Seifert, T.; Jaiswal, S; Martens, U; Hannegan, J; Braun, L.; Maldonado, P.; Freimuth, F; Kronenberg, A; Henrizi, J; Radu, I *et al.* 'Efficient metallic spintronic emitters of ultrabroadband terahertz radiation'. *Nat. Photon.* 2016, **10**, 483.

[182] Walowski, J. and Münzenberg, M. 'Perspective: Ultrafast magnetism and THz spintronics'. *J. Appl. Phys.* 2016, **120**, 140901.

[183] Sinova, J.; Valenzuela, S. O.; Wunderlich, J; Back, C. and Jungwirth, T. 'Spin hall effects'. *Rev. Mod. Phys.* 2015, **87**, 1213.

[184] Wu, Q. and Zhang, X.-C. 'Free-space electro-optic sampling of terahertz beams'. *Appl. Phys. Lett.* 1995, **67**, 3523–3525.

[185] Horowitz, P. and Hill, W. *The art of electronics.* Cambridge Univ. Press, 1989. Chap. 15.

[186] Goree, J. 'Double lock-in detection for recovering weak coherent radio frequency signals'. *Rev. Sci. Instrum.* 1985, **56**, 1662–1664.

[187] Hieftje, G. 'Signal-to-noise enhancement through instrumental techniques. II. Signal averaging, boxcar integration, and correlation techniques'. *Anal. Chem.* 1972, **44**, 69A–78a.

[188] Nienhuys, H.-K. and Sundström, V. 'Intrinsic complications in the analysis of optical-pump, terahertz probe experiments'. *Phys. Rev. B*, 2005, **71**, 235110.

[189] Mooney, J. and Kambhampati, P. 'Get the basics right: Jacobian conversion of wavelength and energy scales for quantitative analysis of emission spectra'. *J. Phys. Chem. Lett.* 2013, **4**, 3316–3318.

[190] Harbecke, B. 'Coherent and Incoherent Reflection and Transmission of Multilayer Structures'. *Appl. Phys. B*, 1986, **39**, 165–170.

[191] Weber, H. 'The Fresnel equations for lossy dielectrics and conservation of energy'. *J. Mod. Opt.* 2014, **61**, 1219–1224.

[192] El-Amassi, D. M. and Taya, S. A. 'Reflected and transmitted powers of p-polarized electromagnetic waves through a dielectric slab surrounded by double negative materials'. *J. Electromagnet. Wave*, 2018, **32**, 1541–1559.

[193] Phillips, R. 'A numerical method for determining the complex refractive index from reflectance and transmittance of supported thin films'. *J. Phys. D*, 1983, **16**, 489.

[194] Harris, L.; Beasley, J. K. and Loeb, A. L. 'Reflection and transmission of radiation by metal films and the influence of nonabsorbing backings'. *Josa*, 1951, **41**, 604–614.

[195] Campa, A.; Krc, J. and Topic, M. 'Two approaches for incoherent propagation of light in rigorous numerical simulations'. *Prog. Electromagn. Res.* 2013, **137**, 187–202.

[196] Mitsas, C. and Siapkas, D. 'Generalized matrix method for analysis of coherent and incoherent reflectance and transmittance of multilayer structures with rough surfaces, interfaces, and finite substrates'. *Appl. Opt.* 1995, **34**, 1678–1683.

[197] Katsidis, C. C. and Siapkas, D. I. 'General transfer-matrix method for optical multilayer systems with coherent, partially coherent, and incoherent interference.' *Appl. Opt.* 2002, **41**, 3978–3987.

[198] Frezza, F. and Tedeschi, N. 'On the electromagnetic power transmission between two lossy media: discussion'. *JOSA A*, 2012, **29**, 2281–2288.

[199] Mangini, F. and Frezza, F. 'Analysis of the electromagnetic reflection and transmission through a stratified lossy medium of an elliptically polarized plane wave'. *Math. Mech. Complex Syst.* 2016, **4**, 153–167.

[200] Cooke, D. G.; MacDonald, A. N.; Hryciw, A.; Wang, J.; Li, Q.; Meldrum, A. and Hegmann, F. A. 'Transient terahertz conductivity in photoexcited silicon nanocrystal films'. *Phys. Rev. B*, 19 2006, **73**, 193311.

[201] Henning, P. F.; Homes, C. C.; Maslov, S.; Carr, G. L.; Basov, D. N.; Nikolić, B. and Strongin, M. 'Infrared Studies of the Onset of Conductivity in Ultrathin Pb Films'. *Phys. Rev. Lett.* 23 1999, **83**, 4880–4883.

[202] Thorp, D. and Wenham, S. R. 'Ray-tracing of arbitrary surface textures for light-trapping in thin silicon solar cells'. *Sol. Energy Mater Sol. Cells*, 1997, **48**, 295–301.

[203] Kosten, E. D.; Atwater, J. H.; Parsons, J.; Polman, A. and Atwater, H. A. 'Highly efficient GaAs solar cells by limiting light emission angle'. *Light Sci. Appl.* 2013, 1–6.

[204] Durbin, S. and Gray, J. 'Numerical modeling of photon recycling in solar cells'. *IEEE Trans. Electron Devices*, 1994, **41**, 239–245.

[205] Parks Jr, J. W.; Brennan, K. F. and Smith, A. W. 'Two-dimensional model of photon recycling in direct gap semiconductor devices'. *J. appl. phys.* 1997, **82**, 3493–3498.

[206] Helm, R.; Johnson, R. E.; Gamma, E. and Vlissides, J. *Design patterns: elements of reusable object-oriented software*. Addison-Wesley, 1994. Chap. 5.

[207] Yang, Y.; Yang, M.; Li, Z.; Crisp, R.; Zhu, K. and Beard, M. C. 'Comparison of Recombination Dynamics in $CH_3NH_3PbBr_3$ and $CH_3NH_3PbI_3$ Perovskite Films: Influence of Exciton Binding Energy'. *J. Phys. Chem. Lett*, 2015, **6**, 4688–4692.

[208] Piatkowski, P.; Cohen, B.; Ponseca, C. S.; Salado, M.; Kazim, S.; Ahmad, S.; Sundström, V. and Douhal, A. 'Unraveling Charge Carriers Generation, Diffusion, and Recombination in Formamidinium Lead Triiodide Perovskite Polycrystalline Thin Film'. *J. Phys. Chem. Lett.* 2015, **7**, 204–210.

[209] Yamada, Y.; Yamada, T. and Kanemitsu, Y. 'Free carrier radiative recombination and photon recycling in lead halide perovskite solar cell materials'. *Bull. Chem. Soc. Jpn.* 2017, **90**, 1129–1140.

[210] Ha, S.-T.; Shen, C.; Zhang, J. and Xiong, Q. 'Laser cooling of organic-inorganic lead halide perovskites'. *Nat. Photon.* 2015, **10**, 115–121.

[211] Green, M. A.; Emery, K.; Hishikawa, Y.; Warta, W. and Dunlop, E. D. 'Solar cell efficiency tables (version 48)'. *Prog. Photovolt. Res. Appl*, 2016, **24**, 905–913.

[212] Herz, L. M. 'Charge-carrier mobilities in metal halide perovskites: Fundamental mechanisms and limits'. *ACS Energy Letters*, 2017, **2**, 1539–1548.

[213] Galkowski, K.; Mitioglu, A.; Miyata, A.; Plochocka, P.; Portugall, O.; Eperon, G. E.; Wang, J. T. W.; Stergiopoulos, T.; Stranks, S. D.; Snaith, H. *et al.* 'Determination of the exciton binding energy and effective masses for methylammonium and formamidinium lead tri-halide perovskite semiconductors'. *Energy Environ. Sci.* 2016, **9**, 962–970.

[214] Varshni, Y. P. 'Band-to-Band Radiative Recombination in Groups IV, VI, and III/V Semiconductors (I)'. *physica status solidi (b)*, 1967, **19**, 459–514.

[215] Guo, Z.; Manser, J. S.; Wan, Y.; Kamat, P. V. and Huang, L. 'Spatial and temporal imaging of long-range charge transport in perovskite thin films by ultrafast microscopy'. en. *Nat. Commun.* 2015, **6**, 7471–7478.

[216] De Wolf, S.; Holovsky, J.; Moon, S. J.; Löper, P.; Niesen, B.; Ledinsky, M.; Haug, F. J.; Yum, J. H. and Ballif, C. 'Organometallic halide perovskites: Sharp optical absorption edge and its relation to photovoltaic performance'. *J. Phys. Chem. Lett*, 2014, **5**, 1035–1039.

[217] Schlipf, J. and Müller-Buschbaum, P. 'Structure of Organometal Halide Perovskite Films as Determined with Grazing-Incidence X-Ray Scattering Methods'. *Adv. Energy Mater.* 2017, 16146840.

[218] Tiwana, P.; Docampo, P.; Johnston, M. B.; Herz, L. and Snaith, H. 'The origin of an efficiency improving "light soaking" effect in {SnO}$_2$ based solid-state dye-sensitized solar cells'. *Energy Environ. Sci.* 2012, **5**, 9566–9573.

[219] Docampo, P.; Tiwana, P.; Sakai, N.; Miura, H.; Herz, L.; Murakami, T. and Snaith, H. J. 'Unraveling the Function of an MgO Interlayer in Both Electrolyte and Solid-State SnO_2 Based Dye-Sensitized Solar Cells'. *J. Phys. Chem. C*, 2012, **116**, 22840–22846.

[220] Wehrenfennig, C.; Liu, M.; Snaith, H. J.; Johnston, M. B. and Herz, L. M. 'Homogeneous Emission Line Broadening in the Organo Lead Halide Perovskite $CH_3NH_3PbI_{3-x}Cl_x$'. *J. Phys. Chem. Lett.* 2014, **5**, 1300–1306.

[221] Milot, R. L.; Sutton, R. J.; Eperon, G. E.; Haghighirad, A. A.; Hardigree, J. M.; Miranda, L.; Snaith, H. J.; Johnston, M. B. and Herz, L. M. 'Charge-Carrier Dynamics in 2D Hybrid Metal-Halide Perovskites'. *Nano Letters*, 2016, **16**, 7001–7007.

[222] Balenzategui, J. L. and Marti, A. 'Detailed modelling of photon recycling: Application to GaAs solar cells'. *Sol. Energ. Mat. Sol. Cells*, 2006, **90**, 1068–1088.

[223] Parrott, J. E. 'Radiative recombination and photon recycling in photovoltaic solar cells'. *Sol. Energ. Mat. Sol. Cells*, 1993, **30**, 221–231.

[224] Chen, Y.; Yi, H. T.; Wu, X.; Haroldson, R.; Gartstein, Y. N.; Rodionov, Y. I.; Tikhonov, K. S.; Zakhidov, A.; Zhu, X. Y. and Podzorov, V. 'Extended carrier lifetimes and diffusion in hybrid perovskites revealed by Hall effect and photoconductivity measurements'. *Nat. Commun.* 2016, **7**, 12253.

[225] Khan, M. R.; Wang, X.; Asadpour, R.; Lundstrom, M. and Alam, M. A. 'Role of photon recycling in perovskite solar cells'. *arXiv:1612.06731*, 2016, 1–9.

[226] Reuter, H. and Schmitt, H. 'On the efficiency of photon recycling in solar cells'. *Sol. Energ. Mat. Sol. Cells*, 1994, **33**, 369–377.

[227] Poruba, a.; Fejfar, A.; Remeš, Z.; Špringer, J.; Vaněček, M.; Kočka, J.; Meier, J.; Torres, P. and Shah, A. 'Optical absorption and light scattering in microcrystalline silicon thin films and solar cells'. *J. Appl. Phys.* 2000, **88**, 148–160.

[228] Martí, A.; Balenzategui, J. L. and Reyna, R. 'Photon recycling and Shockley's diode equation'. *J. Appl. Phys.* 1997, **82**, 4067–4075.

[229] Polman, A.; Knight, M.; Garnett, E. C.; Ehrler, B. and Sinke, W. C. 'Photovoltaic materials – present efficiencies and future challenges'. *Science*, 2016, **352**, 307.

[230] Hutter, E. M.; Eperon, G. E.; Stranks, S. D. and Savenije, T. J. 'Charge Carriers in Planar and Meso-Structured Organic-Inorganic Perovskites: Mobilities, Lifetimes, and Concentration of Trap States'. *J. Phys. Chem. Lett.* 2015, **6**, 3082–3090.

[231] De Bastiani, M.; D'Innocenzo, V.; Stranks, S. D.; Snaith, H. J. and Petrozza, A. 'Role of the crystallization substrate on the photoluminescence properties of organolead mixed halides perovskites'. *APL Mater.* 2014, **2**, 081509.

[232] Rehman, W.; McMeekin, D. P.; Patel, J. B.; Milot, R. L.; Johnston, M. B.; Snaith, H. J. and Herz, L. M. 'Photovoltaic mixed-cation lead mixed-halide perovskites: links between crystallinity, photo-stability and electronic properties'. *Energy Environ. Sci.* 2017, **10**, 361–369.

[233] Leguy, A.; Azarhoosh, P.; Alonso, M. I.; Campoy-Quiles, M.; Weber, O. J.; Yao, J.; Bryant, D.; Weller, M. T.; Nelson, J.; Walsh, A. *et al.* 'Experimental and theoretical optical properties of methylammonium lead halide perovskites'. *Nanoscale*, 2015, **8**, 6317–6327.

[234] Liu, T.; Jiang, Y.; Qin, M.; Liu, J.; Sun, L.; Qin, F.; Hu, L.; Xiong, S.; Jiang, X.; Jiang, F. *et al.* 'Tailoring vertical phase distribution of quasi-two-dimensional perovskite films via surface modification of hole-transporting layer'. *Nat. Commun.* 2019, **10**.

[235] Liu, J.; Leng, J.; Wu, K.; Zhang, J. and Jin, S. 'Observation of internal photoinduced electron and hole separation in hybrid two-dimentional perovskite films'. *J. Am. Chem. Soc.* 2017, **139**, 1432–1435.

[236] Shang, Q.; Wang, Y.; Zhong, Y.; Mi, Y.; Qin, L.; Zhao, Y.; Qiu, X.; Liu, X. and Zhang, Q. 'Unveiling structurally engineered carrier dynamics in hybrid quasi-two-dimensional perovskite thin films toward controllable emission'. *J. Phys. Chem. Lett*, 2017, **8**, 4431–4438.

[237] Wang, N.; Cheng, L.; Ge, R.; Zhang, S.; Miao, Y.; Zou, W.; Yi, C.; Sun, Y.; Cao, Y.; Yang, R. *et al.* 'Perovskite light-emitting diodes based on solution-processed self-organized multiple quantum wells'. *Nat. Photon.* 2016, **10**, 699.

[238] Yang, R.; Li, R.; Cao, Y.; Wei, Y.; Miao, Y.; Tan, W. L.; Jiao, X.; Chen, H.; Zhang, L.; Chen, Q. *et al.* 'Oriented Quasi-2D Perovskites for High Performance Optoelectronic Devices'. *Adv. Mater.* 2018, **30**, 1804771.

[239] Crothers, T. W.; Milot, R. L.; Patel, J. B.; Parrott, E. S.; Schlipf, J.; Müller-Buschbaum, P.; Johnston, M. B. and Herz, L. M. 'Photon reabsorption masks intrinsic bimolecular charge-carrier recombination in $CH_3NH_3PbI_3$ perovskite'. *Nano Lett.* 2017, **17**, 5782–5789.

[240] Oesinghaus, L.; Schlipf, J.; Giesbrecht, N.; Song, L.; Hu, Y.; Bein, T.; Docampo, P. and Müller-Buschbaum, P. 'Toward Tailored Film Morphologies: The Origin of Crystal Orientation in Hybrid Perovskite Thin Films'. *Adv. Energy Mater.* 2016, **3**, 21967350.